eman ta zabal zazu

Universidad del País Vasco
Euskal Herriko Unibertsitatea

Department of Theoretical Physics and History of Science

Extending and testing observational signatures of Cosmic Strings

Joanes Lizarraga Olano

Ph.D. THESIS
Leioa 2016

eman ta zabal zazu

Universidad del País Vasco
Euskal Herriko Unibertsitatea

Department of Theoretical Physics and History of Science

Extending and testing observational signatures of Cosmic Strings

Supervised by Dr. Jon Urrestilla Urizabal
from the University of the Basque Country

Submitted by Joanes Lizarraga Olano
for the degree of Doctor of Physics

Prologue

The work presented in this Thesis explores and tests the observational signatures of cosmic strings. The Thesis is composed by several different projects made in collaboration with my supervisor Jon Urrestilla and our collaborators: David Daverio, Mark B. Hindmarsh, Martin Kunz, Andrew R. Liddle and Irene Sendra.

The *cosmological standard model* has successfully been confirmed by increasingly accurate observations as the correct description of the universe. Nevertheless there are still several unanswered questions regarding the fundamental physics behind some of the processes taking place at the early universe, which mainly lie in the connection between the cosmological and high energy physics descriptions of the universe. One of the most promising candidates to provide such an answer are topological defects. They are predicted in many well motivated high energy and inflationary models, and could survive the cosmological evolution and have observational consequences. Topological defects could be formed at cosmological phase transitions that occurred in the primitive universe. Thus determining the nature and properties of the cosmic defects would provide an invaluable window towards the physics governing the early universe.

In Part I of this Thesis the required theoretical background is introduced. It is composed of two separate Chapters. In the first, Chapter 1, we review the most important aspects of the standard cosmological model, detailing the theory of the *Cosmic Microwave Background* and data analysis techniques. Cosmic defects, including cosmic strings, are discussed in Chapter 2. In the first part of this Chapter we describe the basic properties of several defects and their formation at cosmological phase transitions. In the second part, in turn, we focus on field theory simulations of defects and the computation of their observational signatures. These two Chapters are based on previous articles, reviews and books in the literature.

The original investigations performed during the PhD research period are presented in Part II of the Thesis. In Chapters 1 and 2 we compare CMB power spectra predictions with measurements, mainly CMB. It has to be noted that the analyses of these Chapters were based on datasets and results available in those years, and hence some assumptions might have changed and results have to be interpreted in that context. For instance, what the cosmological community understands as the standard model has evolved during these years, and now includes some ingredients that were not considered then, such as the non-zero sum of the mass of the neutrinos. On the other hand, in Chapters 3 and 4 we explore different numerical simulations towards a better characterization of the properties of field theoretical models for cosmic strings.

The discussion of Chapter 1 is centered on the possible relation between cosmic strings and the apparent excess of relativistic components. The work, performed in 2012, was motivated by measurements of the CMB anisotropies available then, which indicated that the number of relativistic species present at the primitive universe was higher than predicted by the standard particle model. We investigated whether cosmic strings through the stochastic gravitational wave background induced by them could be the responsible for the measured excess. In order to try to

answer that question, we performed a parameter space likelihood analysis fitting CMB (WMAP7 and SPT) and non-CMB (HST and BAO) data with models containing non-standard ingredients such as defects and/or other relativistic species. The procedure and results of this chapter are published in the following paper:

- **Correlations between cosmic strings and extra relativistic species**
  J. Lizarraga, I. Sendra, J. Urrestilla, *Phys. Rev. D 86, 123014 (2012). arXiv:1207.6266.*

Chapter 2 discusses and analyzes B-mode polarization contributions of different cosmic defects: cosmic strings, semilocal strings and textures. The work presented in this Chapter tried to answer questions placed soon after the release of the BICEP2 data and contributed also in the fast moving research atmosphere of the moment. It is based on two published works:

- **Can Topological Defects Mimic the BICEP2 B-Mode Signal?**
  J. Lizarraga, J. Urrestilla, D. Daverio, M.B. Hindmarsh, M. Kunz, A.R. Liddle, *Phys. Rev. Lett. 112 171301 (2014). arXiv:1403.4924.*

- **Constraining topological defects with temperature and polarization anisotropies**
  J. Lizarraga, J. Urrestilla, D. Daverio, M.B. Hindmarsh, M. Kunz, A.R. Liddle, *Phys. Rev. D 90, 103504 (2014). arXiv:1408.4126.*

In the first, which was made public just a week after BICEP2 announcement, we explored qualitatively the possibility of cosmic string being responsible for the total signal measured by the BICEP2 experiment. The second work complemented the previous qualitative paper by providing a comprehensive analysis of the defect contribution to the microwave anisotropies, both in temperature and polarization. In order to accomplish that, we performed Markov Chain Monte Carlo analyses of the parameter space fitting BICEP2 data with and without other CMB experiments (*Planck*, WMAP9 polarization, SPT/ACT), using models where the contribution of defects were added to other possible B-mode sources such as inflationary gravitational waves and astrophysical dust.

In Chapter 3 we present updated energy-momentum correlations and CMB power spectra for Abelian Higgs cosmic strings. We revisit approximations and assumptions done in previous field theoretical works towards a better characterization of the CMB predictions for cosmic strings. The biggest field theory simulations to date are employed to obtain energy-momentum correlators. The evolution of correlators across cosmological transitions, which had been a source of uncertainties in previous works, has also been addressed in order to get a correct description of the source functions required for CMB power spectra calculations. Finally updated CMB power spectra predictions are shown. The work done in this chapter can be found in the following two papers:

- **Energy-momentum correlations for Abelian Higgs cosmic strings**
  D. Daverio, M.B. Hindmarsh, M. Kunz, J. Lizarraga, J. Urrestilla, *Submitted to Phys. Rev. D. arXiv:1510.05006.*

- **Improving CMB power spectra predictions for Abelian Higgs cosmic strings**
  D. Daverio, M.B. Hindmarsh, M. Kunz, J. Lizarraga, J. Urrestilla, *In preparation.*

In the last chapter of this work, Chapter 4, field theoretical simulations are used to describe and understand the cosmological evolution of interconnected superstrings. Interconnected superstring networks composed of fundamental F-string, string-like D-branes and composed bound states are predicted in brane inflation models. Field theory simulations, using effective models, are one of the most interesting ways to try to characterize the evolution of superstring networks. We perform the biggest and most accurate field theory simulation to date, so as to analyze the origin of some discrepancies between the outcome of simulations and theoretical predictions found in previous works. In order to accomplish that, we propose a new initial configuration for the network, where pq-bound strings are present from the beginning of the simulation, coexisting with another string network. Velocities of the network and bound states are also calculated. This Chapter is based on the following article:

- **Survival of pq-superstrings in field theory simulations**
  J. Lizarraga, J. Urrestilla, *Submitted to JCAP arXiv:1602.08014*.

List of Publications

Published Papers

Correlations between cosmic strings and extra relativistic species
J. Lizarraga, I. Sendra, J. Urrestilla, *Phys. Rev. D 86, 123014 (2012). arXiv:1207.6266*.

Can Topological Defects Mimic the BICEP2 B-Mode Signal?
J. Lizarraga, J. Urrestilla, D. Daverio, M.B. Hindmarsh, M. Kunz, A.R. Liddle, *Phys. Rev. Lett. 112 171301 (2014). arXiv:1403.4924*.

Constraining topological defects with temperature and polarization anisotropies
J. Lizarraga, J. Urrestilla, D. Daverio, M.B. Hindmarsh, M. Kunz, A.R. Liddle, *Phys. Rev. D 90, 103504 (2014). arXiv:1408.4126*.

Submitted Papers

Energy-momentum correlations for Abelian Higgs cosmic strings
D. Daverio, M.B. Hindmarsh, M. Kunz, J. Lizarraga, J. Urrestilla, *Submitted to Phys. Rev. D. arXiv:1510.05006*.

Survival of pq-superstrings in field theory simulations
J. Lizarraga, J. Urrestilla, *Submitted to JCAP arXiv:1602.08014*.

In preparation

Improving CMB power spectra predictions for Abelian Higgs cosmic strings
D. Daverio, M.B. Hindmarsh, M. Kunz, J. Lizarraga, J. Urrestilla, *In preparation*.

Proceedings

Fitting BICEP2 with defects, primordial gravitational waves and dust
J. Lizarraga, J. Urrestilla, D. Daverio, M.B. Hindmarsh, M. Kunz, A.R. Liddle, *J.Phys.Conf.Ser. 600 (2015) 1, 012025. arXiv:1412.0407*.

Contents

Prologue i
List of Publications iv

I Introduction **1**

1 Cosmology and early universe **3**
1.1 Cosmological background 3
1.1.1 FLRW metric and Friedmann equations 4
1.1.2 The concordance model: ΛCDM 6
1.1.3 Inflation 8
1.1.4 Brief thermal history 10
1.2 Cosmic Microwave Background 12
1.2.1 Polarization: B-modes 14
1.2.2 CMB experimets 15
1.3 Data analysis 19
1.3.1 Parameter estimation 19
1.3.2 Markov Chain Monte Carlo 20

2 Cosmic strings and defects **23**
2.1 Topological defects 23
2.1.1 Cosmic strings 30
2.1.2 Semilocal strings 33
2.1.3 Textures 34
2.1.4 Interconnected strings: *pq*-strings 35
2.2 Defect dynamics in expanding universes: field theory simulations 36
2.3 CMB: UETC approach 39

II Results **45**

1 Correlations between cosmic strings and extra relativistic degrees of freedom **47**
1.1 Theoretical Background 48
1.1.1 Effective Number of Neutrinos 48
1.1.2 Cosmological Gravitational Wave Background 49
1.1.3 Gravitational wave background produced by cosmic strings 51
1.2 Method and implementation 52

1.3 Results . . . 54
1.3.1 WMAP 7-year . . . 54
1.3.2 WMAP7 + SPT . . . 57
1.3.3 Harrison-Zel'dovich ($\mathcal{HZ}$), $n_{\rm s} = 1$ . . . 60
1.3.4 $N^*_{\rm eff} = 0$ . . . 60
1.4 Discussion and Conclusions . . . 62

2 Fitting BICEP2 with defects, primordial gravitational waves and dust 65
2.1 *B*-modes of cosmological origin . . . 66
2.1.1 Inflationary tensor modes: r . . . 66
2.1.2 Cosmological defects . . . 67
2.2 Method and implementation . . . 68
2.3 Results . . . 70
2.3.1 Can topological defects mimic the BICEP2 B-mode signal? . . . 70
2.3.2 Constraints from the Monte Carlo Analysis . . . 72
2.4 Discussion and conclusions . . . 76

3 Improving CMB power spectra from Abelian Higgs cosmic strings 79
3.1 UETCs from the simulations . . . 80
3.1.1 Simulation details . . . 81
3.1.2 Scaling . . . 83
3.1.3 UETC merging . . . 84
3.1.4 UETC fitting and small-scale correction . . . 88
3.2 Eigenvector decomposition at cosmological transitions . . . 90
3.2.1 Simple eigenvector interpolation . . . 93
3.2.2 Multi-stage eigenvector interpolation . . . 94
3.2.3 Fixed-k UETC interpolation . . . 96
3.2.4 Interpolating functions $f(\tau)$ and $f_\Lambda(\tau)$ . . . 98
3.2.5 Matter-Λ interpolation . . . 101
3.2.6 Comparison of interpolation methods . . . 103
3.3 New power spectra and error assessment . . . 103
3.3.1 Comparison with 2010: $s = 1$ . . . 105
3.3.2 Effects of the new radiation-matter transition function and multi-stage method . . . 106
3.3.3 Effects of the matter-Λ transition function . . . 106
3.3.4 Effects of fixed-k UETC interpolation . . . 107
3.3.5 Final C_ℓ's . . . 108
3.4 Discussion and Conclusions . . . 110

4 Survival of pq-superstrings in field theory simulations 113
4.1 Model . . . 114
4.1.1 Model and parameter choice . . . 114
4.1.2 Simulation details . . . 116
4.1.3 Output treatment: pq-segment identification . . . 117
4.2 Procedure to combine strings . . . 119
4.3 Results . . . 121
4.3.1 Velocities . . . 127
4.4 Discussion . . . 130

5 General Conclusions **133**

Bibliography **136**

PART I

Introduction

1 Cosmology and early universe

1.1 Cosmological background

The humanity, during its whole history, has observed and studied with curiosity the sky. The complete understanding of its details requires a proper mathematical structure where predictions can be compared with observations. Newtonian mechanics and the newtonian theory of gravity were the first theories that provided the indispensable mathematical structure with remarkable results, predicting successfully the dynamics of celestial bodies and their orbits.

Cosmology is the branch of physics that studies and describes the universe as an entity. Using the most possible general statements, cosmology explores the structure and the formation and evolution of the universe using different perspectives. Newtonian description of the universe was restricted in this regard and such general questions about the universe remained beyond its applicability. It was in the beginning of the last century, when Einstein proposed his theory of *general relativity*, when cosmology was provided with the ideal mathematical framework to develop a predictive and reliable model for the description of the universe.

Within the framework supplied by general relativity, it has been possible to establish a model for the universe that is successful in its predictions, which englobes all its evolution and is widely accepted by the cosmological community. The *standard cosmological model* is based on two fundamental hypotheses, encapsulated in the so-called *cosmological principle*. In the literature, the cosmological principle has been treated as the generalization of the Copernican principle and states the following:

1. The universe is *isotropic*. The universe has rotational invariance and hence it is the same in all directions of the sky.

2. The universe is *homogeneous*. The universe has translational invariance and thus all points are equivalent, *i.e.* there are no privileged points in the universe.

It is worthwhile to note that these two hypotheses should not be taken strictly at all scales. It is evident that the observable stars or galaxies do not follow an isotropic and homogeneous formation and clustering pattern. In other words, the cosmological principle does not hold locally and must be considered as a global feature of the universe at very large scales. Therefore, it is desirable to define our universe as isotropic and homogeneous except for local irregularities. A very robust evidence of the isotropy of the universe is given by *cosmic microwave background* experiments, confirming the existence of such radiation background which is highly isotropic and is composed of photons that decoupled when the universe was really hot and dense (see section 1.2).

On the other hand, our universe is not homogeneous in time, *i.e.* the universe is not static, instead, it is expanding. This was firstly pointed out by E. Hubble in 1929 when he discovered, by analyzing the relative motion of galaxies, that the universe was indeed expanding [113]. What Hubble measured was that the velocity at which galaxies were moving away from us increased with distance and proposed the so-called Hubble's law:

$$v = H_0 d\,, \tag{1.1}$$

where H_0 is the Hubble's constant and d is the physical distance to the galaxy.

The expansion of the universe places an interesting scenario: if the universe is and has been expanding, it must have been smaller. Consequently extrapolation inevitably yields to a very important conclusion: it must have initiated from a singular point, the *big bang* singularity. The current cosmological standard model, or similarly the *hot big bang* model, assumes that the current evolution of the universe started from very energetic singular point and evolved and cooled down due to the expansion. CMB radiation is again one of the central pillars of the hot big bang model.

1.1.1 FLRW metric and Friedmann equations

Einstein's theory of gravity is a geometrical theory, where the space-time is perturbed by the presence of matter, but at the same time dictates how the matter content has to move. Both sectors are related by the Einstein's field equations [143]:

$$R_{\mu\nu} - \frac{1}{2} g_{\mu\nu} R = 8\pi G T_{\mu\nu}, \tag{1.2}$$

where G is the Newton's constant. The metric of the space-time is $g_{\mu\nu}$; $R_{\mu\nu}$ and R are the Ricci's tensor and scalar respectively and can be calculated from the expression of the metric. $T_{\mu\nu}$, in turn, is the energy momentum tensor of the constituents of the universe, which are described by perfect fluids in an homogeneous and isotropic universe [217].

The basic ingredient of the space-time sector of the general relativity is the metric, which dictates how distances have to be measured. In relativistic cosmology the metric that describes the global features of the universe, *i.e.* the isotropy, homogeneity and expansion, are encapsulated in the Friedmann-Lemaître-Robertson-Walker (FLRW) metric ($\eta_{\mu\nu}$). Essentially the FLRW metric includes the isotropy and homogeneity of the universe considering spherically symmetric spaces at each time slicing, which are the most symmetric possible spaces. The line element in the FLRW metric reads [217],

$$ds^2 = \eta_{\mu\nu} dx^\mu dx^\nu = -dt^2 + a(t)^2 \left(\frac{dr^2}{1 - Kr^2} + r^2 (d\theta^2 + \sin^2\theta d\phi^2) \right), \tag{1.3}$$

where $a(t)$ is the scale factor and K is the curvature of the space. The metric represents a slicing of space-time with spatial slices that are rescaled by the scale factor $a(t)$, which is directly related to the expansion. Depending on the curvature parameter the geometry of the space varies:

- $K < 0$ Hyperbolic space or open universe.
- $K = 0$ Flat space.
- $K > 0$ Sphere or closed universe.

The equations of motion are obtained solving Eq. (1.2) considering a FLRW universe and the perfect fluid expression of the energy momentum tensor. In principle without symmetry

assumptions there are 10 such equations, however since the FLRW metric is highly symmetric they reduce just to 2:

$$\left(\frac{\dot{a}}{a}\right)^2 = \frac{8\pi G}{3}\sum_i \rho_i - \frac{K}{a^2}, \tag{1.4}$$

$$\frac{\ddot{a}}{a} = -\frac{4\pi G}{3}\sum_i (\rho_i + 3p_i). \tag{1.5}$$

where ρ and p are the energy density and pressure of each cosmic specie.

These are the so-called Friedmann equations. The first relates the evolution of the different forms of energy to the expansion of the universe. Based on this equation, it it is customary to define the Hubble parameter $H = \dot{a}/a$. With this definition the Hubble constant (H_0) is just the Hubble parameter evaluated today. The second equation, in turn, describes the acceleration of the expansion.

Combining both equations we can obtain the continuity equation or the covariant conservation of the energy-momentum tensor:

$$-\dot{\rho} - 3\frac{\dot{a}}{a}(\rho + p) = 0\,. \tag{1.6}$$

Most of the relevant fluids in cosmology obey the barotropic equation of state: $p = \omega\rho$. Under this consideration, the energy densities evolve as:

$$\rho \propto a^{-3(1+\omega)}\,. \tag{1.7}$$

The *ordinary* matter content of the universe is composed by ultra-relativistic particles or radiation and non-relativistic particles. In the case of ultra-relativistic particles one can prove that $\omega = 1/3$ and therefore Eq.(1.7) becomes,

$$\rho_m \propto a^{-4}. \tag{1.8}$$

For the non-relativistic matter, the pressure is negligible comparing to the density, hence $\omega \approx 0$. Therefore,

$$\rho_r \propto a^{-3}. \tag{1.9}$$

The non-relativistic content of the cosmos is divided into 2 categories. On the one hand, part of the non-relativistic energy density is stored in ordinary matter, that is, baryonic matter that can interact electromagnetically. The rest of the energy, on the other hand, is stored in cold dark matter. Dark matter was hypothesized to account for discrepancies between the motion of large astronomical objects and theoretical predictions based on ordinary matter composition. However, nowadays it is indispensable for the standard model and would account for most of the non-relativistic matter of the universe, though the fundamental physics behind it is still unknown.

Equations (1.8) and (1.9) show that the radiation dominates over other species at early times, while non-relativistic matter become more important at latter times. The history of the universe and the most important epoch of the evolution of the universe will be briefly described in Sec. 1.1.4.

Accelerated expansion and dark energy

In the nineties two independent group of astronomers discovered that not only is the universe expanding, but the expansion is also accelerated. They measured the luminosity of several distant supernovae and found that they were dimmer than expected in an non-accelerated or decelerated universe. Nowadays the acceleration of the expansion has been evidenced and confirmed by a variety of experiments: supernovae [94, 100, 167, 195], measurement of cluster properties [34, 35, 83, 211], anisotropies of the CMB [20, 21, 110], cosmic shear measured by weak lensing [168, 208] and Lyman-α forest absorptions [58, 141].

The acceleration could not be explained by *ordinary* species of the standard model, hence it was evident that an extension of the standard model was required. The most common approach is to consider an additional ingredient into the picture, *dark energy*, a energy component with negative pressure that would counteract the gravitational attraction and drive the acceleration of the expansion. It has to be noted that there exist alternatives that try to explain the observations within modified gravity structures without dark energy, but they require the breakdown of Einstein's gravity at large scales.

1.1.2 The concordance model: ΛCDM

The simplest description of the dark energy is given by a perfect fluid with $\omega = -1$, which historically has been referred as the *cosmological constant* (Λ). It was Einstein himself who postulated in the first place the need of the cosmological constant so as to get a static universe, but abandoned the concept after Hubble's discovery of the expansion of the universe. Life's coincidences, Λ was recovered to account for the accelerated expansion of the universe. It can be included naturally in Einstein's equations in the following way:

$$R_{\mu\nu} - \frac{1}{2} g_{\mu\nu} R = 8\pi G T_{\mu\nu} + \Lambda g_{\mu\nu} \,, \tag{1.10}$$

and the modified Friedmann equations are:

$$\left(\frac{\dot{a}}{a}\right)^2 = \frac{8\pi G}{3} \sum_i \rho_i - \frac{K}{a^2} + \frac{\Lambda}{3} \,, \tag{1.11}$$

$$\frac{\ddot{a}}{a} = -\frac{4\pi G}{3} \sum_i (\rho_i + 3p_i) + \frac{\Lambda}{3} \,. \tag{1.12}$$

It is also convenient to define the dimensionless energy densities for each species:

$$\Omega_i = \frac{\rho_i}{\rho_{\rm c}} \,, \tag{1.13}$$

which are defined in terms of the critical energy density: $\rho_{\rm c} = \frac{3H^2}{8\pi G}$.

With this re-parametrization Eq. (1.11) becomes:

$$(\Omega_{\rm m} + \Omega_{\rm r} + \Omega_\Lambda) - 1 = \frac{K}{(aH)^2} \,, \tag{1.14}$$

where $\Omega_\Lambda = \frac{\Lambda}{3H^2}$ and $\Omega_{\rm m} = \Omega_{\rm b} + \Omega_{\rm c}$ is the sum of the baryonic and dark matter energy densities. Given Eq. 1.14 we can relate the spatial curvature with the total energy content of the universe. Indeed, current observations from the CMB [21] give a value $|\Omega_{\rm K}| = |K/(aH)^2| < 0.005$, which

means that the universe is really close to spatial flatness and that the total energy density of the universe is almost 1.

Currently accurate CMB observations have depicted a detailed picture of the matter content of the universe. According to these measurements, the percentual energy density of the universe today is dominated by dark energy (68.3%), followed by dark matter (26.8%), and ordinary matter (4.9%).

In accordance with Occam's razor, six is the minimum number of independent parameters that is is required to describe properly the concordance model:

1. $\Omega_{\rm b}h^2$: Physical baryon density.
2. $\Omega_{\rm c}h^2$: Physical cold dark matter density.
3. θ: Approximation to the ration of the sound horizon at recombination to the angular diameter distance. It is directly related to the position of the first acoustic peak and very sensitive to changes in the geometry of the universe.
4. κ: Reionization optical depth to last scattering. κ provides information about the ionization state of the universe and gives the probability that a given photon scatters once. In the literature it is also referred as τ.
5. $n_{\rm s}$: Spectral index of scalar perturbations.
6. $A_{\rm s}$: Amplitude of the primordial super-horizon power in the curvature. Usually re-parametrized as $\ln(10^{10}A_{\rm s})$.

The last two parameters of the ΛCDM set are inflation parameters that will be defined in the next section. In principle any other cosmological parameter is either fixed by the model or derived from the independent parameters. Moreover, sometimes it is common to vary the set and include different parameters, for instance a typical alternative set would also include the Hubble's constant H_0 (or its reduced version h) or the age of the universe t_0.

$\Omega_{\rm b}h^2$	0.02225 $\pm$ 0.00016
$\Omega_{\rm c}h^2$	0.1198 $\pm$ 0.0015
$\theta \times 100$	1.04077 $\pm$ 0.00032
κ	0.079 $\pm$ 0.017
$n_{\rm s}$	0.9645 $\pm$ 0.0049
$\ln(10^{10}A_{\rm s})$	3.094 $\pm$0.034
H_0	67.27 $\pm$ 0.66

Table 1.1: *Mean and standard deviations of the $\mathcal{PL}$ parameters as determined by Planck [21]. We also include the value of H_0 for completeness.*

We adopt the nomenclature introduced in [44] and we will denominate the set of parameters that define the ΛCDM cosmology as the *Power-Law* ($\mathcal{PL}$) model. Table 1.1 shows the most up-to-date values for the $\mathcal{PL}$ parameters as determined by the *Planck* experiment [21], where we also include the value of H_0 for completeness. Throughout this Thesis in order to explore possible scenarios beyond the standard model, we will add some extra parameter to the $\mathcal{PL}$ model: relativistic degrees of freedom $N_{\rm eff}$, amount of inflationary gravitational waves r (introduced in the next section) and/or defects parametrized as $G\mu$ (the exact definition of $G\mu$ can be found in the next Chapter).

1.1.3 Inflation

Inflation is an extension of the standard cosmological model that considers a period of very rapid and accelerated expansion in the initial stages of the universe [95, 129]. It was initially proposed in order to avoid some of the shortcomings of the standard Big Bang scenario. The description of the initial phases of the universe given by a universe filled only with *ordinary* matter ($\omega \geq 0$) does not fit with current observations.

Let us now review the shortcomings of the Big Bang model and how inflation can avoid them.

1. The flatness problem or fine tuning of the initial conditions.

   Ω_K is defined as:

   $$\Omega_K = -\frac{K}{a^2 H^2}\,. \tag{1.15}$$

   It scales as a^{-2} and comparing to how radiation (a^{-4}) and matter (a^{-3}) scale, it means that its relevance is greater at late times than at earlier ones. Currently, however, the nearly flat universe picture is robustly confirmed by observations ($|\Omega_K| < 0.005$). Thus, if the curvature parameter is so small today, it must have been much smaller in the early universe, *e.g.* 10^{-18} at big bang nucleosynthesis. A possible solution to this problem is that the universe started from a very precise, but highly unlikely, initial state $K = 0$, which is usually referred as the *fine tuning* problem.

   Inflation proposes a natural and elegant solution to this problem. Assuming that the early universe was dominated by the inflaton field or equivalently by a fluid with negative pressure or $\omega = -1/3$, Eq. (1.11) can be written as:

   $$H^2 \approx \frac{\Lambda}{3}\,, \tag{1.16}$$

   and this means:

   $$a(t) = \exp\left(\sqrt{\frac{\Lambda}{3}}t\right) \quad \Rightarrow \quad |\Omega_K| \propto \exp\left(-\sqrt{\frac{4\Lambda}{3}}t\right)\,. \tag{1.17}$$

   Therefore with the above expression there is no need to fine tune the initial conditions. Regardless of the initial value of the curvature, inflation forces it to be very small.

2. Horizon problem.

   The horizon problem comes from the similarity of regions that apparently had never been causally connected. If we look at the CMB, patches of the background that did not have time to causally connect before recombination, look surprisingly similar. So how can such a similarity be explained? As in the previous point, a possible explanation could be that the universe chose ultra-homogeneous initial conditions, which is again a very unlikely possibility.

   However, the problem disappears if we adopt the inflationary point of view. In an exponential expansion, causal horizons do not grow with time as would do in radiation or matter dominated universes, instead, they decrease. In other words, regions that had once been in causal contact before inflation were moved away rapidly. Therefore regions that appear to be causally uncorrelated in the last scattering surface, could have previously been in contact.

3. Magnetic monopole or relic particle abundance problem.

   Grand unified theories predict the formation of extremely heavy particles at the phase transitions that took place in the early universe. Those non-relativistic relics, such as the magnetic monopole, would immediately dominate the evolution of the universe, *i.e.* the domination of radiation and ordinary non-relativistic mater could never took place.

   Inflation could solve the problem provided that it took place after the creation of such dangerous relic particles. Hence, monopoles and other relics dilute away in the exponential expansion and became irrelevant comparing to radiation and matter.

As with the late accelerated expansion of the universe, we need an extra component that could drive this initial exponential expansion. In the simplest description of inflation the exponential expansion is driven by the vacuum energy of a scalar field, the *inflaton*, with a self-interacting potential. In essence, the inflation *rolls slowly* towards its ground state and under this peculiar conditions acquires negative pressure.

Inflation is also very powerful in its predictions and has successfully been supported by modern and accurate observations as the best model for the origin of density fluctuations that lead to the observed large-scale structure. According to it, quantum fluctuations of the inflaton field were stretched by the exponential expansion and became of macroscopic size. In this sense, the confirmation of inflation will relate for the first time quantum and general relativistic theories.

Quantum fluctuations of the inflaton field perturb the background space-time. These perturbations are classified into density perturbations (scalars) or gravitational waves (tensors). In principle, vector perturbations are also present but they decay and so they are not considered. Scalar and tensor perturbations are characterized by their power spectra, which typically are written as:

$$\mathcal{P}_{\mathcal{R}}(k) = A_{\rm s}\left(\frac{k}{k_*}\right)^{n_{\rm s}-1+\frac{1}{2}dn_{\rm s}/d\ln k\ln(k/k_*)}, \tag{1.18}$$

$$\mathcal{P}_{\rm t}(k) = A_{\rm t}\left(\frac{k}{k_*}\right)^{n_{\rm t}}. \tag{1.19}$$

where k_* is the pivot comoving wavenumber. $A_{\rm s}$ and $A_{\rm t}$ are the scalar and tensor amplitudes, and $n_{\rm s}$ and $n_{\rm t}$ represent the spectral index of both power spectra and determine the tilt of it. Note the different definitions for the spectral indexes, while $n_{\rm s} = 1$ gives the Harrison-Zel'dovich model for scale invariant scalar perturbations [97, 221], $n_{\rm t} = 0$ gives the scale invariance for tensors. Finally, $dn_{\rm s}/d\ln k\ln(k/k_*)$ is the running of the scalar spectral index[1].

In principle the total amount of scalar and tensor perturbations produced by inflation are totally independent, up to a consistency relation for single-field inflation models. Thus, with these definitions, it is very useful to define the *tensor-to-scalar ration*, r, the relative ratio of tensor with respect the scalar perturbations.

$$r = \frac{\mathcal{P}_{\mathcal{R}}(k_*)}{\mathcal{P}_{\rm t}(k_*)}. \tag{1.20}$$

The exact amount of tensor perturbations is strongly model dependent, ranging from almost negligible contributions in string theory (typically $\mathcal{O}(10^{-23})$), to fairly measurable amounts ($\mathcal{O}(10^{-2})$ or $\mathcal{O}(10^{-3})$) in single field inflation models.

[1] Sometimes the running of the running of the scalar spectral index and the running of the tensor spectral index are also included.

1.1.4 Brief thermal history

In this section we will briefly summarize the most important and relevant events of the formation of the current universe from the thermal point of view. The thermal history is the high energetic analysis of the evolution of the universe, which explores how fundamental particles and forces acting on them have evolved. As such, some definitions of cosmological events acquire different meaning. The most characteristic, and sometimes confusing, example is the big bang. In the general relativistic description the big bang represents the hypothetical initial singularity of the space-time. The thermal or high energy interpretation, however, often calls big bang to the moment when the universe filled (or re-populated) with all particles, which in the inflationary cosmology is represented by the reheating.

The events are ordered chronologically following the decreasing of the temperature of the universe. We include also the energy scale and the approximate age of the universe for the events relevant for this Thesis.

- Planck epoch: initial singularity predicted by the standard cosmological model, which cannot be properly studied without a consistent quantum theory of gravity. Hypothetical separation of gravity from other fundamental forces of nature, also known as *graviton decoupling*. The gravitational wave background formed by primordial gravitons would provide the picture of the first instants of the universe.

- Inflation and reheating ($t \sim ?$, duration unknown): inflation is the early accelerated expansion process that solves the flatness, horizon and relic particle abundance problems. In principle driven by a scalar field with negative pressure. Reheating is the hypothetical process that filled the universe with all the particles. Although the theoretical and experimental status of inflation is better stablished, the exact realization of both processes is still very model dependent. The universe after inflation/reheating was composed by a very relativistic and thermalized fluid, the *primordial plasma*, where all the particles were in thermal equilibrium.

- Non-standard model phase transitions and baryogengesis ($10^{16}\text{GeV} \lesssim T \lesssim T_{\text{EW}} \sim 100\text{GeV}$): from the unification of all forces described by *Grand unification theories* (GUT), splitting of the fundamental forces in strong and electroweak nuclear forces through different phase transitions. GUT theories are motivated by the unification of all forces, however there exist many possible realizations for the unified interaction that consider different gauge symmetries: $\text{SU}(5)$, $\text{SO}(10)$... Topological defects might have been created at such symmetry breakings, though the exact sequence of them is still unknown. Moreover, possible origin of the matter/anti-matter asymmetry or *baryogenesis*. It was between the reheating and the electroweak phase transition when the hypothetical supersymetry also may have broken down.

- Standard model phase transitions: particles acquired mass in the electroweak phase transition ($T_{\text{EW}} \sim 100\text{GeV}$) through the Higgs mechanism. Quark and gluons, previously free at high temperatures, formed bound states and are confined to form baryons and mesons. This process is usually known as quantum chromodynamics phase transition ($T_{\text{QCD}} \sim 200\text{MeV}$).

- Neutrino decoupling ($t \sim 0.2$ s, $T \sim 0.8 - 2$ MeV): weak interaction fell out of equilibrium and neutrinos, which only interact weakly with other particles, decoupled from the primordial plasma. Those primordial neutrinos formed the *cosmological neutrino background*, which could allow probing deeper than the CMB in the early universe.

The role played by the neutrinos at early physics goes beyond that. Neutrinos, due to their extreme low masses, act as massless particles and contribute considerably to the radiation energy density. Typically it is defined as,

$$\Omega_{\rm r} = \Omega_\gamma \left(1 + \frac{7}{8}\left(\frac{4}{11}\right)^{4/3} N_{\rm eff}\right) , \tag{1.21}$$

where Ω_γ is the dimensionless energy density of photons and $N_{\rm eff}$ is the number of relativistic species.

The standard model predicts 3 neutrino families and gives $N_{\rm eff} = 3.046$, which also accounts for corrections due to non-instantaneous neutrino decoupling. In principle, any other possible relativistic specie present at the early universe would contribute to $N_{\rm eff}$, *e.g.* another neutrino family would contribute one unit to $N_{\rm eff}$. In Chapter 1 of Part II, we explore extra radiation contributions and their relation with gravitational waves seeded by networks of cosmic strings.

- Electron-positron annihilation: temperature fell below the electron mass threshold and electron-positron pairs began to annihilate. After that a tiny excess of electrons over positrons were left in equilibrium with photons. The temperature of the photons increased due to the energy transferred by the electrons.

- Big Bang nucleosynthesis: temperature decreased so that bound nuclear structures could be formed: mainly Helium-4 nuclei as well as tiny amounts of other light elements such as Helium-3, Deuterium, Lithium-6... The prediction of the abundances of light elements has been one of the most successful predictions made within the hot big bang model.

- Radiation-matter equality ($t \sim 60.000$ years, $T \sim 1$ eV): transition from radiation dominated universe to matter dominated universe happened when the energy densities of radiation and matter equated.

- Recombination and photon decoupling ($t \sim 380.000$ years, $T \sim 0.3$ eV): electrons and protons of the primordial plasma recombine to form neutral hydrogen atoms. Due to the low density of free electrons left by recombination, Thomson scattering was no longer efficient. Photons decoupled from the primordial plasma and the universe become transparent to them. The CMB is composed by photons from decoupling and the moment at which photons decoupled is called the *last scattering surface*. The theory of the CMB will be reviewed in the next section.

- Structure formation ($t \sim 1 - 13.7$ Giga-years): inhomogeneities of the primordial plasma evolved via gravitational instability and formed large scale structure: stars, galaxies, clusters...

- Today ($t \sim 13.7$ Giga-years): current situation, experiencing a transition from matter domination to dark energy domination, characterized by the accelerated expansion of the universe. Total energy is distributed in the following way: 68.3% dark energy, 26.8% dark matter, 4.9% baryonic matter and negligible radiation contribution.

1.2 Cosmic Microwave Background

The *Cosmic Microwave Background* (CMB) is a relic radiation composed of photons that decoupled from the primordial plasma when the universe was approximately 380.000 years old. It is characterized by a thermal blackbody spectrum of $T = 2.725 \pm 0.001K$ which is isotropic up to $\mathcal{O}(10^{-5})$ deviations. Although it had been theoretically predicted within the hot big bang model, it was not measured until the 60's by Penzias and Wilson [156]. Its discovery confirmed the idea of a very hot and dense early universe and ever since it has been one of the most important probes of the standard cosmological model.

Most of the information of the underlying physics of the CMB, nonetheless, is not contained in its isotropy, but in its *anisotropies*. The CMB essentially is a snapshot of the universe at decoupling, when the photons dropped out from the primordial plasma because they were no longer able to ionize atoms. Anisotropies are just the projection of the density inhomogeneities in the primordial photon-baryon plasma predicted by inflation that lead to the large scale structure of the universe. Moreover, the relic photons travelled almost unperturbed until today, thus CMB provides an invaluable window into the physics governing the early universe.

The experimental confirmation of the CMB anisotropies did not come until 1992, when the COBE satellite [191] measured them. Subsequent more accurate experiments [15, 21, 110, 121], improved the measurements producing high precision maps as well as power spectra of the anisotropies. In Fig. 1.2 we show the CMB map measured by the *Planck* collaboration and released in 2015.

CMB anisotropies can be calculated evolving the primordial inhomogeneities within the cosmological perturbation theory. The evolution of the metric perturbations is governed by the linearized Einstein's equations, whereas the evolution of the distribution function of the constituents of the universe by the Boltzmann equation (see [134] and [76] for a wider view of this topic in different gauges). There exist several numerical Einstein-Boltzmann equation solvers publicly available. The most commonly used are `CAMB` [127] and `CLASS` [49, 126].

Temperature anisotropies are usually described by the multipole expansion of the temperature field, which given the spherical symmetry can be expanded in spherical harmonics (Y_ℓ^m):

$$\frac{\Delta T}{T}(\hat{n}) = \sum_\ell \sum_{m=-\ell}^{\ell} \Theta_{\ell m} Y_\ell^m(\hat{n})\,, \tag{1.22}$$

where ℓ is the multipole moment and $\hat{n}$ is an unitary vector pointing in the line of sight. T is the average temperature and ΔT are the deviations from it. The coefficients $\Theta_{\ell m}$ describe the temperature perturbation and obey:

$$\langle \Theta^*_{\ell m} \Theta_{\ell' m'} \rangle = \delta_{\ell\ell'} \delta_{mm'} C_\ell\,, \tag{1.23}$$

where $\delta_{\ell\ell'}$ is the Kroenecker's delta function.

In the Gaussian approximation, anisotropies can be fully characterized by the 2-point correlation function or the power spectrum. One should explore higher order correlations, such as the bispectrum, in order to analyze deviations from gaussianity. The power spectrum in function of the C_ℓ's is written as,

$$\left\langle \left| \frac{\Delta T}{T} \right|^2 \right\rangle = \frac{1}{4\pi} \sum_{\ell=0}^{\infty} (2\ell+1) C_\ell\,. \tag{1.24}$$

The coefficients of the spherical harmonic expansion, Θ_{lm}, are the analogous of the fourier

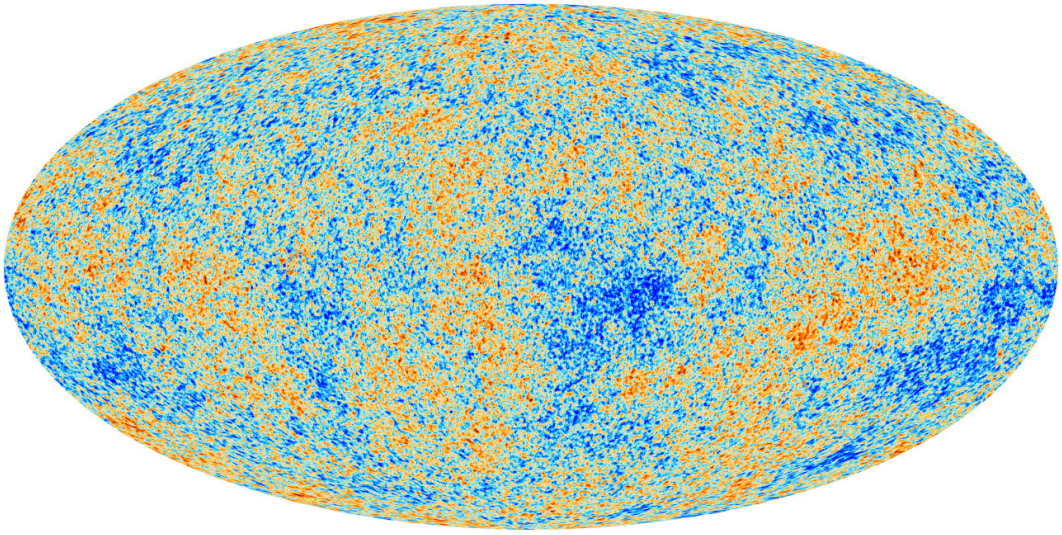

Figure 1.1: *CMB temperature anisotropies measured by the Planck satellite, in red, regions hotter than the average and in blue, colder ones. The equatorial noise produced by our galaxy has been removed from the picture. Picture from the Planck collaboration [11]*

transform coefficients but in spherical surfaces. When we work on small patches of the sky, the curvature can be neglected, thus the relation between the angular wavelength and the multipole moment simplifies to: $\theta = \frac{2\pi}{\ell}$.

The possible contributions to the CMB power spectrum can be distinguished between *primary* and *secondary sources*. Primary sources of anisotropies are those produced directly in the early universe and mainly as a consequence of the inflationary initial conditions. In this sense, the most important feature of the inhomogeneities of the primordial plasma are the acoustic oscillations which converted into acoustic peaks in the power spectrum. Secondary sources on the other hand, perturbed the path and properties of the photons in their travel to us, though to a lesser extent. They are classified as the *Sunyaev-Zel'dovich effect*, the *integrated Sachs-Wolfe effect*, lensing and Doppler effect caused by the motion of cluster gas. Briefly, the thermal Sunyaev-Zel'dovich effect is the energy boost transferred from high energy cluster electrons to photons, via *inverse Compton scattering*. The integrated Sachs-Wolfe effect, in turn, is the gravitational redshift suffered by the CMB because of the evolution of the gravitational potentials.

Beyond the standard cosmological model there are other possible primordial, but subdominant, anisotropy sources. Topological defects are one of the most interesting candidates and the ones analyzed in this Thesis. They could have been produced at primordial phase transitions in the primitive universe, *e.g.* GUT phase transitions. As opposed to inflationary perturbations that are set just by the inflationary initial conditions, defects perturb continuously the CMB, *i.e.* they are

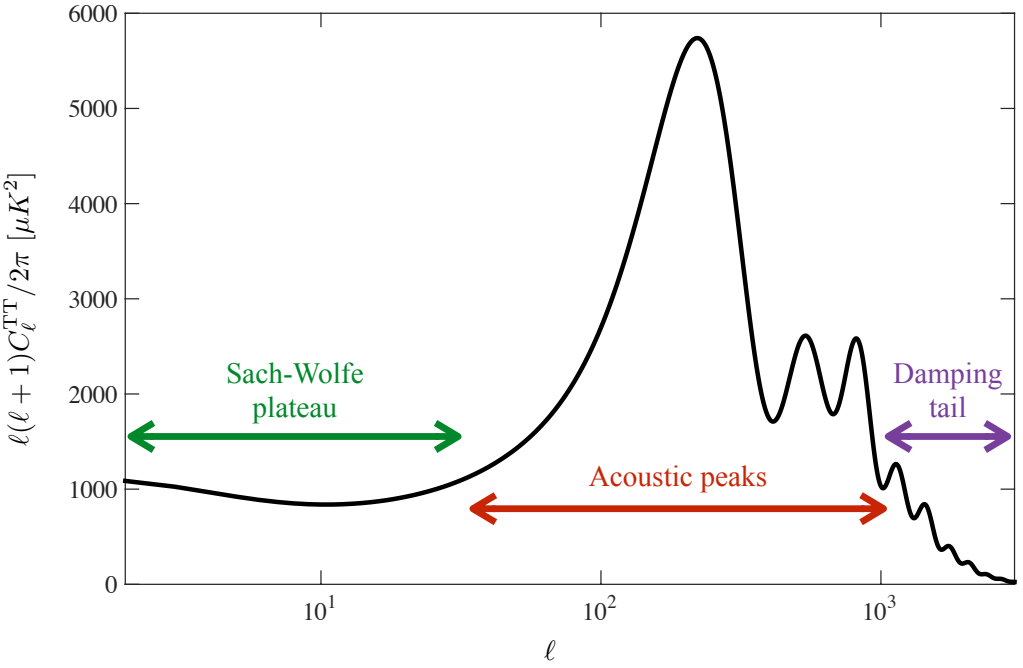

Figure 1.2: *CMB temperature anisotropy power spectrum using the ΛCDM best fit values and calculated with CLASS. The most distinctive features are also indicated: the Sach-Wolfe plateau in green, the region of the acoustic peaks in red and the damping tail at small scales in purple.*

active perturbation seeds. One of the main differences is that while inflationary vector modes decay due to the expansion of the universe, vector modes of active sources are continuously being created and contribute considerably to CMB anisotropies. In Sec 2.1.1 of the next Chapter we will review the theory of CMB anisotropies produced by cosmic defects.

Figure 1.2 shows the schematic description of the CMB temperature power spectrum. The most distinctive feature of the temperature power spectrum are the mentioned acoustic peaks, which are located between $100 \lesssim \ell \lesssim 1000$. The amplitude of the peaks is related to the energy content (proportion matter/radiation) before recombination, whereas the position of the first peak is strictly linked to the spatial curvature of the universe. The small scale or high multipole ($\ell \gtrsim 2000$) behavior of the spectrum is characterized by the *damping tail*. The damping affects multipole momenta that correspond to characteristic scales before recombination and is caused by the imperfect couplings of the photon-baryon fluid that decrease the amplitude of the spectrum. Finally the spectrum at very large scales ($\ell \lesssim 100$) is nearly flat (the *Sach-Wolfe plateau*), describing a nearly scale invariant spectrum for the temperature anisotropies.

1.2.1 Polarization: B-modes

Perturbations of the space-time also affected the polarization distribution of CMB photons. The magnitude of the polarization anisotropies is smaller $\mathcal{O}(10^{-6})$ than the temperature ones $\mathcal{O}(10^{-5})$ and thus their detection is more challenging.

The polarization anisotropy pattern of the CMB photons is described by the polarization field which is decomposed into E- and B-modes. They correspond to the scalar (divergence-free) and pseudoscalar (curl-free) fields that are distinguished by parity. As in the temperature channel, the fluctuation gaussianity assumption enables to describe the two polarization modes via the 2-point

correlation function of their coefficients of the multipole expansion. Polarization modes can be auto-correlated as well as cross-correlated between them and also with the temperature channel, so there could be 3 different cross-correlation channels: TE, EB and TB. However, if parity is not violated in our universe, B-mode polarization has no correlation with temperature and E-modes, and CMB temperature and polarization power spectra are fully described by TT, TE, EE and BB channels.

Regarding their origin, polarization anisotropies can only be produced by Thomson scattering of the CMB photons with free electrons in presence of a local quadrupole temperature anisotropy. Essentially the observed polarization is a projection of the local quadrupole at last scattering surface and reionization, and any quadrupole source would leave its imprint in the polarization. The most important contribution comes from recombination, where the breaking of the tight coupling produced quadrupoles through gradients in the velocity of the primordial fluid and gravitational waves. Free electrons that were present at reionization also contribute to B-modes.

Scalar perturbations produce positive parity polarization and generate directly only E-mode polarization and can produce B-modes indirectly through lensing of the E-modes. Vector and tensor modes, on the other hand, produce directly E and B-mode polarization. It is noteworthy to recall again that though inflationary vector modes are neglected, they can be actively generated by scaling seeds such as cosmic defects and could also contribute to the total CMB polarization anisotropy.

The absence of the dominant scalar perturbations in B-modes makes the detection of such a polarization channel an invaluable tool to explore the physics beyond the stablished cosmological standard model. It could not only confirm the presence of inflationary gravitational waves and set the energy scale of inflation, but uncover also the existence of more exotic objects such as the aforementioned defects or primordial magnetic fields.

Figure 1.3 shows the typical B-mode spectrum produced by inflationary tensor modes (black line), where $r = 0.2$ and the contribution of the lensing of E-modes added (dashed grey line). We also show the total spectrum in blue. As can be seen from the picture, the spectrum of primordial origin have two differentiated main peaks that correspond to the epoch were the contribution to the polarization were higher due to the presence of high amount of free electrons: recombination and reionization. Specifically the first is related to reionization whereas the second to recombination and the positions are given by the horizon size at each epoch.

The detection of B-mode polarization at relatively low-ℓ's ($\ell \lesssim 100$), where the signal is almost uncorrelated with the lensing contribution, would open an unique opportunity to explore the physics beyond the standard model that governed those early times.

1.2.2 CMB experimets

In this section we will review the most important modern CMB experiments. Since the detection of the CMB radiation by Penzias and Wilson, there have been a huge variety of different CMB experiments that have tried to characterize the primordial radiation as precisely as possible.

The selection of experiments is composed of satellites and ground-based experiments. The main difference between space-based and earth-based receivers is their capability to scan the sky. While satellites have been designed to scan most of the sky and obtain as widest angular amplitude as possible, the objective of ground based experiments has been to perform the most accurate small angle measurements concentrating on small patches of the sky.

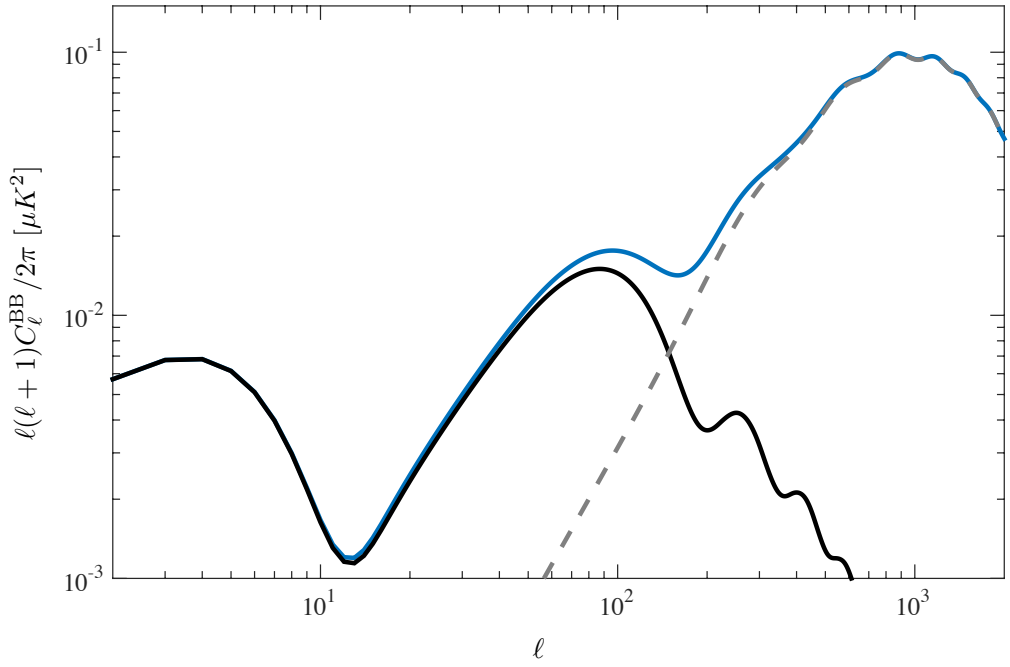

Figure 1.3: *B-mode polarization spectrum produced by inflationary tensor modes for $r = 0.2$ (black line) plus the lensing of the E-modes, calculated using the ΛCDM best fit values, (dashed grey line) and the total spectrum in blue. The power spectrum has been calculated using CLASS. The two main peaks of the black line are associated with reionization ($\ell 5$) and recombination ($\ell 100$) and their position, with the horizon size at each epoch.*

Satellites

Satellite experiments provide accurate whole sky anisotropy maps, which allow to calculate high precision CMB power spectra. The first satellite, and in fact the first experiment that could measure anisotropies, was COBE [191]. It was able to uncover the first peak of the acoustic sequence of the power spectrum. Subsequent satellites, principally WMAP and *Planck*, improved considerably those initial measurements. Figure 1.4 shows an illustrative evolution of the precision of whole sky temperature anisotropy maps: starting from COBE, passing through WMAP and ending in *Planck*.

- *Wilkinson Microwave Anisotropy Probe* (WMAP) [4]. The successor of the COBE satellite and developed in a collaboration between NASA and Princeton University. WMAP operated from 2001 to 2010, measuring CMB anisotropies in the temperature as well as in the polarization channel (E-modes).

  The WMAP power spectra cover the $2 \leq \ell \leq 1200$ multipole range and determines with high accuracy the acoustic pattern of the CMB. The binned power spectra points of the TT channel can be seen in Fig. 1.5 (red points with black error bars).

- *Planck* [2]. The Planck spacecraft was designed by the European Space Agency (ESA) and operated between 2009 and 2013. The *Planck* mission scanned the whole sky improving the accuracy of WMAP measurements and reaching much smaller scales.

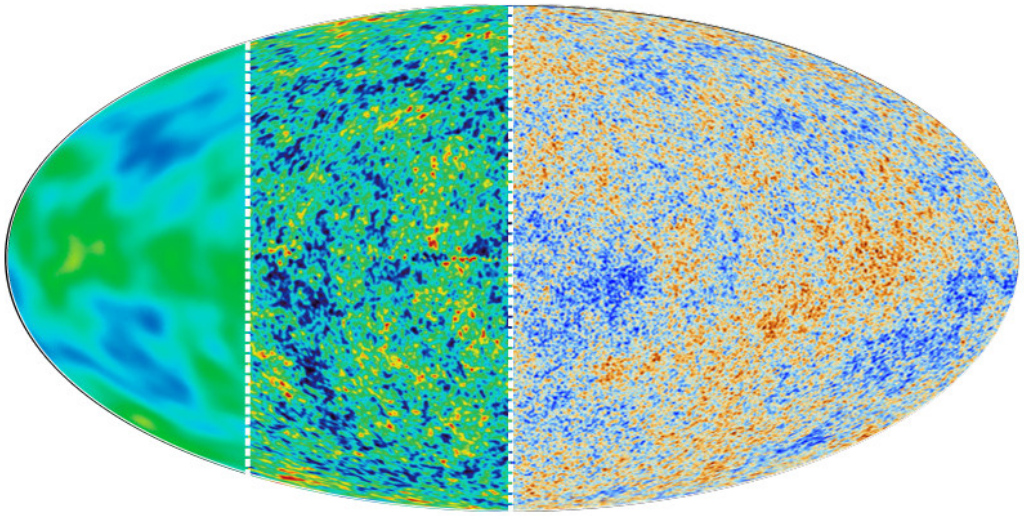

Figure 1.4: *Evolution of the whole sky CMB temperature maps. From left to right: COBE, WMAP and Planck. Credits (2013): www.lefigaro.fr*

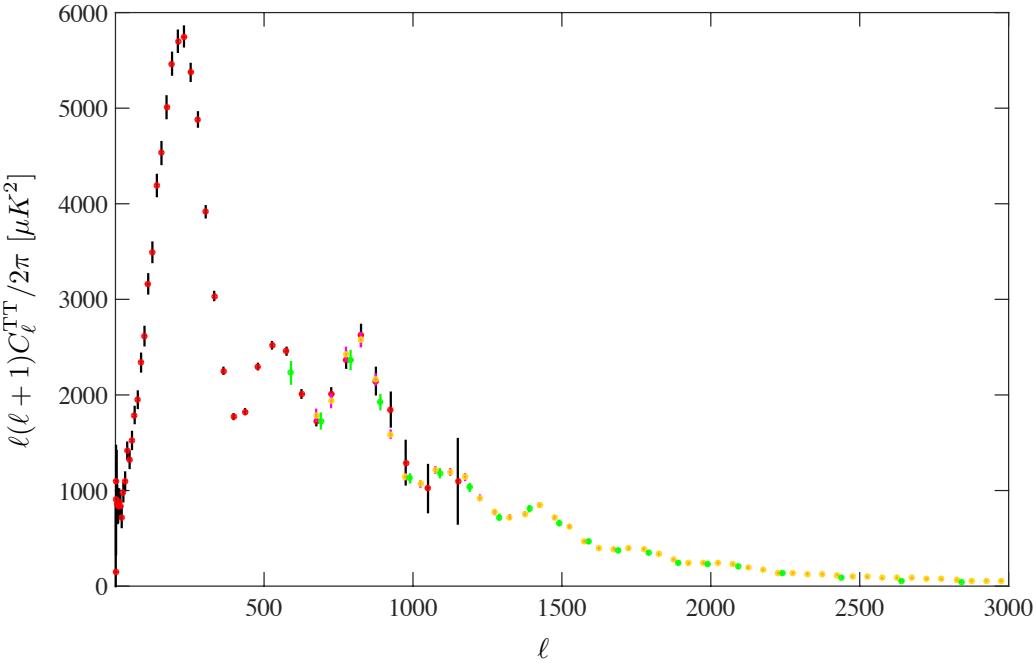

Figure 1.5: *CMB temperature power spectrum given by the WMAP 9-year (red points with black error-bars), SPT (yellow points) and ACT (green points).*

Planck power spectrum ranges a wider multipole region $2 \leq \ell \leq 2500$, combining 2 independent detectors that covered the low-ℓ sector and high-ℓ sector. The CMB temperature power spectrum measured by *Planck* can be seen in Fig. 1.6, where the low-ℓ and high-ℓ parts of the mission have been divided in logarithmically and linearly spaced regions respectively.

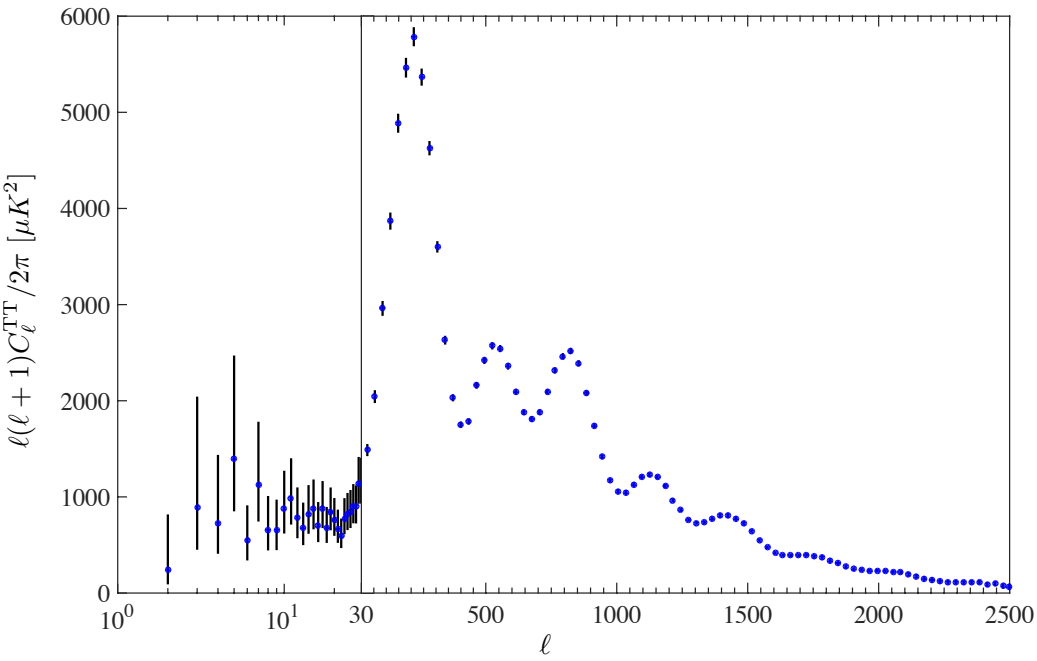

Figure 1.6: *CMB temperature power spectrum as measured by the Planck experiment. The spectrum is divided according to the different detectors used to measure the signal: low multipole region (in logarithmic scale) and the high-ℓ data (linearly spaced).*

Ground based experiments

In general ground-based experiments aimed to complement whole sky surveys with accurate measurements of small patches of the sky. Some of them, however, specifically designed to be able to measure the still undetected B-mode either at high multipoles, *i.e.* lensing (SPTPol, PolarBear), or at low-ℓs, *i.e.* primordial B-modes (BICEP2/Keck). A compilation of the B-mode measurements made by different experiments can be found in Fig. 1.7.

Such telescopes are usually located in *clean* parts of the earth such as the south pole so as to minimize atmospherical contamination sources. Here we will list some of them:

- South Pole Telescope (SPT/SPTPol) [96, 194]. Composed of two different experiments that measured the very high-ℓ temperature power spectrum (yellow points in Fig. 1.5) and the lensing profile of the B-modes (SPTPol) (red error bars in Fig. 1.7).

- Atacama Cosmology Telescope (ACT) [149, 188]. Located at the Atacama Desert, it measures high resolution CMB anisotropies both in temperature in polarization (green points in Fig. 1.5).

- PolarBear [19]. First measurement of B-mode lensing polarization (green error bars in Fig. 1.7).

- BICEP2/Keck [16, 22]. It was claimed to be the first experiment that measured the B-modes relevant for primordial cosmology (black error bars in Fig. 1.7). Subsequent combined analysis with *Planck* showed that the measured signal could have astrophysical origin [18].

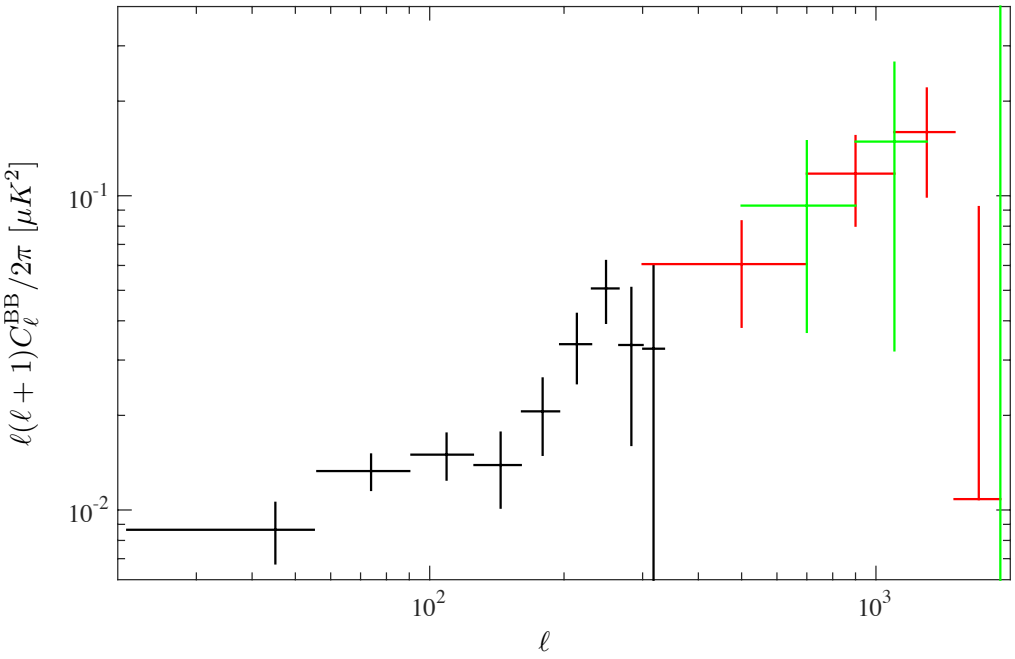

Figure 1.7: *CMB B-mode polarization power spectrum as measured by BICEP2 (black error bars), SPTPol (red error bars) and PolarBear (green error bars).*

1.3 Data analysis

In the last few decades, the amount and quality of cosmological experimental data has considerably increased and observational cosmology has become one of the best scenarios to compare and test theoretical predictions with precise measurements. Along with this, the corresponding statistical tools have also been improved and new techniques developed so as to efficiently analyze the wide variety of cosmological datasets.

The data analysis of cosmological data is based on Bayesian statistics, which tries to reproduce observations of the universe with theoretical predictions produced by models under study. The goals of the statistical analysis are in general twofold: first to determine the most likely values of the parameters that the models depend on (*parameter estimation*) and similarly to evaluate the quality or goodness of fit provided by the best fit parameters (*model selection*).

In this section we will review the most important aspects of parameter estimation procedures in cosmology. In this sense, after a short statistical description of the parameter estimation theory, we will describe one of the most used methods to explore the parameter space in cosmology: Markov Chain Monte Carlo.

1.3.1 Parameter estimation

The likelihood function is the basic tool for the Bayesian data analysis. The likelihood function ($\mathcal{L}(\mathbf{x}|\boldsymbol{\alpha}^{\mathcal{M}})$) is the probability of measuring the data or event $\mathbf{x}$ given the model $\mathcal{M}$ and the set of parameters of that model $\boldsymbol{\alpha}^{\mathcal{M}} = \{\alpha_1, ..., \alpha_n\}$. In other words, it measures the ability of our model, with its parameters, to predict the observed data.

Parameter estimation in the Bayesian framework is performed simulating posterior distributions or probability density functions of the parameters given the data and assuming the model under

consideration is the correct. Hence, it is provided by Bayes' theorem [69]:

$$\mathcal{P}(\boldsymbol{\alpha}^{\mathcal{M}}|\mathbf{x}) = \frac{\mathcal{L}(\mathbf{x}|\boldsymbol{\alpha}^{\mathcal{M}})\pi(\boldsymbol{\alpha}^{\mathcal{M}})}{\int \mathcal{L}(\mathbf{x}|\boldsymbol{\alpha}^{\mathcal{M}})\pi(\boldsymbol{\alpha}^{\mathcal{M}})d\boldsymbol{\alpha}^{\mathcal{M}}}, \tag{1.25}$$

where $\mathcal{P}(\boldsymbol{\alpha}^{\mathcal{M}}|\mathbf{x})$ is the posterior distribution. $\pi(\boldsymbol{\alpha}^{\mathcal{M}})$ is the prior probability density function where we include all our previous knowledge on the limits of the parameters of the model.

In cosmology there is a unique realization of the measurements, *i.e.* there is only one universe where we can perform our observations. Therefore, while in the frequentists approach the parameter estimation procedure maximize the posterior distribution by repetition of the experiment, the Bayesian approach maximizes the likelihood function. It is customary to define the chi-square function, which in terms of the likelihood function can be written as:

$$\chi^2(\boldsymbol{\alpha}^{\mathcal{M}}) \propto -2\log(\mathcal{L}(\mathbf{x}|\boldsymbol{\alpha}^{\mathcal{M}})). \tag{1.26}$$

Sometimes instead of maximizing the likelihood, we will minimize the chi-square function, which of course is equivalent.

In our specific case we will compare measurements of the CMB power spectra given by $\hat{C}_\ell$'s with predictions made by our models $C_\ell^{\boldsymbol{\alpha}}$, therefore the likelihood function will be

$$\mathcal{L}(\mathbf{x}|\boldsymbol{\alpha}^{\mathcal{M}}) \quad \Rightarrow \quad \mathcal{L}(\hat{C}_\ell|C_\ell^{\boldsymbol{\alpha}}), \tag{1.27}$$

where the parameters will be given by the usual 6 $\mathcal{PL}$ parameters plus additional extra parameters coming from our models.

1.3.2 Markov Chain Monte Carlo

When a large amount of parameters are involved in the analysis, the exploration of the whole likelihood parameter space can become a very painful and implausible objective. The *Markov Chain Monte Carlo* (MCMC) method [40] offers the most commonly used procedure to avoid that problem. It optimizes the exploration by drawing samples, *i.e.* chains of points of the parameter space, rather than exploring the parameter space by brute force. The advantage of the MCMC method is that from a relatively small amount of samples the most important features of the likelihood surface can be obtained: marginalized posterior distributions, correlations between different parameters and best-fit configuration of the parameters. Furthermore, the inclusion of extra parameters into the analysis implies small additional cost, adding valuable flexibility to the analysis.

The parameter space is scanned by Markov chains, which consist of stochastic processes that examine the parameter space jumping from point to point following a probability given by a transition kernel. Although the kernel varies from method to method, a general feature of Markov chains is that they are memoryless. The future step in parameter space does not depend on the past history, but only in the current point. The chain moves from a point in parameter space $\boldsymbol{\alpha_1}^{\mathcal{M}}$, which is a vector containing all parameters, to the next $\boldsymbol{\alpha_2}^{\mathcal{M}}$ with transition probability $\mathcal{T}(\boldsymbol{\alpha_1}, \boldsymbol{\alpha_2})$, where we have omitted the subscript $\mathcal{M}$ that refers to the model under study.

The most commonly used algorithm for MCMC processes in cosmology is the *Metropolis-Hastings* algorithm [99, 142]. According to it, a new point $\boldsymbol{\alpha}_{n+1}$ is proposed using a symmetric proposal density distribution $q(\boldsymbol{\alpha}_n, \boldsymbol{\alpha}_{n+1})$, considering that the system is in the $\boldsymbol{\alpha}_n$ point. The transition kernel $\mathcal{T}(\boldsymbol{\alpha}_n, \boldsymbol{\alpha}_{n+1})$ satisfies the balance equation to ensure that the process recovers the posterior distribution:

$$\mathcal{P}(\boldsymbol{\alpha_n}|\mathbf{x})\mathcal{T}(\boldsymbol{\alpha_n},\boldsymbol{\alpha_{n+1}}) = \mathcal{P}(\boldsymbol{\alpha_{n+1}}|\mathbf{x})\mathcal{T}(\boldsymbol{\alpha_{n+1}},\boldsymbol{\alpha_n}). \tag{1.28}$$

The balance equation is fulfilled if the new point is accepted with the following probability:

$$\mathcal{P}(\boldsymbol{\alpha_n},\boldsymbol{\alpha_{n+1}}) = \min\left[1, \frac{\mathcal{P}(\boldsymbol{\alpha_{n+1}}|\mathbf{x})q(\boldsymbol{\alpha_{n+1}},\boldsymbol{\alpha_n})}{\mathcal{P}(\boldsymbol{\alpha_n}|\mathbf{x})q(\boldsymbol{\alpha_n},\boldsymbol{\alpha_{n+1}})}\right], \tag{1.29}$$

where the transition kernel is defined as:

$$\mathcal{T}(\boldsymbol{\alpha_n},\boldsymbol{\alpha_{n+1}}) = \mathcal{P}(\boldsymbol{\alpha_n},\boldsymbol{\alpha_{n+1}})q(\boldsymbol{\alpha_n},\boldsymbol{\alpha_{n+1}}). \tag{1.30}$$

The new point is accepted if the likelihood is improved. If the new likelihood is worse than the current, the new point is accepted with a probability given by the ratio inside brackets of Eq. (1.29).

A schematic representation of the MCMC procedure used throughout this Thesis is shown in Figure 1.8, where the acceptance or rejection criteria set by the Metropolis-Hastings algorithm is described by a flow-chart. A point in parameter space is picked randomly and sent to the Einstein-Boltzmann equation solver to obtain the corresponding power spectra prediction (C_ℓ). Then, the quality of the prediction is evaluated, using the likelihood function, by comparing it with the experimental data. The new point is accepted if the new likelihood is better than the previous or momentarily rejected if it is worse. In the latter case, it can still be accepted if the ratio of the two likelihoods is greater than a randomly chosen number. The point is then stored as a new piece of the chain and the process reseted. Finally, once the code has collected enough points or the chain has converged, we can calculate marginalized posterior distributions and/or best-fit points.

When do we know we have sampled enough? In principle the Markov process will reach the exact unknown probability distribution asymptotically, that is, in infinite steps and computational time. The convergence criterion determines whether the Markov chain is a good representation of the likelihood space and can describe it accurately. The *convergence ratio* is the magnitude that encapsulates that information and is defined as the ratio of the variance of the mean of the samples and the variance of the underlying distribution, which is usually 1 if we assume standard deviations. Typically convergence of the chains is thought to be guaranteed with $r = 0.01$.

Due to the randomness of the choice of the initial point, it is probable that the initial region explored by the chain could be far form the high probability region and take too long to get the correct description of the asymptotic posterior distribution. This initial period is called *burn in* period. It is thus highly desirable to run short initial chains that not only would help to decide the best starting point, but would also set the correct correlations of the parameters via the *covariance matrix*. The covariance matrix technique ensures that longer chains will sample properly the likelihood space and increases considerably the effectivity of the MCMC.

Provided the flexibility of the MCMC method to include new partakers into the analysis, it has widely been used to study models beyond the standard cosmological model through the small details and windows that extremely accurate cosmological data still offer. There are a couple of different publicly available codes that perform the parameter estimation procedure and can be easily modifiable: `CosmoMC` [127] and `Monte Python` [1, 28]. Although they are written in different languages (`Fortran` and `Python`) and use different Einstein-Boltzmann solvers for the evolution of the cosmological perturbations (`CAMB` and `CLASS` respectively), they are equivalent. Throughout the different projects of this Thesis we use modified versions of both codes that account for the possible contribution of cosmic defects in CMB power spectra. Schematically

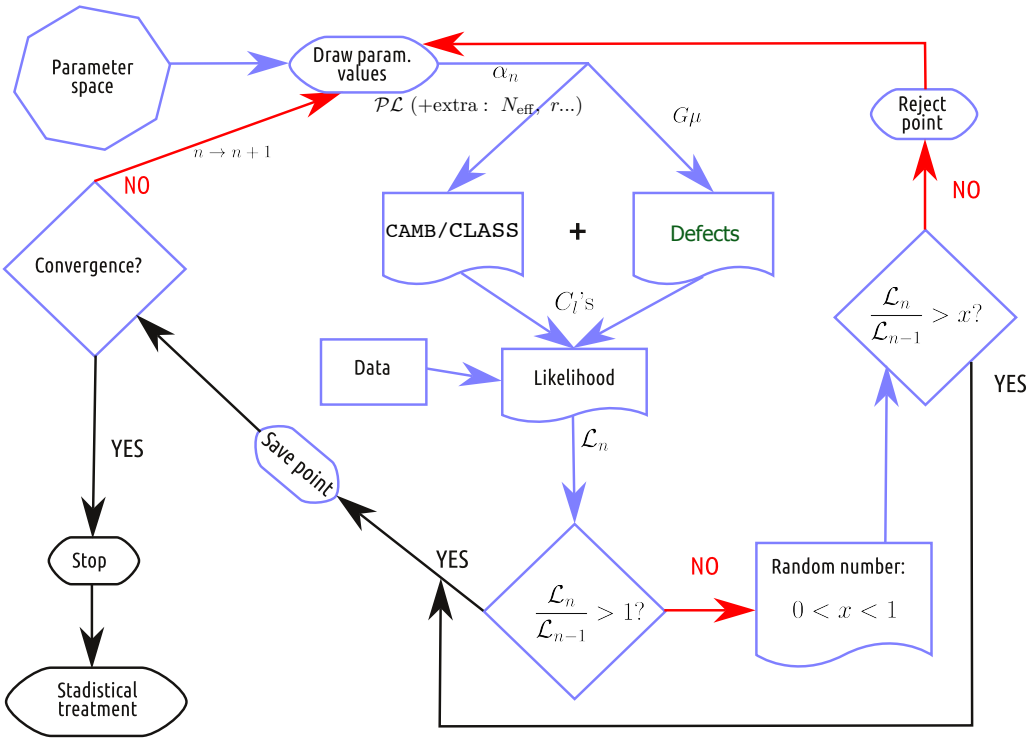

Figure 1.8: *Schematic summary of the MCMC process and the Metropolis-Hastings algorithm. It describes the most general setup used in this work, where we include the contribution of cosmic defects into the analysis.*

the structure of the codes is summarized in Figure 1.8. As we will see in the next section, the back-reaction induced by the defect perturbations in the usual cosmological parameters can be neglected, therefore the defect spectra is calculated for a fixed set of values of the parameters (usually the ΛCDM best fit parameters). These fixed spectra are normalized using an appropriate normalization factor, which indeed is part of the parameter space and is randomly set, and added to the inflationary contribution before calculating the likelihood.

2 Cosmic strings and defects

2.1 Topological defects

The Hot Big Bang describes an universe that from a very hot and energetic configuration expanded and cooled down. It is believed that this cooling process leaded to phase transition that altered the underlying symmetry of the universe. Topological defects are relic energetic objects that could have been formed at phase transitions occurred in the early universe. They can play a very important role in connecting the particle and cosmological standard models, since they are predicted in high energy models and their implications can be cosmologically relevant.

Phase transitions are intrinsic in high energy models for particle physics. The standard model for particle physics already establishes some low-energy phase transitions such as the electroweak transition at about $T \sim 10^2$GeV. Phase transitions are also typical in fundamental models beyond the standard model, *e.g.* the supersymmetry breaking or the breaking of the symmetry of *Grand Unified Theories* at about $T \sim 10^{16}$GeV. Topological defects are commonly predicted in the phase transitions occurred at GUT theories [214], where the symmetry of the universe is transformed, in a sequence of different spontaneous symmetry breakings, from an unified symmetry down to the current symmetry of the universe as described by the standard model,

$$\mathrm{G} \to ... \to \mathrm{SU}(3) \times \mathrm{SU}(2) \times \mathrm{U}(1) \to \mathrm{SU}(3) \times \mathrm{U}(1)_{\mathrm{EM}} \tag{2.1}$$

where G is a larger and still undetermined symmetry group.

Spontaneous symmetry breaking occurs when the vacuum state of a physical system is not invariant under a given symmetry transformation, but the physical laws remain symmetric. This is easily illustrated considering the so-called *Goldstone model* which is invariant under a $\mathrm{U}(1)_{\mathrm{G}}$ global symmetry and is described by the following Lagrangian at zero temperature:

$$\mathcal{L} = (\partial_\mu \phi)^\dagger (\partial^\mu \phi) + \frac{1}{4}\lambda(\phi^\dagger \phi - \phi_0^2)^2 \,, \tag{2.2}$$

where ϕ is a complex scalar field, ϕ_0 its vacuum expectation value (*vev*) and λ the self-coupling constant. The last term is the potential of the system typically called the *mexican-hat* potential.

The ground state of the system lies on a circle in the complex plane ($|\phi| = \phi_0$) and its expectation value is characterized by a non-zero value:

$$\langle \phi \rangle = \phi_0 e^{i\theta} \,. \tag{2.3}$$

It is evident that even though the Lagrangian is invariant under global phase transformations $\phi \to \phi e^{i\alpha}$ ($\mathrm{U}(1)_{\mathrm{G}}$), its ground state is not. When the fields drops from the top of the potential

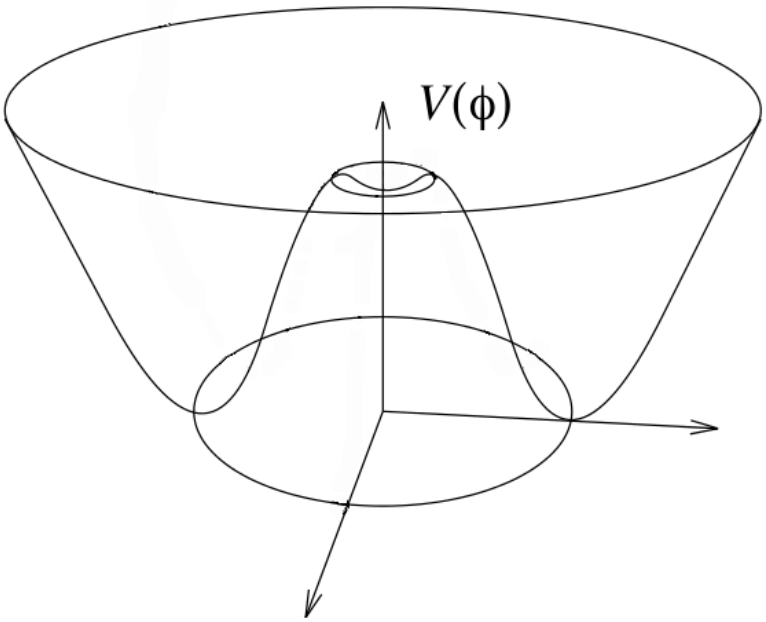

Figure 2.1: *Mexican-hat potential.*

it *chooses* a concrete ground state (determined by the value of θ) spontaneously.

It can easily be proven that the vacuum state of the system is composed by a massive and a massless particle. Let us re-parameterize one of the vacuum states, in this case we chose $\theta = 0$. The result is, of course, valid for any other ground state since all of them are equivalent. The re-parametrization reads

$$\phi = \left(\phi_0 + \frac{1}{\sqrt{2}}\psi\right) e^{i\eta}\,, \tag{2.4}$$

where ψ and η are real scalar fields with *vev* equal to zero. Substitution of this into Eq. (2.2) gives,

$$\mathcal{L} = \frac{1}{2}(\partial_\mu\psi)^2 + \phi_0^2(\partial_\mu\eta)^2 - \frac{1}{2}\lambda\phi_0^2\psi^2 + \mathcal{L}_{\rm int}\,. \tag{2.5}$$

where $\mathcal{L}_{\rm int}$ is the interaction part that include higher order terms in ψ and η. The form of the re-parametrization expresses clearly what the role of each real scalar field is: ψ represents radial oscillations around the ground state, hence it is massive with $m_\psi = \sqrt{\lambda}\phi_0$. On the other hand, η describes the motion around the circle of minima and is massless. The massless particle is called the *Goldstone* boson and their existence is inevitable in systems with broken global symmetries.

In the universe symmetries can be spontaneously broken at thermal phase transitions due to thermal effects. Generally the system tends to minimize the free-energy $F = E - TS$, where S is the entropy and E the internal energy. At high temperatures the second term dominates over the first, hence minimizing the free-energy and minimizing the internal energy are not equivalent. Nevertheless, as the universe expands and cools down, the entropy term become less important and internal energy dominates. Thermal effects are typically included in the *effective potential* of the system, which in the case of the Goldstone model reads [214]

$$V_{\rm eff} = V(\phi) + \frac{\lambda + 3e^2}{12}T^2|\phi|^2 - \frac{2\pi^2}{45}T^4 \tag{2.6}$$

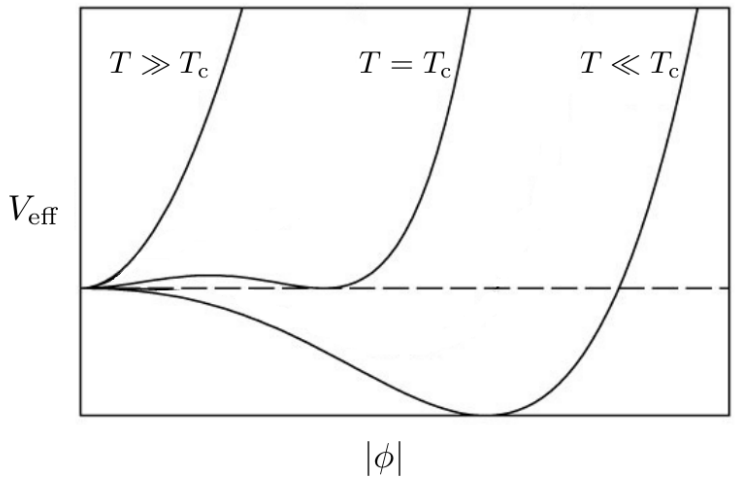

Figure 2.2: *Effective potential.*

At zero temperature the mexican-hat potential is recovered ($V(\phi) = \frac{1}{4}\lambda(\phi^\dagger\phi - \phi_0^2)^2$), but at finite temperatures thermal effects become relevant. Fig 2.2 shows the evolution of a typical effective potential during a cosmological thermal phase transition. At very high temperatures the expectation value of the field vanishes, *i.e.* the minimum of the effective potential lies at $\phi = 0$ ($T \gg T_c$ line in the picture). In other words, the symmetry is not broken and the ground state is as symmetric as the system. When the temperature drops, however, the barrier of the potential becomes increasingly more relevant and the ground state acquires a non-zero expectation value ($T \ll T_c$ line in the picture). The limit temperature that separates the two different phases is called the *critical temperature* T_c (represented as the line in the middle of the picture). As the temperature falls below T_c, the ground state is not longer invariant under rotations, though the total symmetry of the Lagrangian itself is maintained. The field sits at a specific ground state and the symmetry between different vacua is lost, *i.e.* the symmetry is spontaneously broken.

Symmetries can also be broken during inflation or at the end of it. An interesting and different mechanism for symmetry breaking is placed by some inflationary models, such as hybrid inflation scenarios, where the breaking of the symmetry is a consequence of a vacuum phase transition rather than a thermal phase transitions. The complex scalar field is coupled to the inflaton field, which replaces the temperature as the parameter that controls the phase transition. During inflation, *i.e.* when the inflaton is slowly rolling, the field is at $\phi = 0$. At the end of the slow-roll period, the complex field becomes unstable and rolls towards its real vacuum ($V(|\phi|) = 0$), where it has to chose between equivalent minima and the symmetry is spontaneously broken. The formation of defects is well justified in these inflationary models [181, 216, 219, 220].

Topological defects appear whenever the vacuum state has a non-trivial configuration. Defect formation is directly linked to the nature and topology of the vacuum manifold ($\mathcal{M}$), which can be analyzed studying homotopy groups. The homotopy group classifies distinct mappings of the n-dimensional sphere S^n in the vacuum manifold $\mathcal{M}$. Strictly speaking topological defects arise as a consequence of a non-trivial homotopy of the vacuum manifold, which means that the vacuum manifold can have disconnected components, unshrinkable loops or unshrinkable surfaces (see [214] for a detailed analysis of the homotopy groups and defect formation). Table 2.1 shows different topological defects that can arise depending on the topology of the vacuum manifold.

As an illustrative example the formation of string-like defects in the Goldstone model will be explored. Let us consider a closed path in a plane in physical space. If we move along this

$\pi_0(\mathcal{M}) \neq \mathbb{1}$	$\mathcal{M}$ disconnected	Domain walls
$\pi_1(\mathcal{M}) \neq \mathbb{1}$	non-contractible loops in $\mathcal{M}$	Cosmic strings
$\pi_2(\mathcal{M}) \neq \mathbb{1}$	non-contractible 2-spheres in $\mathcal{M}$	Monopoles
$\pi_3(\mathcal{M}) \neq \mathbb{1}$	non-contractible 3-spheres in $\mathcal{M}$	Textures

Table 2.1: *List of different topological defects and the topology of the vacuum manifold $\mathcal{M}$.*

path the field is at its ground state everywhere, the only difference between points of the closed trajectory is the complex phase. Since the path is closed the change of the phase along the curve can only vary in $\Delta\theta = 2\pi n$. Strings appear when there is a net winding of the complex phase, *i.e.* $n \neq 0$. One can try to locate such a twist in the complex phase by drawing smaller and smaller trajectories, until at some point the phase is no longer well defined. This can only be explained if there the field leaves the vacuum manifold and rises to the top of the potential ($\phi = 0$) in order to ensure field continuity. Figure 2.3 shows a typical representation of a string-like defect located where the complex phase has a non-continuum jump. The string is formed at points where the complex field is at the top of the potential, where the energy density is higher and the symmetry is also higher. In other words, topological defects retain the properties and symmetries of the old phase, embedded in the new one. This is why defect detection and their study could enlighten the unknown phase evolution of the universe and provide a unique way to explore the physics on those previous stages of the universe.

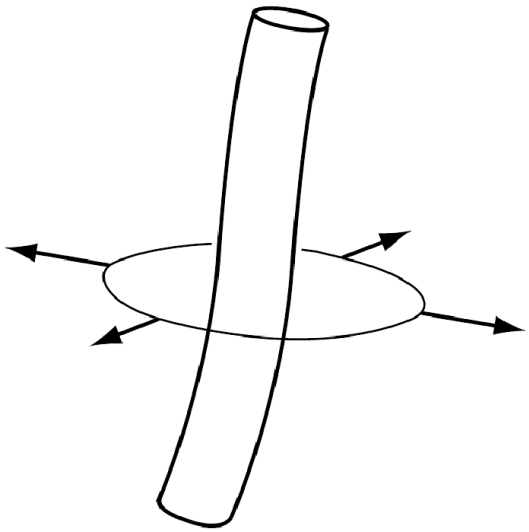

Figure 2.3: *Physical space representation of the core of a cosmic string and the complex phase pointing outwards. Figure from [68]*

This model contains string-like topological defects due to a non-trivial fundamental homotopy group of the vacuum manifold $\pi_1(\mathcal{M}) \neq \mathbb{1}$, *i.e.* non-trivial mappings of S^1 to the vacuum manifold. The topology does not allow to remove the defect points. One can imagine that the same process occur at every two-dimensional plane and obtain the string profile by continuity of the field. The topological nature of the defects imposes several interesting properties, for instance: since net windings cannot be removed, strings cannot have a definite end, they are either infinitely long or form closed loops.

Interestingly there are cases where defect formation is not governed by the topology of the vacuum manifold. *Non-topological* defects are also highly energetic extended objects, which also form in cosmological symmetry breaking processes, but which do not have topological restrictions. Their existence is linked to energy arguments rather than to topology. For instance, they can form when the system prefers to leave $\mathcal{M}$ and rise to the top of the potential because it is the most energetically favorable choice. Once such configurations are not so favored, they can decay and disappear. As we will see, however, non-topological defects can also be of cosmological interest.

Interestingly, the existence of defects is not restricted only to cosmology. They are very common in condensed matter physics, where they were firstly studied. Domain walls can be formed in ferromagnetic materials which develop a non-trivial vacuum structure after a symmetry breaking. Similarly, magnetic flux lines can appear in Type II superconductors, quantized vortex lines in ^{4}He and complicated textures in ^{3}He superfluids. Moreover, line defects in the form of dislocations are formed in some crystal liquids [214].

Defects in cosmology: Kibble-Zurek mechanism

The *Kibble-Zurek mechanism* for defect formation [119, 222, 223] provides an intuitive and qualitative way to understand how stochastic networks of defects can be formed in our universe. A region of the space where a spontaneous symmetry breaking happened would tend to smooth the complex phase distribution and decrease field gradients so as to minimize the energy of the system. Such a region therefore would acquire a energetically favorable aligned distribution of the phases and in principle avoid defect formation.

Causality is the key ingredient for defect formation in cosmology. Causality imposes a maximum correlation length, above which different regions of the space are not causally connected and can follow different paths towards their vacuum state. In terms of cosmological phase transitions, one can expect that the transitions could not have occurred simultaneously at regions that are not causally correlated. Each region would approach gradually its ground state choosing the vacuum state independently from other regions. The Kibble-Zurek mechanism predicts that when these uncorrelated region come to causal contact, there is some probability of forming defects at the boundaries of those regions.

Fig 2.4 shows a schematic representation of the Kibble-Zurek mechanism in 3 steps. In the upper part the spatial representation is shown, while the lower is the complex space representation of the potential of the system. The spatial representation includes regions of the space that underwent phase transitions; the old phase configuration in shown in grey, whereas the patches in the new one in white. Initially due to causal disconnection each white region choses the vacuum state independently from the other regions, the vacuum choice is shown below. As time goes by, horizons grow in a bubble-like manner and regions that were uncorrelated come to causal connection. Due to the nature of the initial choice of phases, drawing a closed path in physical space (dashed lines in the upper part) a non-zero winding of the phase is obtained. This winding cannot be removed, topology forbids it, and thus the field rises to the top of the potential since it is the only way to guarantee field continuity. In regions where the field leaves the vacuum manifold defects are formed, which as we mentioned earlier retain the properties of the old hotter phase (grey circle inside the dashed closed path in the upper part of the last picture). Kibble-Zurek mechanism claims that there is always a possibility to develop such non-trivial winding configurations and therefore defect formation in cosmology is an unavoidable possibility.

Even though defect formation *a la* Kibble-Zurek is very intuitive, it has to be noted that its applicability beyond systems with global symmetries has been doubted. It has been argued that for models with continuum gauge symmetries the mechanism is somewhat different, since not only

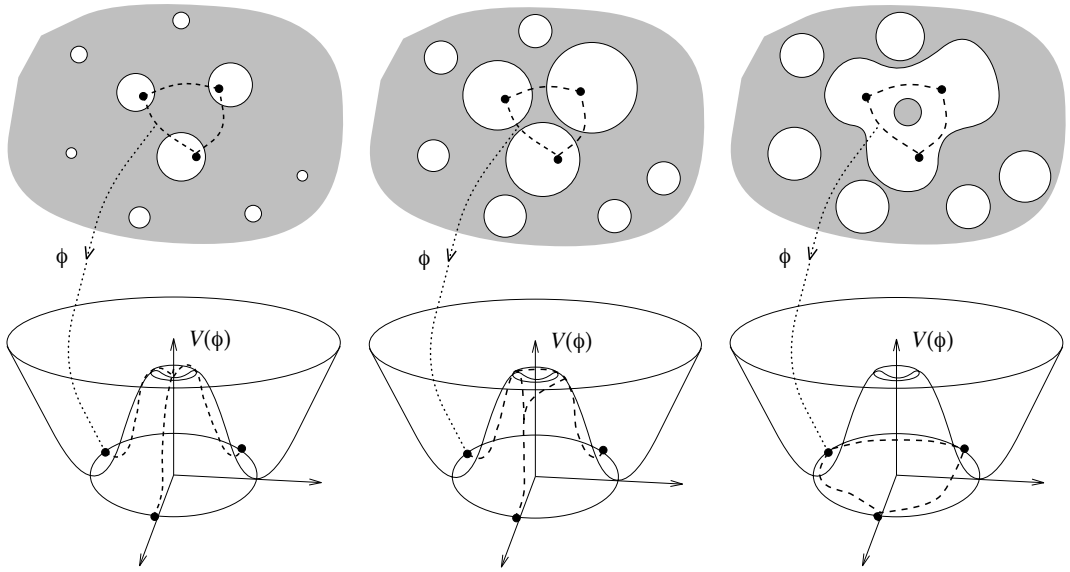

Figure 2.4: *Pictorial representation of the Kibble-Zurek mechanism. The upper part describes a spatial region of the universe where phase transitions took place at different moments and horizons of regions in the new phase (in white) grow with time. In the lower part the complex phase representation of the potential is shown. The sequence evolves from left to right. Initially regions choose independently the vacuum state since they are not causally connected. As time goes by, horizons keep growing and come to causal contact. In the end, a non-zero winding of the complex field appears (topological defect) as a consequence of the initial choice of the phases. Picture courtesy of M.B. Hindmarsh [104]*

the scalar field has to be taken into account, but also the effect produced by the presence of the gauge field. In [105, 163–165] the authors propose an alternative mechanism for defect formation, which would be more suitable for more complicated gauged theories. Essentially the formation of local vortices is linked to the confinement of the magnetic flux into tubes with quantized flux, which tend to be aligned in scales smaller than the characteristic scale, as opposed to what occurs in Kibble-Zurek [105].

Cosmological viability: Scaling

Historically some type of defects, such as magnetic monopoles or domain walls, have been regarded as problematic. For instance, networks of monopoles and domain walls formed at typical GUT scales would contain at least one defect per horizon volume and would inevitably end dominating the universe. One of the initial reasons to propose the inflation mechanism was indeed to avoid the problems caused by such unwanted relics (see Sec. 1.1.3).

The reason why some cosmic defects, *e.g.* cosmic strings, textures or global monopoles, have been so extensively studied is that they exhibit a feature known as *scaling*. Scaling implies that characteristic scales of the network, such as the correlation length or inter-string distances, grow linearly with time, *i.e.* their characteristic length remain constant with respect to the horizon. It not only prevents defects from dominating the universe, but ensures also that they will never disappear. Therefore if such scaling sources have once formed at the end of inflation, they should still be around today.

Scaling is the key ingredient that makes scaling defects cosmologically viable and compatible

with the description of the universe provided by different observations. Furthermore, scaling is an immensely valuable property, as it allows to extrapolate numerical simulations to required cosmological scales. Logically it is impossible to perform simulations that would cover the whole cosmological evolution of a given defect network. Neither is it possible to simulate defects at the exact moment they have been created, since the energy scale of the phase transition is beyond our knowledge. Instead, one considers relatively small periods of time, as compared to the cosmic time, and obtains statistical samples of the observables of the system. Scaling enables the extrapolation of such limited statistics to cosmological scales, a concrete example is the CMB anisotropy calculation, which will be reviewed in detail in Sec 2.3.

Observational consequences

Cosmic defects interact mainly via gravitational interaction. This is why typically the properties of the perturbations generated by them are characterized by the strength of their gravitational field, encapsulated in the dimensionless parameter $G\mu$. G is the Newton's constant while μ is directly related to the energy scale at which the phase transition took place and defects could have been produced, roughly $\mu \approx \phi_0^2$. In the case of string-like defects μ is directly related to another physical property: it is the string tension or the energy per unit length. Any detection of observational signal produced by defects would determine $G\mu$ and unequivocally set the energy scale of the phase transition.

One of the most studied phenomena induced by the presence of cosmic defect networks is the generation of CMB temperature and polarization anisotropies. Defects are considered to have formed at the end of inflation or in a later phase transition. If formed, they would perturb the cosmological fluid and their contribution to CMB anisotropies should be added to the dominant contribution produced by inflationary perturbations. Despite their relation to inflation, the highly non-linear evolution of defect networks removes any correlation with initial conditions, thus they can be regarded as independent signals. Defects perturb the primordial photon-baryon plasma and induce inhomogeneities in the last scattering source. However, as opposed to the inflationary perturbations, defects would continue creating perturbations and actively seeding anisotropies to the CMB during its path towards us. The theory of CMB anisotropy generation by defects will be reviewed in Section 2.3.

The production of gravitational waves by defects has also attracted huge interest in the defect community. The analysis has mainly been focused on gravitational wave production by cosmic string [6, 70, 111, 152, 187, 206, 213]. String networks contain loops, that soon after formed decay radiating in different manners. The gravitational distortions that occur at such decays is accompanied by several violent high energetic events, such as *kinks* or *cusps*, that could additionally create bursts of gravitational radiation [61–63, 186]. It is noteworthy, however, that the exact gravitational wave production mechanism is still very model dependent and ranges from relatively small amounts expected in field theories to larger contributions from Nambu-Goto (see next section) models. Gravitational wave backgrounds are also expected from other type of defects, such as *self-ordering scalar fields* or $\mathrm{O}(N)$ models [85, 88, 93].

Furthermore, cosmic defects are also candidates for the generation of other observable astrophysical events including gravitational lensing, high-energy cosmic rays and gamma ray burst by strings [50, 104, 178, 214], creation of cosmic magnetic fields [71] or generation of non-Gaussian signatures in cosmological perturbations [87, 107, 109, 169].

2.1.1 Cosmic strings

Cosmic strings are probably the most studied and most relevant topological defects. They were considered as a possible candidate, together with inflation, for structure formation in the universe. Accurate CMB observations established inflation as the correct paradigm for the creation of primordial perturbations and downgraded the possible role played by the cosmic strings. Nevertheless, they can still play a secondary role in a mixed inflation-defect scenario, even more when they are predicted by many inflationary models.

As it has been mentioned before, cosmic strings are one dimensional topological defects where the energy density is confined in a string-like configuration. The simplest model that leads to local cosmic string formation is the *Abelian Higgs model* (AH). The Lagrangian of the AH model reads:

$$\mathcal{L} = -\frac{1}{4e^2} F_{\mu\nu} F^{\mu\nu} + (D_\mu \phi)^* (D^\mu \phi) - \frac{\lambda}{4} (|\phi|^2 - \phi_0^2)^2 \,, \tag{2.7}$$

where $D_\mu = \partial_\mu + iA_\mu$, $F_{\mu\nu} = \partial_\mu A_\nu - \partial_\nu A_\mu$ and A_μ is the vector gauge field. e is the charge of the scalar field with respect to the gauge field and λ the self-coupling constant. The system is equivalent to that presented in the previous section, with the exception of the gauge field and covariant derivatives that appear as a consequence of promoting the symmetry to local. It obeys the local $\mathrm{U(1)_L}$ symmetry:

$$\phi \;\rightarrow\; \phi\, e^{i\alpha(x)} \tag{2.8}$$

$$A_\mu \;\rightarrow\; A_\mu - \partial_\mu \alpha(x), \tag{2.9}$$

The low-energy states of this system, as opposed to what happens in the global case, are two massive particles. Applying the same procedure one can obtain that the vacuum solution is composed by a charged scalar field with $m_{\mathrm{Sca}} = \sqrt{\lambda}\phi_0$ and a massive gauge field with $m_{\mathrm{Gauge}} = \sqrt{2}e\phi_0$. Gauge symmetry imposes the existence of the vector gauge field, which absorb the Goldstone boson of the global case, and acquires mass.

Similarly to the global case it is possible for the field to wrap around the circle of minima, developing a non-zero winding of the phase $\Delta\theta = 2\pi n$. Although the system is invariant under local phase transformations, this solution cannot be rotated to the vacuum by a gauge transformation if $n \neq 0$. In other words, the non-trivial topology of the vacuum enables the creation of unremovable defect points. Local strings, just like global ones, cannot have ends and are either infinite or closed.

The AH model admits infinite, axisymmetric and stable solutions, string-like solitons called *Abrikosov-Nielsen-Olesen* vortex lines [5, 150]. The solution is built around the following cylindrically-symmetric and straight ansatz for a string with arbitrary winding number n:

$$\phi = \phi_0 f(r) e^{in\theta} \,, \quad A_i = \frac{n}{er} A_\theta(r) \hat{\theta}_i \,, \quad A_0 = 0 \,. \tag{2.10}$$

where r and θ are the radial and azimuthal angle coordinates.

Substituting this into the Euler-Lagrange equations of Eq. (2.7),

$$\frac{d^2 f}{dr^2} + \frac{1}{r}\frac{df}{dr} - \frac{n^2 f}{r^2}(A_\theta - 1)^2 - \frac{\lambda}{2} f(f^2 - 1) = 0 \tag{2.11}$$

$$\frac{d^2 A_\theta}{dr^2} - \frac{1}{r}\frac{dA_\theta}{dr} - 2e^2 f^2 (A_\theta - 1) = 0\,. \tag{2.12}$$

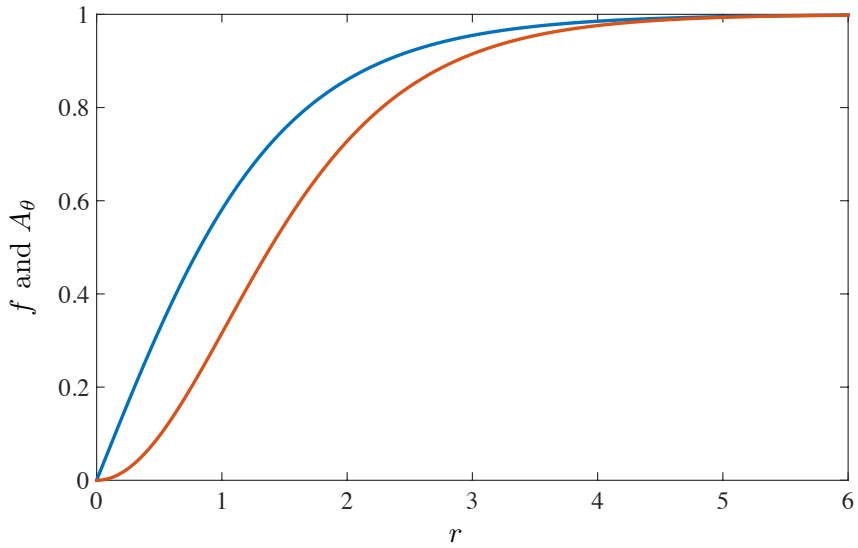

Figure 2.5: *Solutions of the Euler-Lagrange equations (Eq. (2.12)) of the Abrikosov-Nielsen-Olsen vortex lines in the Bogolmon'yi limit: f in blue and A_θ in red.*

Fig. 2.5 shows the numerical solutions of Eqs. (2.12) in the critical coupling (see next paragraph) obtained using relaxation techniques with proper boundary conditions that ensure finite energy requirement. It can be seen that the scalar field (blue line) and the gauge field (red line) leave the vacuum at small radius, where in fact most of the energy is concentrated. Moreover, the size of this region is approximately given by $m_{\rm Sca}^{-1} = (\sqrt{\lambda}\phi_0)^{-1}$ for the scalar function and $m_{\rm Gauge}^{-1} = (\sqrt{2}e\phi_0)^{-1}$ for the massive gauge function. In other words, the string is composed by two well defined but independent *cores*, where the complex scalar field and the massive vector are confined. Far from the cores, both functions approach gradually the vev, as they should.

The only relevant parameter of this model is $\beta = \lambda/2e^2 = m_{\rm Sca}/m_{\rm Gauge}$ [214]. When both masses become identical, $\beta = 1$, the equations are in the critical coupling or in the *Bogomol'nyi limit* and the equations of motion simplify considerably. Furthermore, the scalar core and the vector core have same size. Local vortices with $\beta < 1$ are always stable, whereas strings with $n > 1$ and $\beta > 1$ tend to split into *simple* or $n = 1$ vortices [104, 150]. The forces acting between strings depend also on β. When $\beta > 1$ the forces between strings are repulsive. In this case the vector core is bigger than the scalar core, thus the forces between different strings are governed by the repulsion of the vector fields. When $\beta < 1$ on the other hand, the scalar core is bigger and the force between strings is attractive. In the Bogomol'nyi limit the AH model can be promoted to a supersymmetric model. In other areas like the superconductivity theory $\beta = 1$ distinguishes Type I and Type II behaviours. For the remainder of this Thesis we will consider the critical coupling $\beta = 1$.

An important distinction must be made between strings of gauge origin and global strings.

Whilst global defects exhibit long range interaction driven by Goldstone bosons, local defects are screened by the presence of massive gauge fields that appear because of the gauge symmetry breaking.

String networks: global properties and scaling

The string network is not a static entity, it is evolving and changing continuously. It is formed by infinitely long strings and closed loops. Strings interact with each other and new loops and new strings are formed due to the partner exchange that occurs at string collisions. Usually the probability of string reconnection when different strings cross is determined by the parameter p. For solitonic strings like AH strings examinations of numerical simulations [145, 182] reveal that at every string collision new string configurations are formed. Therefore the usual assumption is to take $p = 1$ for solitonic strings. Nevertheless, there are situations in which the probability of intercommutation of solitonic strings is less than one [7, 41, 210].

The evolution of a cosmic string network towards the scaling regime can be understood exploring the interactions of the strings inside the network and their energy loss mechanisms. In a realistic cosmological scenario, that is, in an expanding universe infinite string would be stretched. In absence of any energy loss mechanism the string energy would be proportional to the scale-factor and the string network would soon dominate the universe. However, due to the high reconnection probability of cosmic string, infinite strings intercommute and loops also can be generated. Loops soon after created radiate and decay, via several channels which can include gravitational radiation, electromagnetic radiation or particle emission. Therefore, the energy growth coming from the stretching of infinite strings, is compensated by a highly efficient energy loss by loop radiation, which enables scaling of the networks. Moreover, though it will not be demonstrated here, it can be proven that scaling is an attractor solution for string networks (for more details we refer the reader to [214]).

Nambu-Goto approximation

The *Nambu-Goto* (NG) approximation is applied to situations when the width of the string is negligible comparing to the curvature radius of the string [25, 26, 53, 90]. In such situations the cosmic string could be thought as an infinitesimally thin object that has a cosmological length. Based on that, the Nambu-Goto model approximates cosmic strings to one dimensional objects and describes them by the Nambu-Goto action [104, 214]. The action of the NG string is proportional to the area of the world-sheet formed by the string as it travels and it reads:

$$S = -\mu \int d\sigma d\tau \sqrt{-\gamma}\,, \tag{2.13}$$

where σ and τ are the spatial and temporal coordinates and γ is the determinant of the induced metric.

An interesting feature of the NG model is that in Minkowski space the equations of motion reduce just to wave equations of the 4-dimensional coordinate variables of the string. Therefore all the dynamics of the string can be described by left- and right-moving solutions of the wave equation. Such a simplification implies that NG simulations require less computational power than field theory simulations and obtain bigger dynamical ranges. As a counterpart of this simulation time gain, NG simulations are not able to account for strings interactions since the microphysical details are ignored. For instance, reconnection and intercommutation have to be included *ad hoc* in the NG action by rules supplemented by the underlying field theory.

The most controversial difference between field theoretical simulations and NG simulations is the amount and evolution of string loops. There is no consensus in the cosmic string community: NG model string loops appear to oscillate more and live longer (see [48] for a recent study in NG loops) than the field theoretical ones, which decay soon after they are formed. One of the main reasons for such a difference might come from the fact that NG strings could only decay via gravitational radiation of loops. Massive modes that appear to be relevant in field theoretical models are absent in the NG case. We refer the reader to [103, 108] for detailed discussions on the relevance of small-scale structure and loop generation in AH cosmic strings.

Nambu-Goto loops also exhibit high energy events known as *kinks* and *cusps*, which given their violence could be perfect for gravitational wave creation. This is why NG models have extensively been used to determine the hypothetical stochastic gravitational wave background produced by string networks [61, 62, 152], which is more developed than the field theoretical case even though there have been some attempts [74]. NG gravitational wave probes are the ones that put the strongest constraints in NG string tensions, $G\mu < 10^{-9}$ [48].

Unconnected segment model

The *unconnected segment model* (USM) is a phenomenological model for the description of cosmic strings. It is based on the *velocity-dependent one-scale* (VOS) model [139, 140], which models analytically the large scale behavior of the string network. Essentially VOS model macroscopical equations for the energy and the velocity distribution of the system are derived averaging the microphysical effects of the network. As in the NG case, defect interactions must be included using phenomenological considerations.

The string networks as described by the USM model is composed by extremely thin and moving time-like segments of length proportional to the horizon size. It fundamentally introduces an extra layer of modeling, since the length of the strings and their velocity depend on two undetermined parameters: ξ and v [23, 24, 38, 215]. Moreover, it has also been extended to account for the small-scale structure of the string via the *wiggliness* parameter β [158]. Finally, the scaling regime is achieved by removing periodically certain amount of segments.

The USM model was proposed in the context of computation of CMB anisotropies by strings [23, 24, 38]. Provided it high degree of modeling, the USM model is able to mimic the evolution and CMB pattern produced by a network of NG strings as well as to reproduce the results obtained using field theoretical simulations (see [36] for a detailed comparison of models).

Nevertheless, it has to be noted that the USM model is not a predictive model, *i.e.* the model is not able to determine general properties of string networks and produce CMB power spectra based on those results. Instead, experimental data can be used to infer the values of the parameters of the model, which will determine which is the string model that explains best the observed signal.

2.1.2 Semilocal strings

A minimal extension of the Abelian-Higgs model, promoting the single scalar field to a $\mathrm{SU}(2)_{\mathrm{G}}$ doublet, yields to the semilocal model [8, 101, 205]. The semilocal model is described by the following Lagrangian:

$$\mathcal{L} = -\frac{1}{4e^2} F_{\mu\nu} F^{\mu\nu} + (D_\mu \Phi)^\dagger (D^\mu \Phi) - \frac{\beta}{4} (\Phi^\dagger \Phi - \phi_0)^2 \,, \tag{2.14}$$

where $\Phi = (\phi,\ \psi)$ is a doublet composed by two complex scalar fields. The covariant derivative D_μ and the field strength tensor $F_{\mu\nu}$ are defined just as in the Abelian-Higgs case. It can be

easily proven that removing one scalar field, the Abelian-Higgs model is recovered.

The vacuum manifold in this case is a three-sphere S^3 and its first homotopy group is trivial $\pi_1(S^3) = \mathbb{1}$. Therefore, topology does not enforce Φ to leave the vacuum manifold and defect formation is not as straightforward as in the AH model. One can prove, however, that one dimensional flux tubes exist as a solution of this model. In order to smooth the complex phase configuration the system either rotates the phases or leaves the vacuum and rise to the top of the potential. The difference in this case is that the choice depends on what the most energetically economic process is. If gradient terms associated to the rotation exceed the energy barrier of the potential, the system prefers to leave $\mathcal{M}$ and semilocal strings will be formed. The stability of semilocal strings is not trivial and like in the previous example it is mainly governed by $\beta = \lambda/2e^2 = m^2_{\rm Sca}/m^2_{\rm Gauge}$. For $\beta < 1$ semilocal strings are stable and for $\beta = 1$ they are neutrally stable [101]. For $\beta > 1$ on the other hand, they are unstable and if they form, they decay.

The symmetry breaking sequence that produces such defects is: $SU(2)_{\rm G} \times {\rm U}(1)_{\rm L} \to {\rm U}(1)_{\rm G}$. This is why the semilocal model can be thought as a particular case of the electroweak model, where the ${\rm SU}(2)$ symmetry is local instead of global. Alternatively one can obtain the semilocal model setting to zero the gauge coupling to the gauge field associated to the $SU(2)_{\rm L}$ symmetry in the Glashow-Weinberg-Salam model. Defect formation has also been studied in the electroweak model [204]. Nevertheless, it was found that for realistic values of the electroweak symmetry breaking, electroweak strings are unstable and thus unviable [114].

Semilocal strings are the typical example of non-topological and stable defects. As such, they exhibit special features that cannot be observed in topological strings. Unlike AH strings which are either infinite or closed due to topology restrictions, semilocal strings are finite in size and can have ends. Indeed, interestingly, the ends of such strings behave as global monopoles that can interact via long range interactions. Because the attraction of the effective monopoles it is possible for two strings to meet and form a longer string, and also for a segment to form a loop. Moreover, semilocal strings can suffer longitudinal oscillations, *i.e.* they can stretch or shrink, depending on the forces acting on their ends. Recently some effective models have been proposed, which take advantage of the fact that semilocal strings can be considered as composite string-global monopole defects [9].

2.1.3 Textures

Topological textures arise in models with broken non-Abelian ${\rm O}_{\rm Global}$(4) global symmetries. The Lagrangian of the model reads,

$$\mathcal{L} = \frac{1}{2}(\partial_\mu \Phi_i)(\partial^\mu \Phi_i) - \frac{\lambda}{4}(\Phi_i \Phi_i - \phi_0^2)^2 \,, \tag{2.15}$$

where $i = 1, ..., 4$. Models with broken ${\rm O}_{\rm Global}$(N), where $N > 4$, produce non-topological textures in three spatial dimensions where the dynamics is dictated by the evolution of non-linearly coupled Goldstone bosons.

Non-trivial mappings of S^3 spheres into the vacuum manifold yields to texture formation. The imposition of spatial uniformity at infinity effectively compactifies the physical space ($\mathbb{R}^3$) to S^3, which maps non-trivially into the vacuum manifold since $\pi_3(\mathcal{M}) \neq \mathbb{1}$. In contrast to other defects, in a texture the scalar field Φ is at the vacuum manifold everywhere, in other words, it is not topologically constrained to leave the minimum of the potential.

Imposition of spatial uniformity at infinite is what makes non-trivial windings of the complex scalar phase possible and enables the creation of textures. Unlike cosmic strings, whose energy comes from the potential term, the energy of textures comes entirely from the gradient energy of

the field. However, when textures enter into the horizon their *knots* collapse at relativistic speed. When the gradient of the field becomes sufficient, the field lifts over the potential barrier, the non-trivial windings around the vacuum manifold *unwinds* and textures decay radiating Goldstone bosons.

There exist different approaches to simulate the dynamics described by Eq. 2.15. One of the most famous one is the so-called non-linear sigma model [78, 79, 155]. As we mentioned the textures are formed even though the field never leaves the vacuum manifold, *i.e.* $\Phi_i\Phi_i - \phi_0^2 = 0$ everywhere. In the non-linear sigma model the dynamics of the scalar fields is dictated by the kinetic term, and the previous condition is included as a constraint of the system by considering λ a Lagrange multiplier. In other words, the field is forced by hand to be in the vacuum manifold. Alternatively, full field theory simulations have also been performed, which solve the equations of motion derived from the original Lagrangian [201]. Interestingly, it has been observed that in terms of CMB anisotropies the predictions of both models are very close [201].

Textures before unwinding and collapsing could induce background perturbations that could eventually produce observable effects in CMB anisotropies. In this sense, textures has been proposed as a possible candidate for the *cold spot* region measured by WMAP and *Planck* satellites [52, 59, 60, 84, 192, 212]. Furthermore, as with cosmic strings, their power spectra can be calculated from numerical simulations of an underlying field theory in an expanding cosmological model (see next section). The spectra have been calculated for $\mathrm{O}(4)_{\mathrm{G}}$ non-linear [78, 79, 155] or linear [201] σ-model. In Ref. [201] a comparison between the linear and non-linear σ-model can be found, showing that they are very close. There is also an analytic approximation in the large N limit of the $\mathrm{O}(N)$ non-linear σ-model [122].

2.1.4 Interconnected strings: *pq*-strings

Interconnected string models arise in brane inflation models, where fundamental strings or F-strings and string-like objects such as D-branes could form due to brane-antibrane annihilation processes [56, 81, 116, 136, 177]. Such *superstrings* could survive the cosmological evolution and can have cosmological sizes [68, 159], which implies that they can play a similar role of cosmic strings. Nevertheless, unlike solitonic strings, cosmic superstrings do not necessarily intercommute, instead they can join together forming heavy and stable bound states composed of *p* F-strings and *q* D-strings and called *pq*-strings [56, 81]. The boundaries of these segments are determined by 3-way Y-junctions where 3 different strings meet.

The evolution and description of F and D interconnected networks is rather complicated and approximations are highly desirable. Early works on cosmic superstring networks analyze non-Abelian field theories of the kind $\mathrm{G} \to \mathrm{Z}_3$, where 3-way type junctions can form, both analytically [27, 207] and numerically [106, 193]. More sophisticated analytical models include effective field theories such as VOS models, see for instance [30, 199], where different type of strings with different tension ranges can be considered.

Field theories have also been employed to describe interconnected string networks [166, 174, 176, 200]. The evolution of F and D-strings is approximated by *ordinary* solitonic cosmic strings, which are formed by usual spontaneous symmetry breaking mechanisms. Obviously field theories do not represent the totality of the properties of fundamental interconnected string networks, but they can be very useful in trying to study their possible cosmological or measurable consequences. The main differences between ordinary cosmic strings and cosmic superstrings are essentially the following: firstly the intercommutation probability of solitonic strings is of order 1, while it is expected to be lower for cosmic superstrings that live in more dimensions. Secondly, ordinary cosmic string networks are composed by infinitely long strings and loops, but do not have stable

bound states where 3 different type of strings meet, which are characteristic of interconnected superstring networks. Finally, there is a whole range of different possible tensions for cosmic superstrings, whereas networks of ordinary cosmic strings are composed by strings with same tension, unless strings with different windings are considered.

There are several field models that try to reproduce the dynamics of FD networks [166, 174]. These models are built considering a pair of complex scalar fields coupled to two $\mathrm{U}(1)_{\mathrm{L}}$ gauge fields and an attractive potential term so as to induce stable bound states. Field theory simulations of interconnected cosmic strings will be analyzed in Chapter 4 where we use the first model [174]. Let us briefly review the most important features of this model: it is invariant under $\mathrm{U}(1)_{\mathrm{L}} \times \mathrm{U}(1)_{\mathrm{L}}$ gauge symmetry. The Lagrangian thus reads,

$$\mathcal{L} = (D_\mu \phi)^* (D^\mu \phi) + (\mathcal{D}_\mu \psi)^* (\mathcal{D}^\mu \psi) - \frac{1}{4e^2} F_{\mu\nu} F^{\mu\nu} - \frac{1}{4g^2} \mathcal{F}_{\mu\nu} \mathcal{F}^{\mu\nu} - V(|\phi|, |\psi|)\,, \tag{2.16}$$

where ϕ and ψ are the two complex scalar fields, which represent each sector of the double $\mathrm{U}(1)_{\mathrm{L}}$ gauge symmetry. Each of them is independently charged with respect to its $\mathrm{U}(1)_{\mathrm{L}}$ gauge field: A_μ with coupling constant e (ϕ) and B_μ with g as the coupling constant (ψ).

The potential takes into account the symmetry breaking of each sector as well as the interaction between the two sectors:

$$V(|\phi|, |\psi|) = \frac{\lambda_{\mathrm{A}}}{4} (|\phi|^2 - \eta_{\mathrm{A}}^2)^2 + \frac{\lambda_{\mathrm{B}}}{4} (|\psi|^2 - \eta_{\mathrm{B}}^2)^2 - V_{\mathrm{int}}(|\phi|, |\psi|)\,, \tag{2.17}$$

where λ_{A} and λ_{B} are dimensionless coupling constants and η_{A} and η_{B} the vacuum expectation values for each kind of scalar fields.

Unless the last interaction term is considered, this Lagrangian describes the evolution of two independent networks of local cosmic strings. The last term includes the interaction between both type of fields, enabling the formation of stable bound states.

2.2 Defect dynamics in expanding universes: field theory simulations

Field theory simulations are aimed to reproduce defect's physics in realistic cosmological situations. Unlike other models, such as the Nambu-Goto model, the procedure to derive the equations of motion is not based on any approximation. Instead the full field equations of the underlying theory are considered in order not to leave any physical effect behind. In this section we will explain the procedure behind field theory simulations of Abelian-Higgs cosmic strings. The cosmic string case will be regarded as the characteristic example, but the theory and procedures explained below can be applied to any other scaling defect.

The equations of motion of the AH model in a spatially flat Friedmann-Lemaître-Robertson-Walker (FLRW) cosmology with scale factor a and choosing the temporal gauge ($A_0 = 0$) read:

$$\ddot{\phi} + 2\frac{\dot{a}}{a}\dot{\phi} - D_j D_j \phi = -a^2 \frac{\lambda}{2} (|\phi|^2 - \phi_0^2)\phi\,, \tag{2.18}$$

$$\dot{F}_{0j} - \partial_i F_{ij} = -2a^2 e^2 \mathrm{Im}(\phi^* D_j \phi)\,, \tag{2.19}$$

where $F_{0i} = \dot{A}_i$, which are supplemented with the Gauss law constraint

$$-\partial_i F_{0i} = -2a^2 e^2 \mathrm{Im}(\phi^* \dot{\phi})\,. \tag{2.20}$$

In these equations, the dot represents derivatives with respect to the conformal time; and the spatial derivatives are taken with respect to the comoving coordinates.

The dynamics of string networks, as can be seen in Eqs. (3.1) and (3.2), is highly non-linear. They cannot be analyzed analytically and thus numerical simulations are necessary. The approach to solve such equations and obtain general properties of string networks is to solve them on discretized lattices. Lattices are typically represented in comoving coordinates, where the comoving distance between points remains constant but the physical distance grows with time, due to the expansion of the universe. On lattices one reproduces small copies of the real universe and solve the equations of motion so as to analyze the cosmological evolutions of defects. A limitation always present in cosmological simulations is that in practice it is not possible to simulate exactly *our* universe. However, despite this uncertainty, numerical experiments can easily be repeated and an averaged statistical description of the universe obtained. Moreover, taking advantage of the scale-invariant evolution of cosmic string networks one can extrapolate such statistical samples to cosmological sizes of interest.

The discretization of the field equations on lattices is based on the *lattice link variable* method, which preserves the gauge invariance of the equations and recovers the original equations of motion in the continuum limit. The lattice link variable approach includes gauge invariance by taking literally the nature of gauge fields as affine connections which parallel transports the scalar fields. For further details on the lattice link variable approach see [120, 145]. Strings can be localized in the lattice by calculating the magnetic flux or equivalently calculating the windings of the complex phase. Gauge invariant winding identification is based on the method proposed in [117].

The equations of motions are not directly discretized, instead the Hamiltonian or, in the methodology adopted in this Thesis and proposed in [42], the action is discretized. The equations of motion are then derived varying the action with respect to the complex and gauge fields. Discretized field equations are then solved using the *leapfrog* method. The leapfrog method solves the equations of motion for the canonical conjugate of the complex field (similarly for the equation of the gauge field) and afterwards the complex field is updated from the value of the conjugate. This process must be made simultaneously in all the points of the cubic lattice, *i.e.* the values of the Higgs field and gauge fields are updated in the whole simulation space at each step. The reason for that is that the next time-step requires information of the actual as well as of the surrounding lattice points to update due to the presence of spatial derivatives.

Computationally the cost of updating the whole lattice at every time step is really high. Field theoretical simulations require efficient parallelization schemes that enable feasible implementations in current computational resources. Parallelization offers an economic way to separate the cubic lattice in small mini-lattices that can be distributed among different nodes of a computer and evolved independently, up to a step to step update of the boundaries of the mini-lattices. One of the most interesting parallelization structure for field theoretical models on lattices is provided by the publicly available `LATField2` library [67]. Based on the `C++` programming language, among other interesting options `LATField2` proposes an asymmetric lattice separation framework very useful for Fourier based massive calculations.

The most challenging task of lattice field simulations is to balance the computational cost/time and the dynamical range of the network evolution. In this sense, one of the main source of uncertainties of cosmic string simulations in expanding universes is to resolve simultaneously the

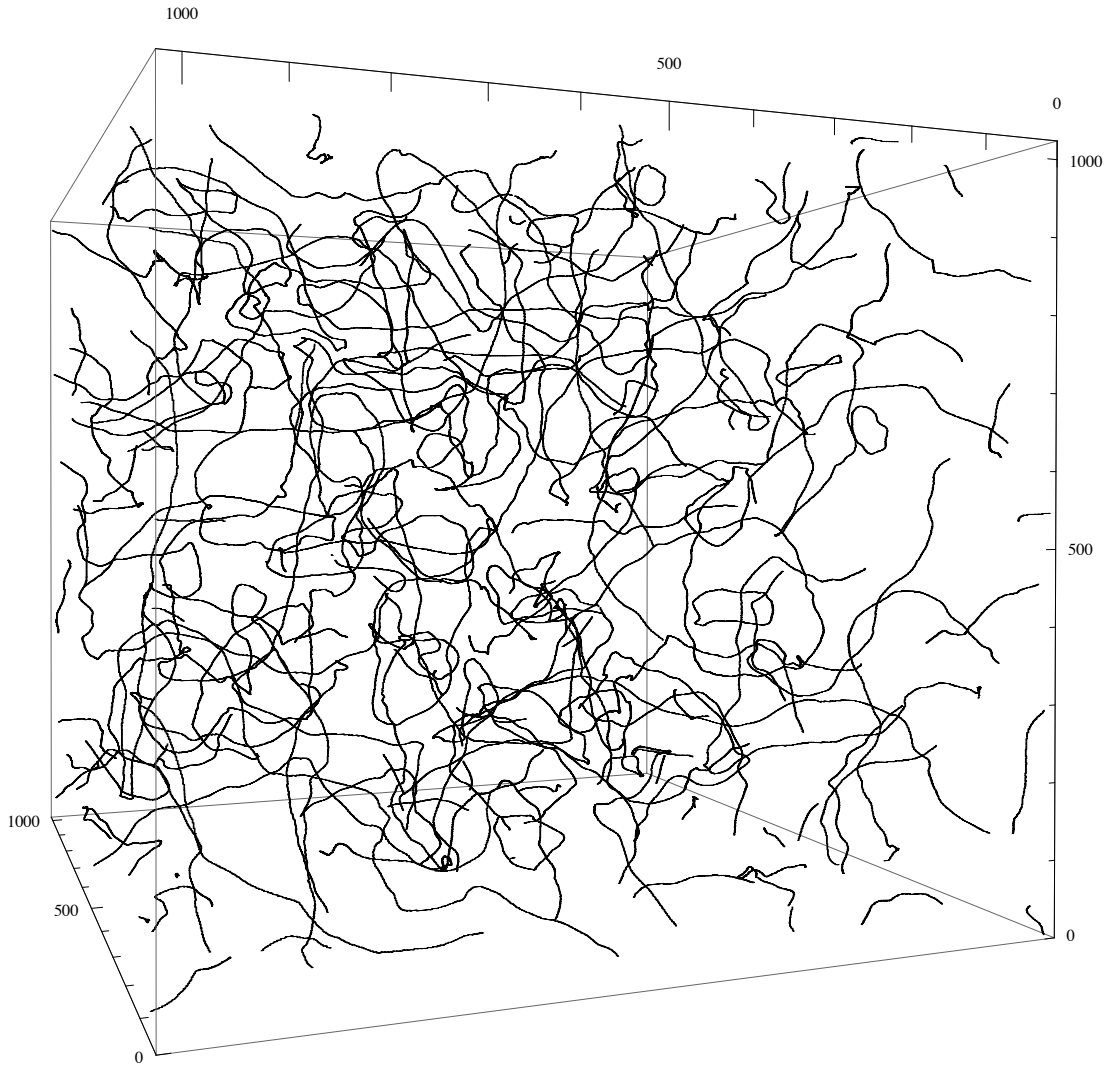

Figure 2.6: *Snapshot of a simulation of AH cosmic strings on a lattice with* 1024^3 *points.*

string core and the expansion of the universe. While the cosmic string core width is set by the mass scale of the field theory and remains unaltered by the expansion, the equations of motion are solved on lattices with comoving coordinates. As the universe expands the comoving string width shrinks. At some point in the evolution the comoving string width becomes less than the separation of adjacent lattice points, and we can no longer resolve the string core on the grid.

In order to be able to simultaneously resolve the width of the string and the expansion of the universe in comoving coordinates, the equations of motion can be modified so that the physical width grows, and the comoving width does not shrink as fast as it should [42, 144, 162]. Field equations are derived from a gauge-invariant action with time dependent coupling constants so as to not violate energy conservation and Gauss's law [42, 45]. Writing the time varying coupling constants as

$$\lambda = \frac{\lambda_0}{a^{2(1-s)}}\,, \quad e = \frac{e_0}{a^{(1-s)}}\,, \tag{2.21}$$

where we call s the core growth parameter, leads to the equations

$$\ddot{\phi} + 2\frac{\dot{a}}{a}\dot{\phi} - D_j D_j \phi = -a^{2s}\frac{\lambda_0}{2}(|\phi|^2 - \phi_0^2)\phi, \tag{2.22}$$

$$\dot{F}_{0j} + 2(1-s)\frac{\dot{a}}{a}F_{0j} - \partial_i F_{ij} = -2a^{2s}e_0^2 \mathrm{Im}(\phi^* D_j \phi). \tag{2.23}$$

These equations preserve Gauss's law and reduce to the true field equations when $s = 1$. With the help of the core growth parameter we can write the comoving string width as:

$$w = \frac{w_0}{a^s}\,. \tag{2.24}$$

If $s < 1$, the strings have growing physical width. However, the string mass per unit length and tension is preserved, and therefore the string dynamics are unaffected for configurations where the width can be neglected. The extreme case is given by $s = 0$ in which the width of the string is constant in comoving coordinates. Extensive testing showed that taking $s = 0$ is an acceptable approximation, which improves considerably the dynamical range of the simulations and with errors which are subdominant to those introduced by the finite size and finite duration of the simulations [42].

As an illustrative example, we include a snapshot of a AH cosmic string field theory simulation on a lattice in Fig. 2.6, where the simulation box has 1024^3 points.

2.3 CMB: UETC approach

The evolution of the string network perturbs the background space-time; those perturbations evolve and affect the contents of the universe, eventually producing cosmologically observable effects. Among them, CMB anisotropy creation has been one of the most analyzed defect effect. In contrast to the inflationary perturbations, which were seeded primordially and then evolve "passively", defects induce perturbations actively during their whole existence. As we mentioned previously, those are estimated to be roughly of the order of the magnitude of $G\mu$.

Therefore, in principle, in order to calculate the anisotropy pattern induced by string networks we have to solve the Einstein-Boltzmann equations with active sources, which account for scaling seeds such as cosmic strings. Fortunately, however, given the high degree of gaussianity of CMB anisotropies their properties are fully characterized by the 2-point correlation function. This means that *unequal time correlators* (UETCs) of the energy momentum tensor are the only object needed to derive the power spectrum of CMB anisotropies [122, 155, 197]. Let us briefly review the UETC approach: the system of dynamical equations for the evolution of cosmological perturbations in Fourier space can be summarized in the following way:

$$\hat{\mathcal{D}}_{ab}(k, a, \dot{a}, ...)X_a(\mathbf{k}, \tau) = S_b(\mathbf{k}, \tau) \tag{2.25}$$

where the differential operator $\hat{\mathcal{D}}_{ab}$ includes the FLRW background quantities and acts upon the metric, matter and photon perturbations described by the vector X_a. The active seed presence is included in S_b (see [42] for exact expressions of the source functions in the AH model and [76–78] for detailed implementation of scaling seeds in gauge invariant perturbation formalism). If S_b is known from network simulations, then the power spectra can be calculated solving the inhomogeneous set of equations using Green's functions ($\mathcal{G}_{ac}(k, \tau, \tau')$):

$$\langle X_a X_b^* \rangle = \int\int \mathrm{d}\tau' \mathrm{d}\tau'' \mathcal{G}_{ac}(\tau') \mathcal{G}_{bd}(\tau'') \langle S_c(\tau') S_d(\tau'') \rangle \,. \tag{2.26}$$

This equation shows that the only quantity needed from simulations to compute the CMB power spectrum is the bracketed term on the r.h.s., which is strictly related to UETCs. By definition UETCs of the energy momentum tensor are,

$$U_{\lambda\kappa\mu\nu}(\mathbf{k}, \tau, \tau') = \langle \mathcal{T}_{\lambda\kappa}(\mathbf{k}, \tau) \mathcal{T}^*_{\mu\nu}(\mathbf{k}, \tau') \rangle \,, \tag{2.27}$$

where $\mathcal{T}_{\alpha\beta}(\mathbf{k}, \tau)$ is the AH energy-momentum tensor. In principle considering all possible degrees of freedom of the energy-momentum tensor (2.27), there seem to be $\frac{1}{2}10(10+1) = 55$ such correlators that would be functions of 5 variables (3 components of $\mathbf{k}$ plus two times). Fortunately, rotational symmetry simplifies the problem considerably and reduces the UETC group to 5 independent correlators that depend on 3 variables [42, 77, 78]: k (the magnitude of $\mathbf{k}$), τ and τ'.

The source terms of Eq (2.25) and (2.26) are then just the projections of the energy momentum tensors:

$$S_a(\mathbf{k}, \tau) = P_a^{\mu\nu}(\mathbf{k}) \mathcal{T}_{\mu\nu}(\mathbf{k}, \tau), \tag{2.28}$$

where $P_a^{\mu\nu}(\mathbf{k})$ project onto scalar, vector and tensor parts. In principle there are two of each, but the two vector and the two tensor components are related by parity for a symmetric source like Abelian Higgs strings [42]. Hence, we may consider that the indices a, b take four values corresponding to the independent components of the energy momentum tensor: two scalar, one vector and one tensor. Usually the scalar indices are denoted by 1 and 2 (corresponding to the longitudinal gauge potentials ϕ and ψ), the vector component with 'v' and the tensor component with 't'.

Taking everything into account, we can write

$$U_{ab}(\mathbf{k}, \tau, \tau') = \frac{\phi_0^4}{\sqrt{\tau\tau'}} \frac{1}{V} C_{ab}(k, \tau, \tau'), \tag{2.29}$$

where ϕ_0 is the symmetry breaking scale, V a formal comoving volume factor, and the functions $C_{ab}(k, \tau, \tau')$ defined by this equation are dimensionless. Note that the scalar, vector and tensor contributions are decoupled for linearized cosmological perturbations, and therefore cross correlators between them vanish, except in the scalar sector: hence the 5 independent correlators. Note also that we adopt the definition of C_{vv} used in [64] that differs by a factor $(k\tau)^2$ from other works.

A further simplification occurs when the times τ and τ' are both in epochs during which the scale factor grows with the same constant power of conformal time, that is, when the network is expected to be in scaling regime. In this case the correlation functions do not depend on k, τ and τ' separately, but only on $k\tau$ and $k\tau'$ (or $k\sqrt{\tau\tau'}$ and τ'/τ) [77, 154]. Scaling correlators can be written as,

$$U_{ab}(\mathbf{k}, \tau, \tau') = \frac{\phi_0^4}{\sqrt{\tau\tau'}} \frac{1}{V} \bar{C}_{ab}(k\tau, k\tau') \,. \tag{2.30}$$

Here, the over-bar represents the scaling form of the UETC in a FLRW background.

Whilst our approach measures UETCs from network simulations, we do not in fact use Eq. (2.26) with such quadratic terms. Instead we decompose the scaling correlators, which are positive

definite and symmetric, into their eigenfunctions $c^n(k,\tau)$ defined through [54, 155]

$$\int_{\tau_{\rm i}}^{\tau_{\rm now}} d\tau' \bar{C}_{ab}(k\tau, k\tau') c_b^n(k,\tau') = \lambda_n c_a^n(k,\tau). \tag{2.31}$$

The scaling UETC is recovered through the sum

$$\bar{C}_{ab}(k\tau, k\tau') = \sum_n \lambda_n c_a^n(k,\tau) c_b^{n*}(k,\tau')\,. \tag{2.32}$$

Formally, the power spectra and cross-correlations of a perturbation in a cosmological variable X_a can be written

$$\langle X_a(\mathbf{k},\tau) {X_b}^*(\mathbf{k},\tau)\rangle = \frac{\phi_0^4}{V} \sum_n \lambda_n I_a^n(k,\tau) I_b^{n*}(k,\tau)\,, \tag{2.33}$$

where the contribution of each linear term, $I_a^n(k,\tau)$, is

$$I_a^n(k,\tau) = \int_{t_{\rm i}}^{\tau} d\tau' \mathcal{G}_{ab}(k,\tau,\tau') \frac{c_b^n(k,\tau')}{\sqrt{\tau'}}\,, \tag{2.34}$$

and $\mathcal{G}$ is the Green's function for the quantity X as in Eq. (2.26). The integration is performed numerically, using a modified version of one of the standard Einstein-Boltzmann (EB) integrators `CMBEASY` [72], `CLASS` [49, 126], or `CAMB` [127]. Hence, if UETCs are decomposed into their eigenfunctions, they can be used as sources for an EB solver. In practice, the square root of the eigenvalue (which should be positive) and the eigenfunction are combined together into an object called the source function. The total power spectra is reconstructed by taking the sum of the power spectra obtained for each source function:

$$C_\ell^{\rm Tot} = \sum_n \lambda_n^{\rm S} C_{\ell,n}^{\rm S} + \sum_n \lambda_n^{\rm V} C_{\ell,n}^{\rm V} + \sum_n \lambda_n^{\rm T} C_{\ell,n}^{\rm T}\,. \tag{2.35}$$

Scaling is an immensely valuable property, as it allows to extrapolate numerical simulations to the required cosmological scales. However, perfect scaling is not a feature of the true UETCs, as the universe undergoes a transition from radiation-dominated to matter-dominated expansion during times of interest, and more recently to accelerated expansion. Hence the UETCs also depend explicitly on $\tau_{\rm eq}$ and τ_Λ, the times of equal radiation and matter density, and equal matter and dark energy density. Exploring UETCs with broken scaling, and improving the previous method of accounting for cosmological transitions, will be an important part of Chapter 3.

The UETC method has widely been used in field theory simulations to calculate CMB power spectra. In the case of cosmic strings the calculation of power spectra is a particularly active research area, which is adapting to new computational and technical resources. CMB power spectra of cosmic strings calculated using field theory simulations were first published in [42, 43], and updated in [45]. In addition to cosmic strings, the possible CMB contributions of other cosmic defects have been similarly calculated: semilocal strings and textures in [201] and self-ordering scalar fields in [86]. An important part of this Thesis, Chapter 3 and [64], is devoted to update and extend the cosmic string power spectra predictions using the biggest simulations to date. The UETC method has also been adapted to other simulation schemes such as NG [125] and USM [32]. Roughly, NG, USM and field theory calculations predict the same pattern for the CMB power spectrum, except for a global normalization factor [36].

For a proper parameter estimation analysis that aims to determine the cosmological parameters

in models containing defects, the power spectra of defects should be calculated for every set of possible cosmological parameters, *i.e.* for a huge number of different cases. Moreover, CMB calculations for active perturbing objects like scaling seeds require much more computational time and cost than those produced passively by inflation. It is clear that such calculations are not feasible in current computational systems. Nevertheless, the relative contribution of defects to the total temperature perturbations has been restricted to be no more than a few percent, corresponding to an upper bound on $G\mu < 10^{-6}$ or on the symmetry-breaking scale of about 4×10^{15} GeV [14, 125, 132, 203], and the back-reaction of defects in the background cosmology is expected to be of order $\mathcal{O}((G\mu)^2)$. In other words, the result of a possible change in the cosmological parameters produced by the presence of defects would produce a second order effect and would be negligible. Hence, the defect contribution needs only to be calculated once, using currently favored values of the cosmological parameters.

The shape and profile of the spectra can be determined by simulations, but not the overall normalization. It is customary to represent defect power spectra in $\propto (G\mu)^{-2}$ units. This choice exhibits our lack of knowledge about when the string network was formed. Higher energy scale of the symmetry breaking implies higher $G\mu$ and thus strings would produce bigger perturbations which translate into higher amplitude of the anisotropy power spectrum. In fact, it is the normalization of defects ($G\mu$) what parameter fitting analyses including models with defects try to determine. Alternatively to $G\mu$, it is also typical to determine the string contribution to the total CMB using f_{10}. f_{10} measures the relative contribution of strings to the total, *i.e.* inflation plus strings, at multipole $\ell = 10$. In CMB contexts $G\mu$ and f_{10} are equivalently used and for small contributions from defects $f_{10} \propto (G\mu)^2$.

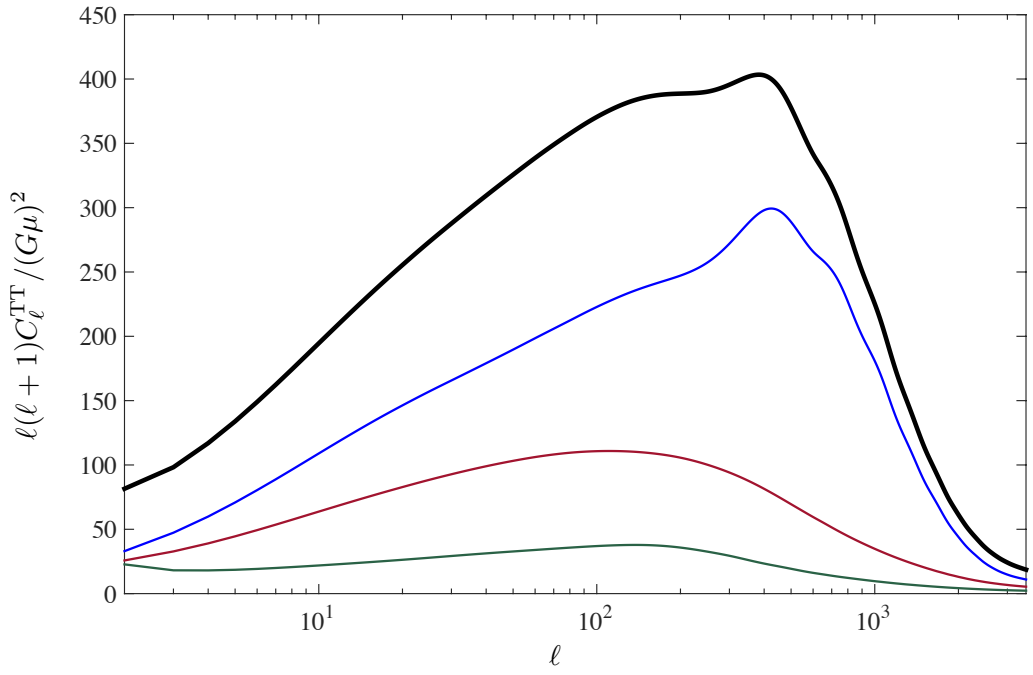

Figure 2.7: *CMB temperature anisotropy power spectrum of AH strings decomposed into scalar (blue line), vector (red line) and tensor (green line) perturbations together with the total in thick black line. The power spectra were calculated in [45].*

Fig. 2.7 shows the temperature power spectrum produced by a network of cosmic strings.

The spectrum was calculated following the UETC approach and published in [45]. We show in different color the decomposition into scalar (blue), vector (red) and tensor (green) together with the total contribution (thick black line). As it can be seen from the picture, the dominant contribution comes from scalar perturbations, while the amplitude of the vector and tensor spectra are significantly smaller. The total contribution is characterized by a single peak at $\ell \sim 500$ and a decay at high-ℓ-s which follows a power-law behaviour.

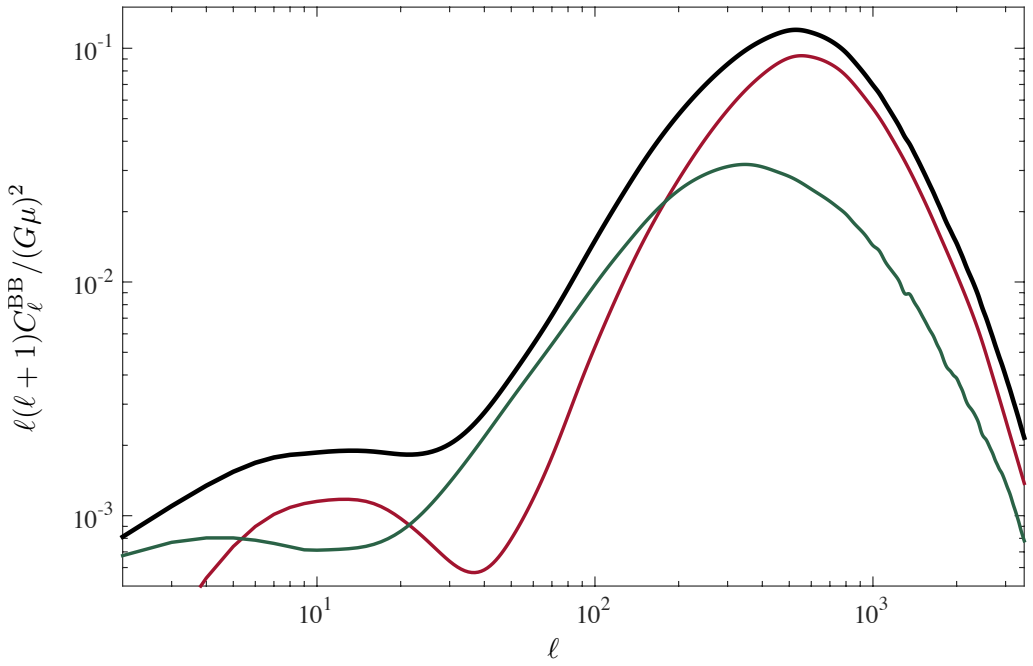

Figure 2.8: *CMB B-mode polarization anisotropy power spectrum of AH strings decomposed into vector (red line) and tensor (green line) perturbations together with the total in thick black line. The power spectra were calculated in [45].*

As mentioned in the previous chapter of the Introduction, defects are considered one of the few cosmological objects that can directly produce B-mode polarization of the CMB. The detection of B-modes is referred as the *smoking gun* for inflation, which can produce B-modes via primordial gravitational waves; but it could also be for defects. The amount of inflationary gravitational waves predicted can vary enormously from model to model (from $r \sim \mathcal{O}(10^{-2})$ to $\mathcal{O}(10^{-23})$). Furthermore, the scalar perturbations that are dominant in the temperature channel are absent in B-modes, they only contribute via lensing of E-modes. Indeed primordial contributions to B-modes, inflation gravitational waves and defects, will not be masked by such lensing signal, as can be seen in Fig 2.9 and Fig 1.3 of Chapter 1. This is why even though the relative contribution of defects to temperature anisotropies is highly constrained by accurate measurements, they could still be dominant in the B-mode channel.

Cosmic defects perturb continuously the cosmological fluid. Vector and tensor modes are continuously seeded and both contribute significantly to CMB B-modes, as opposed to the inflationary case where only tensor can produce directly B-modes. Another interesting difference between inflation and defects, is that the amplitude of the temperature perturbations and polarization perturbations are completely correlated in defects, *i.e.* they depend upon a single parameter $G\mu$, whereas they are almost independent in the inflationary, apart from the inflationary consistency

relation [128]. It essentially means that any bound derived for one of the channels must be applied and imposed in all of them. As we will see in Chapter 2 of Results, this has important consequences when fitting CMB polarization data with defect predictions.

B-mode spectra predictions are shown in Fig. 2.8 and Fig 2.9. In Fig. 2.8 we show the decomposition of the prediction for AH strings into vector (red line) and tensor (green line) together with the total contribution (thick black line). Vectors peak at smaller scales, while tensors do at lower multipoles. Both of them contribute almost at the same level to B-modes. Figure 2.9, in turn, shows the comparison of the CMB B-mode power spectrum calculated for different defects: AH strings in blue, semilocal strings in black and textures in red. The semilocal and texture spectra were calculated in [201].

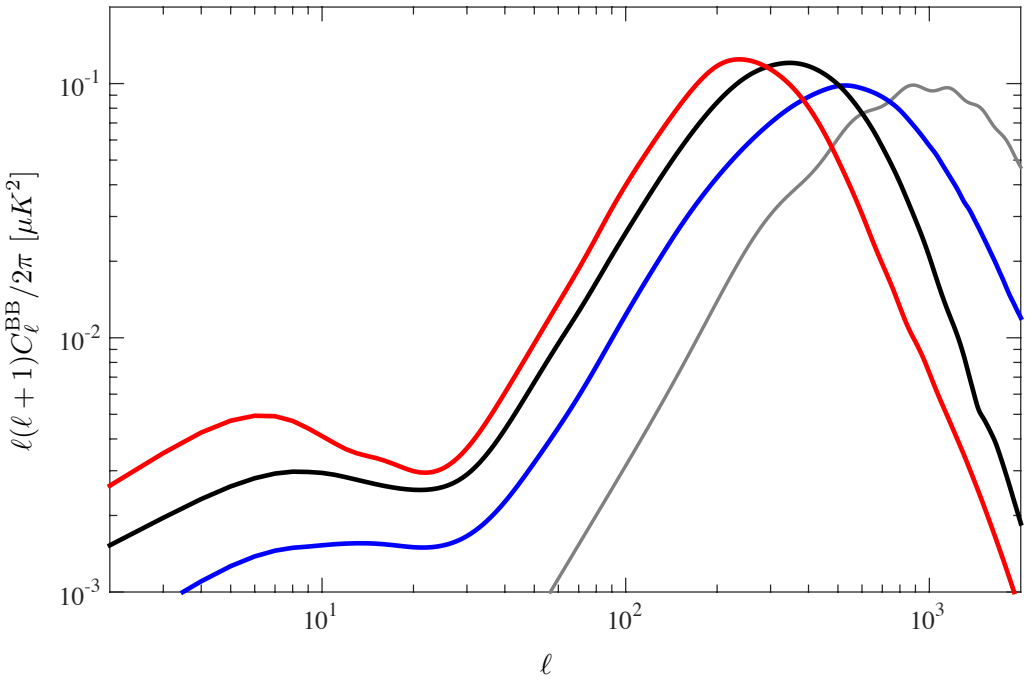

Figure 2.9: *CMB B-mode polarization anisotropy power spectra of AH strings (blue line), semilocal strings (black line) and textures (red line). The lensing of the E-modes obtained using Planck best fit values for the cosmological parameters is also included (thin grey line).*

As can be shown from the picture, different defects produce roughly the same spectrum pattern for the polarization. The most significant difference is the position of the peak, which is located at higher multipoles for AH strings $\ell \sim 500$, at $\ell \sim 300$ for semilocal strings and at $\ell \sim 200$ for textures. A future B-mode detection made by a experiment with enough precision, similar to already proposed ones such as CORE or QUIJOTE, would be able to distinguish between the signal of inflationary gravitational waves and defects, and also to discriminate between different type of defects [92, 148, 202]. Determining the nature of cosmic defects would provide invaluable information on high-energy symmetry breaking.

PART II

Results

1 Correlations between cosmic strings and extra relativistic degrees of freedom

Increasingly accurate cosmological measurements, specifically analysis of the cosmic microwave background, have stablished the Standard Cosmological model as the description of the universe that the community agrees upon. Yet there exist some unanswered questions, which mainly lie between the link of the standard cosmological model and the standard model for high energy physics. It is in the small details and small windows that the data allow us to try different approaches where a promising road to understanding the constituents of the cosmological standard model lies.

An interesting example of that is the presumable excess on the relativistic species present at the early universe. The standard model for high energy physics predicts 3 neutrino flavours, giving $N_{\rm eff} = 3.046$ (see section 1.1.1 for exact definitions) which also accounts for some corrections from incomplete decoupling [137]. However, some cosmological measurements seem to indicate that this number is bigger, which in fact would be a signal of extra relativistic energy in the early universe. The excess could be a hint of the existence of an extra neutrino flavour, or even it could be a hint of other kinds of relativistic energy present at those early stages of the universe.

As we mentioned, the high energy physics standard model predicts three neutrino flavours, giving $N_{\rm eff} = 3.046$. However, when this work was accomplished, analysis on $N_{\rm eff}$ from some cosmological data seemed to prefer values greater than 3.046 indicating the presence of an extra relativistic energy component at the early universe: a value of $N_{\rm eff} = 4.34^{+0.86}_{-0.88}$ at 68% C.L. can be found for the combination of CMB data from *Wilkinson Microwave Anisotropy Probe* 7-year (WMAP7) with *Baryon Acoustic Oscillation* (BAO) data presented in [121] and the value of H_0 given by the *Hubble Space Telescope* (HST) [171]. Also the inclusion of CMB data at small scales, which provides tighter constraints, still showed a preference for the existence of an extra component of radiation different from neutrinos. In combination with WMAP7 data, BAO and the value of H_0, an $N_{\rm eff} = 4.56 \pm 1.5$ at 68% C.L was published from the *Atacama Cosmology Telescope* (ACT) [75] and $N_{\rm eff} = 3.86 \pm 0.42$ from the *South Pole Telescope* (SPT) data [118].

Along these lines, some groups investigated the option of gravitational waves being the extra component [190]. Those gravitational waves could account for the extra radiation component needed to explain the observed $N_{\rm eff}$. The Cosmic Gravitational Wave Background (CGWB) behaves as noninteracting massless particles [143], so their effect on the CMB is the same as massless neutrinos when their energy-density perturbations are adiabatic, as one would expect from inflation.

One important question, though, is to give the source of those gravitational waves. If they were there at the early Universe, what was creating them? One of the possible answers put forward in the literature has been that cosmic strings could be the source of this CGWB [180]. Besides CMB anisotropies, cosmic strings would also be (active) sources of gravitational waves. There have

been several works trying to obtain the gravitational wave spectra coming from cosmic strings, although there is still some debate in the community [61, 62, 152, 184–187]. A full field theory simulation would be very helpful. The loop distribution of strings is not completely understood either [46, 47, 73, 108, 133, 153, 160, 161, 172, 173, 209], and that parameter could be key in estimating the gravitational wave production from strings. Besides, the decay products of strings are also important, since strings could be decaying directly into gravitational modes or could decay into other particles. For example, pulsar timing bounds on cosmic string tension can change significantly due to those factors mentioned above, i.e., loop production and decay mechanisms.

All in all, the excess energy stored in relativistic components could come from gravitational waves originated in cosmic strings. In Ref. [180] the authors discussed this possibility and gave an upper bound on the cosmic string tension $(G\mu)^2 < 10^{-7}$ at 95% confidence level (C.L.). However, that zero order approach can be improved by noting the following: If the excess in $N_{\rm eff}$ comes from cosmic strings, cosmic strings were there in the early Universe. Then, cosmic strings would have also contributed to the temperature (and polarization) CMB anisotropies, and thus the parameter estimation should be done by including the contribution from string from the beginning.

It is also known that cosmic strings have degeneracies and correlations with other parameters in the ΛCDM model. For example, it was shown in Refs. [39, 44] that an $n_{\rm s} = 1$ was possible with the (then) current data if strings were included in the analysis, due to a suite of degeneracies. Thus, it is interesting to investigate whether such correlations exist between the string contribution and $N_{\rm eff}$ and what implications this may have in both the string tension and the extra neutrino species.

In this Chapter we present the work performed in [130], where we addressed the presented issue exploring the cosmological parameter space through a likelihood analysis. We performed a Markov Chain Monte Carlo type analysis to estimate cosmological parameters, including cosmic string contributions, either letting $N_{\rm eff}$ be a free parameter or inferring it from the value obtained by the cosmic string parameter. We used CMB data both for relatively small ℓ (WMAP7 [123]) and for larger ℓ (SPT data [118]). We will also considered non-CMB experimental data given by HST measurement of the Hubble constant (H_0) by Riess *et al* [171] and BAO data by Percival *i.e.* [157].

1.1 Theoretical Background

1.1.1 Effective Number of Neutrinos

The amplitude and the position of the acoustic peaks of the CMB power spectrum are determined by the energy content of the Universe before recombination, *i.e.* by the matter and radiation content. According to the standard cosmological model the relativistic matter content at Big Bang Nucleosynthesis (BBN) consisted of photons, electrons and three neutrino flavours, which in term of degrees of freedom can be written as:

$$\frac{43}{4} = 2 + \frac{7}{8}(4+6), \tag{1.1}$$

where photons, electrons and positrons have 2 helicity states, while neutrinos and antineutrinos only one. The factor $\frac{7}{8}$ appears because these last are fermions.

The effective number of neutrinos ($N_{\rm eff}$) encapsulates the contribution of any extra radiation

component: for instance, an extra neutrino specie would contribute one unit to $N_{\rm eff}$. In general, however, $N_{\rm eff}$ is not an integer and any extra relativistic specie contributes in the following way:

$$\frac{43}{4} + \sum_i g_i \left(\frac{T_i}{T_\gamma}\right)^4 + \frac{7}{8}\sum_j g_j \left(\frac{T_j}{T_\gamma}\right)^4 = 2 + \frac{7}{8}(4 + 2N_{\rm eff}), \tag{1.2}$$

where i and j stand for any extra boson and fermion contribution respectively, and g_i and g_j represent the internal degrees of freedom of each extra specie. Out of thermal equilibrium, the temperature of the extra particle (T_i) differs from the temperature of the photons (T_γ).

The main effect produced by a change of the radiation density before recombination comes from the shift of the redshift of the matter-radiation equality, $z_{\rm eq}$. The more (less) relativistic contributors present at recombination, the later (sooner) enters the Universe in the matter domination, which translates into smaller (bigger) $z_{\rm eq}$. Therefore, $N_{\rm eff}$ can be represented equivalently as:

$$N_{\rm eff} = 3.04 + 7.44\left(\frac{\Omega_m h^2}{0.1308}\frac{3139}{1+z_{eq}} - 1\right). \tag{1.3}$$

An increase in $N_{\rm eff}$ also affects the evolution of the acoustic oscillations of the primordial baryon-photon plasma, and thus also the acoustic peaks of the power spectrum. On the one hand, higher values of $N_{\rm eff}$ heighten the first two peaks: due to the shift in the matter-radiation equality, modes that entered earlier in the horizon enhance their amplitude [112]. On the other hand, such a change also affects the damping tail of the spectrum, which causes the decrease of the amplitude of the higher peaks and displacement of them to higher multipoles. A graphical representation can be found in Fig. 1.1.

1.1.2 Cosmological Gravitational Wave Background

Gravitational Waves are solutions of the linearized Einstein equations [143]:

$$g_{\mu\nu} = \eta_{\mu\nu} + h_{\mu\nu}, \tag{1.4}$$

where $\eta_{\mu\nu}$ is the Friedmann-Lemaître-Robertson-Walker (FLRW) metric and $h_{\mu\nu}$ the perturbation, $|h_{\mu\nu}| \ll 1$. In the isotropic, homogeneous and expanding universe, the spatial-spatial Transverse-Traceless degrees of freedom of the perturbation verify the wave equations [143]:

$$\ddot{h}_{ij} + 3H\dot{h}_{ij} - \frac{1}{a^2}\nabla^2 h_{ij} = 16\pi G\Pi_{ij}^{TT}, \tag{1.5}$$

where $h^k_k = h_{ik,k} = 0$. Π_{ij}^{TT} is the source of the perturbations.

It is assumed that the detection of a stochastic gravitational wave background of cosmological origin would open a window to the very high energy physics. Its constituent particles, the gravitons, decoupled very soon from the primordial plasma with an extremely small cross section. Even though their weak interaction is the reason for the difficulties in their detection, it is also what makes them so interesting towards the understanding of the physics of the early universe, since the weaker the interaction of the particles, the higher the energy scale when they drop out of thermal equilibrium. In other words, they have travelled nearly unperturbed and thus they have not lost the memory of the conditions in which they had been produced carrying invaluable information.

The stochastic background is expected to be isotropic, stationary and unpolarized [135]. Under these assumptions, it can be fully characterized by the spectrum of its dimensionless energy

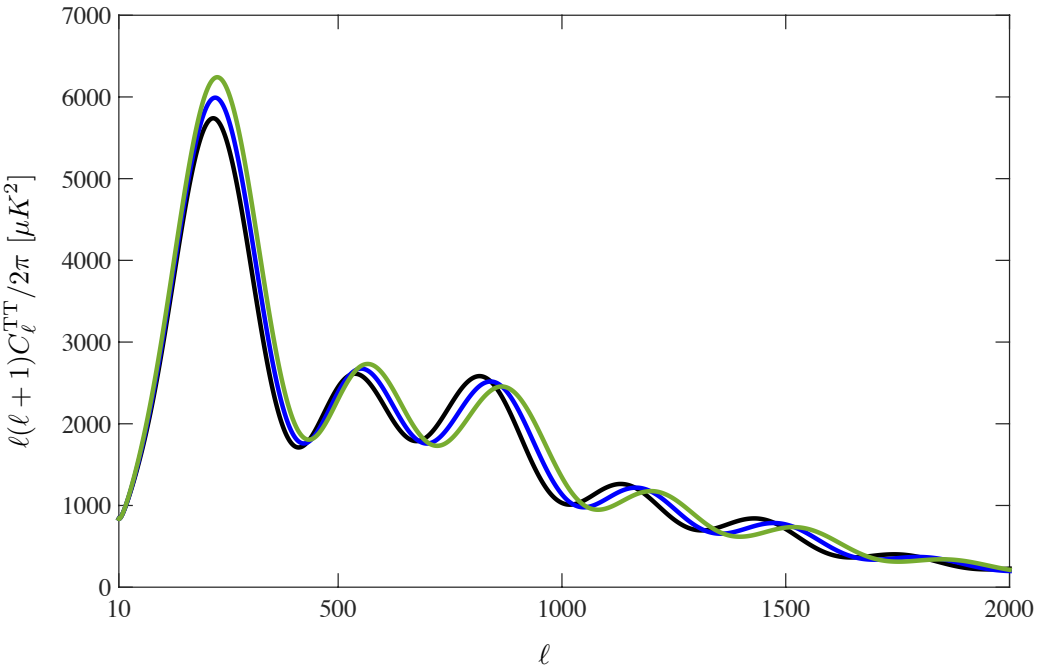

Figure 1.1: *CMB temperature power spectra using three different values of $N_{\rm eff}$, $N_{\rm eff} = 3$ in black, $N_{\rm eff} = 4$ in blue and $N_{\rm eff} = 5$ in green, other cosmological parameters fixed to the ΛCDM best-fit value given in [21]. As we increase $N_{\rm eff}$ the amplitude of the first peak increases while the higher peaks shift toward smaller scales.*

density:

$$\Omega_{\rm GW}(f) = \frac{1}{\rho_{\rm c}} \frac{d\rho_{\rm GW}}{d\log f}, \tag{1.6}$$

where f is the frequency and $\rho_{\rm c}$ is the present value of the critical energy density for a flat universe.

Gravitational wave contribution to $N_{\rm eff}$

Gravitational waves of cosmological origin have been considered as a plausible candidate to be responsible for the excess of relativistic degrees of freedom. For perturbations inside the horizon, GW can be considered to be propagating in Minkowski background [143]. In this case, the equation of motion for the tensor perturbation of the metric becomes $\partial^\sigma \partial_\sigma h_{\mu\nu} = 0$, whose solution is a plane-wave $h_{\mu\nu} = \mathbb{R}\{A_{\mu\nu} e^{ik_\sigma x^\sigma}\}$, with a wave vector k. We can then obtain an expression of the effective energy-momentum tensor:

$$T^{GW}_{\mu\nu} = \frac{A^2 k_\mu k_\nu}{32\pi}, \tag{1.7}$$

which is the same as the energy-momentum tensor of a beam of non-interacting massless particles. Thus, the effects on the CMB and the matter power spectra of CGWB are equal to those produced by massless neutrinos. If gravitons, particles with spin$= 2$ or equivalently $g = 2$, are one of the possible sources of the extra signal, Eq. (1.2) can be written as:

$$\left(\frac{\rho_{\rm GW}}{\rho_\gamma}\right)_{\rm BBN} \leq \frac{7}{8}(N_{\rm eff} - 3), \tag{1.8}$$

which under standard evolution of the photon and graviton densities (for detailed derivations see [135]), the relation can be written in terms of present densities in the following way:

$$\frac{\rho_{GW}}{\rho_\gamma} \leq 0.227(N_{\rm eff} - 3), \tag{1.9}$$

where $\rho \propto T^4$ for each species. The relation between $N_{\rm eff}$ and the spectrum of gravitational waves is obtained rewriting the last equation using Eq. (1.6):

$$\int d(\log f) h^2 \Omega_{GW}(f) \leq 5.6 \times 10^{-6}(N_{\rm eff} - 3). \tag{1.10}$$

This allows us to translate any constraint on the $N_{\rm eff}$ into an upper bound on the gravitational wave energy density $\Omega_{\rm gw}h^2$, for those with a frequency larger than $\sim 10^{-15}$Hz which correspond to the size of the sound horizon at decoupling. This bound, of course, holds only for tensor modes already present at BBN. It does not apply to any other background produced latter, like backgrounds of astrophysical origin.

1.1.3 Gravitational wave background produced by cosmic strings

Active perturbation sources such as cosmic strings produce CMB anisotropies and could also be source of gravitational waves that contribute to the stochastic cosmological gravitational wave background. The theory of anisotropy production has been widely studied during years and there exists a standard procedure for the calculation of their contribution to the CMB power spectra (see detailed discussion on this issue in Sec. 2.3 of the Introduction); however the contribution from cosmic strings to the gravitational wave background is less understood than their CMB imprints. The production of tensor modes from strings has been studied for a number of years now [61, 62, 186, 213], where the cusps and kinks on the strings where considered, mostly in a Nambu-Goto approximation. For those predictions, the size and distributions of loops are also of crucial importance. One of the main focus of some of those works was to study how the gravitational wave contributions from strings would change when considering cosmic superstrings, and more specifically the probability of intercommutation of the strings p. For the present work, we only consider solitonic cosmic strings, and will consider $p = 1$, that is, the string segments always reconnect when they meet, which is an excellent approximation.

Even though the form of the GW spectra coming from strings is still under study (see [74] for a different approach), as is also the size and distribution of loops [108, 133, 183], for the present work we will use the approach put forward in [152, 187] since it is one of the few that gives a direct translation from $G\mu$ to gravitational waves (and hence, to $N_{\rm eff}$ via Eq. (1.10)).

The authors of [152, 187] show that under adiabatic initial conditions, incoherent superposition of cusp bursts from a network of cosmic strings (or superstrings) can produce a spectrum of gravitational waves. The procedure used in the paper is summarized in the following lines.

It is assumed that kinks and cusps in strings would be the only measurable events in terms of gravitational wave emissions. Hence, the authors calculate the form of the spectrum of the metric perturbation for such energetic events and showed that for both cases the emission only happens in a cone and that the perturbation per loop length and per redshift is proportional to $G\mu$. They give the following expression for the spectrum:

$$\Omega_{\rm GW}(f) = \frac{4\pi^2}{3H_0^2} f^3 \int dz \int dl h^2(f, z, l) \frac{d^2R(z, l)}{dzdl}, \tag{1.11}$$

where f is the frequency, l the loop length, z redshift, h the trace of the perturbation and

$\frac{d^2R(z,l)}{dzdl}$ the observable burst rate per l and per z, which is proportional to the loop density. The last terms distinguishes between the observability of cusps and kinks. Indeed, kinks travel around string loops emitting in a strip, whereas cusps are instantaneous events whose radiation can only be measured when the line of sight and the cone of radiation coincide.

Finally the Eq. (1.11) is integrated for loops created at radiation domination era. The authors find that both kinks and cusps contribute at almost the same level, though the results are quite different for different loops. For those smaller than the horizon we have:

$$\Omega_{\rm GW}(f) \approx 5 \times 10^{-2} \frac{G\mu}{p}, \tag{1.12}$$

while the spectra given by loops of the size of the horizon:

$$\Omega_{\rm GW}(f) \approx 3.2 \times 10^{-4} \frac{\sqrt{G\mu}}{p}. \tag{1.13}$$

Different hypothesis on the creation of different sized loops lead to the different dependence on $G\mu$: small loops are supposed to emerge due to gravitational backreaction, which implies that the density is proportional to $(G\mu)^{-1}$. As for the large-loops, backreaction is assumed to be irrelevant and they appear as a consequence of large-scale dynamics of the network. For this case assuming an scaling network they obtain that the density is proportional to $(G\mu)^{-5/2}$.

Therefore, once we have a value for $G\mu$ we can link it to a $\Omega_{\rm GW}h^2$ which in turn is linked to an effective number of relativistic species $N_{\rm GW}^{\rm CS}$ whose effect would be analogous to the one produced by the gravitational waves produced for those strings, all according to [152]. In order to get the correspondence between $G\mu$ and $N_{\rm eff}$ we would need to integrate Eq. (1.10) using Eqns. (1.12) or (1.13) for sub-horizon or horizon sized loops respectively, as done in [180]. The limits for the integral can be obtained approximately as follows: the lower-bounds determine the range of validity of the approximations given in [152] where the GW spectra is almost flat and gets the main contribution from the loops in the radiation era. The upper limit is given by the horizon size at the time of the phase-transition which produced the string network.

The lower-bound to the spectrum is $f_{\rm min} \sim H_0 z_{\rm eq}^{1/2}$ for sub-horizon sized loops and $f_{\rm min} \sim 3.6 \times 10^{-18}/G\mu$ Hz for horizon-sized loops. The upper-bound for both cases is given by the horizon size at the time of the phase-transition $f_{\rm max} \sim M_{\rm pl} G\mu$, giving for the sub-horizon sized loops

$$G\mu \ln\left(\frac{G\mu M_{\rm pl}}{H_0 z_{\rm eq}^{1/2}}\right) \sim \frac{5.6 \times 10^{-6} N_{\rm GW}^{\rm CS}}{5 \times 10^{-2} h^2}\,. \tag{1.14}$$

For horizon-sized loops, it gives

$$\sqrt{G\mu} \ln\left(\frac{(G\mu)^2 M_{\rm pl}}{3.6 \times 10^{-18}\ {\rm Hz}}\right) \sim \frac{5.6 \times 10^{-6} N_{\rm GW}^{\rm CS}}{3.2 \times 10^{-4} h^2}\,, \tag{1.15}$$

where $M_{\rm pl}$ is the reduced Planck mass and $z_{\rm eq}$ is the redshift of matter-radiation equality.

1.2 Method and implementation

We explore the multi-parameter space using the Markov Chain Monte-Carlo (MCMC) parameter estimation and likelihood space exploration procedure. The base model considered is that of a ΛCDM with the usual six parameters ($\mathcal{PL}$):

$$\{\Omega_{\rm c}h^2, \Omega_{\rm b}h^2, \tau, H_0, A_{\rm s}, n_{\rm s}\} \tag{1.16}$$

In order to consider non zero extra relativistic contribution, we add one more parameter: the effective number of neutrino species $N_{\rm eff}$ (or equivalently the extra radiation component). These parameters are fed into `CAMB` [127] to get the corresponding power spectrum. Depending on the case under study, the cosmic string contribution is added to the power spectrum using a previously calculated spectrum template, which is normalized by the parameter $(G\mu)^2$ (see Sec. 2.3 of the Introduction for explanations of this procedure). As we will show later, for certain cases we find that the data prefers $n_s = 1$, in a similar way to what the authors in [37, 39, 44, 201] found. Therefore, we will also consider a model with n_s fixed to one. We will refer to this model as the Harrison-Zel'dovich ($\mathcal{HZ}$) model. Once again, $N_{\rm eff}$ and $G\mu$ will be added to the $\mathcal{HZ}$ model. Thus by permutation of the free parameters, we build four different models in combination to those base parameters of the $\mathcal{PL}$ and $\mathcal{HZ}$ models,

1. $\mathcal{PL} + G\mu$: When the string normalization parameter is added.
2. $\mathcal{PL} + N_{\rm eff}$: When relativistic degrees of freedom are left to vary freely.
3. $\mathcal{PL} + G\mu + N_{\rm eff}$: When both are considered.
4. $\mathcal{HZ} + G\mu + N_{\rm eff}$: The Harrison-Zel'dovich ($\mathcal{HZ}$) model, $n_{\rm s} = 1$, with both parameters freed. This fourth case corresponds to a base model consisting of 5 base parameters, since $n_{\rm s} = 1$ is fixed.

We use flat priors with gaussian probability distribution at each step that can be found in Table 1.1.

Parameter	Prior
$\Omega_{\rm b}h^2$	[0.005, 0.1]
$\Omega_{\rm c}h^2$	[0.01, 0.99]
θ	[0.5, 10]
κ	[0.01, 0.8]
$n_{\rm s}$	[0.5, 1.5]
$\ln(10^{10}A_{\rm s})$	[2.7, 4]
$N_{\rm eff}$	[1.047, 10.0]
$(G\mu)^2$	[0, 4×10^{-12}]
$D_{3000}^{\rm PS}$	[0, 100]
$D_{3000}^{\rm CL}$	[0, 100]
$D_{3000}^{\rm SZ}$	[0, 100]

Table 1.1: *Priors for the parameters used in our analysis, in the most general case with all parameters left free. For the different models we considered, some of this parameters will be kept fixed, as explained in the text.*

Besides the parameters mentioned above, we consider some derived parameters that are also shown on the following tables. One of them is the Hubble constant (H_0) or equivalently its reduced version ($h = H_0/100$) in km s^{-1} Mpc^{-1}. We also show the contributions of strings using their relative contribution to the total power spectrum at $\ell = 10$ f_{10}. Finally, we include two extra relativistic numbers: $N_{\rm GW}^{\rm CS}$, which is the contribution to the effective number of extra species solely coming from strings, and $N_{\rm eff}^{*}$, which is the contribution needed once the three neutrinos and the cosmic strings contribution has been subtracted. These last two numbers are given for both, horizon sized and sub horizon sized loops.

Our models will be compared with both CMB and non-CMB experimental data with the help of the MCMC method, using a modified version of `CosmoMC` (version 2012) [127] that accounts for the string spectra contribution. Specifically we compare our predictions to the following datasets (see Section 1.2.2 of the Introduction for detailed analysis of the CMB datasets):

- WMAP 7-year [123] for the relatively low-ℓ region $l \leq 1300$.
- High-ℓ: SPT [118]. When data from the SPT experiment is used, foreground contaminants have to be taken into account, therefore three extra parameters are used (normalized, as usual, at $\ell = 3000$): Poisson point source power $D^{\rm PS}_{3000}$; Clustered point source power $D^{\rm CS}_{3000}$; and the Sunyaev-Zel'dovich power $D^{\rm SZ}_{3000}$.
- Non-CMB data: *Hubble Space Telescope* (HST) measurement of the Hubble constant ($H_0 = 74.2 \pm 3.6$) by Riess *et al* [171] and the *Baryon Acoustic Oscillation* measurements by Percival *et al* [157].

The analysis of the likelihood surface data compiled for the Markov chains have been statistically analyzed. We obtain 2D marginalized distributions, 68% (1σ) and 95% (2σ) Confidence Contours (C.C), to find correlations between different parameters under study. In some cases the 2σ is out of the bounds, *e.g.* cosmic string amount that is compatible with no contribution at all; in such cases we express 95% Confidence Limits (C.L) in order to illustrate upper bounds. The goodness of fit of each model is explored using the *temperature* parameter, which controls the size of the step in parameter space and allows to sample from $P^{1/T}$ rather than from P. Therefore, low temperature chains are very useful to explore accurately local maxima and to get precise best-fit parameters as well as likelihood values.

1.3 Results

1.3.1 WMAP 7-year

First of all, we started by fitting relatively low multipoles using the simplest model containing strings: $\mathcal{PL} + G\mu$. We have been able to identify how strings correlate with usual cosmological parameters. The two-dimensional likelihood confidence contours of the correlations between strings and some standard cosmological parameters are illustrated in Fig. 1.2. They show that strings are positively correlated with $\Omega_{\rm b}h^2$ and $n_{\rm s}$. As in previous works, when we fitted WMAP7 data with the $\mathcal{PL}$+$G\mu$ model, the value of string normalization just got an upper limit with value: $f_{10} < 0.107$ at 95% (C.L.), very close to what points out [203]. The contours also show that the Harrison-Zel'dovich scale invariant model for scalar perturbations ($n_{\rm s} = 1$) is well inside the 1σ contour, confirming that when fitting data with cosmic strings it is a plausible model, as noted in [44]. In the analysis non-CMB data (HST+BAO) was also added for later convenience; comparison between the upper and the lower part of Fig. 1.2 shows that the results are quite similar in both cases.

The results of fitting WMAP7 data to the $\mathcal{PL}$ model with $N_{\rm eff}$ and/or $G\mu$ is shown in Table 1.2. When we only allow $N_{\rm eff}$ to be a free parameter and set $G\mu$ to zero, it is clear that, as it was pointed in previous works [75, 118], the preferred value for $N_{\rm eff}$ is larger than three, indicating that there is a preference for some extra radiation component in the early universe. When including cosmic strings also into the analysis, the preferred value is found to be still larger than three, but smaller than when considering only $N_{\rm eff}$. Thus, not only would cosmic strings be the source for

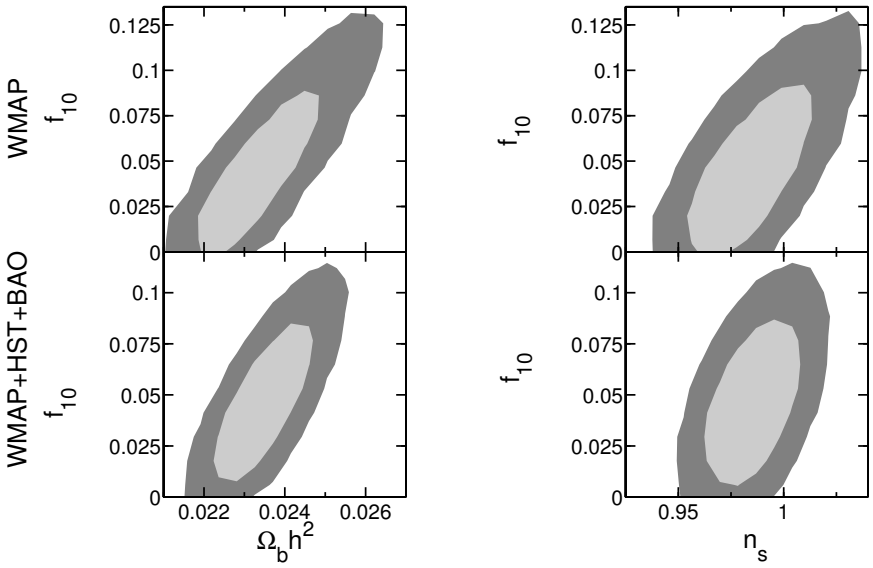

Figure 1.2: *Two-dimensional likelihood contours where degeneracies of the string parameter f_{10} with $\Omega_{\rm b}h^2$ and $n_{\rm s}$ are shown when fitting for WMAP7 and WMAP7+HST+BAO, using the $\mathcal{PL}+G\mu$ model. The 1σ contour is represented in light grey, whereas the 2σ in dark grey. The figure shows that the there exists a positive correlation of strings with such parameters when both datasets are considered.*

the extra radiation component by means of creating gravitational waves, but they also lower the need of the extra component; that is, $G\mu$ and $N_{\rm eff}$ are *anticorrelated*. However, the value of $N_{\rm eff}$ is quite poorly constrained by using only WMAP7 data [123]. As an explanatory example the upper pane of Fig. 1.3 shows that it is almost impossible to form a judgment about what happens with $N_{\rm eff}$ and its correlations with other cosmological parameters, especially with $G\mu$.

It is customary therefore to include other type of data. As mentioned before, we use H_0 and BAO data, and the results can be seen in Table 1.2. The first noticeable feature is that in general the inclusion of non-CMB data reduces the uncertainties of the parameters, see lower pane of Fig. 1.3. The BAO and the H_0 data push most of the parameters in different ways; more specifically, BAO pushes the string contribution down and the $N_{\rm eff}$ up; whereas H_0 pushes $N_{\rm eff}$ down. When considering both data sets together, the tension between the two data comes into play, but the contribution from H_0 is more important in that the overall value of the parameters are tilted towards the preferences of the HST value of H_0; maybe because when fitting the data without the H_0 prior, the value of h is rather high, and including the prior pushes it down considerably. Comparing the results from fitting to WMAP7 only, to WMAP7+H_0+BAO, we see that the mean value for the extra neutrino species is significantly lower. When this last dataset is fitted by the most general model, $\mathcal{PL}+G\mu+N_{\rm eff}$, the previously mentioned anticorrelation between $N_{\rm eff}$ and cosmic strings is clearly confirmed, as can be seen from the lower pane of Fig. 1.3.

Table 1.2 also shows the best-fit χ^2 differences between different models and data-sets, taking as the base model the one corresponding to $\mathcal{PL}+G\mu+N_{\rm eff}$ fitting for CMB data only. In other words, we compare all the other models to this one, and give the difference in χ^2 in the table. In order to compare the best-fit values, one should be careful about the number of parameters and the data-sets used to perform the likelihood analysis. For example, the first two columns

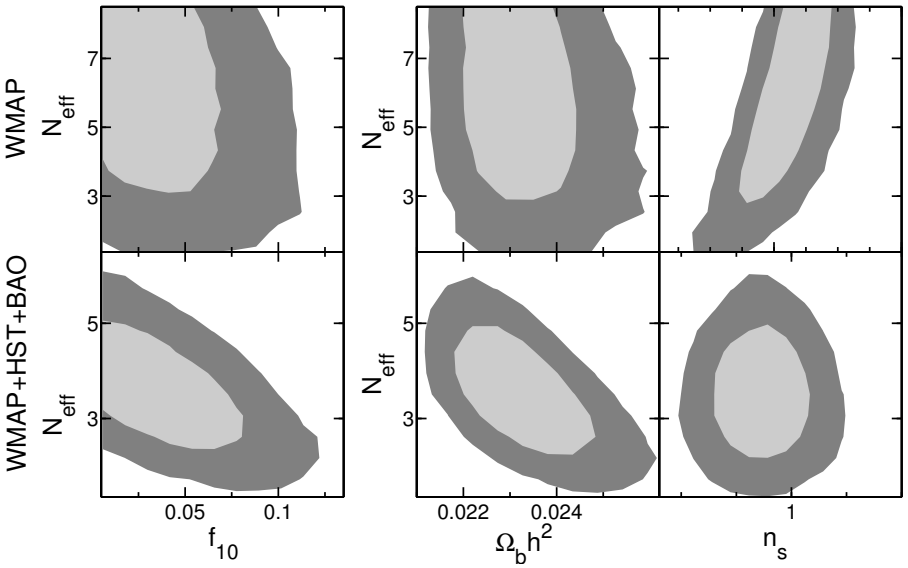

Figure 1.3: *Two-dimensional likelihood contours where degeneracies of $N_{\rm eff}$ with f_{10} as well as with $\Omega_{\rm b}h^2$ and $n_{\rm s}$ are shown when fitting for WMAP7 and WMAP7+HST+BAO, using the $\mathcal{PL}+G\mu+N_{\rm eff}$ model. The 1σ contour is represented in light grey, whereas the 2σ in dark grey.*

Dataset	WMAP7			$+H_0$+BAO	$+H_0$	+BAO	$+H_0$+BAO
Model	$\mathcal{PL}$+Gμ	$\mathcal{PL}+N_{\rm eff}$	$\mathcal{PL}$+Gμ+$N_{\rm eff}$	$\mathcal{PL}$+Gμ	$\mathcal{PL}$+Gμ+$N_{\rm eff}$		
$100\Omega_{\rm b}h^2$	2.4±0.1	2.21±0.06	2.3±0.1	2.35±0.01	2.32±0.09	2.29 ± 0.07	2.31±0.01
$\Omega_{\rm c}h^2$	0.108±0.006	0.18±0.03	0.16±0.04	0.11±0.04	0.12±0.02	0.19 ± 0.03	0.12± 0.02
θ	1.041±0.003	1.029±0.005	1.034±0.007	1.041±0.003	1.039±0.006	1.028± 0.004	1.038± 0.006
κ	0.09±0.02	0.09±0.02	0.09±0.02	0.09±0.02	0.09±0.02	0.09 ± 0.02	0.09± 0.02
$n_{\rm s}$	0.99±0.02	1.00±0.02	1.00±0.02	0.98±0.01	0.99±0.02	1.02 ± 0.02	0.99± 0.02
$\ln(10^{10}A_{\rm s})$	3.10±0.05	3.12±0.04	3.10±0.07	3.10±0.05	3.12±0.06	3.13 ± 0.05	3.13± 0.07
$10^{12}(G\mu)^2$	0.18 (< 0.37)	–	0.15 (< 0.33)	0.15 (< 0.33)	0.15 (< 0.33)	0.10 (< 0.26)	0.15 (< 0.34)
$N_{\rm eff}$	–	7±2	6±2	–	3.6±0.9	8±2	4±1
h	0.74±0.04	0.84±0.08	0.83±0.08	0.74±0.02	0.74±0.02	0.88 ± 0.07	0.75± 0.02
f_{10}	0.05 (< 0.107)	–	0.04 (< 0.096)	0.05 (< 0.093)	0.04 (< 0.091)	0.03 (< 0.073)	0.04 (< 0.096)
$N_{\rm GW}^{\rm CS}$(sm)	0.16±0.06	–	0.18±0.08	0.15±0.06	0.14±0.05	0.15±0.07	0.14±0.05
$N_{\rm GW}^{\rm CS}$(lar)	2.2±0.6	–	2.8±0.8	2.3±0.6	2.1±0.4	2.5±0.7	2.1±0.4
$N_{\rm eff}^{*}$(sm)	–	4±2	3±2	–	0.4±0.9	4±2	0.3±0.9
$N_{\rm eff}^{*}$(lar)	–	4±2	0±2	–	-1±1	1±2	-2±1
$\Delta\chi^2$	-0.78	-0.45	0	-0.94	-0.36	-1.55	-0.68

Table 1.2: *Marginalized likelihood constraints on model parameters, for three different models and with different datasets. The models differ in that $N_{\rm eff}$ and/or $G\mu$ are parameters that we fit for, or are fixed parameters. The first three columns corresponds to the fitting to WMAP7 data, the fourth to the fitting of WMAP7+H_0+BAO with $\mathcal{PL}+G\mu$ and the last three correspond to WAMP7+H_0, WMAP7+BAO, and WMAP7+H_0+BAO, respectively. The table shows the 6 usual parameters, plus the cosmic string contribution $G\mu$ and the extra radiation component $N_{\rm eff}$. We also give the derived parameters h (the Hubble parameter) and f_{10} (the contributions of strings to the total power spectrum at $\ell = 10$). Following the discussion in Section 1.1.3, the values of $N_{\rm GW}^{\rm CS}$ and $N_{\rm eff}^{*}$ are given for two cases: subhorizon-sized string loops (sm) and horizon-sized loops (lar). The goodness-of-fit is characterized by $\Delta\chi^2$, where the difference is taken with respect to the model in the third data column. The values shown are the means and standard deviations, whereas the $\Delta\chi^2$ shown corresponds to the case that best fits the data. In the cases where only upper limits can be placed, we give the mean value and next to it the 95% confidence limit in parenthesis.*

of the table have the same number of parameters (7) and fit to the same data-set (WMAP7), so the χ^2 can be directly compared, showing that they are similar, with a slight preference for the model with $N_{\rm eff}$. The third column has one more parameter (8) so the comparison is not as straightforward. A similar situation happens in the last three columns, where the number of parameters is the same in all of them (8) but the data-sets change from case to case; rendering the comparison of the goodness of fit by the best-fit likelihood value more difficult. However, note that the $\Delta\chi^2$ numbers are only a rough tool to compare different scenarios; in order to compare different models a proper model selection analysis should be done, and moreover, models fitting different data sets should not strictly be compared this way.

1.3.2 WMAP7 + SPT

The relative importance of the contribution of cosmic strings to the power spectrum is higher at very-small scales, due to a slower damping. Thus little changes in $G\mu$ lead to significant alterations in this sector of the spectrum, which could be translated into considerable changes of the posterior distributions. In order to measure such changes, we include SPT data to the CMB dataset expanding the spectrum up to $\ell = 3000$.

Dataset	WMAP7+SPT			$+H_0$+BAO	$+H_0$	+BAO	$+H_0$+BAO
Model	$\mathcal{PL}+G\mu$	$\mathcal{PL}+N_{\rm eff}$	$\mathcal{PL}+G\mu+N_{\rm eff}$	$\mathcal{PL}+G\mu$	$\mathcal{PL}+G\mu+N_{\rm eff}$		
$100\Omega_{\rm b}h^2$	2.21 ± 0.05	2.27±0.05	2.37±0.08	2.22±0.04	2.25 ± 0.05	2.40±0.07	2.25±0.05
$\Omega_{\rm c}h^2$	0.108 ± 0.005	0.13±0.01	0.15±0.02	0.106±0.004	0.13 ± 0.01	0.14± 0.01	0.13±0.01
θ	1.040 ± 0.002	1.040±0.002	1.036±0.002	1.040±0.001	1.038 ± 0.002	1.037±0.002	1.038±0.002
κ	0.08 ± 0.01	0.09±0.02	0.09±0.02	0.08±0.01	0.09 ± 0.02	0.09±0.02	0.08±0.01
$n_{\rm s}$	0.96 ± 0.01	0.98±0.02	1.01±0.02	0.96±0.01	0.97 ± 0.01	1.01±0.02	0.98±0.01
$\ln(10^{10}A_{\rm s})$	3.17 ± 0.05	3.14±0.07	3.06±0.07	3.16±0.04	3.16 ± 0.04	3.01±0.06	3.16±0.04
$10^{12}(G\mu)^2$	0.11 (< 0.22)	–	0.24±0.09	0.12 (< 0.22)	0.14 (< 0.27)	0.26±0.06	0.14 (< 0.25)
$N_{\rm eff}$	–	3.9±0.6	6±1	–	3.9 ± 0.5	5.7±0.9	4.0±0.5
D^{SZ}_{3000}	6 ± 3	6±3	5±3	5±2	6 ± 2	5±3	6±3
D^{PS}_{3000}	20 ± 3	20±3	19±3	20±3	20 ± 3	21±3	20± 3
D^{CL}_{3000}	5 ± 2	5±2	5±2	4 ± 2	4 ± 2	6±2	5±2
h	0.72 ± 0.03	0.75±0.04	0.87±0.07	0.73± 0.02	0.75 ± 0.02	0.89±0.06	0.75±0.02
f_{10}	0.03(< 0.057)	–	0.07±0.03	0.03 (< 0.058)	0.04 (< 0.072)	0.08±0.02	0.04 (< 0.067)
$N^{\rm CS}_{\rm GW}$(sm)	0.11±0.04	–	0.25±0.08	0.12±0.05	0.14±0.04	0.25±0.07	0.14±0.04
$N^{\rm CS}_{\rm GW}$(lar)	1.8±0.4	–	3.4±0.7	2.0±0.5	2.1±0.4	3.3±0.8	2.2±0.3
$N^{*}_{\rm eff}$(sm)	–	0.9±0.6	2±1	–	0.8±0.5	2.2±0.9	0.8±0.5
$N^{*}_{\rm eff}$(lar)	–	0.9±0.6	-0.6±0.6	–	-1.3±0.5	-0.8±0.6	-1.2±0.5
$\Delta\chi^2$	-6.54	-8.01	0	-6.93	-2.78	-0.08	-4.03

Table 1.3: *Analogous table to Table 1.2, but in this case the CMB data sets used are WMAP7 and SPT data. Because of the presence of the SPT data, we have to incorporate 3 more parameters, responsible for taking care of foreground effects.*

As in the preceding section, we first ran several chains fitting the data using the $\mathcal{PL}+G\mu$ model in order to seize the effect of the inclusion of the high ℓ data in models containing only strings; the results can be found in the fourth column of table 1.3 and the confidence contours in Fig. 1.4. The first thing that drew our attention was the similarity between the results obtained with and without non-CMB data. Regarding the correlations, we saw that taking into account small-scale CMB data, those are still positive. However the correlation between Gμ and n_s is nearly broken or inexistent when adding HST+BAO. Moreover $n_{\rm s} = 1$ is not longer endorsed by these models, since that value is not even inside the 2σ contour. We found that the addition of SPT lowered the value of f_{10} giving an upper bound of $f_{10} < 0.057$ at 95% (C.L.).

The constraints on the number of effective neutrinos, on the other hand, gets tighter by the inclusion of high ℓ data as compared to when no high ℓ data is considered. The results can be found in Table 1.3, both with and without non-CMB data. It is noticeable that when adding the

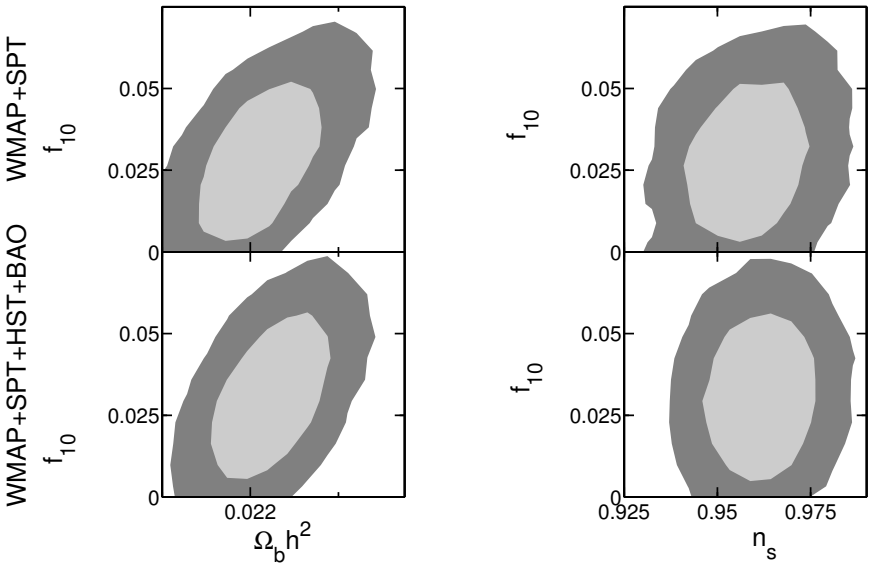

Figure 1.4: *Two-dimensional likelihood contours where degeneracies of the string parameter f_{10} with $\Omega_{\rm b}h^2$ and $n_{\rm s}$ are shown when fitting for WMAP7+SPT and WMAP7+SPT+HST+BAO, using the $\mathcal{PL}+G\mu$ model. The 1σ contour is represented in light grey, whereas the 2σ in dark grey. The figure shows that the there still exists a positive correlation of strings with $\Omega_{\rm b}h^2$, but the correlation of string with $n_{\rm s}$ is gone with the addition of SPT into the dataset.*

high ℓ data to the analysis, the effective number of neutrinos stays roughly the same or decreases. Another difference is that the string contribution is favoured in this case: when comparing the model with only a string contribution ($\mathcal{PL}+G\mu$), and the model with only $N_{\rm eff}$ ($\mathcal{PL}+N_{\rm eff}$), the likelihood is better for the model with strings (note that both models have the same number of parameters). Moreover, the model that fits both strings and neutrinos gives a 2σ preference for strings.

One striking difference from the case where only WMAP7 data was used is the fact that now the string contribution and the effective number of neutrinos are *correlated*, that is, when the contribution of strings is pushed up, so is the effective number of neutrinos. Fig. 1.5 shows the two dimensional likelihood plots for some combinations of the parameters, for two sets of data: on the one hand WMAP7+H_0+BAO, and on the other WMAP7+SPT. The figure shows clearly that whereas f_{10} and $\Omega_{\rm b}h^2$ are correlated in the same way for both datasets, $N_{\rm eff}$ is correlated or anticorrelated with the other two, depending on the datasets that are being fitted for. Thus, when fitting for the WMAP7+SPT dataset, an increase in the number of neutrinos brings an increase in the string contribution. Likewise, by allowing for strings to be present in the analysis, we not only pick up a string contribution, but the string contribution prompts the neutrino contribution to rise.

The inclusion of the non-CMB data, and most importantly of the HST value of H_0, constrains the parameters drastically better, and most of the degeneracies are broken. Fig. 1.6 shows two dimensional likelihood contours for some of the parameters, when fitting for WMAP7+SPT with and without non-CMB data included. The shaded lines correspond to only CMB data, whereas the solid and dashed lines take into account also the H_0+BAO data. It is very clear how the available parameter space has shrunk considerable, and also how the degeneracies are broken, specially between $N_{\rm eff}$ and f_{10}. Note that the 2σ preference for strings is lost when non-CMB

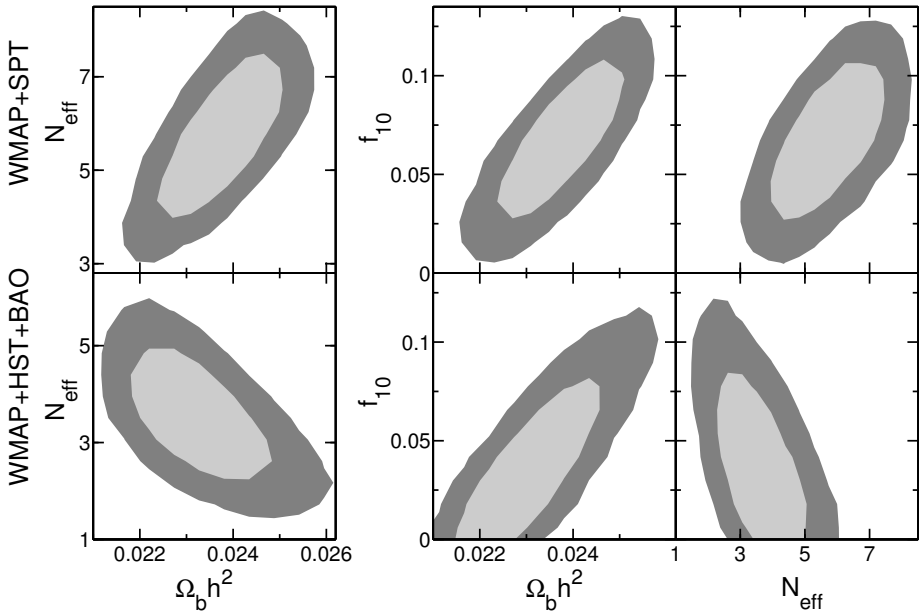

Figure 1.5: *Two dimensional likelihood contours, where degeneracies between f_{10}, $N_{\rm eff}$ and $\Omega_{\rm b}h^2$ are shown, when fitting for WMAP7+H_0+BAO, and when fitting for WMAP7+SPT. The shaded contours correspond to 1σ and 2σ contours. The figure shows that $\Omega_{\rm b}h^2$ and f_{10} keep the same correlation for both datasets; but $N_{\rm eff}$ is correlated with the other two for one case, and anticorrelated for the other.*

data are included.

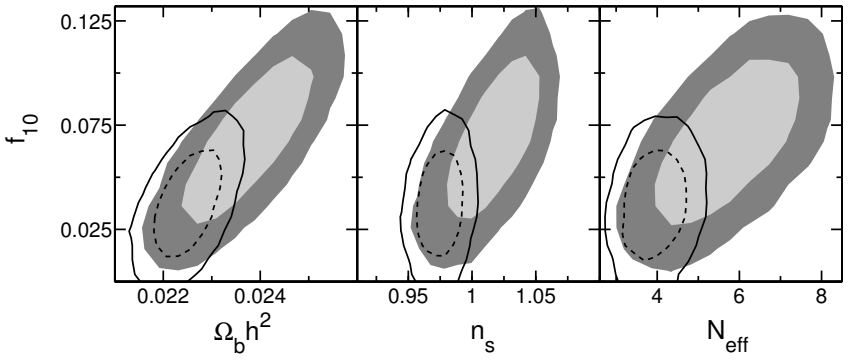

Figure 1.6: *Two dimensional likelihood contours for some of the parameters in the model PL+$N_{\rm eff}$+$G\mu$. The shaded regions correspond to 1σ and 2σ confidence levels, where only CMB data are used for the analysis (i.e., WMAP7+SPT). The smaller contours depicted by solid and dashed lines correspond also to 1σ and 2σ confidence levels, but when also non-CMB (i.e., BAO+H_0) data are included.*

The shrinking of the parameter space can be understood if one considers what is happening to the Hubble parameter. The inclusion of the HST value of H_0 narrows the prior space for the Hubble parameter $h \sim 0.742 \pm 0.036$, and the values of h that the parameter fitting prefers for the cases where the H_0 prior is not included are much higher. Fig. 1.7 shows the two dimensional

likelihood contours for h versus $N_{\rm eff}$ and f_{10}. It is clear that the HST value of H_0 just catches the lower end of the contour, and it is this effect which shrinks so noticeably the parameter space.

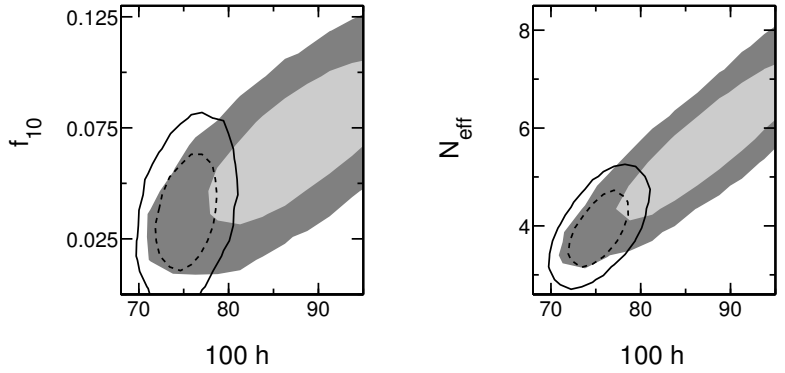

Figure 1.7: *Two dimensional likelihood contours for $N_{\rm eff}$ and f_{10} with respect to h. The shaded region represents the 1σ and 2σ results obtained when only CMB data are used. Note that the mean of h is higher than the value that the HST experiment gives. That is why the allowed parameter space shrinks considerable when the h prior is also included (solid and dashed lines).*

1.3.3 Harrison-Zel'dovich ($\mathcal{HZ}$), $n_{\rm s}=1$

Harrison-Zel'dovich ($\mathcal{HZ}$) model for the scalar perturbation has been supported in some of the cases in previous section, specifically when SPT is considered and for the model $\mathcal{PL}+G\mu+N_{\rm eff}$ $n_{\rm s}=1$ lies right in the center of the confidence contours for the CMB only case, and inside the 2σ level for the other case, see Fig. 1.6. A similar phenomenon was studied in some previous papers [37, 39, 44, 201] where the Harrison-Zel'dovich model was then considered as a viable model to explain the data. We have performed the same exercise, and the result is shown in Table 1.4, where a model with $n_s=1$ ($\mathcal{HZ}$) plus strings and $N_{\rm eff}$ is used to fit the CMB data (WMAP7+SPT). The values of the parameters change slightly from the case where n_s was a free parameter, all within 1σ, which is expected since $n_s=1$ was right in the middle of the confidence contours. Thus, it is not surprising that in this case the value of the likelihood is very similar; but bear in mind that the number of parameters is different: $\mathcal{PL}$ has one more parameter than $\mathcal{HZ}$. If one wishes to compare models with the same number of parameters, one should compare $\mathcal{HZ}+G\mu+N_{\rm eff}$ with $\mathcal{PL}+G\mu$ or with $\mathcal{PL}+N_{\rm eff}$; and in both those cases, the likelihood of the former is much better. Note, however, that also in this case the value of h is rather higher than what the HST value of h prefers, so the inclusion of non-CMB data will disfavour this model.

1.3.4 $N^*_{\rm eff}=0$

In all the analysis above there is one point of view that has not been taken into account: the strings that the different models prefer do in fact produce gravitational waves which will contribute to the $N_{\rm eff}$, but that extra contribution is not taken into account as yet. In all three tables we have included $N_{\rm GW}^{\rm CS}$ for subhorizon-sized and horizon-sized loops, which is the effective number of relativistic species analogous to the gravitational waves coming from the strings. The numbers that we are quoting are the ones obtained following the procedure of [152, 180], and the big difference between the numbers of subhorizon-sized and of horizon-sized loops is already clear. As we have mentioned before, this is a very rough estimate; therefore we only use it as a hint of

Dataset	WMAP7+SPT
Model	$\mathcal{HZ}+G\mu+N_{\rm eff}$
$100\Omega_{\rm b}h^2$	2.31±0.04
$\Omega_{\rm c}h^2$	0.14±0.01
θ	1.037±0.002
κ	0.09±0.01
$n_{\rm s}$	1
$\ln(10^{10}A_{\rm s})$	3.11±0.04
$10^{12}(G\mu)^2$	0.19±0.07
$N_{\rm eff}$	5.3±0.6
D^{SZ}_{3000}	6±2
D^{PS}_{3000}	20±3
D^{CL}_{3000}	5±2
h	0.84±0.02
f_{10}	0.05±0.02
$N^{\rm CS}_{\rm GW}$(sm)	0.20±0.04
$N^{\rm CS}_{\rm GW}$(lar)	2.9±0.4
$N^{*}_{\rm eff}$(sm)	2.0±0.6
$N^{*}_{\rm eff}$(lar)	-0.6±0.6
$\Delta\chi^2$	-0.25

Table 1.4: *Analogous table to Tables 1.2 and 1.3. In this case, the model we are fitting for is a HZ model, i.e., the scalar index is fixed to one ($n_s = 1$). The data we are fitting for is CMB only (WMAP7+SPT). This model fits the data better than any of the other models considered so far, even taking into account the number of parameters. Including non-CMB data would render this model less successful, partly because of the high value of h that the model prefers.*

Dataset	WMAP7		WMAP7+H_0+BAO		WMAP7+SPT		WMAP7+SPT+H_0+BAO	
Loops	Subhorizon	Horizon	Subhorizon	Horizon	Subhorizon	Horizon	Subhorizon	Horizon
$100\Omega_{\rm b}h^2$	2.4±0.1	2.37±0.08	2.34±0.07	2.22±0.05	2.22±0.05	2.34±0.08	2.22±0.05	2.20±0.05
$\Omega_{\rm c}h^2$	0.109±0.006	0.160±0.009	0.110±0.004	0.142±0.009	0.110±0.005	0.16±0.01	0.108±0.004	0.14±0.01
θ	1.040±0.003	1.032±0.002	1.040±0.003	1.033±0.003	1.039±0.002	1.036±0.001	1.040±0.001	1.036±0.002
κ	0.09±0.02	0.09±0.02	0.09±0.02	0.08±0.01	0.08±0.01	0.09±0.02	0.08±0.01	0.08±0.01
$n_{\rm s}$	0.99±0.02	1.02±0.02	0.99±0.01	0.98±0.01	0.96±0.01	1.01±0.02	0.96±0.01	0.98±0.01
$\ln(10^{10}A_{\rm s})$	3.10±0.07	3.08±0.06	3.11±0.05	3.18±0.04	3.18±0.05	3.09±0.06	3.16±0.04	3.19±0.04
$10^{12}(G\mu)^2$	0.18(<0.37)	0.21 (<0.33)	0.17 (<0.31)	0.06 (<0.13)	0.11 (<0.22)	0.18±0.08	0.12(<0.22)	0.05 (<0.14)
$N^{\rm CS}_{\rm GW}$	0.16±0.06	3.1±0.6	0.14±0.05	1.6±0.4	0.11±0.04	3.1±0.7	0.12±0.04	1.5 ± 0.5
D^{SZ}_{3000}	-	-	-	-	5±2	7±2	5±2	8±2
D^{PS}_{3000}	-	-	-	-	21±3	20±3	20±2	22± 3
D^{CL}_{3000}	-	-	-	-	5±2	5±2	5±2	6±2
h	0.75±0.04	0.87±0.05	0.74±0.02	0.75±0.02	0.73±0.03	0.87±0.06	0.73±0.02	0.76 ± 0.02
f_{10}	0.05(<0.108)	0.06(<0.095)	0.05 (<0.088)	0.02(<0.037)	0.03 (<0.058)	0.05±0.02	0.03(<0.059)	0.01(<0.037)
$\Delta\chi^2$	-0.62	-0.04	-0.69	-0.77	-5.11	-0.66	-5.41	-4.96

Table 1.5: *Marginalized likelihood constraints on model parameters, analogous to Table 1.2 and 1.3. In all these cases $N^{*}_{\rm eff}=0$, implying that there is a possibility of extra radiation, but all that extra radiation comes from the cosmic strings. For each different set of data, we study the cases of subhorizon-sized loops (1.14) and horizon-sized loops (1.15).*

what could be happening and the rich information we could obtain with it once the uncertainties are more under control.

In other words, the $N_{\rm eff}$ that we are obtaining from the parameter fitting has three possible sources: one that comes from the three species of neutrinos, another one given by $N_{\rm GW}^{\rm CS}$, and a third one that is not accounted for in the ingredients of our model. The parameter $N_{\rm eff}^*$ gives a measure of the level of those unaccounted effects. Note that the predictions for smaller sized loops need a higher level of $N_{\rm eff}^*$. If $N_{\rm eff}^*$ were exactly zero it would mean that the model is able to produce all the $N_{\rm eff}$ it needs to fit the data. Note that even though the errors in these parameters are rather large, most cases show no need for yet another contribution from another relativistic particle or source (at 2σ), though do not exclude it. The cases were $N_{\rm eff}^*$ is negative indicate that the model is not good: the amount of cosmic strings predicted is too high since their gravitational wave production is too high.

As we have just mentioned, the case with $N_{\rm eff}^* = 0$ is an interesting case, because it corresponds to the case where all the extra relativistic signal needed to fit the data comes from the strings, which is a possibility that most models accommodate. Therefore, we study a new set of models, where $N_{\rm eff}^*$ is set to zero, i.e., we allow for the possibility of having an extra radiation component, but the extra radiation comes only from the cosmic string contribution. This way, the direct link between strings and gravitational waves is fully taken into account. The results are shown in Table 1.5. There is some complicated *dynamics* between the parameters and the datasets. When no h priors are used, the models with horizon-sized loops allow for a larger value of $G\mu$, but with the penalty of a higher value of h. They fit the data rather well, and their respective χ^2 are roughly the same as their base model ($\mathcal{PL} + G\mu + N_{\rm eff}$), but remember that these have one parameter less. The $N_{\rm GW}^{\rm CS}$ contribution from horizon-sized loops is always larger than for subhorizon-sized loops for the same value of $G\mu$ (see Eqns (1.14) and (1.15)). Therefore, when the h prior is included, since in general lower values of h prefer lower relativistic components, the string contribution from models with horizon-sized loops is suppressed with respect to the models with subhorizon-sized loops. Nevertheless, the extra radiation component is higher for horizon-sized loops in all cases.

1.4 Discussion and Conclusions

In this chapter we have studied the correlation between cosmic strings and extra relativistic species (or effective number of neutrino species) by fitting different models to cosmological data. We considered the possibility of cosmic strings being the source of a cosmological gravitational wave background, which in turn act as the extra relativistic species which the data seem to favor over the usual three neutrino species. Cosmic strings are predicted in several inflationary scenarios, and therefore, they seem to be perfect candidates to seed GW and account for the extra radiation. The idea of cosmic strings being the sources of CGWB is not new, but this work expands the previous works in that the cosmic string contribution is included from the beginning, already in the parameter fitting process, and thus we are able to study different correlations between the different ingredients in these models. The inclusion of strings in the parameter fitting changes the value of $N_{\rm eff}$ that the data needs.

We have shown that the correlation between cosmic strings ($G\mu$) and extra neutrino species ($N_{\rm eff}$) depends on the data sets used. When relatively low ℓ data is used (WMAP7) these two components are anticorrelated; thus, the inclusion of cosmic strings into the model not only did account for the extra radiation species needed, but it actually lowered the need for them. However, when relatively higher ℓ are included, the anticorrelation becomes correlation, and an

extra cosmic string component asks for a higher contribution from extra relativistic species. This (at first sight) unexpected effect may be understood by noting that a change in $N_{\rm eff}$ changes the CMB temperature anisotropies power spectrum basically in two ways: the height of the first peak and the position of the higher peaks. When only WMAP7 data are taken into account, only the height of the first peak is of importance, and cosmic strings are used to help in this endeavor. However, when higher ℓ-s are taken into account, the position of the higher peaks gains more relative importance, and this is counteracted by a correlation with cosmic strings. This correlation/anticorrelation effect not only happens between $G\mu$ and $N_{\rm eff}$, the same effect can be observed also between $\Omega_{\rm b}$ and $N_{\rm eff}$.

When non-CMB data are taken into account, the available parameter space shrinks considerably. This effect comes mostly from the HST value for h. Typically, when the HST value of h is not taken into account in the analysis, rather high values of h are favoured, and this is why adding the more stringent prior given by HST the parameters get much more constrained. The non-CMB data help constrain $N_{\rm eff}$ considerably better when only WMAP7 data are used, and they break most of the degeneracies when also SPT data are used. Apparently something similar happens when *Planck* data is included [14, 15], where most of the degeneracies are broken. Interestingly, however, the same correlation behaviour between cosmic strings and $N_{\rm eff}$ has been observed [14].

The analysis also shows other remarkable results. CMB data alone prefer a high value for $N_{\rm eff}$, higher than the standard three neutrino species, when strings are present. However, when the HST value of h is included, the results are consistent with only three neutrinos. In most cases, the string contribution is small, and models with no strings are consistent with the data; the case where WMAP7+SPT are used is the most permissive with strings, since a 2σ *preference* (or rather, *hint*) is obtained. In many cases an $n_s = 1$ is perfectly consistent with the data. In fact, we studied what the goodness of fit is for a $\mathcal{HZ} + G\mu + N_{\rm eff}$ model, fitting to all the CMB data, and found that the model fits the data extremely well. Actually, the likelihood for $\mathcal{HZ}+G\mu+N_{\rm eff}$ is actually very similar to a $\mathcal{PL} + G\mu + N_{\rm eff}$, even though the latter has one more parameter. However, the inclusion of non-CMB data will also disfavour this model.

A certain number of cosmic strings are preferred to fit the data, and those cosmic strings would create some gravitational waves that are responsible for part of the $N_{\rm eff}$. We have tried to factor out this contribution, as well as the contribution of the standard three neutrinos, to estimate whether some other source to $N_{\rm eff}$ was still needed, and encoded it in $N^*_{\rm eff}$. A value $N^*_{\rm eff} = 0$ would mean that all the players in the model are enough to account for all the $N_{\rm eff}$ needed to fit the data, i.e., the three neutrinos and the cosmic strings present do the job. We find that, even though the errors are rather high, in most cases the strings can account for all the extra radiation component, although the need for yet another extra relativistic source is not excluded. More importantly, sometimes $N^*_{\rm eff}$ is negative, hinting for some incongruence: the amount of strings chosen from the fitting is too high. It could be a good measure to disqualify models as not viable, but unfortunately our feeling is that the uncertainties in obtaining $N^{\rm CS}_{\rm GW}$ are too high to make any kind of claim. One measure for the level of uncertainty could be the big difference in numbers for smaller and bigger cosmic strings loops. After this work was published, among other works in the field, the gravitational wave production of string loops using numerical simulations was presented in [48]. Essentially, it was found that the main contribution to gravitational waves come from large loops, and that the contribution of small loops can be neglected.

In order to fully exploit the direct link between cosmic strings, gravitational waves and $N_{\rm eff}$, models with $N^*_{\rm eff} = 0$ were also studied. These models allow for an extra radiation component, but consider that all the extra radiation come from the cosmic string contribution. Thus, these models have only seven parameters, but include cosmic strings and an extra radiation component.

In general terms, these models fit the data rather well (in many cases their goodness of fit is similar to models with one parameter more), and if, as mentioned before, the gravitational radiation from cosmic strings was more under control, these models would be excellent candidates to fit the data well, with fewer parameters.

As already mentioned several times, the main source of uncertainty comes from the production of gravitational waves from cosmic strings. There is intense work in this subject from different groups, using different approaches, and there is no consensus in the community. Unlike in the case of CMB predictions from strings, where different approaches give relatively fairly similar results, the loop production and decay process of strings is still a very open issue. One could guess that the outcomes from Nambu-Goto type approaches or from Abelian-Higgs like approaches will be rather different, since the string density, decay mechanisms and loop density and sizes seem to be rather different. In this work we have used one of the few works which give a recipe to translate from cosmic string $G\mu$ to gravitational waves, which in turn we transform into $N_{\rm eff}$, but we believe there are many uncertainties and assumptions that need to be checked an improved. We, therefore, consider this work as a first step into the analysis of the role of cosmic strings as sources of extra radiation component in the universe, which demands further understanding of the underlaying cosmic string dynamics.

2 Fitting BICEP2 with defects, primordial gravitational waves and dust

The detection of B-mode polarization on large angular scales [16] opened a new window to test and constrain models that predict primordial perturbations. The leading candidate for such measured signal, as claimed by the BICEP2 team, is primordial inflationary gravitational waves: for a tensor-to-scalar ratio r of around 0.2, these give a good match to the spectral shape in the region $\ell \approx [40\ 150]$. The claim by the BICEP2 collaboration generated great excitement, and stimulated the search for other possible B-mode polarization sources signaling new physics, such as cosmic defects [131, 132, 147], self-ordering scalar fields [80] or primordial magnetic fields [51].

The alternative explored in this chapter is cosmic defects, which produce B-mode polarization through both tensor and vector modes (see e.g. Refs. [55, 79, 88, 103, 104, 214] for reviews). The relative proportions of scalar, vector and tensor perturbations are essentially fixed for a given type of defect, so a constraint on one of the modes will imply constraints on the others. It is worth noting that even though defects are highly constrained via the CMB temperature anisotropies [14, 31, 36, 44, 75, 203, 218], they can still contribute importantly to the B-mode polarization.

In our analysis we study three types of cosmic defects: Abelian Higgs strings [150], $\mathrm{O}(4)$ global textures [198], and semilocal strings [8, 101, 102, 205]. Other defect models exist, such as self-ordering scalar fields, global monopoles, and global strings. However, with the three types of defects under consideration we are able to obtain a global view of the interplay between cosmic defects and the other signals, and can also study where the differences between the different defect predictions are important. The imprints of defects on the temperature and polarization power spectra are qualitatively similar [42, 43, 45, 78, 79, 155, 201, 202], though there are important quantitative differences.

Alongside possible primordial contributions, B-modes could have non-cosmological contributions. In this sense, when the project of this Chapter was being done, it became subsequently more apparent that conventional astrophysics can plausibly account for the entire observed B-mode signal with polarised dust emission [89, 146]. At the very least it is clear that dust contamination must be explored.

This chapter is based on two published works [131] and [132]. Both of them tried to answer questions placed soon after the release of the BICEP2 data and contributed also in the fast moving research atmosphere of the moment. The first [131] analysis was motivated by the BICEP2 data release and it was soon published in *Physical Review Letters*. There we explored qualitatively the possibility of cosmic defects being responsible for the total signal measured by the BICEP2 experiment. The second work [132] (published in *Physical Review D*), in turn, complemented the previous short paper by providing a comprehensive analysis of the defect contribution to the microwave anisotropies, both in temperature and polarisation, allowing all three of the above signal sources, i.e., inflationary gravitational waves, dust, and cosmic defects.

We thus adopt a chronological approach to present both works into this chapter: we start by showing qualitative results published in the first work, which will be complemented later by the quantitative statements obtained in the second work.

2.1 *B*-modes of cosmological origin

2.1.1 Inflationary tensor modes: r

The inflationary process in addition to the initial scalar perturbations (responsible for the large scale structure) could also produce tensor perturbations, as explained in Section 1.2.1 of the Introduction. Those perturbations, usually known as primordial tensor modes, are encoded in the cosmological parameter r which measures the amount of those with respect to the scalar perturbations (see Eq. (1.20) of the Introduction).

Inflationary tensor modes produce CMB anisotropies both in temperature and in polarisation. Specifically, they are one of the few ingredients of cosmological (or primordial) origin that can produce directly B-modes. The relative amount of tensor perturbations has been constrained by analysis of the CMB temperature channel to be: $r < 0.11$ at $k_* = 0.002\mathrm{Mpc}^{-1}$ [17, 18]. In Fig. 2.1, we show a typical B-mode spectrum produced by inflationary tensor modes for a value $r = 0.2$. The two main peaks associated with reionization and recombination are evident as stated in Sec. 1.2.1 of the Introduction.

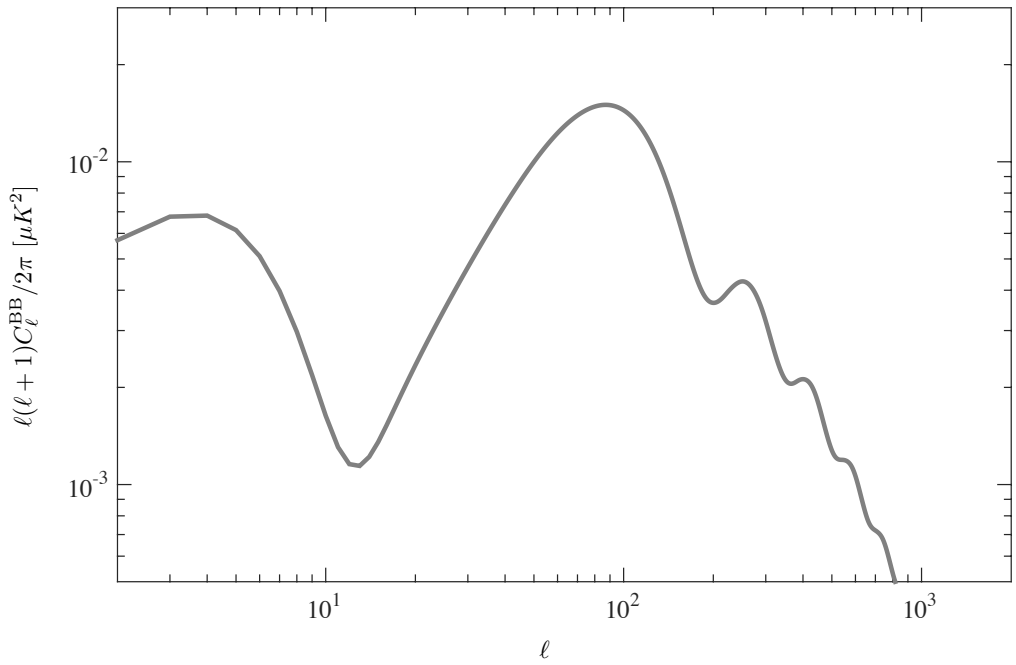

Figure 2.1: *B-mode polarisation (BB) spectrum produced by inflationary tensor modes with $r = 0.2$. The two main peaks are associated to reionization (first) and recombination (second) and their position to the horizon size at each epoch.*

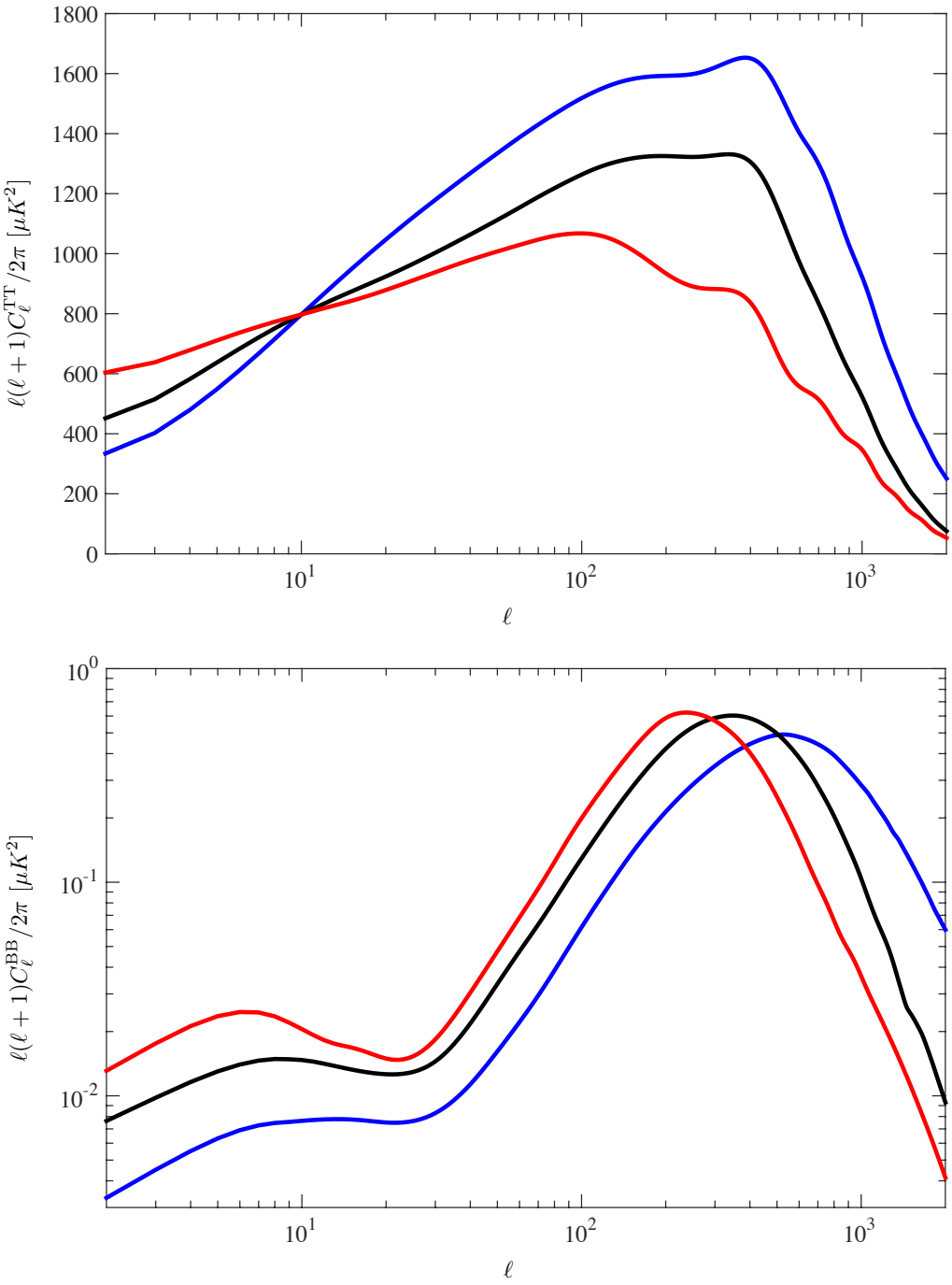

Figure 2.2: *Temperature (TT) and B-mode polarization (BB) defect spectra, normalized to make the temperature spectra match Planck data at $\ell = 10$. Different lines correspond to textures (red line), semilocal strings (black line), and Abelian Higgs strings (blue line).*

2.1.2 Cosmological defects

As with inflationary tensors, a distinctive signature of topological defects lies in the B-mode polarization. Figure 2.2 shows the power spectra obtained from the field theoretical simulations of

	$G\mu_{10}$	$G\mu$ ($< 95\%$)	f_{10} ($< 95\%$)
Abelian Higgs strings	19×10^{-7}	3.2×10^{-7}	0.024
Semilocal strings	53×10^{-7}	11×10^{-7}	0.041
Textures	44×10^{-7}	11×10^{-7}	0.054

Table 2.1: *$G\mu_{10}$ is the normalization of different defects to match the observed $\ell = 10$ multipole value (i.e. to explain the full temperature signal at that multipole, $f_{10} = 1$). The last two columns show the 95% confidence upper limit obtained by the Planck collaboration [14] for the Planck + WP + High-ℓ dataset.*

Abelian Higgs strings (AH) [45], semilocal strings (SL), and textures (TX) [201], for the temperature and B-mode polarization spectra, normalised to the *Planck* temperature power spectrum at $\ell = 10$. The values of $G\mu$ needed to fit the *Planck* data at $\ell = 10$ (i.e. the value for which $f_{10} = 1$), and the *Planck* 95% upper bounds for $G\mu$ and f_{10}, can be found in Table 2.1. Note that $G\mu_{10}$ is calculated as the normalization of strings needed to match the *observed* power at $\ell = 10$, whereas the limit on f_{10} is the upper bound on the ratio of the power in defects to the total power in the best-fit model at $\ell = 10$.

There are important differences between the power spectra obtained from defects or from inflation. As can be seen in Fig. 2.1 and in the lower panel of Figure 2.2, the defect spectrum have a quite different shape to the inflationary tensors, peaking towards smaller scales. On the other hand, defects produce scalar, vector and tensor perturbations in proportions which are fixed for a given defect model, while in inflationary models vector modes are absent and the tensor contribution can vary almost independently of the scalar, apart from the inflationary consistency relation [128]. In addition, defect-induced polarization is suppressed on large angular scales, as causality requires their fluctuations to be uncorrelated beyond the horizon distance at decoupling [80].

2.2 Method and implementation

We faced the questions placed in this work from two separate points of view which require the use of different methodologies. While in the first part we discuss our results from an observational and qualitative point of view, in the second we complement those preliminary predictions with parameter fittings. Therefore in order to accomplish such a quantitative approach, we perform a set of parameter estimations for models where defects coexist with other sources of B-mode polarisation, namely inflationary gravitational waves, dust and lensing. E-modes inevitably convert to B-modes through lensing, thus the lensing signal is always present in our analysis.

In order to reliably explore the parameter space we perform Markov Chain Monte-Carlo (MCMC) runs with the publicly-available `Monte Python` code [1, 28], which uses `Class` [49, 126] as its Einstein-Boltzmann equation solver for the inflationary component of the power spectrum. We compare our predictions to the following CMB datasets (see Section 1.2.2 of the Introduction for detailed analysis of different experiments):

- *Planck*+WP: *Planck* 2013 data [15] (low-ℓ and high-ℓ), including WMAP 9 year [110] low-ℓ polarisation data.[1]

[1] Lensing B-modes had already been detected by POLARBEAR [12, 19]. However, the extra constraining power of the POLARBEAR data is weak, and for clarity we did not include it in our analysis.

- High-ℓ: SPT [170, 194] and ACT [188].

- BICEP2: BICEP2 BB polarization data [16].

The likelihoods are the official codes provided by each experiment.[2]

Our base model is the inflationary ΛCDM model ($\mathcal{PL}$) and as introduced in Section 1.1 of the Introduction is represented by the following set of parameters:

$$\{\Omega_{\rm c}h^2, \Omega_{\rm b}h^2, \tau, H_0, A_{\rm s}, n_{\rm s}\} \tag{2.1}$$

We add a number of extra ingredients to the $\mathcal{PL}$ model, sometimes by themselves, sometimes in combinations. Our main extra ingredient is given by topological defects parametrized as $(G\mu)^2$, for each of the three defect models considered: Abelian Higgs cosmic strings AH, textures TX, or semilocal strings SL. We also show the contributions of defects using their relative contribution to the total power spectrum at $\ell = 10$, namely f_{10}. The defect spectra used in this paper were calculated in Refs. [45, 201] using a modified version of `CMBeasy` [72], with the best-fit parameters of the WMAP 7-year analysis [121] (see Sec. 2.3 of the Introduction).

Another parameter describing an extra ingredient is r which parametrises the amount of inflationary gravitational waves through the tensor-to-scalar ratio (at $k = 0.002\,{\rm Mpc}^{-1}$). Scalar perturbation quantities are also specified at a pivot scale $k = 0.002\,{\rm Mpc}^{-1}$.

The BICEP2 collaboration included also the running of the scalar spectral index $\alpha_{\rm s}$ in order to improve the agreement between the BICEP2 and *Planck* data [16]. Although several papers [29, 138, 189], showed that there is no worrying tension between BICEP2 and *Planck* data, we nevertheless also study the impact of $\alpha_{\rm s}$ here.

As mentioned in the introduction of this chapter, the observed B-mode polarization signal may have a contribution from polarised dust emission [89, 146]. We characterized this B-mode channel by $A_{\rm dust}$:

$$C_\ell^{BB,{\rm dust}} = A_{\rm dust}\ell^{-2.3}\,. \tag{2.2}$$

Another parametrisation of dust is used in the literature, given by Δ^2_{BB}, which is related to ours via

$$\Delta^2_{BB,{\rm dust},\ell} = \frac{\ell^2}{2\pi}C_\ell = \frac{A_{\rm dust}}{2\pi}\ell^{-0.3}\,,$$

using the dust model proposed by the *Planck* collaboration [3].

Our models are constructed using those building blocks, starting from the models with just one extra ingredient, and moving to more complex models where several additional ingredients are present simultaneously.

The results showed in the Tables in the subsequent sections state only the relevant parameters for the given case. In all cases flat parameter priors were used, in the case of defects the prior being flat in $(G\mu)^2$ which is proportional to the fractional defect contribution to the power spectra f_{10}. The prior ranges were $0 < 10^{12}(G\mu)^2 < 4$ and $0 < A_{\rm dust}/(\mu K)^2 < 0.75$. All other parameters, including foreground parameters with the exception of the new polarised dust amplitude, were modelled as in the *Planck* collaboration papers [13, 15].

[2] Although there may be minor differences between the likelihood used by the BICEP2 collaboration in their publication [16] and the public version [29], we expect that this is not important for our main conclusions.

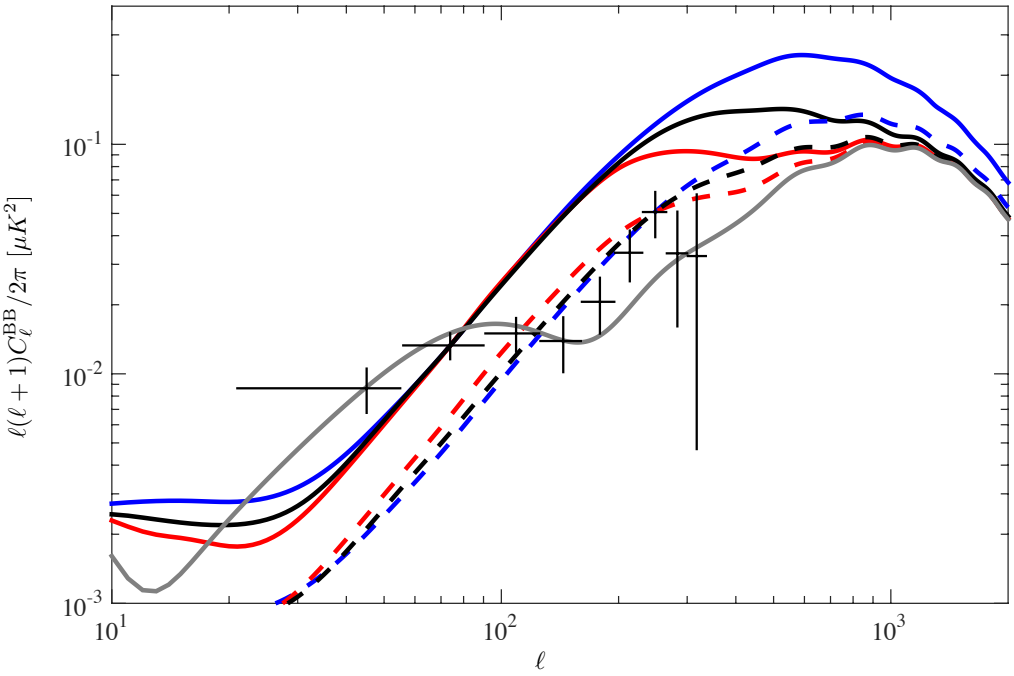

Figure 2.3: *B-mode polarization power spectra compared to the BICEP2 B-mode polarization data. All curves show the combined contribution from defects (blue AH, black SL and red TX) and the lensing of the scalar perturbations, and match the BICEP2 B-mode polarization at* $\ell = 80$ *(solid lines for* $f_{10} = 0.24,\ 0.17,\ 0.09$ *respectively) and at* $\ell = 250$ *(dashed lines for* $f_{10} = 0.08,\ 0.06,\ 0.04$ *respectively)*

2.3 Results

2.3.1 Can topological defects mimic the BICEP2 B-mode signal?

We first attempt to match the cosmic defect B-mode spectra to the BICEP2 data, the results are shown in Figure 2.3. It is clear that the defect spectra have the wrong shape, and could only match the low-multipole data at $\ell < 100$ by substantially over-predicting the high multipole data ($\ell > 100$). In detail, we see that we need $f_{10} \simeq 0.24$ (AH), $f_{10} \simeq 0.17$ (SL) and $f_{10} \simeq 0.09$ (TX) to generate the necessary power at $\ell = 80$, which in turn leads to a B-mode amplitude which is a factor of about 5 too large at higher ℓ. On the other hand, if we try to fit relatively high-ℓ data using defect spectra, we significantly underestimate the prediction of the large scale region.

CMB data, mainly through the increasingly accurate measurement of the temperature power spectrum to higher and higher multipoles [14, 31, 36, 44, 75, 203, 218], already puts strong constraints on the defect contribution in models which combine it with a primordial inflationary power spectrum. Figure 2.4 shows the temperature and B-mode spectra for AH, SL and TX at the upper 95% level for defects obtained in Ref. [14] and shown in Table. 2.1. Even though the shapes of the spectra are similar (see Fig. 2.2) the peaks are not exactly at the same ℓ, and they fall off at different rates at high ℓ. The cosmic string model (AH) has the slowest fall-off, and its amplitude is the most tightly constrained by the temperature data. As a result, the possible B-mode contribution is the smallest at low ℓ (blue line in the upper panel).

We can therefore immediately conclude that the shape of the power spectrum of the defects is

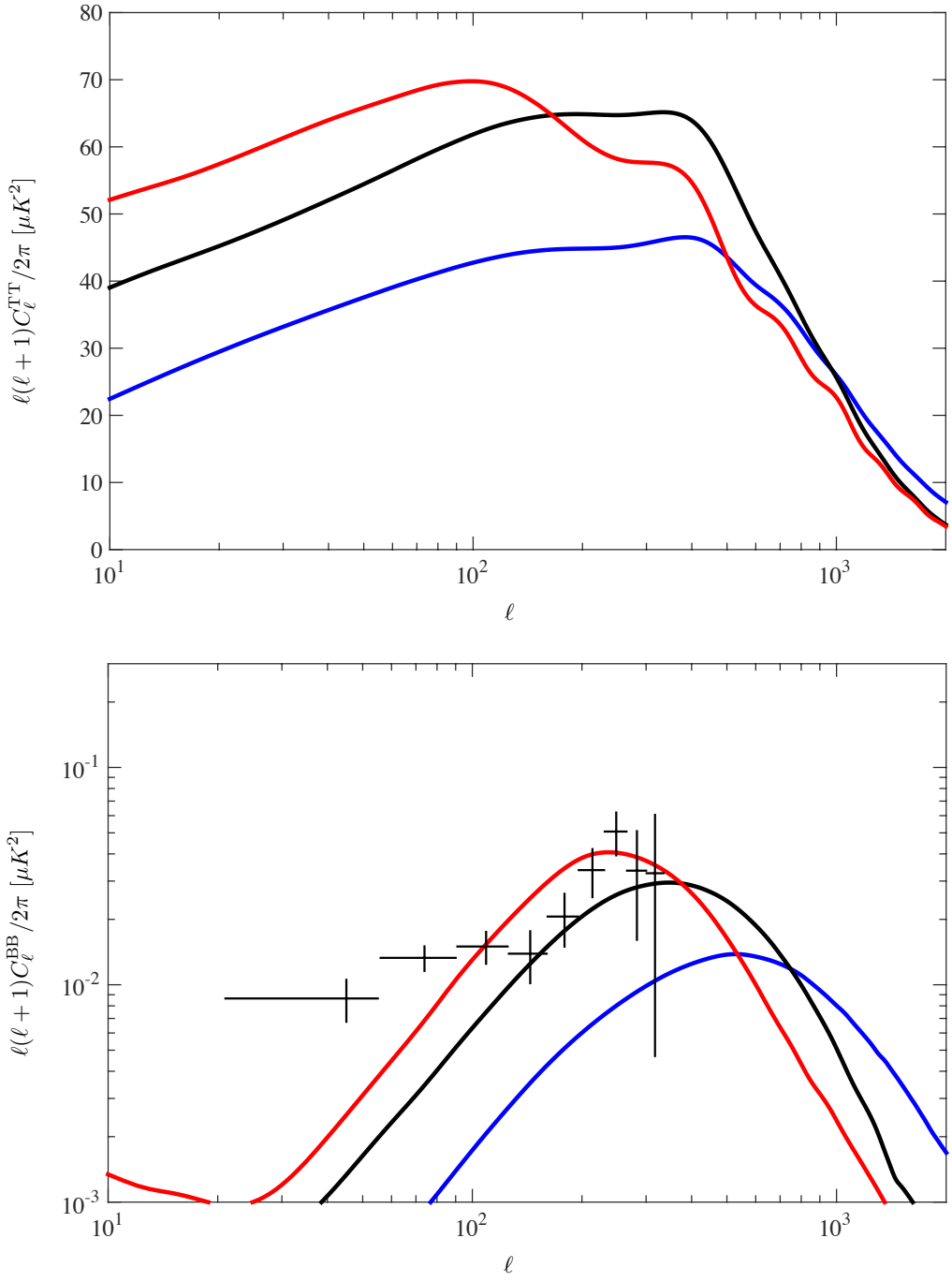

Figure 2.4: *Defect spectra normalised to the 95% upper limits obtained using Planck + WP + High-ℓ. Different lines correspond to textures (red line), semilocal strings (black line), and Abelian Higgs strings (blue line).*

qualitatively wrong, and cannot give a good fit to BICEP2 data.

A similar conclusion was obtained in Ref. [80] for self-ordering scalar fields, which is understandable since self-ordering scalar fields are closely related to the $\mathrm{O}(4)$ model under study here (see Section 2.1.3 of the Introduction). An apparently contradictory conclusion was obtained in Ref.

Dataset	BICEP2 (only *BB*)						
Model	$\mathcal{PL}+G\mu$			$\mathcal{PL}+r+G\mu$			$\mathcal{PL}+r$
Param	AH	SL	TX	AH	SL	TX	-
r	-	-	-	$0.14^{+0.04}_{-0.06}$	$0.14^{+0.04}_{-0.06}$	$0.14^{+0.04}_{-0.06}$	$0.21^{+0.04}_{-0.05}$
$10^{12}(G\mu)^2$	$0.40^{+0.07}_{-0.08}$	$1.73^{+0.29}_{-0.32}$	$0.86^{+0.14}_{-0.16}$	$0.20^{+0.08}_{-0.09}$	$0.87^{+0.34}_{-0.39}$	$0.43^{+0.17}_{-0.20}$	-
$-\ln\mathcal{L}_{\max}$	8.1	7.4	6.8	1.6	1.6	1.8	4.3

Table 2.2: *Parameter estimations and best-fit likelihood values for various cosmological models, fitting for the BICEP2 data. Only the B-mode is used for these estimations.*

[147], where the BICEP2 data was fitted to the USM (see Sec. 2.1.1 of the Introduction), allowing the inter-string distance parameter to vary. They found that a string-only model fitted well the data and differed only slightly from the best-fit model with primordial tensor modes, albeit for inter-string distance values larger than the causal horizon at decoupling. It was suggested that the spectrum of the model was representative of global strings or textures. Numerical simulations of textures do show that they have a larger correlation length than the other defects, and hence a B-mode peak at lower ℓ, but it is also apparent from a comparison of Fig. 2.4 to Fig. 1 of Ref. [147] that the shape of the texture power spectrum at low ℓ is not accurately modelled by the USM. For example, at $\ell = 70$, the best-fit USM spectrum is approximately 50% higher than the texture spectrum, and twice as high at $\ell = 40$, which will tend to make the texture spectrum a worse fit to the data.

2.3.2 Constraints from the Monte Carlo Analysis

Having discarded the role of cosmic defects as primary source of BICEP2 B-modes, we change the perspective and explore how they could assist, as a secondary player, the primary contribution coming from inflationary tensor modes or dust. As an explanatory example we include Figure 2.5, where we consider a mixture of inflationary tensor modes and AH strings. Defects peak at smaller scales, *i.e.* they contribute more significantly at higher multipoles than gravitational waves, hence a mixture of both ingredients could improve the fitting. We indeed observe that the fit is improved, an AH string fraction of around 0.04 would explain the excess signal at $\ell \approx 200$, while a fraction above about 0.06 is disfavoured. We can anticipate a similar effect will occur when considering a mixture of dust and defect contribution, since as it is shown in Figure 2.6 the most important contribution of the foreground dust coincides with the spectrum coming from r.

Prompted by this preliminary results, we extend the qualitative observations of the previous section with a quantitative analysis of the datasets. Therefore we fit different combinations of datasets with various cosmological models. First we fit CMB data with our basic model ($\mathcal{PL}$) with defects $G\mu$ and/or with r. The CMB data chosen are the BICEP2 data alone (for which we only fit for the B-mode spectrum), or all the CMB data. We also considered the case where the data used did not include the High-ℓ data, but the results for both these two choices of data (with and without High-ℓ) were identical, so we only show the parameter constraints with all the CMB data. In the second part we consider a model where the running of the scalar spectral index $\alpha_{\rm s}$ is also free. The last case, corresponds to models which include a dust contribution as described previously.

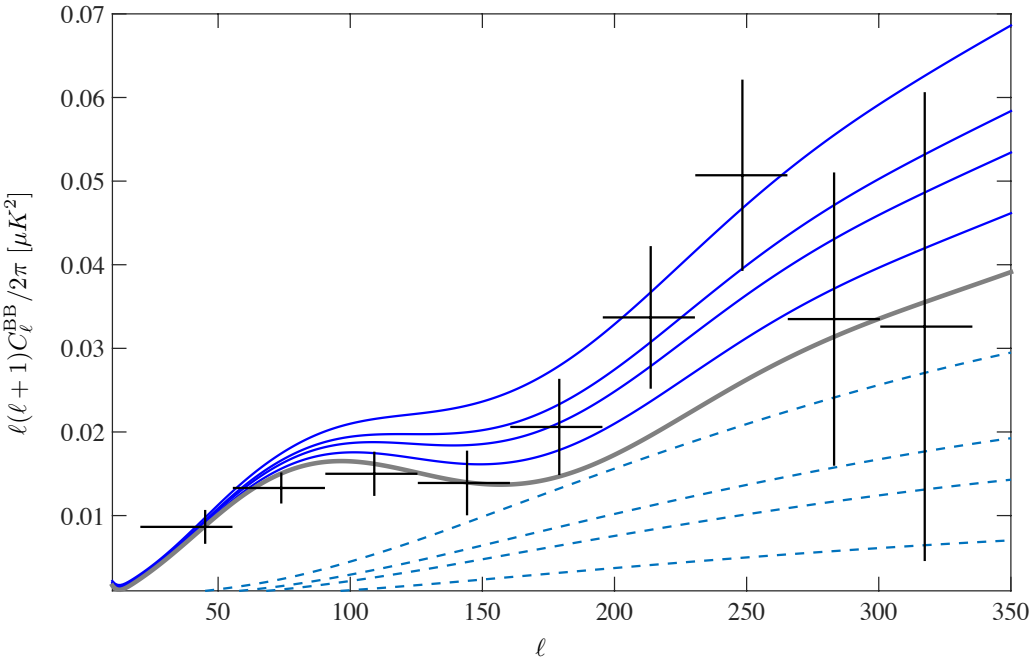

Figure 2.5: *A contribution from AH strings (blue dashed) is added to the prediction from $r = 0.15$ plus scalar lensing (solid grey) to give a total spectrum shown in solid blue. The data points are from BICEP2. From bottom to top the string fractions are 0.015, 0.03, 0.04, and 0.06. A marginal improvement to the overall data fit is given for a string fraction around 0.04, which is about the maximum permitted by current constraints from Planck .*

Primordial tensor modes and defects

All results, using only BICEP2 BB data and using the full CMB set, can be found in Tables 2.2 and 2.3 respectively. The structure of the tables is the following: on the left we show results from chains containing defects; on the right-hand side, we show results from models without defects, included here as reference values.

The values in Table 2.2, especially best-fit likelihoods, show that the fit is rather poor, as suggested in the previous section. Actually, for a model with only one extra component, none of the defect models ($\mathcal{PL} + G\mu$) provides a fit that is comparable to the model including only inflationary gravitational waves ($\mathcal{PL} + r$), although the texture fit is only moderately worse.

We then fit the BICEP2 data with a model which contains both defects and gravitational waves ($\mathcal{PL}+r+G\mu$), in order to assess whether defects could assist tensor modes. As mentioned before, at low ℓ defects cannot explain the power measured. Nevertheless, defects peak at higher ℓ, which might help to fit those points that lie above the lensing curve. The fit is improved (the likelihood is better), although it should be noted that this last model has 2 extra ingredients compared to $\mathcal{PL}$.

As a next step we use the full CMB dataset (*Planck* + WP + High-ℓ + BICEP2) and include the contributions to temperature and polarization (both E- and B-modes) from the different ingredients. If we compare models with only one extra ingredient, we find that $\mathcal{PL}+G\mu[\mathrm{AH}]$ fits the data quite poorly, whereas $\mathcal{PL}+r$, $\mathcal{PL}+G\mu[\mathrm{TX}]$ and $\mathcal{PL}+G\mu[\mathrm{SL}]$ fit the data at roughly the same level, with r being the best model followed closely by TX.

The $G\mu$ constraint obtained from the full set of CMB data is tighter than that from only

Dataset	*Planck* + WP + High-ℓ + BICEP2						
Model	$\mathcal{PL}+G\mu$			$\mathcal{PL}+r+G\mu$			$\mathcal{PL}+r$
Param	AH	SL	TX	AH	SL	TX	-
n_s	$0.955^{+0.007}_{-0.008}$	$0.964^{+0.007}_{-0.008}$	$0.962^{+0.007}_{-0.007}$	$0.963^{+0.007}_{-0.008}$	$0.966^{+0.008}_{-0.008}$	$0.965^{+0.007}_{-0.007}$	$0.962^{+0.007}_{-0.007}$
r	-	-	-	$0.14^{+0.03}_{-0.04}$	$0.10^{+0.03}_{-0.04}$	$0.09^{+0.03}_{-0.04}$	$0.15^{+0.03}_{-0.04}$
$10^{12}(G\mu)^2$	$0.084^{+0.026}_{-0.025}$	$1.34^{+0.27}_{-0.29}$	$0.73^{+0.14}_{-0.15}$	< 0.083	< 1.3	< 0.74	-
f_{10}	$0.021^{+0.006}_{-0.006}$	$0.044^{+0.009}_{-0.010}$	$0.035^{+0.006}_{-0.007}$	< 0.020	< 0.042	< 0.035	-
$-\ln\mathcal{L}_{\max}$	5280.1	5268.8	5266.8	5264.4	5262.9	5263.0	5265.8

Table 2.3: *Parameter estimations and best-fit likelihood values for various cosmological models, fitting for all the CMB data.*

BICEP2, especially for the AH case. For this case, *Planck* bounds are strong enough to push the corresponding BB spectrum far below the BICEP2 data, in other words, the BICEP2 data do not constrain further the AH model in the combined *Planck* + BICEP2 case. By contrast, temperature bounds for SL and TX [14] leave their BB power spectra around the values of BICEP2 (for high ℓ), such that BICEP2 alone is able to put comparable constraints on the level of allowed defects. Our results are consistent with the observation that accurately-determined B-modes can distinguish between different types of defects [148].

The final possibility is the mixture of inflationary gravitational waves and cosmic defects, $\mathcal{PL}+r+G\mu$. We observe that there is less room for defects, and we only obtain upper 95% bounds. Roughly, the mean values in the previous cases become 95% values now. Here again SL and TX do marginally better than AH strings, which are not able to lower r. The reason has already been mentioned: their contribution is so suppressed by the constraints from the *Planck* data that the effect on tensor modes is negligible.

Running of the scalar index

In this case we fit to the full CMB dataset and not BICEP2 alone, since the running of the scalar spectral index affects mainly the temperature channel. The results from a fit to the full CMB dataset can be found in Table 2.4.

The model which contains gravitational waves plus running is slightly preferred over $\mathcal{PL}+r+G\mu$, possibly because if one also allows for running, r could take higher values (e.g. see $\mathcal{PL}+r+\alpha_{\rm s}$ of Table 2.4) and therefore a better fit of B-modes. Another typical effect of including $\alpha_{\rm s}$ is that the scalar spectral index is pushed up, which in principle implies more room for a defect contribution, though in this case it only affects AH strings. Running also changes the tilt of the temperature spectrum, causing an unexpected anticorrelation between $G\mu$ and f_{10}.

It is worth noting that for the TX and SL cases, allowing for the running of the scalar index does not increase the value of r; it remains around the same values as for cases without $\alpha_{\rm s}$. At the same time, allowing for defects does not reduce the magnitude of the running.

Dataset	*Planck* + WP + High-ℓ + BICEP2			
Model	$\mathcal{PL}+r+G\mu+\alpha_{\rm s}$			$\mathcal{PL}+r+\alpha_{\rm s}$
Param	AH	SL	TX	-
$n_{\rm s}$	$1.061^{+0.028}_{-0.028}$	$1.048^{+0.026}_{-0.031}$	$1.049^{+0.030}_{-0.032}$	$1.055^{+0.031}_{-0.031}$
$\alpha_{\rm s}$	$-0.032^{+0.008}_{-0.009}$	$-0.027^{+0.010}_{-0.008}$	$-0.027^{+0.010}_{-0.010}$	$-0.030^{+0.010}_{-0.010}$
r	$0.19^{+0.04}_{-0.05}$	$0.15^{+0.04}_{-0.06}$	$0.14^{+0.04}_{-0.06}$	$0.20^{+0.04}_{-0.05}$
$10^{12}(G\mu)^2$	<0.10	<1.3	<0.71	-
f_{10}	<0.030	<0.047	<0.038	-
$-\ln\mathcal{L}_{\rm max}$	5260.3	5259.2	5258.6	5261.6

Table 2.4: *Parameter estimations and best-fit likelihood values for different cosmological models, fitting for all the CMB data when the running of the scalar index is included.*

Dataset	BICEP2 (only *BB*)							
Model	$\mathcal{PL}+G\mu+A_{\rm dust}$			$\mathcal{PL}+r+G\mu+A_{\rm dust}$			$\mathcal{PL}+r+A_{\rm dust}$	$\mathcal{PL}+A_{\rm dust}$
Param	AH	SL	TX	AH	SL	TX	-	-
r	-	-	-	<0.11	<0.10	<0.18	<0.22	-
$10^{12}(G\mu)^2$	$0.17^{+0.08}_{-0.10}$	$0.74^{+0.40}_{-0.40}$	$0.37^{+0.16}_{-0.24}$	$0.17^{+0.05}_{-0.08}$	$0.72^{+0.32}_{-0.41}$	$0.36^{+0.16}_{-0.21}$	-	-
$A_{\rm dust}\,[\mu K^2]$	$0.20^{+0.06}_{-0.08}$	$0.20^{+0.06}_{-0.08}$	$0.19^{+0.06}_{-0.09}$	<0.26	<0.25	<0.25	$0.19^{+0.10}_{-0.10}$	$0.30^{+0.06}_{-0.07}$
$-\ln\mathcal{L}_{\rm max}$	1.7	1.7	1.8	1.5	1.5	1.7	3.3	3.3

Table 2.5: *Parameter estimations and best-fit likelihood values for different cosmological models, fitting for the BICEP2 data. This is similar to Table 2.2, but in this case a dust model is included.*

Dust

As discussed in Section 2.2, we consider a dust model proposed by the *Planck* collaboration [3], given by[3]

$$C_\ell^{BB,\rm dust}=A_{\rm dust}\ell^{-2.3} \tag{2.3}$$

A similar model has been used by Mortonson and Seljak [146] and Flauger *et al.* [89] to examine the robustness of the BICEP2 result's interpretation as primordial, and we follow their approach.

In Fig. 2.6 we show the contributions to the B-mode power spectrum from inflationary tensors, AH strings, textures, and dust, together with the data points from BICEP2. The normalization is the one obtained from fitting only the BICEP2 data to a model $\mathcal{PL}$ plus one extra ingredient (see Tables 2.2 and 2.5). Note that the lensing spectrum is added in all cases. In the figure it can be seen that dust and r have more importance for lower ℓ; therefore, in B-modes dust is in more direct competition with r than with defects.

We start analyzing BICEP2 B-mode data only. The first thing we notice is that a model including just dust as an extra ingredient is able to improve the fit of $\mathcal{PL}+r$. Moreover, if we consider a composite model ($\mathcal{PL}+r+A_{\rm dust}$), the gravitational wave detection disappears and the fit does not improve (as previously found in Ref. [146]). The best-fit value for r is at $r=0$, i.e. a model with dust alone provides the best fit.

Dust combined with defects gives better results than with gravitational waves. Note that in

[3]While this work was being refereed the *Planck* collaboration submitted a paper [10] where they update their dust model to $C_\ell^{BB}\propto\ell^{-2.45}$. We do not expect our results to change significantly with this new power law. We tested the case of $\mathcal{PL}+G\mu[\rm AH]+A_{\rm dust}$ fitted to the full CMB dataset, and found that the upper 95% confidence limit in $G\mu$ moves from 2.7×10^{-7} to 2.9×10^{-7} (see Table 2.7), which supports our expectations.

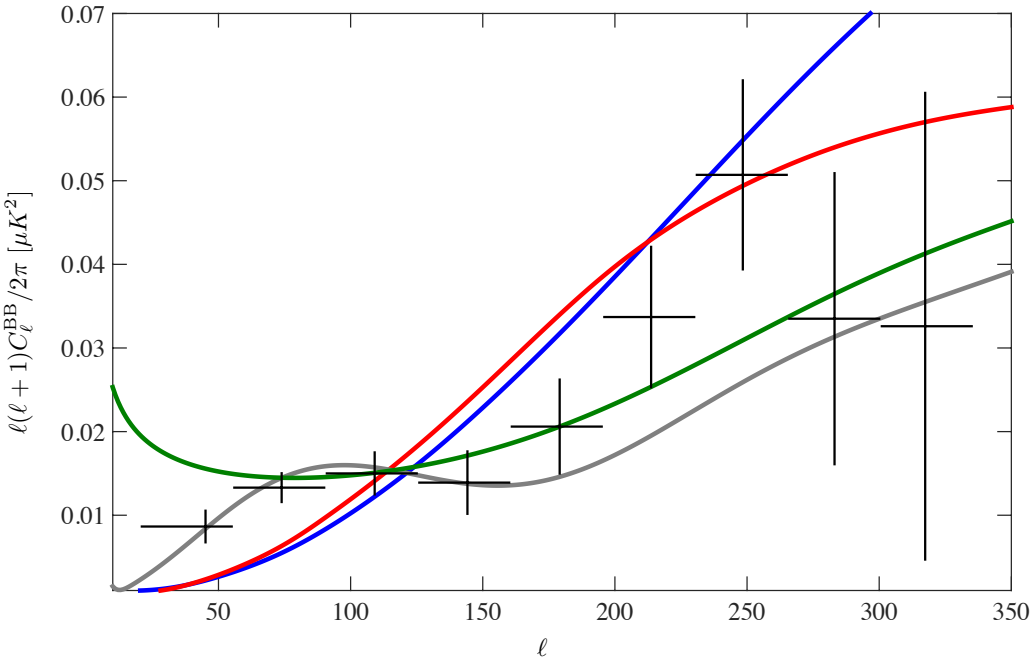

Figure 2.6: *B-mode spectra, including the lensing contribution, using best-fit normalization values given in Tables 2.2 and 2.5, for tensors (grey), dust (green), AH strings (blue) and textures (red). BICEP2 data points are also shown.*

all cases (be it with r or with any $G\mu$) the dust contribution is at the same level. However, dust lowers the amount of defects to about half the one obtained using $\mathcal{PL}+G\mu$, and more or less at the level of $\mathcal{PL}+r+G\mu$. This last set of models does not improve the best-fit likelihood. Finally, in a model with all ingredients ($\mathcal{PL}+r+G\mu+A_{\rm dust}$), we find that a model with no dust is possible at one-sigma, and thus we quote an upper 95% confidence limit. This is due to the fact that dust and inflationary tensors can both account for the low ℓ part of the spectrum, whereas defects account for the higher ℓ.

Considering the full CMB dataset, the picture is roughly the same. Dust does a very good job on its own, and any other combination improves only marginally the best-fit likelihood. Once again, since the temperature power spectrum is also constraining the defect contribution, we find only 95% upper bounds for defects. The bounds for SL and especially TX are tighter than those from *Planck* (see Table 2.1). In all cases, the combination $\mathcal{PL}+G\mu+A_{\rm dust}$ does better than the equivalent $\mathcal{PL}+r+G\mu$.

Note that the different mean values of $A_{\rm dust}$ are due to the differences in the lensing spectra due to different cosmologies used in Tables 2.5 and 2.6.

2.4 Discussion and conclusions

Motivated by the detection of B-mode polarization by the BICEP2 collaboration, we study the possible implications of such measurements on models considering cosmic defects. We perform the analysis from two complementary points of view: from an observational or qualitative point of view and form a quantitative approach, where we explore the likelihood parameter space in order to constrain models containing defects.

Dataset	*Planck* + WP + High-ℓ + BICEP2							
Model	$\mathcal{PL}+G\mu+A_{\rm dust}$			$\mathcal{PL}+r+G\mu+A_{\rm dust}$			$\mathcal{PL}+r+A_{\rm dust}$	$\mathcal{PL}+A_{\rm dust}$
Param	AH	SL	TX	AH	SL	TX	-	-
r	-	-	-	< 0.10	< 0.09	< 0.10	< 0.11	-
$10^{12}(G\mu)^2$	< 0.074	< 0.97	< 0.54	< 0.075	< 0.97	< 0.56	-	-
f_{10}	< 0.019	< 0.031	< 0.026	< 0.019	< 0.032	< 0.027	-	-
$A_{\rm dust}\,[\mu K^2]$	$0.24^{+0.05}_{-0.06}$	$0.21^{+0.06}_{-0.06}$	$0.19^{+0.06}_{-0.07}$	$0.20^{+0.06}_{-0.07}$	$0.16^{+0.07}_{-0.07}$	$0.15^{+0.06}_{-0.07}$	$0.21^{+0.07}_{-0.06}$	$0.25^{+0.05}_{-0.06}$
$-\ln\mathcal{L}_{\rm max}$	5259.6	5259.4	5258.5	5259.5	5259.3	5258.4	5259.6	5260.0

Table 2.6: *Parameter estimations and best-fit likelihood values for different cosmological models, fitting for all the CMB data. This is similar to Table 2.3, but in this case a dust model is included.*

Specifically, in the first part of this chapter we have shown that cosmic defects on their own are a poor fit to the signal. Hence, the need of an additional contribution (gravitational waves or polarized dust) is manifest. Nevertheless, we also evidenced that defects can help the possible gravitational wave contribution to lift the spectrum at high multipoles. The analysis shows that when a defect contribution is added the overall fit is improved.

We also investigate quantitatively the impact of the recent detection of B-mode polarisation by the BICEP2 collaboration on models containing topological defects, extending the results of our earlier study. In accordance with our qualitative expectations we confirm the results obtained in the first part of this work, *i.e.* that topological defects on their own are a poor fit to the signal and that we need an additional contribution, either inflationary gravitational waves or polarised dust emission.

When considering only the BICEP2 B-mode polarization data, we find that the combination of topological defects and inflationary gravitational waves ($\mathcal{PL}+r+G\mu$) or topological defects and dust ($\mathcal{PL}+G\mu+A_{\rm dust}$) slightly improves the fit over inflationary gravitational waves alone ($\mathcal{PL}+r$) or dust alone ($\mathcal{PL}+A_{\rm dust}$). This is because topological defects help to fit the BICEP2 data points at $\ell \gtrsim 200$, which lie above the lensing B-mode contribution (Fig. 2.6). The combination of inflationary gravitational waves and dust on the other hand does not improve the fit over either contribution alone. We note that there are hints in the cross-correlation between BICEP2 and Keck array data [16] that the central values of the B-mode power spectrum will decrease in the future, which will have the effect of more strongly constraining the defect contribution.

The situation changes slightly when we consider the full CMB dataset, consisting of *Planck* + WP + High-ℓ + BICEP2. In this case the texture model on its own ($\mathcal{PL}+G\mu[\rm TX]$) is only slightly worse than inflationary gravitational waves ($\mathcal{PL}+r$), while cosmic strings ($\mathcal{PL}+G\mu[\rm AH]$) are ruled out as the sole source of B-modes. Dust on the other hand is much better, so that $\mathcal{PL}+A_{\rm dust}$ is the globally-preferred model, and neither defects nor inflationary gravitational waves are able to improve the goodness of fit significantly.

	$G\mu$ at $< 95\%$	f_{10} at $< 95\%$
Abelian Higgs strings	2.7×10^{-7}	0.019
Semilocal strings	9.8×10^{-7}	0.031
Textures	7.3×10^{-7}	0.026

Table 2.7: 95% *confidence limits for* $G\mu$ *and* f_{10} *obtained using* $\mathcal{PL}+G\mu+A_{\rm dust}$ *and the full CMB dataset.*

When considering parameter constraints on $G\mu$, we find that BICEP2 on its own constrains the SL and TX models to roughly the same level as *Planck* data do. In other words, the constraints obtained from BICEP2 alone for SL and TX are as strong as the ones obtained from *Planck* data. On the other hand, *Planck* data constrains AH strings more strongly than BICEP2. The reason is that the combined temperature anisotropy dataset constraints on defects come from $\ell \gtrsim 100$, where the string-induced power spectrum peaks higher and decays more slowly than those of the other defects for a given $G\mu$.

The constraints become tighter when including a contribution from inflationary gravitational waves or dust. For the full CMB dataset and for a model with defects and dust (see Table 2.7), we find $G\mu < 2.7 \times 10^{-7}$ for AH, $G\mu < 7.3 \times 10^{-7}$ for TX and $G\mu < 9.8 \times 10^{-7}$ for SL (all at 95%). These constraints are tighter than ones found by the *Planck* collaboration for the temperature data alone [14] (especially for texture, see Table 2.1), which shows the importance that even the current B-mode polarisation data has for constraining topological defects.

3 Improving CMB power spectra from Abelian Higgs cosmic strings

Cosmic strings [57, 103, 104, 214] are relics of the possible phase transitions occurring in the earliest stages of the universe, predicted in many well-motivated models of high energy particle physics and cosmology [115, 116, 177]. Increasingly accurate observations of the cosmic microwave background (CMB) [14, 15, 82, 110] and increasingly robust theoretical predictions [36, 39, 44, 91, 124, 202, 203, 218] have established that strings do not contribute more than a few percent to the temperature perturbations, corresponding to an upper bound on the symmetry-breaking scale of about 4×10^{15} GeV. The majority of the temperature perturbations can be accounted for by an inflationary model with scalar spectral index $n_s = 0.968 \pm 0.006$ and tensor-to-scalar ratio $r < 0.12$ (95% CL) [17].

Since the contribution of defects to CMB temperature fluctuations is small, accurate measurements of the CMB polarization channels, especially B-modes, acquire major importance to detect strings, where they could still contribute at the same level as inflation. The continuing improvement in data motivates us to reduce the remaining theoretical uncertainties in the cosmic string CMB calculations. In previous works [42, 43, 45] energy-momentum and CMB power spectra contributions from cosmic string networks using field theory simulations of the Abelian Higgs (AH) model were calculated. The principal uncertainties in this approach are due to approximations used to handle a field theory in an expanding universe; modelling of the strings across cosmological transitions between the radiation, matter and Λ eras; and extrapolations to large times and small angular scales.

In order to get a complete description of the CMB anisotropies produced by defects, numerical simulations compute the unequal time correlators (UETCs) of the energy-momentum tensor of the strings, from which CMB power spectra can be computed (as we show in Section 2.3 of the Introduction) [78, 79, 104, 155, 196]. The UETC approach has been widely used in field theory simulations, and in recent years, it has also been adapted to other cosmic string simulation schemes such as the Unconnected Segment Model (USM) [32] and the Nambu-Goto (NG) approximation [125].

In this chapter we present updated energy-momentum correlations and CMB power spectra obtained from the largest field theory simulations performed to date. Thanks to a considerable increase in computational resources and in their programming management through the LATField2 [67] framework, significant progress has been possible. These improvements enabled us to tackle the challenges outlined above. We have been able to increase the size of the simulation box from 1024^3 to 4096^3 lattice sites ("4k" simulations), so that we cover a patch of the universe 64 times bigger than in [45], and to simulate for four times longer. Therefore, some of the scales that could only be accessed by extrapolation in previous works can now be directly simulated.

The first uncertainty mentioned above comes from the requirement that we simulate a massive

field theory in an expanding universe. While the cosmic string core width is set by the mass scale of the field theory and remains unaltered by the expansion, the field equations are solved on lattices with comoving coordinates. As the universe expands the comoving string width shrinks. At some point in the evolution the comoving string width becomes less than the separation of adjacent lattice points, and we can no longer resolve the string core on the grid.

An effective proposal to avoid that situation has been to change the equations of motion so that the cosmic strings have an artificially growing physical core width, so that they can be resolved on a comoving lattice throughout the simulation [42, 162] (see Section 2.2 of the Introduction). It was shown that the uncertainties thereby introduced were less than those originating from the limited volume and time of the simulations. However, the great increase in both volume and time of the simulations demand a re-examination of the core growth technique. Our new resources have made it possible to simulate string networks following the *true* equations of motion for both matter and radiation eras, at the cost of some dynamic range, as the system takes longer to settle into its scaling evolution. We find that, as argued previously, the differences in the UETCs with and without core growth are small, in the range $10 - 20\%$ near the peak of the correlators.

The new simulations extend the wave-number range of previous measurements both at low and high wave-number. We measure correlators at the horizon scale more accurately, and we are able to measure directly at values of k a factor four higher than before, which we had previously reached only by extrapolation. We confirm the power-law behaviour of the scalar correlators at large wave-numbers, although the behaviour of the vector and tensor correlators is less clear.

We also address the modeling of the cosmological transitions in our simulations, not only the transition from radiation to matter but also that to a universe dominated by a cosmological constant. We perform the first simulations of Abelian Higgs strings across cosmological transitions, essential for checking and improving previous modelling. We find that string networks evolve in a close to adiabatic way across the radiation-matter transition; their properties are at all times close to those of a network simulated with a constant expansion rate equal to the instantaneous rate.

We introduce a new technique for deriving the source functions for Einstein-Boltzmann integrators, which are a crucial step in the pipeline for calculating CMB and matter perturbations, and a source of significant uncertainty in the past. We call our new method fixed-k UETC interpolation. We compare it to previous methods [42, 86], finding that it is significantly more accurate in reproducing the UETCs at cosmological transitions.

Finally and considering all innovations introduced in this work, we calculate new CMB power spectra. The new CMB predictions are derived from the correlators of the real equations of motion and in the new fixed-k interpolation framework for cosmological transitions, which uses the new interpolation functions derived in this work.

The chapter is structured as follows. We show how we merge the data from our simulations and correct for the effects of the finite string width in Sec 3.1. In Sec 3.2 we describe the three methods for deriving transition-era source functions from the correlators, including our new fixed-k UETC interpolation method, comparing to new numerical simulations of transition-era correlators. New CMB power spectra and comparisons between different cases are presented in Sec 3.3. Finally, we discuss and conclude in Sec 3.4.

3.1 UETCs from the simulations

In this section we present the details of the numerical simulations from which the UETC data was collected, and how the data was merged into a set of 10 scaling UETCs, 5 each in the matter

and radiation eras. These merged scaling UETCs are the inputs for the next section, in which the eigenvector decomposition methods are discussed. Remember that the Abelian-Higgs model as well as the UETC formalism and eigenvector decomposition method have been introduced in Sections 2.1.1 and 2.3 of the Introduction.

3.1.1 Simulation details

The data was obtained from two years of production on the supercomputers Monte Rosa and Piz Daint, the two largest systems of the Swiss National Supercomputer Center (CSCS). On both of those systems we have used 34816 cores/MPI processes, 32768 for computation and 2048 for efficient output operations. Of the order of 35 M CPU hours have been used for this project.

The equations of motion of the Abelian-Higgs model in a spatially flat FLRW universe are (see Sections 2.1.1 and 2.2 of the Introduction):

$$\ddot{\phi} + 2\frac{\dot{a}}{a}\dot{\phi} - D_j D_j \phi = -a^2 \frac{\lambda}{2}(|\phi|^2 - \phi_0^2)\phi \,, \tag{3.1}$$

$$\dot{F}_{0j} - \partial_i F_{ij} = -2a^2 e^2 \mathrm{Im}(\phi^* D_j \phi) \,. \tag{3.2}$$

These field equations were evolved on 4096^3 lattices with comoving spatial separation of $dx = 0.5$ and time steps of $dt = 0.1$, in units where $\phi_0 = 1$. The simulation volume therefore has comoving size $L = 2048$. The couplings were $\lambda_0 = 2$ and $e_0 = 1$, chosen so that the mass of the gauge and scalar fields, $\lambda\phi_0/\sqrt{2}$ and $\sqrt{2}e\phi_0$, are the same, and equal to $\sqrt{2}\phi_0$ at the end of the simulation. The inverse mass of the fields sets the length scale of the string width. With these couplings, the mass per unit length of the string in the continuum is $\mu = 2\pi\phi_0^2$.

We performed 7 individual runs in pure radiation and in pure matter domination eras to determine the scaling form of the UETCs, for two values of the string core growth parameter, $s = 0$ and $s = 1$ (see Section 2.2 of the Introduction for the definition of s). We also performed runs across the radiation-matter and matter-Λ cosmological transitions on 1024^3 lattices, with $s = 0$. In total, we used UETCs from 28 4k and 35 1k production runs. Each 4k run took approximately 400k core-hours.

In the initial field configuration, only the scalar field is non-zero, and set to be a stationary Gaussian random field with a power spectrum

$$P_\phi(\mathbf{k}) = \frac{A}{1 + (kL_\phi)^2}, \tag{3.3}$$

with A chosen so that $\langle|\phi^2|\rangle = \phi_0^2$, and $L_\phi = 5\phi_0^{-1}$.

The UETCs cannot be calculated until cosmic strings are formed and reach their scaling configuration. These early phases contain a huge amount of excess energy induced by the random initial conditions, therefore we smoothed the field distribution by applying a period of diffusive evolution

$$\dot{\phi} = D_j D_j \phi - \frac{\lambda}{2}(|\phi|^2 - \phi_0^2)\phi \,, \tag{3.4}$$

$$F_{0j} = \partial_i F_{ij} - e^2 \mathrm{Im}(\phi^* D_j \phi) \,, \tag{3.5}$$

between the start time of the simulation $\tau_{\mathrm{start}} = 50$ and a time $\tau_{\mathrm{diff}} = 70$. The timestep was $1/30$, in units where $\phi_0 = 1$.

We followed the same technique as in Ref. [42] to accelerate the formation of the strings in the

$s = 1$ case, by setting s negative, so that the cores of the strings grow with the comoving horizon until a time $\tau_{\rm cg}$, staying at most $1/10$ of the horizon size at all times. The cooling and the core growth optimize the speed of approach to a scaling field configuration. The run is stopped soon after half a light-crossing time of the simulation volume, to ensure there are no artefacts from the periodic boundary conditions.

With our current computing power we are able to get scaling string configurations following the real equations of motion, *i.e.* , equations with $s = 1$, even in the matter era where the string width shrinks as the square of conformal time in comoving coordinates. However, in general, the closer the evolution to the true dynamics, the larger the initial relaxation period where UETCs cannot be collected, and the shorter the period during which they exhibit scaling. Conversely, $s = 0$ simulations reach the scaling regime much more quickly: in our current simulation box $s = 0$ simulations scale for a period 4 times longer than $s = 1$ networks.

We measured the UETC by recording the mean value of $C_{ab}(k, \tau_{\rm ref}, \tau)$ (see Eq. (2.29) of the Introduction) for wavevectors binned in the range $2\pi(n-1)/L < |\mathbf{k}| \leq 2N_{\rm b}/L$ $(1 \leq n < N_{\rm b})$, with $N_{\rm b} = 3458$, and 150 logarithmically-spaced times between $\tau_{\rm ref}$ and $\tau_{\rm end} = 1100$. The wavenumber of the nth bin k_n is set to the mean value of $|\mathbf{k}|$ in that bin. Table 3.1 shows the values of $\tau_{\rm ref}$ taken.

Model	$s = 1$		$s = 0$	
Cosmology	Radiation	Matter	Radiation	Matter
$\tau_{\rm cg}$	204	366	–	–
$s_{\rm cg}$	-1	-0.5	–	–
$\tau_{\rm ref}$	450	600	200	200
$\tau_{\rm max}$	600	800	1100	1100
$r^{\rm max}$	1.33	1.33	5.5	5.5
$x^{\rm min}$	1.38	1.84	0.61	0.61
$x^{\rm max}/10^3$	4.90	6.53	2.18	2.18

Table 3.1: *Core growth time $\tau_{\rm cg}$, and the value of the core growth parameter s during the core growth phase of the simulation. Also given are UETC reference times $\tau_{\rm ref}$, the maximum time at which data is taken for the UETC τ_{max}, the ratio between the two $r^{\rm max}$, and the minimum and maximum values of $x = k\tau_{\rm ref}$, $x^{\rm min}$ and $x^{\rm max}$, for each of the sets of 4k simulations in the radiation and matter eras, without $(s = 1)$ and with $(s = 0)$ the string core growth approximation. Times are given in units where $\phi_0 = 1$.*

We also recorded the equal time correlators (ETCs) at each time the UETC is evaluated, with which we can monitor the quality of the scaling. Perfect scaling would mean that the ETCs collapse to a single line when plotted against $x = k\tau$. As mentioned above, the network takes some time to relax to scaling, and in the $s = 1$ case we see some evidence that the vector ETCs depart from scaling towards the end of the simulation, which we believe is a lattice resolution effect. We therefore conservatively take UETC data up to a time $\tau_{\rm max}$. Table 3.1 also shows $\tau_{\rm max}$, and derived parameters which describe the dynamic range of the simulation.

Despite the modest scaling range of the $s = 1$ simulation, it is enough to characterize the region around the peak of the UETCs. This region contains the ETC obtained at the reference time and its surrounding area, where the maximum correlation within the network is set. Although it does not supply all the information required for a CMB calculation, it gives the major contribution to the power spectra. In contrast, because $s = 0$ simulations scale earlier and for a longer period of

time, they probe higher time-ratios and larger length scales.

We will see that the $s = 0$ and $s = 1$ ETCs are very similar, when networks with the same string separation are compared. This similarity motivates a new merged structure for the UETCs, incorporating contributions from simulations with maximum fidelity and with maximum dynamic range: the $s = 1$ measurements establish the central part of the UETCs, while the $s = 0$ are used at large time ratios and large length scales (low $k\tau$).

3.1.2 Scaling

In the merging process special care must be taken concerning the role of the simulation time parameter $\tau_{\rm sim}$. Simulations for different values of the core growth parameter follow different equations of motion (see Eqs. (3.1) and (3.2) which depend explicitly on s). In addition, each simulation starts from different initial conditions and applies different amounts of core growth, depending on the expansion rate and the value of s (see Table 3.1). For these reasons, one cannot directly compare simulations with different s at the same simulation time $\tau_{\rm sim}$.

Hence it is better to define the *physical* time based on the state of the string network itself, and in particular to use a length scale in the network. Specifically, the comoving string separation ξ has been identified as a useful quantity to determine compatible simulation stages. The string separation is defined in terms of the mean string length $L_{\rm s}$ in a horizon volume V as

$$\xi = \sqrt{\frac{V}{L_{\rm s}}}\,. \tag{3.6}$$

The mean string length is usually derived by directly measuring the comoving length of each string (see details in [42, 45, 66, 117, 179]). One way of obtaining the length of string is by summing the number of plaquettes pierced by strings. Such plaquettes are identified from the winding of a gauge-invariant phase around them [117]. We correct the *Manhattan* length so obtained by a factor $\pi/6$ [179]. An alternative way, and the one we use in this work, is to use local field theory estimators to get the above ratio. In our case we employ the mean Lagrangian density $\bar{\mathcal{L}}$, with

$$L_{\rm s} = -\bar{\mathcal{L}}V/\mu. \tag{3.7}$$

We show the measured values of ξ inferred from the mean Lagrangian density in the matter era in Fig. 3.1.

As it was found in previous works, the asymptotic behaviour of the string separation is very close to linear,

$$\xi \to \beta(\tau_{\rm sim} - \tau_{\rm offset})\,, \tag{3.8}$$

where $\tau_{\rm offset}$ is the time offset of the ξ curve (see Fig. 3.1). The time offset as well as the slope of ξ in the linear regime are different for each realization due to the random initial conditions. We define the mean slope β as the average of all different slopes from different realizations. Numerical values of the slopes can be found in Table 3.2.

Simulations at same ξ can be considered to be at the same stage of the evolution. Hence, in order to merge the UETCs from different runs, they should be converted to functions of ξ and ξ' rather than $\tau_{\rm sim}$ and $\tau'_{\rm sim}$, according to

$$C_{ab}^{(\xi)}(k,\xi,\xi') = C_{ab}^{(\rm sim)}(k,\tau_{\rm sim},\tau'_{\rm sim})\sqrt{\frac{\tau_{\rm sim}\tau'_{\rm sim}}{\xi\xi'}}. \tag{3.9}$$

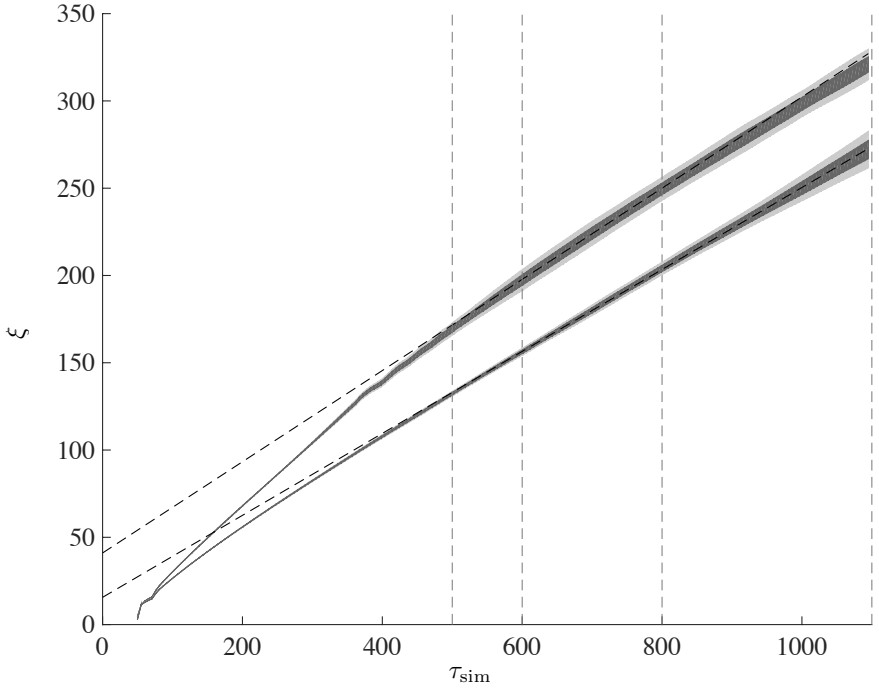

Figure 3.1: *Average string separation ξ from $s = 1$ (top line) and $s = 0$ (bottom line) simulations in the matter era, with ξ obtained from the Lagrangian length measure (3.7). Shaded regions correspond to the 1σ and 2σ deviations from the mean value obtained by averaging over all seven realizations. We also included the linear fit of the function (dashed black line) where the time intervals fitted have been $\tau_{\rm sim} \in [600,\ 800]$ $(s = 1)$ and $\tau_{\rm sim} \in [500,\ 1100]$ $(s = 0)$.*

	$s = 1$		$s = 0$	
	Radiation	Matter	Radiation	Matter
$\beta_{\rm W}$	0.265 ± 0.005	0.277 ± 0.009	0.244 ± 0.005	0.247 ± 0.008
$\beta_{\mathcal{L}}$	0.254 ± 0.005	0.261 ± 0.008	0.234 ± 0.006	0.235 ± 0.008

Table 3.2: *Values of the slope of the average string separation (see Eq. 3.8). In the $s = 1$ case, the time intervals used to fit the function are $\tau_{\rm sim} \in [600\ 800]$ for matter and $\tau_{\rm sim} \in [450\ 600]$ for radiation. In the $s = 0$ case, the time intervals are $\tau_{\rm sim} \in [500\ 1100]$, both for matter and radiation. The quantity $\beta_{\rm W}$ is obtained by measuring the string length using the number of plaquettes pierced by strings (see text), whereas $\beta_{\mathcal{L}}$ is obtained by using the Lagrangian density (3.7).*

Besides allowing comparison of the $s = 0$ and $s = 1$ networks, it is found that the variance between simulations of the ETCs $C^{(\xi)}_{ab}(k, \xi, \xi)$ plotted against $k\xi$ is thereby reduced.

3.1.3 UETC merging

The schematic representation of which UETC contributes to the merged UETC can be found in Fig. 3.2, displayed in the variables

$$z_\xi = k\sqrt{\xi\xi'} \quad \text{and} \quad r_\xi = \xi'/\xi\,. \tag{3.10}$$

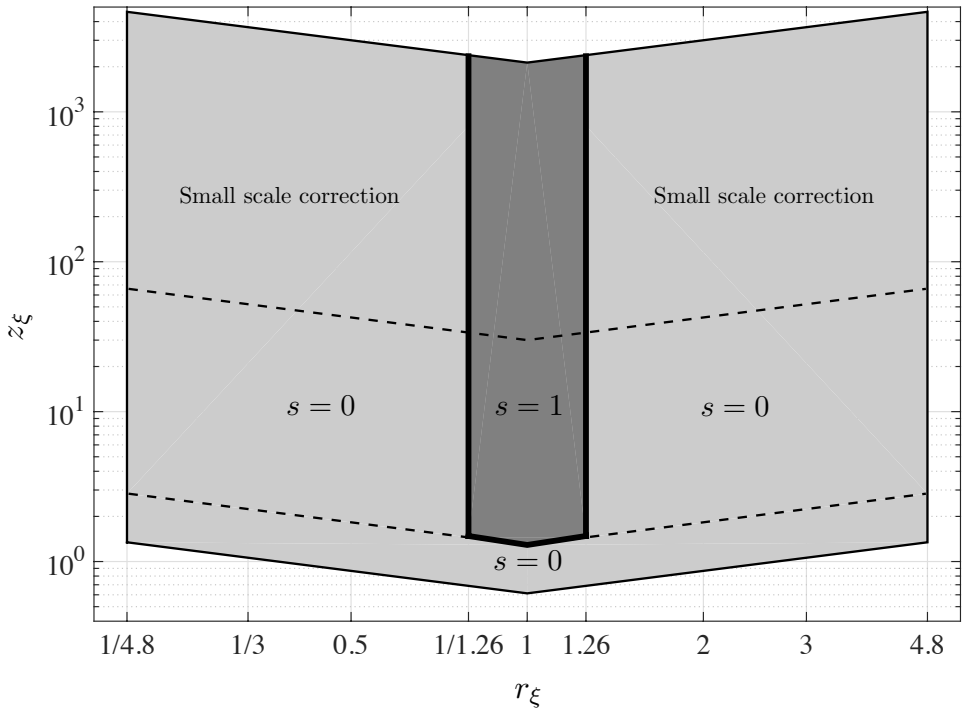

Figure 3.2: *Top view of the scheme of the merged UETC. ETCs and its surroundings are covered by $s = 1$ simulations, while $s = 0$ are used to extrapolate data both to large time ratios and very large scales. The variables are defined in Eq. (3.10).*

Fig. 3.3 and 3.4 show how each simulation contributes to the merged UETC: the $s = 1$ simulations provide the central part of the correlation and the $s = 0$ simulations extend it to higher time-ratios. The numerical values of the limits of the different regions in the merged UETC can be found in Table 3.3.

Model	$s = 1$		$s = 0$	
Cosmology	Radiation	Matter	Radiation	Matter
$\xi(\tau_{\rm ref})$	146.7	198.0	55.8	55.9
$\xi(\tau_{\rm max})$	183.3	248.4	269.5	270.1
$r_\xi^{\rm max}$	1.26	1.26	4.83	4.83
$x_\xi^{\rm min}$	0.45	0.60	0.17	0.17
$x_\xi^{\rm max}/10^3$	1.60	2.16	0.61	0.61

Table 3.3: *Mean string separations ξ at $\tau_{\rm ref}$ and τ_{max}, the ratio between the two, and the minimum and maximum values of $x_\xi = k\xi(\tau_{\rm ref})$, $x_\xi^{\rm min}$ and $x_\xi^{\rm max}$, for simulations in the radiation and matter eras, without $(s = 1)$ and with $(s = 0)$ the string core growth approximation. Lengths are given in units where $\phi_0 = 1$.*

The resulting UETC is shown in the upper pane of Fig. 3.5, viewed along the z_ξ axis. It can be seen that the $s = 0$ and $s = 1$ UETCs differ by less than 20% at the junction at $r_\xi^{\rm lim}$, demonstrating that the $s = 0$ simulations capture the near-equal time energy-momentum correlations rather well.

The equal-time correlations are also close. A comparison of the ETCs and the relative factor

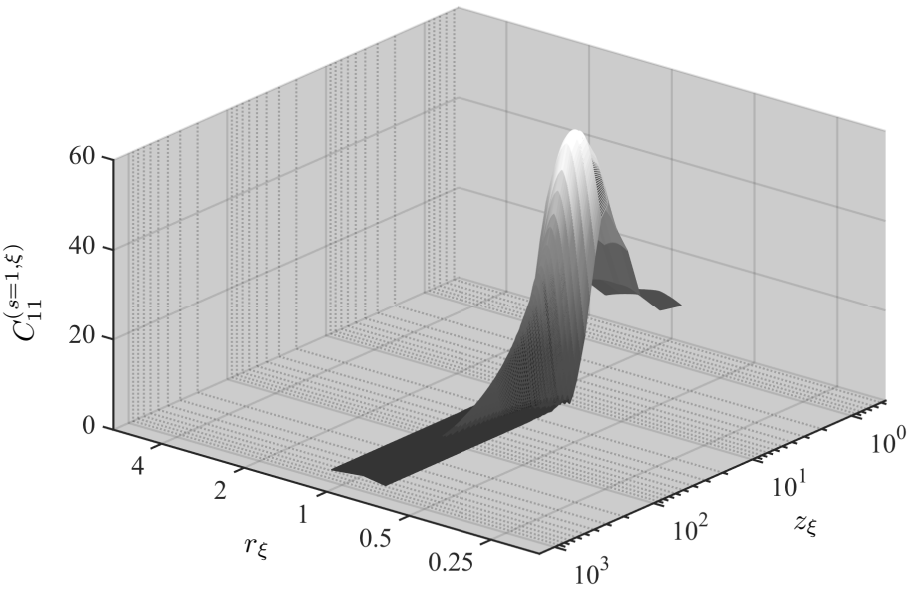

Figure 3.3: *The C_{11} correlator in the matter era, simulated with $s = 1$, in the (z_ξ, r_ξ) region indicated in Fig. 3.2 and Table 3.3.*

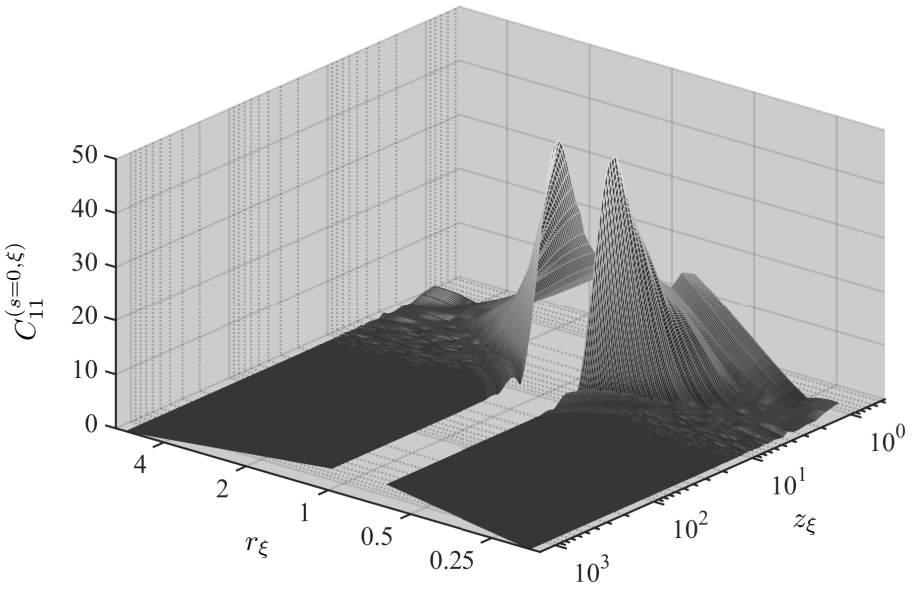

Figure 3.4: *The C_{11} correlator in the matter era, simulated with $s = 0$, in the (z_ξ, r_ξ) region indicated in Fig. 3.2 and Table 3.3.*

between them,

$$\gamma_{ab}(z_\xi) = \frac{C_{ab}^{(s=1,\xi)}(z_\xi, 1)}{C_{ab}^{(s=0,\xi)}(z_\xi, 1)}\,, \tag{3.11}$$

can be found in Fig. 3.6. One can see that the $s = 0$ ETC is approximately 20% higher near the

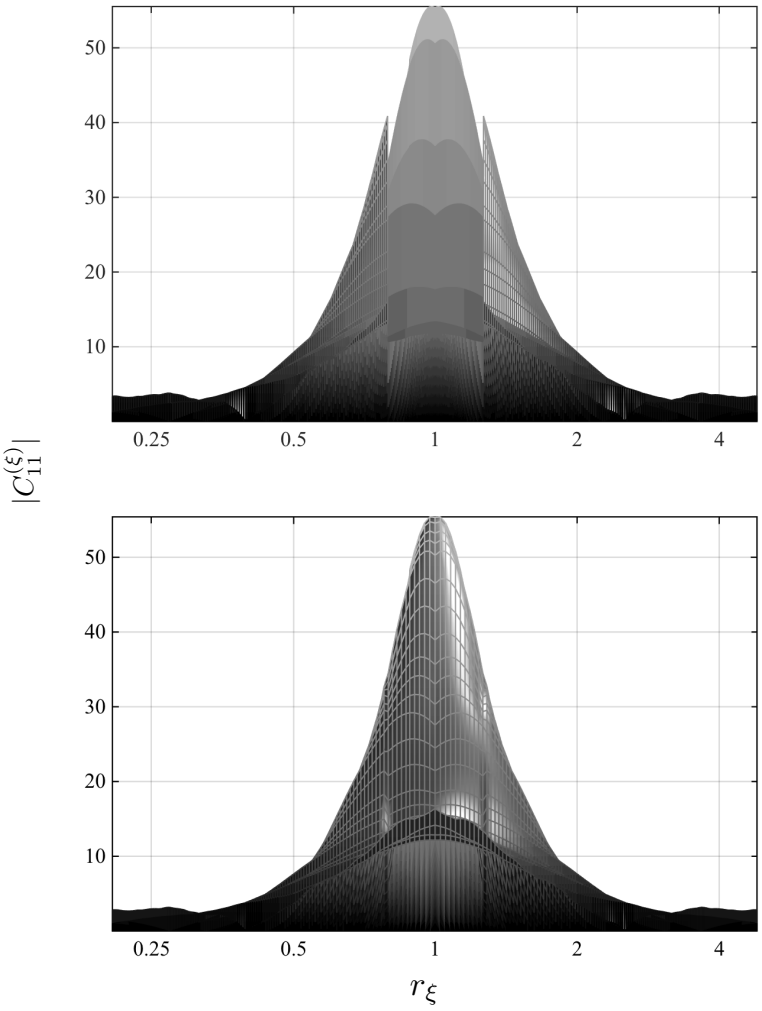

Figure 3.5: *Merged scalar $C_{11}^{(\xi)}$ matter correlator. The upper pane shows the C_{11} before ETC normalization, whereas the lower pane represents the final merged and normalized case.*

peak, although it dips below the $s = 1$ ETC at higher $k\xi$ where the correlators are small.

The normalization factor $\gamma_{ab}(z_\xi)$ is applied to the UETC of the $s = 0$ case, we call this procedure *ETC normalization*. Therefore, the final representation of the merged UETCs for $z_\xi > 1.29\exp(|\ln(r_\xi)|)$ reads as:

$$C_{ab}^{(\mathrm{tot},\xi)}(z_\xi, r_\xi) = C_{ab}^{(\mathrm{s}=1,\xi)}(z_\xi, r_\xi)\theta(\ln(r_\xi^{\mathrm{lim}}) - |\ln(r_\xi)|) + \gamma_{ab}(z_\xi)C_{ab}^{(\mathrm{s}=0,\xi)}(z_\xi, r_\xi)\theta(|\ln(r_\xi)| - \ln(r_\xi^{\mathrm{lim}}))\,. \quad (3.12)$$

Here the values of z_ξ are defined from the $s = 0$ simulations, with the values of the $s = 1$ UETCs obtained by interpolation. The normalised and merged C_{11} is plotted in the lower pane of Fig. 3.5.

It is remarkable that the normalization of the ETC produces a UETC which is very close to continuous at the merging boundary r_ξ^{lim}. This means that the width of the UETCs, which depends on the speed with which the strings move, is very similar.

Finally, we use $s = 0$ UETC data in the range $0.17 < z_\xi \exp(-|\ln(r_\xi)|) < 1.29$, *i.e.* the lowest

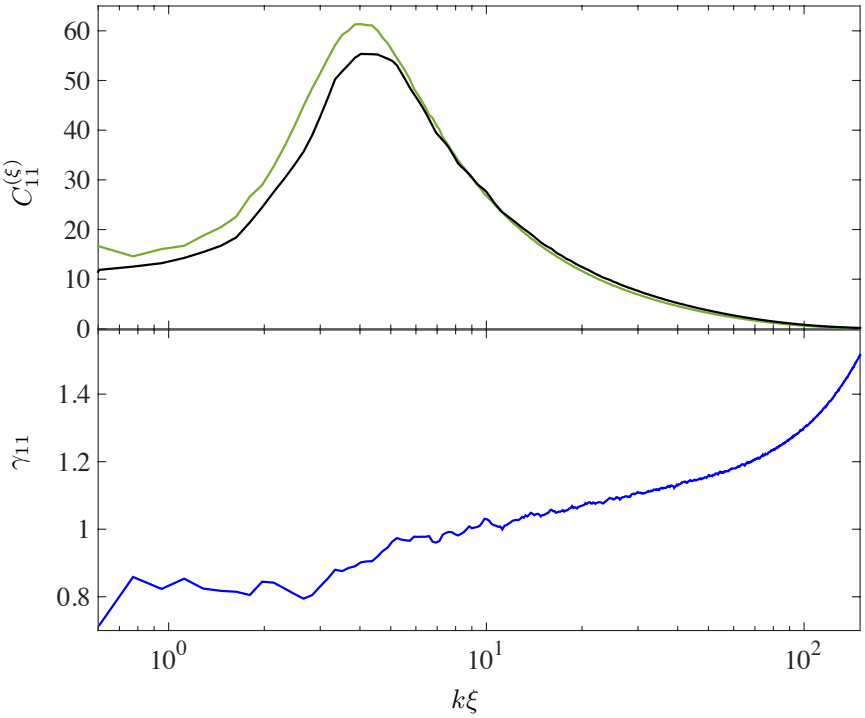

Figure 3.6: *Upper pane: ETCs corresponding to the $C_{11}^{(\xi)}$ for $s = 0$ (green line) and $s = 1$ (black line), in the matter era. The lower pane represents the correction factor $\gamma_{11}(k\xi)$ between them.*

	C_{11}	C_{12}	C_{22}	$C_{\rm vv}$	$C_{\rm tt}$
Matter	0.76	0.42	0.77	0.94	0.91
Radiation	0.71	0.60	0.73	1.23	0.89

Table 3.4: *Normalization factor $\bar{\gamma}_{ab}$ for low z_ξ $s = 0$ data, obtained from weighted average of the first 6 bins of $\gamma_{ab}(z_\xi)$.*

region of Fig. 3.2 delimited by a solid line (bottom) and a dashed line (top), normalised by the average of $\gamma_{ab}(z_\xi)$ in the first six bins, weighted by the number of **k** values contributing to each bin, or

$$C_{ab}^{(\rm tot,\xi)}(z_\xi, r_\xi) = \bar{\gamma}_{ab} C_{ab}^{(\rm s=0,\xi)}(z_\xi, r_\xi)\,. \tag{3.13}$$

The values of $\bar{\gamma}_{ab}$ are given in Table 3.4.

3.1.4 UETC fitting and small-scale correction

We extend the small scale correction performed in [45] (see section III-D). There it was argued that equal-time correlators decay on small scales (deep inside the horizon, $k\tau \gg 1$, but above the scales at which the string width becomes relevant) approximately as $1/k\tau$ ($1/k\xi$ in terms of the string separation scale).

In Fig. 3.7 we show power-law fits of $k\xi C^{(\xi)}$ over the range $k\xi \in [15\ 90]$ ($s = 0$) and $k\xi \in [15\ 70]$ ($s = 1$), denoted by vertical lines, giving the numerical values of the power law in Table 3.5. We

have been able to confirm that the power-law is a reasonable fit to our current ETCs, for both $s = 0$ and $s = 1$ simulations, although the power law is less clear for the vector and tensor cases.

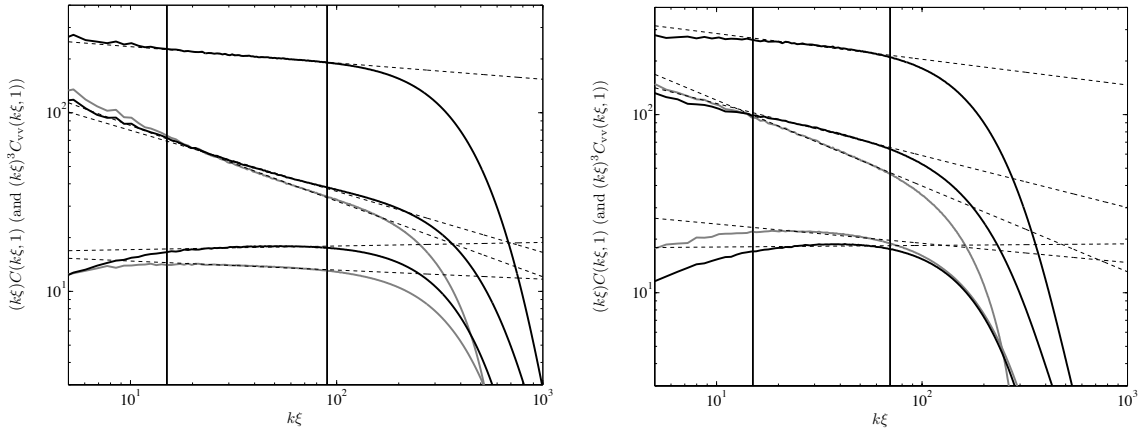

Figure 3.7: *Power law fit for all five correlators for $s = 0$ at the end of the simulation $\tau_{\rm sim} \approx 1100$ (upper pane) and s=1 at the end of the scaling regime $\tau_{\rm sim} \approx 800$ (lower pane). Both cases correspond to the matter era. Fitting ranges lie between the vertical lines: $k\xi \in [15\ 90]$ for $s = 0$ and $k\xi \in [15\ 70]$ for $s = 1$. In both pictures the color election is the same, the uppermost line is the ETC of C_{11}, the middle pair of lines correspond to C_{22} (black line) and $|C_{12}|$ (grey line) and finally the lower pair of lines are $C_{\rm vv}$ (grey line) and $C_{\rm tt}$ (black line).*

The power-law behaviour applies between the string separation scale ξ and the string width w. In our simulations, the ratio ξ/w reaches a maximum of approximately 300. In the true Universe, the power-law behaviour would hold for much longer as the string width at late times is over 50 orders of magnitude smaller than the string separation. Thus using the extrapolation to very high $k\xi$ could be used to improve our estimates of the scaling functions at high values of $k\tau$.

We use the information of the decay trend to correct the behaviour of the UETCs at high values of the binned wave numbers k_n, covering scales between the string width and the lattice spacing. We conservatively do not extrapolate the UETCs beyond the wave vectors contained in time simulations. The UETCs are in any case very small at high $k\tau$.

In order to accomplish that, we follow the procedure presented in [45] and define the attenuation level:

$$R(k,\xi) = \frac{Q(k\xi)^p}{C^{(\xi)}(k\xi,1)} \tag{3.14}$$

where Q and p represent constants of the power-law fit.

This is a measure of how far the equal time correlators are from their corresponding power-law form. As mentioned above, the power-law form is not clear for the tensor and vector ETCs in either $s = 0$ or $s = 1$ simulations, and it is conceivable that there are contributions from the massive radiation which prevent it from ever appearing. Still larger simulations are required to establish the asymptotic form of the vector and tensor ETCs at high $k\tau$. The power laws are at least clear for the scalar correlators.

As the UETCs are quadratic functions relating two separate times, we apply the correction in the following manner:

$$C_c^{(\xi)}(k\sqrt{\xi\xi'},\xi'/\xi) = \sqrt{R(k,\xi)R(k,\xi')}\, C^{(\xi)}(k\sqrt{\xi\xi'},\xi'/\xi)\,, \tag{3.15}$$

	$s=1$		$s=0$	
	Radiation	Matter	Radiation	Matter
C_{11}	-0.22 ± 0.01 2.78 ± 0.01	-0.14 ± 0.01 2.60 ± 0.02	-0.14 ± 0.01 2.60 ± 0.02	-0.10 ± 0.01 2.47 ± 0.01
C_{12}	-0.60 ± 0.02 2.89 ± 0.03	-0.48 ± 0.03 2.56 ± 0.06	-0.51 ± 0.03 2.66 ± 0.06	-0.43 ± 0.03 2.37 ± 0.06
C_{22}	-0.37 ± 0.02 2.63 ± 0.03	-0.29 ± 0.03 2.35 ± 0.07	-0.40 ± 0.03 2.51 ± 0.07	-0.34 ± 0.03 2.26 ± 0.07
$C_{\rm vv}$	-0.134 ± 0.005 1.662 ± 0.008	-0.11 ± 0.01 1.49 ± 0.03	-0.059 ± 0.006 1.35 ± 0.01	-0.059 ± 0.003 1.23 ± 0.02
$C_{\rm tt}$	0.076 ± 0.004 1.153 ± 0.007	0.009 ± 0.003 1.25 ± 0.02	0.045 ± 0.003 1.183 ± 0.008	0.021 ± 0.003 1.21 ± 0.01

Table 3.5: *Values of the parameters p and Q as defined in Eq. (3.14) for each correlator in matter and radiation, and for $s=0$ and $s=1$ at $\tau=\tau_{\rm end}$. The top line gives the value of p and the second of $\log_{10} Q$. The fitting range for the values are the same as in Fig. 3.7, except for the $s=1$ radiation case, where the range is $k\xi \in [10\ 60]$.*

whenever $k\xi > 30$, for every r_ξ (see the upper dashed line in Fig. 3.2).

We show the set of final UETCs in the matter era in Fig 3.8. Note that there is no extrapolation in r_ξ: the UETCs are set to zero for $|\ln(r_\xi)| > \ln(r_\xi^{\rm max})$.

Finally, we transform back from ξ to a scaling time variable τ, by noting that ξ and τ are proportional at large times. Hence we use Eq. (3.8) to write $\tau = \xi/\beta$. Our estimates of the scaling UETCs are therefore

$$\bar{C}_{ab}(k\sqrt{\tau\tau'}, \tau/\tau') = \beta^{-1} C_{ab}^{(\xi)}(k\sqrt{\xi\xi'}/\beta, \xi/\xi')\,, \tag{3.16}$$

where β is the mean slope obtained from the $s=1$ simulations, as given in the $\beta_{\mathcal{L}}$ row of Table 3.2.

3.2 Eigenvector decomposition at cosmological transitions

In this section we derive the source functions needed by Einstein-Boltzmann integrators and used to calculate the CMB power spectra presented in the next section. All the information needed to obtain the power spectra of CMB and matter perturbations is encoded in the UETCs [78, 155, 196]. In general, a UETC is a function of three variables

$$C(k, \tau, \tau'), \tag{3.17}$$

and the correlator is non-vanishing in the region

$$\tau_{\rm i} \leq (\tau', \tau) \leq \tau_0, \tag{3.18}$$

where τ_0 is the current (conformal) time, and $\tau_{\rm i}$ is the time at which the defect-forming phase transition takes place.

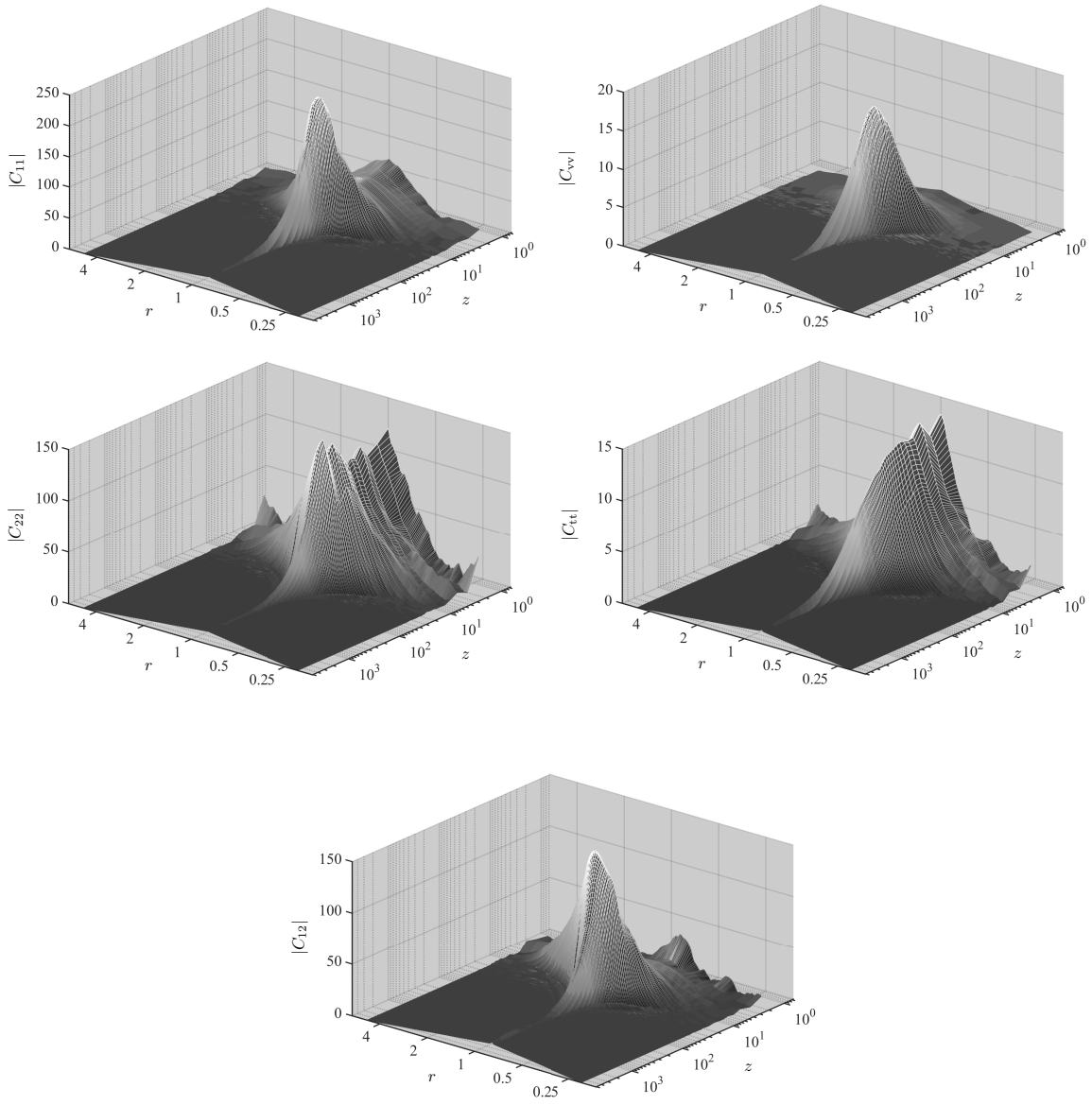

Figure 3.8: *Full set of merged scaling UETCs the matter era, calculated from the average of 7 $s = 0$ and 7 $s = 1$ runs.*

The UETCs can be decomposed into their eigenfunctions $c^n(k,\tau)$ defined through

$$\int_{\tau_\mathrm{i}}^{\tau_0} d\tau' C_{ab}(k,\tau,\tau') c_b^n(k,\tau') = \lambda_n(k) c_a^n(k,\tau). \tag{3.19}$$

Note that the eigenvalues λ_n, which are real and positive, are functions of the wavevector k. As the domain is finite, there are a countable infinity of eigenvalues for each wavevector. The UETC is recovered through the sum

$$C_{ab}(k,\tau,\tau') = \sum_n \lambda_n c_a^n(k,\tau) c_b^{n*}(k,\tau')\,. \tag{3.20}$$

Formally, the power spectra and cross-correlations of a perturbation in a cosmological variable X_a can be written

$$\langle X_a(\mathbf{k},\tau) X_b{}^*(\mathbf{k},\tau)\rangle = \frac{\phi_0^4}{V}\sum_n \lambda_n I_a^n(k,\tau) I_b^{n*}(k,\tau)\,, \tag{3.21}$$

where the contribution of each linear term, $I_a^n(k,\tau)$, is

$$I_a^n(k,\tau) = \int_{\tau_\mathrm{i}}^{\tau} d\tau' \mathcal{G}_{ab}^X(k,\tau,\tau') \frac{c_b^n(k,\tau')}{\sqrt{\tau'}}\,, \tag{3.22}$$

and $\mathcal{G}^X$ is the Green's function for the quantity X. The integration is performed numerically, using a modified version of one of the standard Einstein-Boltzmann (EB) integrators `CMBEASY` [72], `CLASS` [49, 126], or `CAMB` [127]. Hence, if UETCs are decomposed into their eigenfunctions, they can be used as sources for an EB solver, and the power spectra reconstructed by taking the sum of the power spectra obtained for each eigenfunction, weighted by the eigenvalue. In practice, the square root of the eigenvalue (which should be positive) and the eigenfunction are combined together into an object we call the *source function*.

The EB time integration range is generally much larger than the range of any conceivable defect simulation. However, the scaling property of the UETCs allows us to reconstruct the eigenvectors in an economical way. Scaling means that

$$C_{ab}(k/\sigma,\sigma\tau,\sigma\tau') = C_{ab}(k,\tau,\tau'), \tag{3.23}$$

and therefore scaling UETCs can be written as a function of two variables, which when diagonalising are most conveniently chosen to be $x = k\tau$, $x' = k\tau'$,

$$C_{ab}(k,\tau,\tau') = \bar{C}_{ab}(x,x'). \tag{3.24}$$

The overbar represents the scaling form of the UETC in a FLRW background (see Section 2.3 of the Introduction).

Scaling is an immensely valuable property, as it allows to extrapolate numerical simulations to the required cosmological scales. However, perfect scaling is not a feature of the true UETCs, as the universe undergoes a transition from radiation-dominated to matter-dominated expansion during times of interest, and more recently to accelerated expansion. Hence the UETCs also depend explicitly on τ_eq and τ_Λ, the times of equal radiation and matter density, and equal matter and dark energy density.

Strictly speaking, scaling is broken by τ_eq and τ_Λ, but given that UETCs decay quickly for

$(x, x') \gg x_\mathrm{p}$, where the peak of the UETC is $x_\mathrm{p} = \mathcal{O}(10)$, they will closely approximate radiation era scaling UETCs for $k \gg x_\mathrm{p}\tau_\mathrm{eq}^{-1}$, matter era scaling UETCs for $x_\mathrm{p}\tau_\Lambda^{-1} \gg k \gg x_\mathrm{p}\tau_\mathrm{eq}^{-1}$, and Λ-era UETCs for $x_\mathrm{p}\tau_\Lambda^{-1} \gg k$. The eigenfunctions of the scaling UETCs will approximate the true eigenfunctions under the same conditions. Scaling eigenfunctions are functions of $k\tau$, and so we infer that the eigenfunctions of the true UETCs will be well approximated by radiation era scaling eigenfunctions for $\tau \ll \tau_\mathrm{eq}$, by matter era scaling eigenfunctions for $\tau_\mathrm{eq} \ll \tau \ll \tau_\Lambda$, and Λ-era scaling eigenfunctions for $\tau_\Lambda \ll \tau$.

These observations underlie our discussion of methods to construct the true eigenfunctions from the scaling UETCs, which are derived from numerical simulations as discussed above. We will discuss two existing methods, based on interpolating between sets of eigenfunctions in time, and introduce a third, which interpolates between UETCs in k-space. The new method is superior: it reproduces better the actual (non-scaling) UETC during the radiation-matter transition, which we have measured for the first time, and also maintains the orthogonality of the approximate eigenfunctions.

3.2.1 Simple eigenvector interpolation

In the simple eigenvector interpolation method [42, 45, 78], scaling UETCs are extracted from radiation and matter cosmologies separately. Each correlator is diagonalised to obtain two sets of eigenfunctions.

The diagonalisation proceeds by sampling the numerically measured UETCs $\bar{C}_{ab}(x, x')$ at a number of values of x in the range available from the numerical simulations. For the results from our 4k simulations we took $N_\mathrm{i} = 2048$ linearly spaced values in the interval $0.6 \leq (x, x') \leq 2300$.

The two sets of eigenvectors, one from the radiation era and one from the matter era, are ordered by the magnitude of their eigenvalues, so that the first ones correspond to the most important contributions. We assume that the eigenvectors ordered by eigenvalue size form matching pairs (one from radiation with one from matter), and choose their relative sign by requiring that the scalar product of the two eigenvectors is positive. Through this pairing we then define the source function for the EB integrator as

$$\sqrt{\lambda_n} c_n(k, \tau) = e_\Lambda(\tau) \left(e(\tau) \sqrt{\lambda_n^\mathsf{R}} c_n^\mathsf{R}(x) + (1 - e(\tau)) \sqrt{\lambda_n^\mathsf{M}} c_n^\mathsf{M}(x) \right). \tag{3.25}$$

Note that the eigenfunctions at Λ domination are assumed to be zero. The eigenvector interpolation functions $e(\tau)$ and $e_\Lambda(\tau)$ for radiation-matter and matter-Λ transitions respectively are taken to be [42, 45],

$$e(\tau) = \frac{1}{1 + \chi[a(\tau)]}, \tag{3.26}$$

$$e_\Lambda(\tau) = \frac{1}{1 + \chi_\Lambda[a(\tau)]}, \tag{3.27}$$

where $\chi[a] = a\Omega_\mathrm{m}/\Omega_\mathrm{r}$ and $\chi_\Lambda[a] = a^3\Omega_\Lambda/\Omega_\mathrm{m}$ are the ratio between the density fractions at the given value of the scale factor.

For a given k, the source function is defined only at a set of times which are in general not those used by the EB integrator. The values of $\sqrt{\lambda_n} c_n(k, \tau)$ at an arbitrary time τ are found by spline interpolation, with all eigenfunctions set to zero at $\tau = 0$ and for $x > 2000$.

Recently some inconsistencies of this approach have been highlighted [86]. First, the signs of a set of eigenvectors are undetermined, and so a rule must be applied to decide on the relative sign when interpolating between a radiation-era eigenvector and a matter-era one. As described

above, the nth radiation and the nth matter eigenvectors are matched, and their relative sign chosen so that their scalar product is positive. Abrupt jumps in the shape of the functions are reduced, although the qualitative similarity between the two matched eigenvectors does not hold in all cases. However, if one goes beyond the nth to nth eigenvector sign matching and explores the whole eigenvector scalar product space, usually there are cases where the nth eigenvector in radiation has the biggest scalar product (≈ 1) with the mth eigenvector in matter ($n \neq m$). Even worse, for the higher eigenvectors there is often no clear partner and the matching scheme breaks down.

Finally, even if eigenvectors can be paired off successfully, the set of interpolated source functions are not in general orthonormal, and therefore not eigenvectors.

3.2.2 Multi-stage eigenvector interpolation

A second method of generating a set of source functions [86] (see also [155]), which we call multi-stage eigenvector interpolation, improves on simple eigenvector interpolation by generating a set of linear combinations of the pure radiation and pure matter UETCs, whose eigenvectors can be more easily matched. We write the "transition" UETCs as

$$C_i^{\mathrm{RM}}(k\tau, k\tau') = f_i \bar{C}^{\mathrm{R}}(k\tau, k\tau') + (1 - f_i)\bar{C}^{\mathrm{M}}(k\tau, k\tau')\,, \tag{3.28}$$

with $0 \leq i \leq N_{\mathsf{U}}$, $f_0 = 1$, $f_{i+1} < f_i$, and $f_{N_{\mathsf{U}}} = 0$. For every transition UETC C_i^{RM} we will have a set of orthonormal eigenvectors. We can have as many transition UETCs as we want: in practice we choose N_{U} so that there is no arbitrariness in the eigenvector matching left: the scalar products between the ith and the $(i+1)$th sets of eigenvectors are close to one or close to zero. Each set of eigenvectors $c_i^n(k\tau)$ can then be uniquely mapped to its neighbours $i-1$ and $i+1$, with $i = 0$ being the pure radiation eigenvectors and $i = N_{\mathsf{U}}$ the pure matter eigenvectors.

We then divide up the radiation-matter transition era into $N_{\mathsf{U}} + 1$ intervals with a set of N_{U} times τ_i, and define a monotonically decreasing interpolating function $f(\tau)$, which will define the linear combination in (3.28) according to

$$f_i = f(\tau_i). \tag{3.29}$$

We discuss the interpolating function in Section 3.2.4.

The transition basis functions $c^n(k,\tau)$ are then defined from the set of eigenvectors $c_i^n(k\tau)$ with the help of a set of indicator functions $J_i(\tau)$

$$\begin{aligned} J_0(\tau) &= \begin{cases} 1 & 0 \leq \tau \leq \tau_1 \\ 0 & \text{otherwise} \end{cases}, \\ J_i(\tau) &= \begin{cases} 1 & \tau_i \leq \tau \leq \tau_{i+1} \\ 0 & \text{otherwise} \end{cases}, \\ J_{N_{\mathsf{U}}}(\tau) &= \begin{cases} 1 & \tau_{N_{\mathsf{U}}} \leq \tau \leq \infty \\ 0 & \text{otherwise} \end{cases}. \end{aligned} \tag{3.30}$$

The source functions are then

$$\sqrt{\lambda_n} c^n(k,\tau) = \sum_{i=0}^{N_{\mathsf{U}}} J_i(\tau) \sqrt{\lambda_{n,i}} c_i^n(x)\,. \tag{3.31}$$

We see that the simple eigenvector interpolation is related to multi-stage interpolation with $N_{\mathsf{U}} = 1$, and would be identical with a step function $e(\tau)$.

This process can also be generalized in the obvious way to take into account the transition from matter domination to Λ domination.

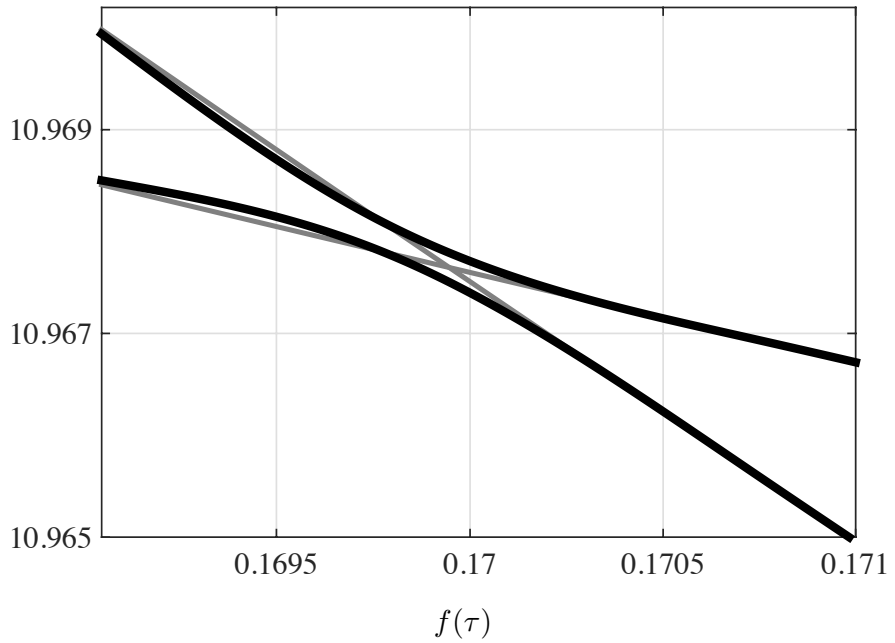

Figure 3.9: *Evolution of the 34$^{\text{th}}$ and 35$^{\text{th}}$ eigenvalues of the tensor correlator, as a function of the interpolation parameter f (Eq. (3.28)). The thin grey lines show eigenvalue crossings, which happen when the time region is divided into few intervals (in this case, 3 intervals). The thick black line, on the other hand, represents the situation when the time region is divided into 18 intervals. It is apparent that the eigenvalues avoid crossing each other, as they should.*

Before discussing the choice of the function $f(\tau)$, we study how the eigenvectors evolve with f, the parameter determining the linear combination of the UETCs according to Eq. (3.28). In particular we can check that a radiation eigenvector evolves into a unique matter eigenvector. We can also plot the value of the corresponding eigenvalue. As each eigenvector is uniquely associated to its eigenvalue, and as the eigenvalues evolve also in a continuous way with f, the order of matching eigenvectors can only change if the associated eigenvalues cross along their evolution. However, the eigenvalues of a Hermitian matrix which is a continuous function of a parameter f do not in general cross, unless a symmetry appears at a particular value of f. Hence we can expect that the eigenvectors can be uniquely ordered and matched by their eigenvalues.

In order to illustrate this point, we show explicitly an example in Fig. 3.9, where we consider the 34$^{\text{th}}$ and 35$^{\text{th}}$ eigenvalues of the tensor correlator. Judging only by the scalar product method of the corresponding eigenvectors, the eigenvector corresponding to the larger eigenvalue on the left (34$^{\text{th}}$) has the largest dot-product with the eigenvector of the lowest eigenvalues on the right (35$^{\text{th}}$). Following the eigenvalue evolution, they appear to cross. If we split this time region into three intervals, and perform a UETC interpolation, we find exactly the same situation (thin grey lines). However, if we split the time region into more intervals (in our example, 18) to perform the UETC interpolation, the crossing of the eigenvalues is avoided. This is apparent in the eigenvalue

evolution: the lines repel (thick black lines).

We conclude that we can select an eigenvector c_i^n unambiguously in the sum (3.31), and that corresponding eigenvectors can be found by ordering them by eigenvalue $\lambda_{n,i}$, and that there is no ambiguity about the construction of the source function $\sqrt{\lambda_n} c_a^n(k,\tau)$. However, the source functions are still not orthogonal, a property which is possessed by the eigenfunctions of the true UETC. We will see how the third method addresses this problem in the next section.

3.2.3 Fixed-k UETC interpolation

Going back to the whole (non-scaling) UETCs $C_{ab}(k,\tau,\tau')$ we see that it is natural to think of them as symmetric functions of τ and τ' for a given k. They contain the full information about the cosmic transitions, and can be discretised and then diagonalised as discussed above. This approach also fits very naturally into the scheme used by Einstein-Boltzmann codes, which solve the perturbation equations with an outer loop over k and an inner time integration for fixed values of k.

In fixed-k UETC interpolation we construct approximations to $C_{ab}(k,\tau,\tau')$ from the scaling matter and radiation sources, at each value of k. The relative mixture of matter and radiation UETCs is determined by $\tau/\tau_{\rm eq}$ and $\tau'/\tau_{\rm eq}$. First, we display how a real UETC changes with k in Fig. 3.10. The figure shows C_{11} obtained from our seven transition era simulations, plotted against $(\tau/\tau_{\rm eq}, \tau'/\tau_{\rm eq})$, for the values of $k\tau_{\rm eq} \simeq 600$, 10 and 1.

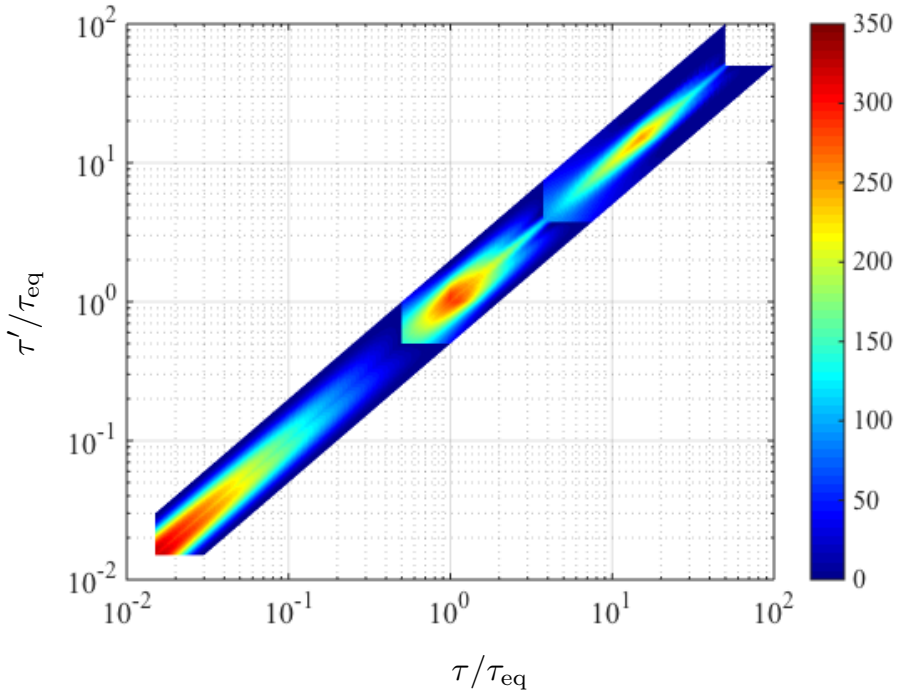

Figure 3.10: *The UETC C_{11} plotted for values of $k\tau_{\rm eq}$ nearest to 600, 10 and 1, obtained from the radiation-matter transition simulations listed in Table 3.6.*

To obtain this graph, we simulated string networks at intermediate stages of the radiation-

matter transition, where the scale factor evolves as

$$a(\tau) = a_{\rm eq}\left(\left[\left(\sqrt{2}-1\right)\left(\frac{\tau}{\tau_{\rm eq}}\right)+1\right]^2-1\right). \tag{3.32}$$

These 1k (1024^3) numerical simulations had the same Lagrangian parameters as the 4k simulations, with lattice spacing $dx = 0.5$, core growth parameter $s = 0$, and the same $\tau_{\rm start}$ and $\tau_{\rm diff}$. There is limited range between the time when correlator data taking starts at $\tau_{\rm ref} = 150$ and the end of the simulation $\tau_{\rm end} = 300$, so each simulation spans only a part of the transition. UETC and ETCs are written at $N_\tau = 50$ logarithmically-spaced intervals between these times.

We performed five independent simulations for seven values of $\tau_{\rm eq}$ ($N_{\tau_{\rm eq}} = 7$), so that the simulations covered most of the transition epoch. Table 3.6 shows the values of $\tau_{\rm eq}$ and the time periods that we have simulated, five of which are used in Fig. 3.12. We also give the expansion rate parameter

$$\alpha(\tau) = \frac{d\ln a}{d\ln\tau}. \tag{3.33}$$

$\tau_{\rm eq}$	600	300	150	80	40	10	3
$\tau_{\rm ref}/\tau_{\rm eq}$	0.25	0.5	1.0	1.875	3.75	15	50
$\tau_{\rm end}/\tau_{\rm eq}$	0.5	1.0	2.0	3.75	7.5	50	100
$\alpha(\tau_{\rm ref})$	1.05	1.09	1.17	1.28	1.44	1.76	1.91
$\alpha(\tau_{\rm end})$	1.09	1.17	1.29	1.44	1.60	1.86	1.95

Table 3.6: *Selected parameters for simulations across the radiation-matter transition. The parameters are $\tau_{\rm eq}$ in units of ϕ_0^{-1}, the ratio of the reference time $\tau_{\rm ref}$ for UETC data-taking and the simulation end time $\tau_{\rm end}$ to $\tau_{\rm eq}$, and the expansion rate parameters $\alpha = d\ln a/d\ln\tau$ at $\tau_{\rm ref}$ and $\tau_{\rm end}$. In the simulations with constant α (see Section 3.2.4), we take the value of α at $\tau_{\rm ref}$.*

In Fig. 3.10, data is taken from the unique UETC which contains a value of k whose product with each of the seven values of $\tau_{\rm eq}$ is nearest to the chosen values 600, 10 and 1. For each of these three values of $k\tau_{\rm eq}$, we therefore have a $N_{\tau_{\rm eq}} \times N_\tau$ array. We plot this array with $\tau' = \tau_{\rm ref}$, and also its transpose.

The general behaviour as a symmetric function peaked near $(\tau/\tau_{\rm eq}, \tau'/\tau_{\rm eq}) \sim (10/k\tau_{\rm eq}, 10/k\tau_{\rm eq})$ is clear. It is also clear that the height of this peak makes a smooth transition from higher values at $k\tau_{\rm eq} \gg 1$, where the UETC resembles the UETC in a radiation-dominated universe, to lower values at $k\tau_{\rm eq} \ll 1$, where the UETC resembles the UETC in a matter-dominated universe.

A proposal for the UETCs which models this behaviour across the radiation-matter transition is

$$C_{ab}(k,\tau,\tau') = f\left(\frac{\sqrt{\tau\tau'}}{\tau_{\rm eq}}\right)\bar{C}^{\rm M}_{ab}(k\tau,k\tau') + \left(1-f\left(\frac{\sqrt{\tau\tau'}}{\tau_{\rm eq}}\right)\right)\bar{C}^{\rm R}_{ab}(k\tau,k\tau'). \tag{3.34}$$

This is manifestly symmetric in τ,τ'. It approximates the UETC in the entire region $\tau\tau' \sim \tau_{\rm eq}^2$ by the linear combination of pure radiation and pure matter era scaling correlators at extreme values of $\tau/\tau_{\rm eq}$. At sufficiently unequal times bracketing $\tau_{\rm eq}$ the true UETC may depart significantly from the model, but this should not matter in practice as the UETC is very small there for any

value of k. We will see in Sect. 3.2.6 that of the UETCs reconstructed from the source functions, the fixed-k UETC interpolation method gives the most accurate results.

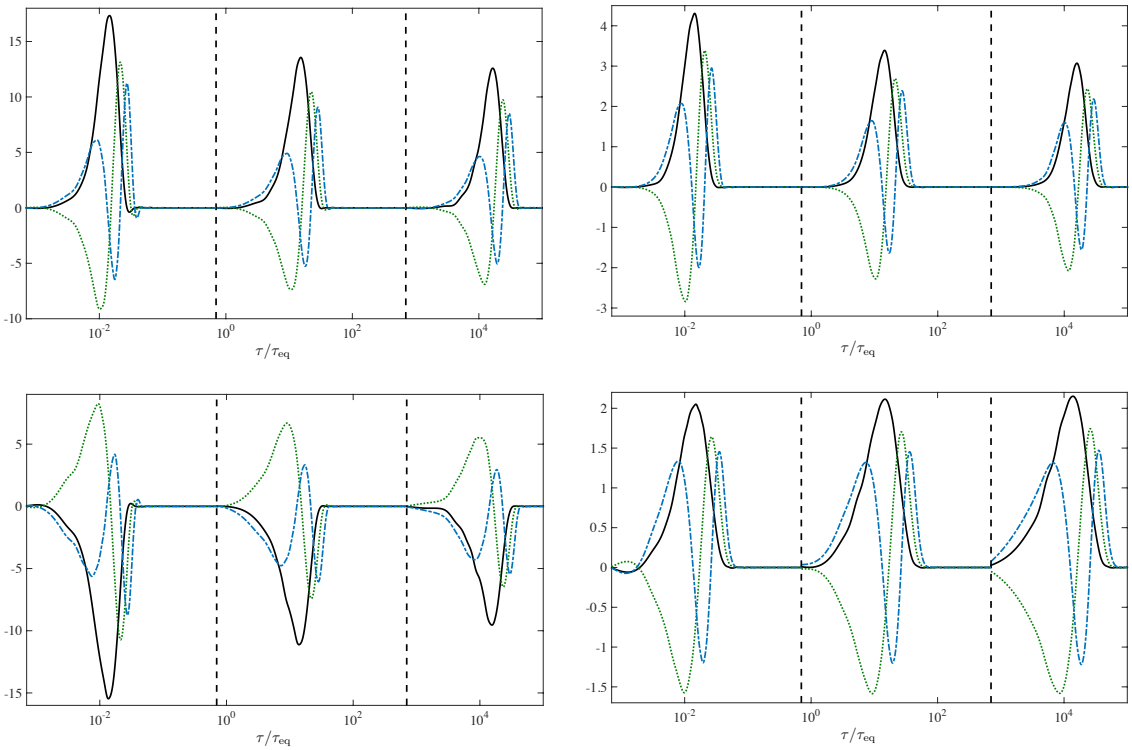

Figure 3.11: *First (black solid line), second (green dotted line) and third (blue dash-dotted line) source functions for $k\tau_{eq} = 1000,\ 1$ and 0.001 from left to right. The two left figures show scalar ϕ (upper pane) and ψ (lower pane) components, whereas the top-right figure is for vector and the bottom-right one for tensors.*

We note that the source functions for the EB integrators at a given k are now just the eigenvectors of these model UETCs, multiplied by the square root of the associated eigenvalues, and so they are indeed orthogonal, unlike in the previous two methods. In Fig. 3.11 we show the first three source functions extracted by this method as a function of $\tau/\tau_{\rm eq}$, for $k\tau_{\rm eq} = 1000,\ 1$ and 10^{-3}. The corresponding UETCs are therefore largest in the radiation, transition, and matter eras respectively. It can be seen that the source functions are indeed peaked in different ranges of τ, at around $\tau \sim 10/k$, and that the peak amplitude decreases as k gets smaller, consistent with the matter-era UETCs having a smaller amplitude that the radiation era ones.

3.2.4 Interpolating functions $f(\tau)$ and $f_\Lambda(\tau)$

We adopt the recipe given in [86] to define the interpolating function such that it reproduces the equal-time correlators $E_{ab}(k,\tau) = C_{ab}(k,\tau,\tau)$. First we define

$$f_{ab}(k,\tau) = \frac{E^{\rm RM}_{ab}(k,\tau) - \bar{E}^{\rm M}_{ab}(k\tau)}{\bar{E}^{\rm R}_{ab}(k\tau) - \bar{E}^{\rm M}_{ab}(k\tau)} \qquad \forall k\,, \tag{3.35}$$

where $\bar{E}^{\rm R}(k\tau)$ and $\bar{E}^{\rm M}(k\tau)$ are the scaling ETCs in the radiation and matter eras respectively, and $E^{RM}(k,\tau)$ is the true ETC during the transition.

Parameters	E_{11}	E_{12}	E_{22}	$E_{\rm vv}$	$E_{\rm tt}$	Mean and σ
ζ	0.232 ± 0.006	0.244 ± 0.012	0.246 ± 0.010	0.242 ± 0.006	0.203 ± 0.010	0.235 ± 0.004
η	-1.01 ± 0.02	-1.01 ± 0.04	-1.03 ± 0.03	-0.96 ± 0.01	-1.10 ± 0.05	-0.984 ± 0.008

Table 3.7: *Mean values together with the standard deviations for the parameters ζ and η of Eq. (3.36) needed to reproduce the radiation-matter transition.*

We will see that the functions $f_{ab}(k,\tau)$ extracted from our simulations are consistent with being independent of k and thus the above definition will reproduce Eq. (3.28) when evaluated at equal times. We will also see that it is a good approximation to take the same function $f(\tau)$ for each of the five ETCs.

We extracted ETCs from 1k simulations with $\tau_{\rm eq} = 3$, 10, 40, 150 and 300, and used Eq. (3.35) to compute the function $f(\tau)$. As illustrative examples, Fig. 3.12 shows the results obtained for correlators E_{11} and $E_{\rm vv}$; the results for the other correlators are very similar. The five grey shaded regions represent the raw transition functions (3.35) obtained during the five transition periods simulated. The two grey levels indicate 1σ and 2σ deviations from the mean value calculated averaging over a set of wavevectors much less than the inverse string width: $0.12 < |\mathbf{k}| < 2$. We also include in the pictures the best-fit line (solid red line) obtained fitting data using the following functional form:

$$f(\tau) = \left(1 + \zeta \frac{\tau}{\tau_{\rm eq}}\right)^{\eta} . \tag{3.36}$$

The narrowness of the shaded regions confirms the initial assumption of the scale independence of the function.

Table 3.7 shows the mean values and standard deviations for the parameters of Eq. (3.36); it is clear that the transition applies in a very similar form for all correlators, implying that they evolve in a similar way across the transition. In order to simplify further calculations we consider the following function as the radiation-matter transition UETC interpolation function that applies equally to all correlators of the Abelian-Higgs cosmic string model:

$$f(\tau) = \left(1 + 0.24 \frac{\tau}{\tau_{\rm eq}}\right)^{-0.99} , \tag{3.37}$$

We note that function (3.37) is almost the square root of the interpolation function for large-N self-ordering scalar fields obtained in [86]

$$f_N(\tau) = \left(1 + \frac{1}{4} \frac{\tau}{\tau_{\rm eq}}\right)^{-2} . \tag{3.38}$$

The conjecture [86] that the interpolation function is universal is therefore not supported by our findings.

We also compared the transition-era ETCs at time τ_n with scaling ETCs evaluated with a constant expansion rate parameter $\alpha(\tau_n)$. We performed five simulations with constant α chosen to coincide such that the expansion rate fell within the range of expansion rates explored by our

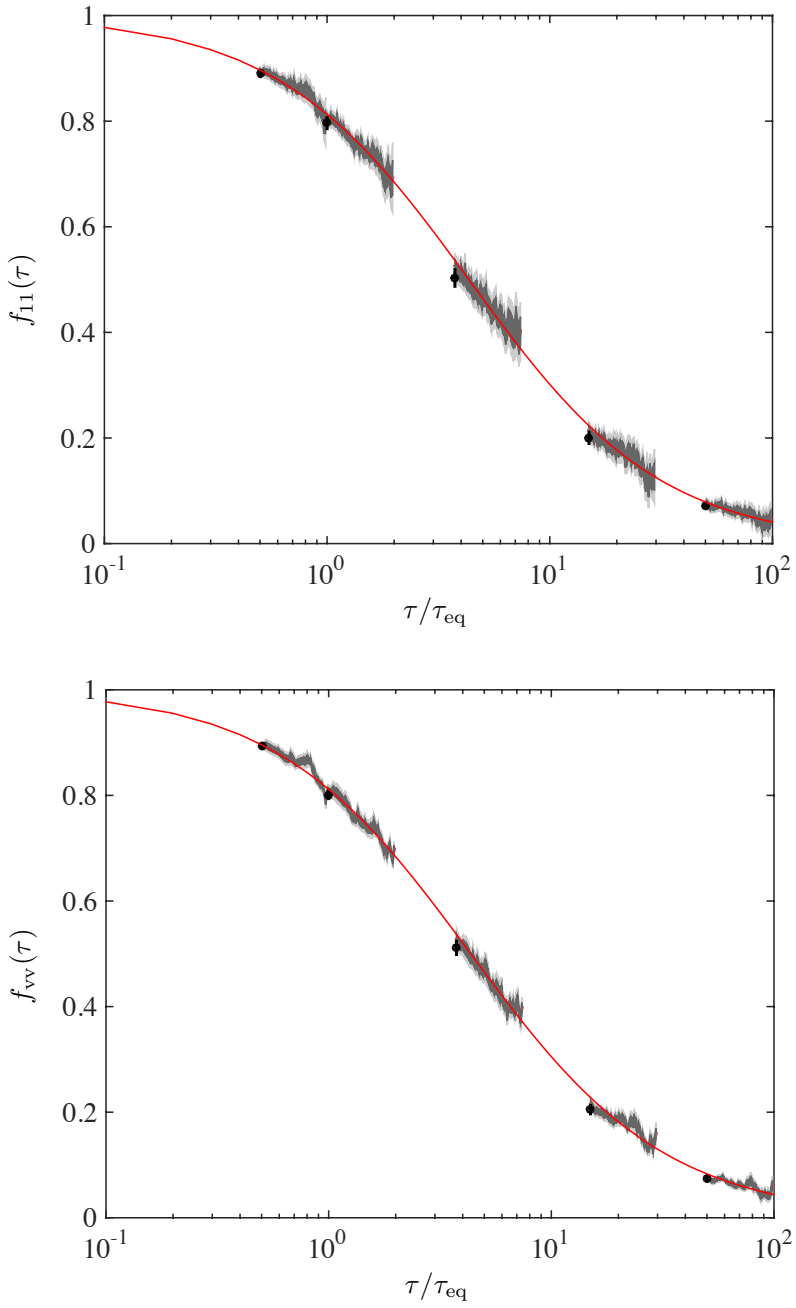

Figure 3.12: *UETC interpolation functions derived from simulations performed during the radiation-matter transition (thick grey line). The five patches correspond to simulations with* $\tau_{\rm eq} = 3,\ 10,\ 40,\ 150$ *and* 300*. The shaded regions represent the* 1σ *and* 2σ *deviations from the mean value of the function obtained from Eq. (3.35) calculated from the averaging over* k*. In the upper pane the correlator used is* E_{11}*, while in the lower pane is* $E_{\rm vv}$*. The red line, in both cases, corresponds to the best-fit function obtained using the functional form of Eq. (3.36). The black points (with error bars) correspond to constant* α *simulations, which would mimic the adiabatic cosmology transition.*

simulations across the radiation-matter transition (values can be found in Table 3.6). Defining

$$f_{ab}^{\alpha}(k,\tau) = \frac{\bar{E}_{ab}^{\alpha}(k\tau) - \bar{E}_{ab}^{\mathrm{M}}(k\tau)}{\bar{E}_{ab}^{\mathrm{R}}(k\tau) - \bar{E}_{ab}^{\mathrm{M}}(k\tau)}, \tag{3.39}$$

we can plot the average values of f_{ab}^{α} in Fig. 3.12, where the five points (black dot points with corresponding 1σ bars obtained from k-averaging) come from the constant expansion rate simulations.

Interestingly, the best-fit function lies almost on top of the constant expansion rate points f^{α}. We therefore conclude that the string network reacts quickly to changes in the expansion rate, and we can treat the ETCs as being adiabatic: in other words, the properties of the string network at any given time during the radiation-matter transition corresponds well to the properties of a scaling network at the same instantaneous expansion rate. In principle we expect the same behavior for other types of defects, therefore, a good approximation could be found by performing a series of smaller/shorter simulations at intermediate constant expansion rates.

3.2.5 Matter-Λ interpolation

We also applied the same procedure to incorporate the effects of the accelerated expansion of our universe, extending our analysis to the matter-Λ transition. In a Λ dominated universe, one expects the string velocity to decay and the network effectively to freeze with a length scale ξ_{fr}.

The metric perturbations induced by a straight string moving with a velocity v were computed in [151], and from the expressions in that article we can see that for $v \to 0$ the scalar potential ψ as well as the vector perturbations vanish, while the scalar potential ϕ and the tensor perturbations remain finite. Based on this we expect that the tensor and the E_{11} UETCs do not vanish, while E_{12}, E_{22} and E_{vv} go to zero.

Therefore, the counterpart of Eq. (3.35) is

$$f_{ab}(k,\tau) = \frac{E_{ab}^{\mathrm{M}\Lambda}(k,\tau) - \bar{E}_{ab}^{\Lambda}(k\tau_{\mathsf{fr}})}{\bar{E}_{ab}^{\mathrm{M}}(k\tau) - \bar{E}_{ab}^{\Lambda}(k\tau_{\mathsf{fr}})}, \tag{3.40}$$

where τ_{fr} is a time derived from the length scale ξ_{fr} of a frozen string network in de Sitter space, and $\bar{E}_{12}^{\Lambda} = \bar{E}_{22}^{\Lambda} = \bar{E}_{\mathrm{vv}}^{\Lambda} = 0$. We show the decay of the correlators $E^{\mathrm{M}\Lambda}(k,t)$ in Fig. 3.13, based on simulations evolving in a ΛCDM background. These simulations covered mainly the late matter dominated era and the beginning of the dark energy domination. Table 3.8 shows the cosmological parameters at the end of each of the regimes simulated. We have been able to go farther towards the ΛCDM singularity where the conformal time reaches its asymptotic de Sitter value, and where therefore the scale factor diverges as a function of τ (around $\tau \approx 1.35\tau_0$ for a value of $\Omega_m = 0.315$). As our estimate of the de Sitter correlators we measure the functions $\bar{E}_{11}^{M\Lambda}$ and $\bar{E}_{\mathrm{tt}}^{M\Lambda}$ at $\tau_{\mathsf{end}} = 1.33$, and take $\tau_{\mathsf{fr}} = \beta^{-1}\xi_{\mathsf{fr}}$, where β is the slope of the relation between time and network length scale (see Eq. (3.8)), and we use its value during the matter era, given in Table 3.2.

The interpolation functions related to each of the different correlators can be fitted by the following set of functions:

$$f^{\Lambda}(\tau) = \left(1 + \zeta\left(\frac{\tau}{\tau_0}\right)^{\eta}\right), \tag{3.41}$$

where the best fits of the parameters ζ and η for each case are shown in Table 3.9.

τ_0	300	225
$\tau_{\rm ref}/\tau_0$	0.5	0.665
$\tau_{\rm end}/\tau_0$	1	1.33
$\Omega_m(\tau_{\rm end})$	0.315	$1.29 \cdot 10^{-4}$
$\Omega_r(\tau_{\rm end})$	$9.24 \cdot 10^{-5}$	$2.81 \cdot 10^{-9}$

Table 3.8: *Values of the current conformal time τ_0 in simulation time units, the ratio of the reference time $\tau_{\rm ref}$ for UETC data-taking and the simulation end time τ_{end} to τ_0. Also given are the cosmological parameters $\Omega_{\rm m}$ and $\Omega_{\rm r}$ at the end of each simulation across the matter-Λ transition.*

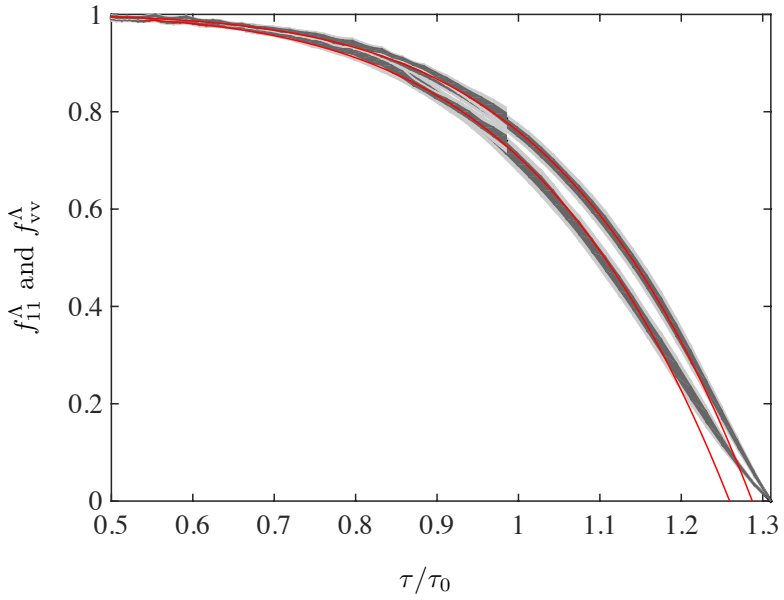

Figure 3.13: *Matter-Λ UETC interpolation function for different correlators plotted against the conformal time relative to current time (τ_0), from top $E_{\rm vv}$ and bottom E_{11}. The other two scalar correlators, E_{12} and E_{22}, lie roughly between the two red lines. The different shades correspond to 1σ and 2σ confidence limits, and the red line corresponds to the best fit.*

Parameters	E_{11}	E_{12}	E_{22}	$E_{\rm vv}$	$E_{\rm tt}$
ζ	-0.302±0.003	-0.276±0.003	-0.292±0.003	-0.241±0.001	–
η	5.2±0.1	5.4±0.1	5.3±0.1	5.63±0.03	–

Table 3.9: *Best fit values for parameters ζ and η in Eq. (3.41) corresponding to the Matter-Λ transition function.*

It can be seen that there is greater variation in the parameters than in the radiation-matter case. Note that $E_{\rm tt}$ changes little during the transition and so the errors in $f_{\rm tt}$ are very large. Hence it is a good approximation not to interpolate $E_{\rm tt}$ at all.

We can anticipate that the effect of taking into account a ΛCDM background cosmology will slightly decrease the amplitude of the late time correlators. Consequently, this decay will affect the power spectra at lower multipoles, decreasing the contribution at scales that entered late the

horizon.

3.2.6 Comparison of interpolation methods

In this section we compare simple and multistage eigenvector interpolation, as used in [42] and [86], with the fixed-k UETC interpolation introduced in this paper. We perform the comparison by reconstructing the UETC from the interpolated source functions

$$C^{\rm rc}(k,\tau,\tau') = \sum_n \lambda_n c_n(k,\tau) c_n^*(k,\tau'). \tag{3.42}$$

This is then compared with a measured transition correlator. We choose an intermediate stage of the radiation-matter transition, $1 < \tau/\tau_{eq} < 1.5$ and restrict the analysis to scales around the peak of the correlator ($8.3 < k\tau < 30$), where the most important contribution is encapsulated. Note that though the eigenvectors of the time-interpolated UETCs do not strictly form an orthonormal set, their product forms an effective UETC, see Eq. (3.42). Time evolving eigenvectors for the eigenvector interpolation method, in turn, are calculated using (3.25) and (3.26).

We show in Fig. 3.14 the relative difference of the reconstructed UETC using 128 eigenvectors for the scalar C_{11} function for the three proposed methods. There can be seen that the resemblance of the fixed-k interpolation to the real case is the highest and is clearly better than the multi-stage eigenvector interpolation method, which is in turn better than simple eigenvector interpolation. The values of the relative differences at $z = 10$, near the peak of the UETCs, are approximately 0.03, 0.09, and 0.2 respectively.

3.3 New power spectra and error assessment

In this section we present updated CMB power spectra contributions from AH cosmic string. The power spectra have been calculated using the source enabled version of `CMBEASY` [72]. In order to account for source functions of the multi-stage eigenvector and fixed-k UETC interpolation methods the program has been additionally modified. The cosmological parameters used for these calculations are the best-fit values obtained by the *Planck* collaboration [21]: $h = 0.6726$, $\Omega_{\rm b}h^2 = 0.02225$, $\Omega_\Lambda = 0.6844$ and optical depth to last-scattering $\kappa = 0.079$. As it has been mentioned previously, we interpolate UETC matrices to $N_{\rm i} = 2048$ points. After the diagonalisation, the total contribution of strings to temperature and polarization anisotropies is calculated summing the contribution of each individual source function. We observe that convergence of 1% is obtained for ~ 200 eigenvectors and so as to avoid uncertainties we set the standard number of eigenvectors to 256.

This section contains the final power spectra and their corresponding error assessments obtained bootstrapping over realizations in the merging process. However, its aim is not only to present those new results, but also to analyze separately the changes introduced by the innovations proposed during this work. Therefore, we compare the differences introduced by the new UETCs from the real equations of motion, which are described by the new merged structure, with the previous CMB predictions from [45]. On the other hand, the new cosmological transition handling has been one of the most important and innovative aspects of this work, hence we also want to measure the changes created by the incorporation of the new interpolation framework as well as by the new interpolation functions. In this sense, we compare multistage and fixed-k interpolation methods with each other and with the simple eigenvector interpolation method. The effects produced by the new matter-Λ transitions are also studied.

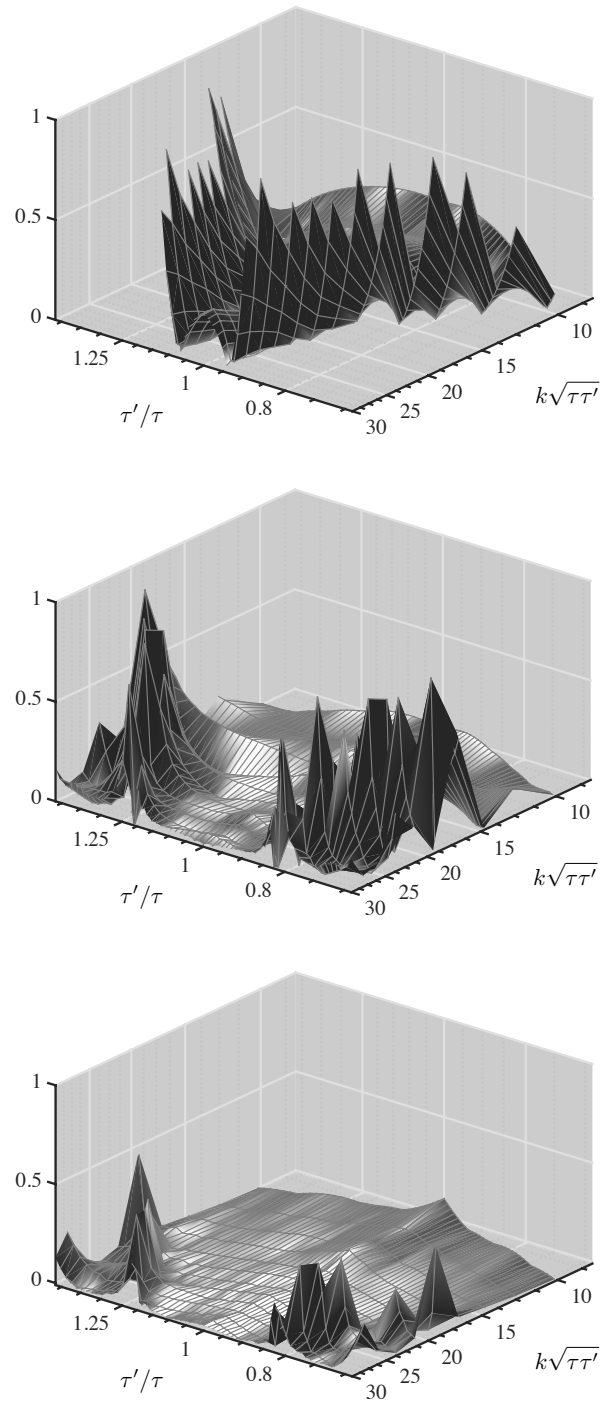

Figure 3.14: *Relative difference of the reconstructed scalar C_{11} UETC with respect to the measured UETC. The UETCs are reconstructed using three different methods: simple eigenvector interpolation (first pane), multi-stage eigenvector interpolation (second pane) and fixed-k UETC interpolation (third pane). In the simple eigenvector interpolation method the interpolating function is (3.26), whereas for the multi-stage eigenvector interpolation at the correlator level we use (3.37). Only the region around the peak of the correlator, $1/1.5 < r < 1.5$ and $8.3 < k\tau < 30$, is shown. Note that in order to represent the relative difference as neatly as possible, we remove values greater than 1 from the two top pictures.*

3.3.1 Comparison with 2010: $s = 1$

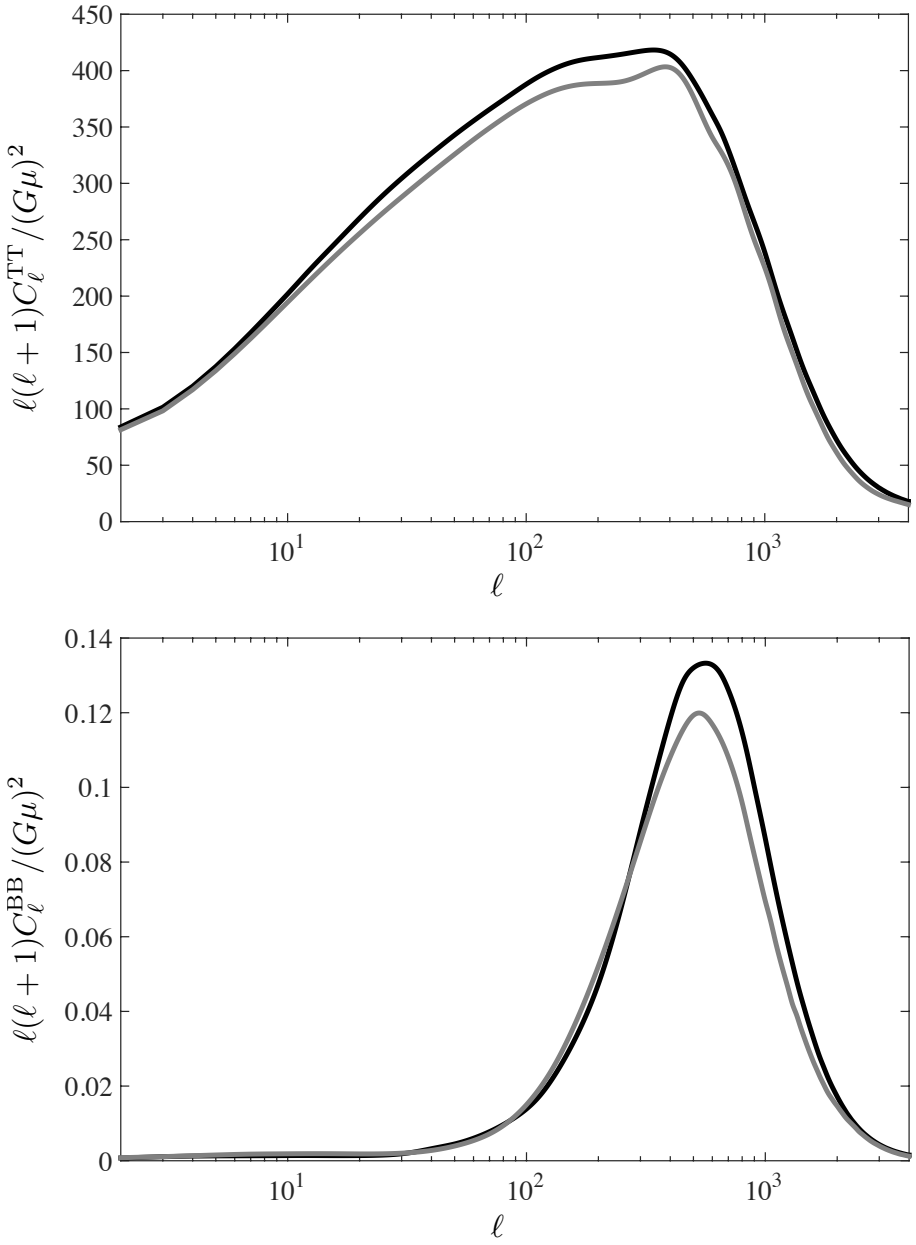

Figure 3.15: *Comparison of the spectra obtained in [45] (grey line) and in this work (black line). The latter are obtained using UETCs from new simulations constructed following the merging scheme and interpolating eigenvectors by the simple eigenvector interpolation method.*

Energy-momentum correlations of this work have been derived from the biggest field theoretical simulation of AH cosmic string to date. Current simulations cover a spatial patch 64 times bigger than in [45], thus we have been able to simulate for four times longer and scales that previous works could only reproduce by extrapolation can now be directly simulated. Specifically, new simulations extend the data both in low and high wavenumber, measuring more accurately horizon scale correlations and the small scale power-law behavior. Moreover, it has been possible to reproduce

the real equation of motion, *i.e.* $s = 1$, and reach the scaling regime both in matter and radiation domination eras. Everything is taken into account in the new merged UETC functions.

In this section we compare the changes produced by the new set of UETCs, produced by the new merging method, and the previous CMB predictions form [45]. The aim of this comparison is to capture the effect created by the change in data obtained from new simulations and separate it from the eigenvector derivation method. This is why the spectra of this section have been calculated using the same simple eigenvector interpolation method used in [45], where transition is driven by a density weighted interpolation function (see Eq. (3.25), (3.26) and (3.27)).

Figure 3.15 shows the comparison of the temperature and B-modes for this case. The 2010 spectra are in grey whereas the new ones in black. As it can be seen the difference is not significant: only the peaks in both channels are slightly increased, which can be a direct consequence of higher correlators. Note also that the new spectra are smoother and the small details around the peak of the temperature spectrum have disappeared. Considering the new UETCs are derived from the biggest simulations of the AH model to date and from the real equations of motion ($s = 1$), it is noteworthy to highlight that the 2010 guesses are remarkably accurate.

3.3.2 Effects of the new radiation-matter transition function and multi-stage method

Once having determined the effect caused by the new UETC data, the next effect to study is the multi-stage cosmological transition treatment and the new interpolation function of Eq.(3.37). From here on, all spectra are calculated using the new merged $s = 1$ and $s = 0$ dataset. The multi-stage interpolation method was proposed in [86] and it interpolates between eigenvectors of UETCs calculated at intermediate time intervals between radiation and matter, see Eq. (3.28). The most important difference comes from the fact that now we have an orthonormal set of eigenvectors at each time slicing, while in the simple eigenvector interpolation method only the eigenvector of the pure radiation and matter correlators are considered. Regarding the interpolation function, the density weighted interpolation function has been substituted by an ETC weighted interpolation function Eq. (3.37), which has been calculated following the recipe of Eq. (3.35). The matter-Λ transition will be analyzed in the next section.

We show the comparison for this case in Figure 3.16. The spectra obtained by the simple eigenvector interpolation method is represented in black and the multi-stage case in green. For the multi-stage case we observe that $N_{\rm U} = 11$ time slices are enough to reach convergence. As it can be seen in Fig. 3.16, in contrast to the previous case, the differences are substantial. The most drastic change is the increase of the amplitude of the spectra both in temperature and in B-mode channels. The matter-radiation transition depicted by the ETCs and described by $f(\tau)$, is much slower than previous transition functions. The slower transition reflects in more contribution to the total from radiation correlators, which are higher in amplitude than the matter ones.

Table 3.10 shows the percentual changes of the height of the peak for the different UETC interpolation methods with respect to the simple eigenvector interpolation. It reflects that the increase affects all channels, but more considerably the polarization channels, which is a signal that the slower transition affects in higher degree vector and tensor perturbations than scalars.

3.3.3 Effects of the matter-Λ transition function

The effect of including the matter-Λ transition with its corresponding ETC based interpolation function function (Eq. (3.41) and Table 3.9) is represented in Figure 3.17, where the spectra that includes this latter transition is plotted in red against the case without Λ transition in

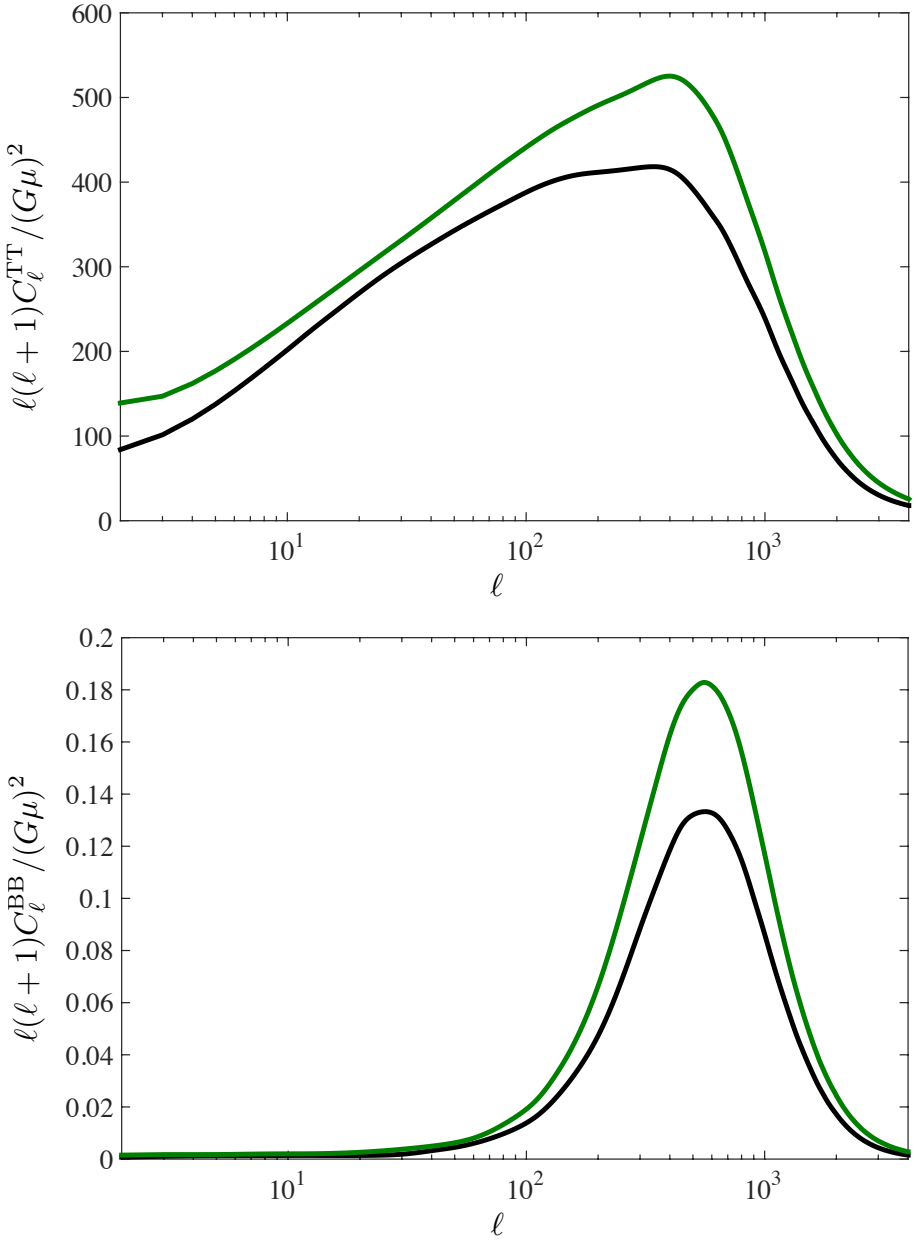

Figure 3.16: *Comparison of spectra obtained using same UETC data but different eigenvector interpolation method. The black line represents the simple eigenvector decomposition and the green line is for the multi-stage interpolation method.*

green. In accordance with our previous expectations the inclusion of the matter-Λ transition only affects scales that entered late into the horizon, *i.e.* very low multipoles, decreasing slightly their amplitude.

3.3.4 Effects of fixed-k UETC interpolation

Finally we calculate the spectra for the fixed-k UETC interpolation method. This method interpolates UETCs in k-space rather than in time (see Eq. (3.34) and similarly for the matter-Λ

	TT	EE	BB
Multistage	$+25\%$	$+37\%$	$+37\%$
Fixed-k	$+29\%$	$+37\%$	$+36\%$

Table 3.10: *Percentual changes of the height of the peak of CMB power spectra in TT, EE and BB calculated using the multistage and fixed-k interpolation methods with respect to the simple eigenvector interpolation method.*

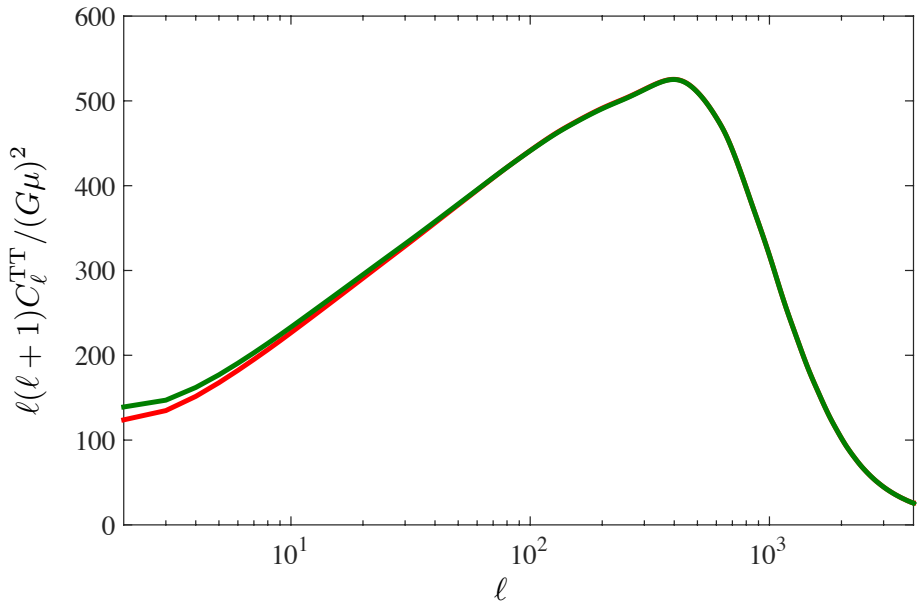

Figure 3.17: *Effect of including the matter-Λ transition into the multi-stage eigenvector interpolation structure, in green without the Λ transition and in red with it.*

transition). Conceptually this method fits naturally into usual Einstein-Boltzmann integrators and reproduces better the transition UETCs. The effect of switching from the multi-stage interpolation method to the fixed-k interpolation is shown in Figure 3.18, where the spectra of the multi-stage eigenvector set is plotted in red and the result of the source function of the fixed-k interpolated UETCs in blue. The matter-Λ interpolation has also been included in both cases. By inspection we get that the minimum number of k intervals needed to reach convergence in spectra is $N_k = 55$.

Figure 3.18 and Table 3.10 show that the change introduced by the new interpolation method is small, only the amplitude of the spectra around the peak is affected. Interestingly, as the lower panel of Fig. 3.18 and Table 3.10 show, whilst the new interpolation framework increases the temperature peak, it decreases slightly the height of the peak in B-modes.

3.3.5 Final C_ℓ's

This section contains the final CMB anisotropy power spectra of this work. This new baseline set of C_ℓ's is based on the following ingredients:

1. UETCs from $s = 1$ and $s = 0$ 4k simulations and combined by the new UETC merging

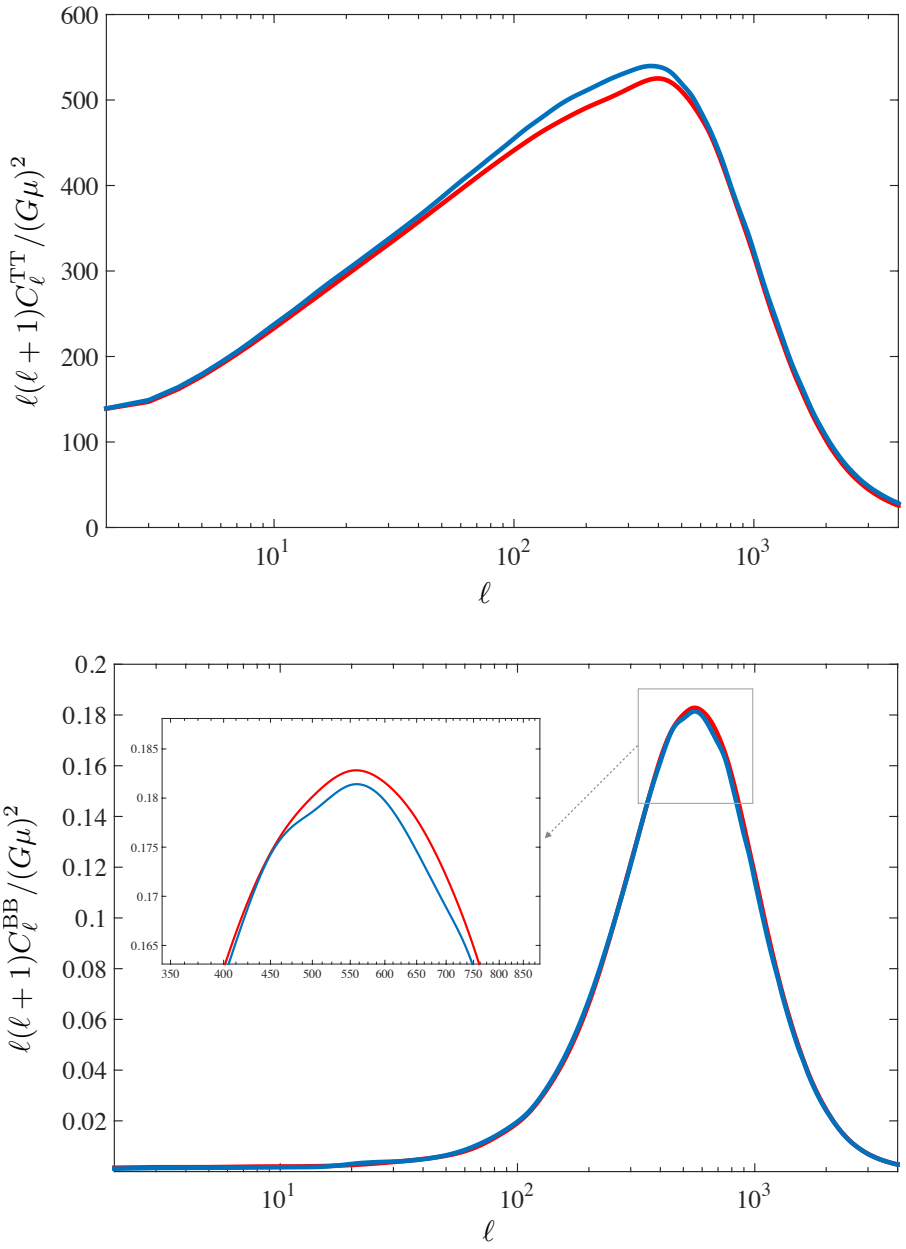

Figure 3.18: *Comparison of spectra obtained using different cosmological transition interpolation methods: multi-stage eigenvector interpolation (red line) and fixed-k UETC interpolation (blue line). The difference in the height of the peak in B-modes has been highlighted by zooming.*

scheme.

2. Fixed-k UETC interpolation for the cosmological transitions: radiation-matter and matter-Λ.

3. Interpolation functions for radiation-matter Eq. (3.37) and matter-Λ Eq. (3.41) (Table 3.9) transitions.

The evolution of the temperature spectrum by the inclusion of new improvements is shown in Figure 3.19. We maintain the same color scheme as in previous plots: the spectrum of [45] is the grey line, while the spectra obtained using new UETCs are shown in black (single eigenvector interpolation), red (multistage eigenvector interpolation) and blue (fixed-k interpolation). The upward trend is clear and as we mentioned the main change is due to the new and slower radiation-matter interpolation function.

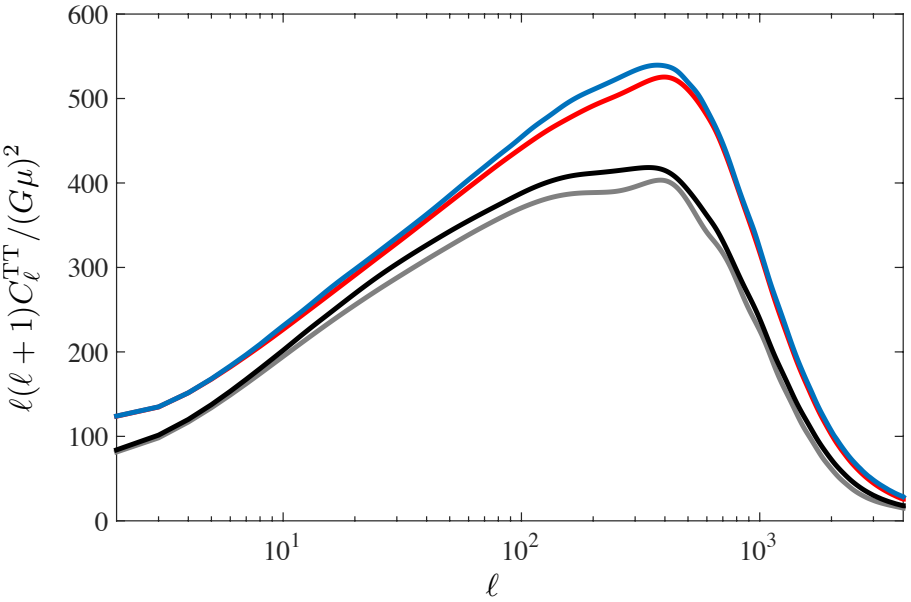

Figure 3.19: *Evolution of the effects produced by the improvements of this work. On the one hand, the change produced by the merged UETCs of the new simulations (black line) as compared to the [45] spectra (grey line). On the other, the effect of different treatment of the cosmological transitions: simple eigenvector interpolation (black), multi-stage eigenvector interpolation (red) and fixed-k UETC interpolation (blue).*

Our final power spectra with their corresponding error bars are included in Figure 3.20. The black line represents the mean curve and the grey regions systematic errors obtained by bootstrapping 10 times over 7 radiation and 7 matter realizations in the UETC merging process.

3.4 Discussion and Conclusions

In this work we compute the unequal time correlators (UETCs) from numerical simulations of Abelian Higgs strings, and describe and implement a new method of deriving source functions from them. We use those source functions in source-enabled versions of Einstein-Boltzmann integrators to obtain new and more accurate CMB anisotropy power spectra.

Our numerical simulations have been improved considerably from previous works due to improvements in both the hardware resources and the software used. The Abelian Higgs code uses the recently-released LATfield2 [67], allowing the efficient numerical integration of the field equations in parallel, and portable parallel fast-fourier transforms on large grids.

Our new production runs took place on lattices of 4096^3 sites, distributed over 34816 CPUs, a great improvement over previous lattice sizes of 1024^3 of [45]. Bigger lattices mean larger dynamical ranges: our simulations cover a larger portion of the evolution of the universe, both in

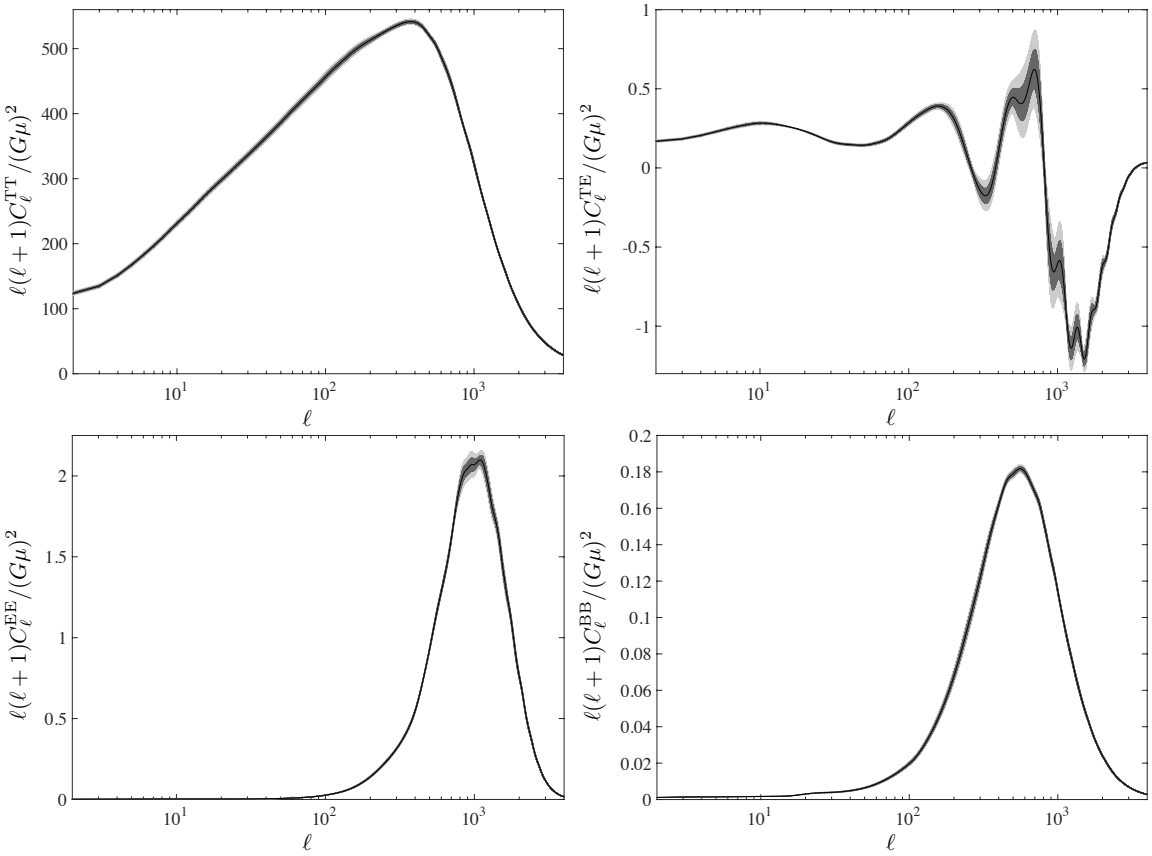

Figure 3.20: *Temperature and all polarization channels for the final CMB power spectra with all improvements implemented: merged UETCs from new simulations, fixed-k UETC interpolation and new radiation-matter and matter-Λ transition functions. Black lines correspond to the mean spectra while grey regions represent 1σ and 2σ confidence limits obtained by bootstrapping 10 times over 7 radiation and 7 matter realizations in the UETC merging process.*

space and time. As the space simulated is 64 times larger, we can obtain more accurate statistics. A factor of 4 longer evolution time allows for a more accurate study of the scaling of the network, and we can explore regions of the UETCs that could only be reached by extrapolation in previous work. Not only that, one of our key approximations in earlier works, the string core growth, can be dropped, and thus the *true* equations of motion have been solved, for the first time in the matter era. We confirm the extrapolations from older simulations.

In summary, our new UETC measurements span a much larger time ratio than in previous Abelian Higgs string simulations when using string core growth, and solve the true equations of motion over a long enough period to achieve scaling and measure the UETCs. We have combined two complementary sets of simulations, one with string core growth, and one with the true equations of motion, to obtain our final correlation functions.

Close to the peak of the UETCs, at near-equal times, we use the simulations with the true equations of motion. Outside this region we use the simulations with string core growth. In order to merge the UETCs, their normalization at equal times was matched, but no other adjustment was necessary. The new UETCs are consistent with previous measurements near the peak of the correlators, reach the horizon scale for the first time, and confirm the power-law behaviour of the

correlators at large wave-numbers. The normalization is slightly higher in the high wave-number tails, due to a small increase in the string density.

Numerical simulations of Abelian Higgs strings across cosmological transitions have been performed for the first time. The radiation-matter transition is particularly important for the accurate computation of CMB perturbations at around a degree scale. We also performed simulations across the matter-Λ transition, important for large angular scales. We have introduced and investigated a new method for calculating the source functions for Einstein-Boltzmann integrators, which better accounts for cosmological transitions. The method is more accurate than two previous methods [42, 86], and is also consistent with the underlying idea of decomposing the UETC into its component eigenvectors. It is also easier to implement.

Armed with the new simulations and an improved procedure to overcome the difficulties of the cosmological transitions, we compute new and more accurate predictions for the temperature and polarization anisotropies in the CMB due to cosmic strings. We present our new CMB predictions and their corresponding errors calculated in the innovative fixed-k interpolation framework and using the radiation-matter and matter-Λ transition functions derived in this work. Furthermore, this has been done using for the first time energy-momentum correlations derived from simulations following the real equations of motion. We also study how different improvements in simulations and cosmological transitions presented in this work affect the CMB power spectra. We observe that the main effect is produced by the new matter-radiation transition function which makes the contribution of the radiation correlators more important and increases considerably the amplitude of the anisotropy power spectra.

4 Survival of pq-superstrings in field theory simulations

The inflationary scenario has successfully been supported by modern and accurate observations [14, 15, 82, 110] as the best model for the origin of density fluctuations and the observed large-scale structure formation. However, the fundamental physics behind inflation still remains as one of the main unanswered questions of modern cosmology. Brane inflation models, proposed in the context of superstring theories, are interesting candidates to provide such an answer. It is expected that fundamental strings as well as string-like objects, such as D-branes, could form at the end of brane inflation due to brane-antibrane annihilation processes [56, 81, 116, 136, 177]. Such *superstrings* could survive the cosmological evolution and can have cosmological size [68, 159], which implies that they can play a role similar to ordinary cosmic strings. Therefore, their possible observational signal could be measurable, which would be invaluable towards an experimental verification of string theories and a remarkable window into the physics behind inflation.

Superstring networks produced after brane annihilation processes differ from ordinary cosmic string networks. Unlike solitonic strings, cosmic superstrings do not always intercommute, instead they can join together forming heavy and stable bound states composed of p F-strings and q D-strings called pq-strings [56, 81]. The boundaries of these segments are determined by 3-way Y-junctions where 3 different strings meet. Y-junctions are particularly interesting because they can perturb and modify the expected evolution of the network, producing observable effects or even preventing the network from achieving the scaling regime [175].

The evolution and description of F and D interconnected networks is rather complicated and numerical explorations are highly desirable. Early works on cosmic superstring networks analyze non-Abelian field theories of the kind $\mathrm{G} \to \mathrm{Z}_3$, where 3-way type junctions can form, both analytically [27, 207] and numerically [106, 193]. More sophisticated analytical models include effective field theories such as the velocity-dependent one-scale models (VOS), see for instance [30, 199], where different type of strings with different tension ranges can be considered. However, there is no consensus among those works on the physics behind the energy loss mechanism that leads to scaling of FD-networks, specifically whether the excess energy is radiated or, in turn, goes to increase the kinetical energy of the strings.

The evolution of F and D-strings can also be modeled by field theoretical *ordinary* solitonic strings, which are formed by usual spontaneous symmetry breaking mechanisms [166, 174]. These models consider a system composed by a pair of complex scalar fields, which is invariant under $\mathrm{U}(1)_\mathrm{L} \times \mathrm{U}(1)_\mathrm{L}$. The formation of stable bound states is typically accomplished by modifying the form of the potential of the system.

Full field theory simulations have been employed to explore the validity of these field theoretical models in reproducing the interconnected string dynamics [166, 176, 200]. Using the previously mentioned models, field theory simulations demonstrated that interconnected string networks can

form at spontaneous symmetry breaking phase transitions. The main goal of the works [166, 176] was to measure the effects produced by long range interactions in the overall dynamics of the network and bound states. Long range interactions were included in the analysis considering that one of the two $\mathrm{U}(1)_{\mathrm{L}}$ symmetries of the system was global. They also performed simulations were an *already-formed* network of pq-strings was present from the beginning. They found that, regardless of the initial conditions, the relative amount and significance of the bound states was considerably low, *i.e.* long range effects mediated by massless Goldstone bosons tend to break bound states. Conversely, they observed that in absence of long range interactions, strings of the initial pq-network remain in bound states for much longer. Scaling of such networks was also confirmed in [176].

Field theoretical simulations of the model presented in [174] were analyzed in [200]. In this work only the cases where short range interactions were present were studied, since long range interactions other than gravity are expected to be of little relevance in FD-networks. The authors successfully confirmed that interconnected string networks modeled by this model reach the scaling regime, which is an indispensable requisite for the cosmological viability of defects. However, as in previously mentioned works, it was observed that bound states constitute only a small fraction of the total string length of the system, of about $\sim 2\%$. Moreover, it was found that the length and lifetime of the bound states were shorter than expected from theoretical predictions.

All these early works, thus, put forward an interesting debate regarding the amount, lifetime and relevance of pq-strings. The observed formation rate and abundance of heavy strings are below the values expected theoretically. This discrepancy has recently been linked to the role played by Y-junctions in the networks, whose importance in the formation and shrinking of bound states may be relevant. Motivated by the tendency exhibited by field theory simulations, in [33] the stabilization and unzipping process conditions have been explored. Unzipping of heavy strings might be an extra ingredient to take into account in the development of effective models.

The main goal of this work is to extend previous field theoretical simulations performing the biggest and most accurate field theory simulations of cosmic superstrings. In order to give a more detailed insight on the late time evolution and relative amount of bound states, we investigate a set of simulations called *combined simulations*, which incorporate an artificial whole network of bound states coexisting with a network of single cosmic strings from the very beginning, similar to the initial conditions used in [166]. This perspective provides a wider view of the decay or unzipping of bound states as well as the interaction with *individual* strings. The average velocity distributions of the network and pq-segments have also been explored for the first time, which, together with the unzipping mechanism, could be fundamental in order to build proper effective theories.

This chapter is structured in the following way: in Sec.4.1 we review the model and explain the numerical procedures utilized in this work to perform the numerical simulations and identify pq-segments. After that, in Sec. 4.2 we introduce the new string combination procedure and present the results in Sec. 4.3. Finally we discuss the results in Sec 4.4.

4.1 Model

4.1.1 Model and parameter choice

The model considered in this work was proposed in [174] and posseses a $\mathrm{U}(1)_{\mathrm{L}} \times \mathrm{U}(1)_{\mathrm{L}}$ gauge symmetry, which leads to a pair of independent local cosmic strings. In addition to the usual *mexican hat* potential for the symmetry breaking, doubled in this case, the potential of this

model also contains an extra interaction term which leads to the formation of stable bound states where both complex fields wind simultaneously. The whole Lagrangian reads,

$$\mathcal{L} = (D_\mu\phi)^*(D^\mu\phi) + (\mathcal{D}_\mu\psi)^*(\mathcal{D}^\mu\psi) - \frac{1}{4e^2}F_{\mu\nu}F^{\mu\nu} - \frac{1}{4g^2}\mathcal{F}_{\mu\nu}\mathcal{F}^{\mu\nu} - V(|\phi|,|\psi|)\,, \tag{4.1}$$

where ϕ and ψ are the two complex scalar fields, which represent each sector of the double $\mathrm{U}(1)$ gauge symmetry. Each of them is independently charged with respect to its $\mathrm{U}(1)$ gauge field: A_μ with coupling constant e (ϕ) and B_μ with g as the coupling constant (ψ). The covariant derivatives and the field strength tensors are then,

$$D_\mu\phi = \partial_\mu\phi - iA_\mu\,, \tag{4.2}$$
$$F_{\mu\nu} = \partial_\mu A_\nu - \partial_\nu A_\mu\,, \tag{4.3}$$
$$\mathcal{D}_\mu\psi = \partial_\mu\psi - iB_\mu\,, \tag{4.4}$$
$$\mathcal{F}_{\mu\nu} = \partial_\mu B_\nu - \partial_\nu B_\mu\,. \tag{4.5}$$

The potential takes into account the symmetry breaking of each sector as well as the interaction between the two sectors:

$$V(|\phi|,|\psi|) = \frac{\lambda_{\mathrm{A}}}{4}(|\phi|^2-\eta_{\mathrm{A}}^2)^2 + \frac{\lambda_{\mathrm{B}}}{4}(|\psi|^2-\eta_{\mathrm{B}}^2)^2 - \kappa(|\phi|^2-\eta_{\mathrm{A}}^2)(|\psi|^2-\eta_{\mathrm{B}}^2)\,, \tag{4.6}$$

where λ_{A}, λ_{B} and κ are dimensionless coupling constants and η_{A} and η_{B} the vacuum expectation values for each kind of scalar fields.

Unless the last interaction term is considered, this potential describes the evolution of two independent networks of local cosmic strings. The last term includes the interaction between both type of fields, enabling the formation of stable bound states. As it can be seen from its form, it is only relevant where both fields are zero simultaneously. Nevertheless, the exact nature of the critical points of the potential, *i.e.* whether they are minima (stable) or maxima (non-stable), depends strongly on the value of κ; it is only in certain values of the parameter κ where stable bound states are formed. As pointed out in [174] stable bound segments appear only if κ obeys the following relation:

$$0 < \kappa < \frac{1}{2}\sqrt{\lambda_{\mathrm{A}}\lambda_{\mathrm{B}}}. \tag{4.7}$$

Under same conditions, the existence of gravitating bound states has also been demonstrated [98].

Field equations of motion are derived in the temporal gauge ($A_0 = B_0 = 0$) and evolved in a spatially flat Friedmann-Lemaître-Robertson-Walker (FLRW) background:

$$\ddot{\phi} + 2\frac{\dot{a}}{a}\dot{\phi} - D_jD_j\phi = -a^2\left(\frac{\lambda_{\mathrm{A}}}{2}(|\phi|^2-\eta_{\mathrm{A}}^2) - \kappa(\psi^2-\eta_{\mathrm{B}}^2)\right)\phi\,, \tag{4.8}$$

$$\ddot{\psi} + 2\frac{\dot{a}}{a}\dot{\psi} - \mathcal{D}_j\mathcal{D}_j\psi = -a^2\left(\frac{\lambda_{\mathrm{B}}}{2}(|\psi|^2-\eta_{\mathrm{B}}^2) - \kappa(\phi^2-\eta_{\mathrm{A}}^2)\right)\psi\,, \tag{4.9}$$

$$\dot{F}_{0j} - \partial_i F_{ij} = -2a^2e^2\mathrm{Im}[\phi^*\mathrm{D_j}\phi]\,, \tag{4.10}$$

$$\dot{\mathcal{F}}_{0j} - \partial_i \mathcal{F}_{ij} = -2a^2g^2\mathrm{Im}[\psi^*\mathcal{D}_\mathrm{j}\psi]\,, \tag{4.11}$$

$$-\partial_i F_{0i} = -2a^2 e^2 \mathrm{Im}[\phi^* \dot{\phi}]\,, \quad -\partial_i \mathcal{F}_{0i} = -2a^2 g^2 \mathrm{Im}[\psi^* \dot{\psi}]\,. \tag{4.12}$$

Here, a is the scale factor of the expanding universe, the dot derivatives represent derivatives with respect to the conformal time and the spatial derivatives are taken with respect to the comoving coordinates. The last couple of equations are Gauss's law for each complex scalar field and rather than equations of motion they are constraints of the system. Note that the Eq. (4.1) is totally symmetric on both scalar and gauge field inversion, *i.e.* $\phi \leftrightarrow \psi$ and $A_\mu \leftrightarrow B_\mu$; so are the equations of motion.

4.1.2 Simulation details

In this section we give explicit details of the simulation setups. We discretize the field equations of motion (Eqs. (4.8)-(4.11)) on a lattice using the standard lattice link variable approach [42, 145]. We perform simulations on radiation and matter dominated FRLW background cosmologies. One of the most important challenges of such simulations in expanding universes is to resolve the string core and the expansion of the universe simultaneously. As the universe expands, the physical distance between adjacent points of the lattice increases, but the physical string width remains constant. Thus, strings will eventually shrink between lattice points and we will not be able to track them. As it was explained in Sec. 2.2 of the Introduction, one of the most used approaches to avoid such an undesirable situation is to consider time varying coupling constants:

$$\lambda_{\mathrm{A}} = \frac{\lambda_{\mathrm{A0}}}{a^{2(1-s)}}\,, \quad e = \frac{e_0}{a^{1-s}}\,, \tag{4.13}$$

and equivalently for λ_{B} and g. In this model, since the potential contains an extra interaction coupling constant κ, it has to also be made time dependent,

$$\kappa = \frac{\kappa_0}{a^{2(1-s)}}\,. \tag{4.14}$$

This procedure is also known as *fat-string* approach, since the parameter s governs the relative width of the string. If $s = 1$ we recover the original equations and the equations of motion give the true dynamics of the system. In the other extreme, if $s = 0$ the physical width of the string grows with the expansion of the universe, or in other words, we obtain constant comoving width strings. The modified equations of motion are obtained including the time dependent coupling constants into the gauge-invariant action and varying it with respect to the fields, which assures self-consistency of the equations [42, 45]. They read as:

$$\ddot{\phi} + 2\frac{\dot{a}}{a}\dot{\phi} - D_j D_j \phi = -a^{2s}\left(\frac{\lambda_{\mathrm{A0}}}{2}(|\phi|^2 - \eta_{\mathrm{A}}^2) - \kappa_0(\psi^2 - \eta_{\mathrm{B}}^2)\right)\phi\,, \tag{4.15}$$

$$\dot{F}_{0j} + 2(1-s)\frac{\dot{a}}{a}F_{0j} - \partial_i F_{ij} = -2a^{2s} e_0^2 \mathrm{Im}[\phi^* \mathrm{D_j}\phi]\,, \tag{4.16}$$

and the same for ψ and $\mathcal{F}_{\mu\nu}$.

Several previous works on field theoretical simulations showed the acceptability of $s = 0$ to describe the dynamics of the system of this approximation [42, 45]. Based on this, we choose this extreme case $s = 0$ for this works so as to extend as much as possible the scaling period. On the other hand, since one of our aims was to improve previous works on the field we tried to balance between dynamical range and precision, hence we have increased the size of the simulation box to 1024^3 and decreased the comoving spatial separation to $dx = 0.5$, with time steps of $dt = 0.1$, which had been shown to yield good resolution. Simulations were parallelized through the publicly

available LatField2 library for parallel field theory simulations [67] and performed at the COSMOS Consortium supercomputer and i2Basque academic network computing infrastructure.

Our initial conditions set the modulo of the complex scalar fields at their corresponding vacuum expectation value and distribute randomly the complex scalar phases along the simulation box. On the other hand, gauge fields and canonical conjugates of the scalar as well as the vector fields are set to zero. This choice of initial conditions yields a very energetic configuration, mainly due to high gradient contributions. In order to smooth this initial situation we applied a combined diffusive-dissipative phase for the first quarter of the simulation, specifically for a time period of $\Delta\tau = 64$. The first diffusive period (between $\tau_{\rm start} = 50$ and $\tau = 60$) consists of a cooling of the equations of motion where we use *fake* time-steps of $1/30$ rather than $dt = 0.1$. The dissipative period, in turn, is performed by applying a non-physical damping of 0.4 between the end of the diffusive phase and the beginning of the natural or core growth evolution of the system (between $\tau = 60$ and $\tau_{\rm CG} = 114$). After $t_{\rm CG} = 114$ the system has been evolved following the usual equations of motion for $s = 0$ until $\tau_{\rm end} = 303$ set by causality.

Throughout this work, we restrict ourselves to the Bogomol'nyi limit where the parameters are related in the following way:

$$\lambda_{\rm A0} = 2e_0^2\,, \quad \lambda_{\rm B0} = 2g_0^2. \tag{4.17}$$

We also treat both type of strings identically, hence we set $e = g$ and $\eta_A = \eta_B$. Moreover, the typical parameter rescaling procedure is adopted and the parameters are reduced to:

$$e_0 = g_0 = \frac{1}{2}\lambda_{\rm A0} = \frac{1}{2}\lambda_{\rm B0} = 1\,, \tag{4.18}$$

$$\eta_{\rm A} = \eta_{\rm B} = 1\,. \tag{4.19}$$

4.1.3 Output treatment: pq-segment identification

Local cosmic strings on a lattice can be identified in several ways, *e.g.* using the energy density, the value of the potential or windings of the field phase. In this work, we use the latter procedure and localize strings calculating the winding of the complex phase of each field in every lattice placket. In order to accomplish that, we use the gauge invariant definition of the winding presented in [117]. A snapshot of a 1024^3 simulation is shown in Fig. 4.1. Blue and green lines represent *raw* individual p- and q-strings respectively, while red points are the points of the lattice where both fields wind simultaneously.

Essentially pq-strings are created as a consequence of the attraction produced by the interaction term in the potential and in theory they are located at points where both complex scalar fields wind simultaneously. However, due to the finite resolution of our simulations there are cases where though individual p- and q-string cores overlap, the winding is not located exactly at the same plaquette and might be displaced by dx distance within a individual pq-segment, giving the impression they do not form a bound state. In order to avoid this confusion, we set a new criterium to identify pq-segments: in addition to points where we find exactly double windings, segments will also be composed by regions where p- and q-strings are separated by less than 2 physical width units or in our lattice units by less than $d_{\rm AB} = 4$, regardless they contain exact double winded points or not. This approach is somewhat different of that proposed in [200], where segments are determined considering the intersegment distance, *i.e. gap* distance between segments, rather than considering the transverse distance between p- and q-strings.

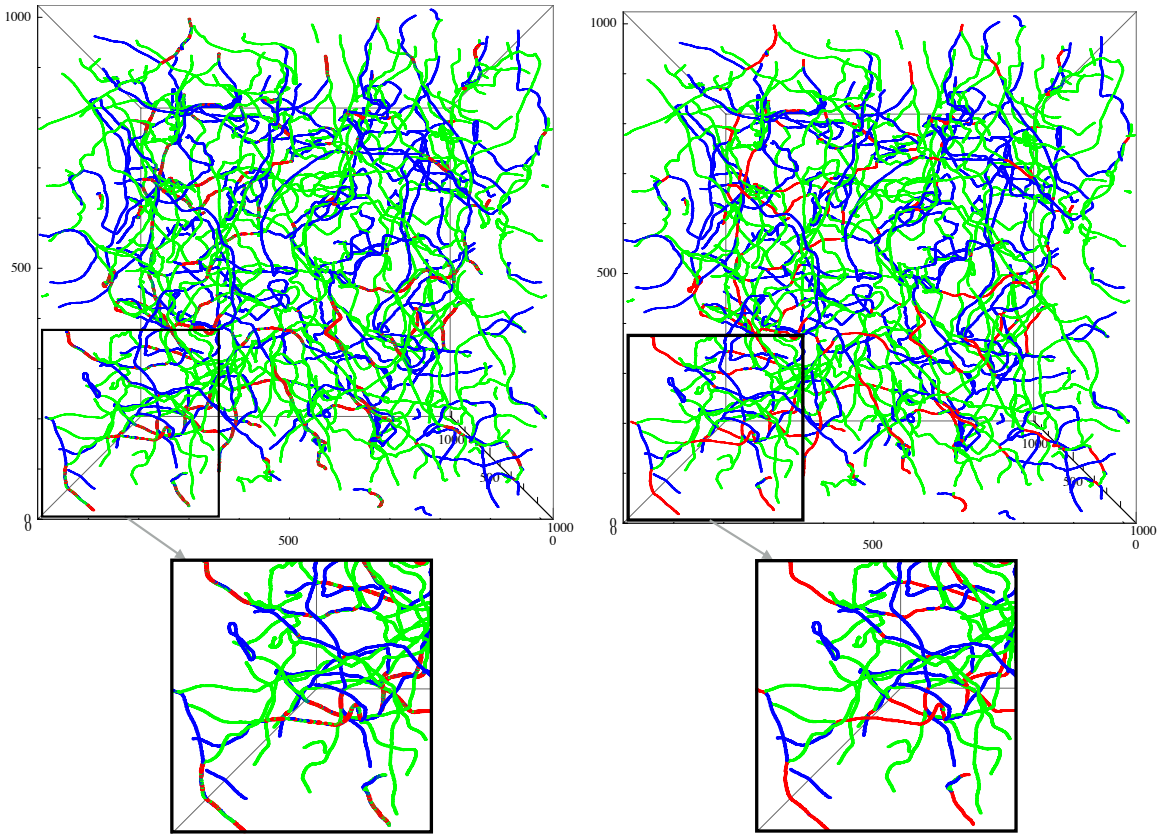

Figure 4.1: *Windings obtained from a 1024^3 combined simulation. Left panel shows raw windings where red points represent double winding points and blue and green lines windings of the ϕ and ψ fields respectively. Right panel shows the same snapshot after the segment identification treatment explained in Sec. 4.1.3.*

In order to complement our segment localization method we perform an approximate consistency check. Besides winding identification, pq-strings can also be located using the interaction potential that is responsible for their formation. By inspection, we observed that pq-strings can be localized in the simulation box for values of the interaction potential greater than a threshold value of $V_{\rm int}^{\rm th} = 0.855$. In the right panel of Fig. 4.2 we show an example of a simulation where we plot every point that exceeds that threshold value. This picture is accompanied by the corresponding winding identification method in the left panel of Fig. 4.2. Comparing the output of both methods, we find a remarkable agreement between both approaches, which supports our segment identification treatment based on windings. We believe that the few differences between both pictures are caused by the uncertainty produced by the arbitrary choice of the threshold value.

Finally we have to discriminate between actual pq double strings and small segments produced as a consequence of crossings of different p- and q-strings. Following the criterium set in [200], we get rid of crossing removing segments smaller than $L_{\rm AB} = 20$ in lattice units. Taking everything into account, the final result is shown in the lower part of Fig 4.2 and 4.1.

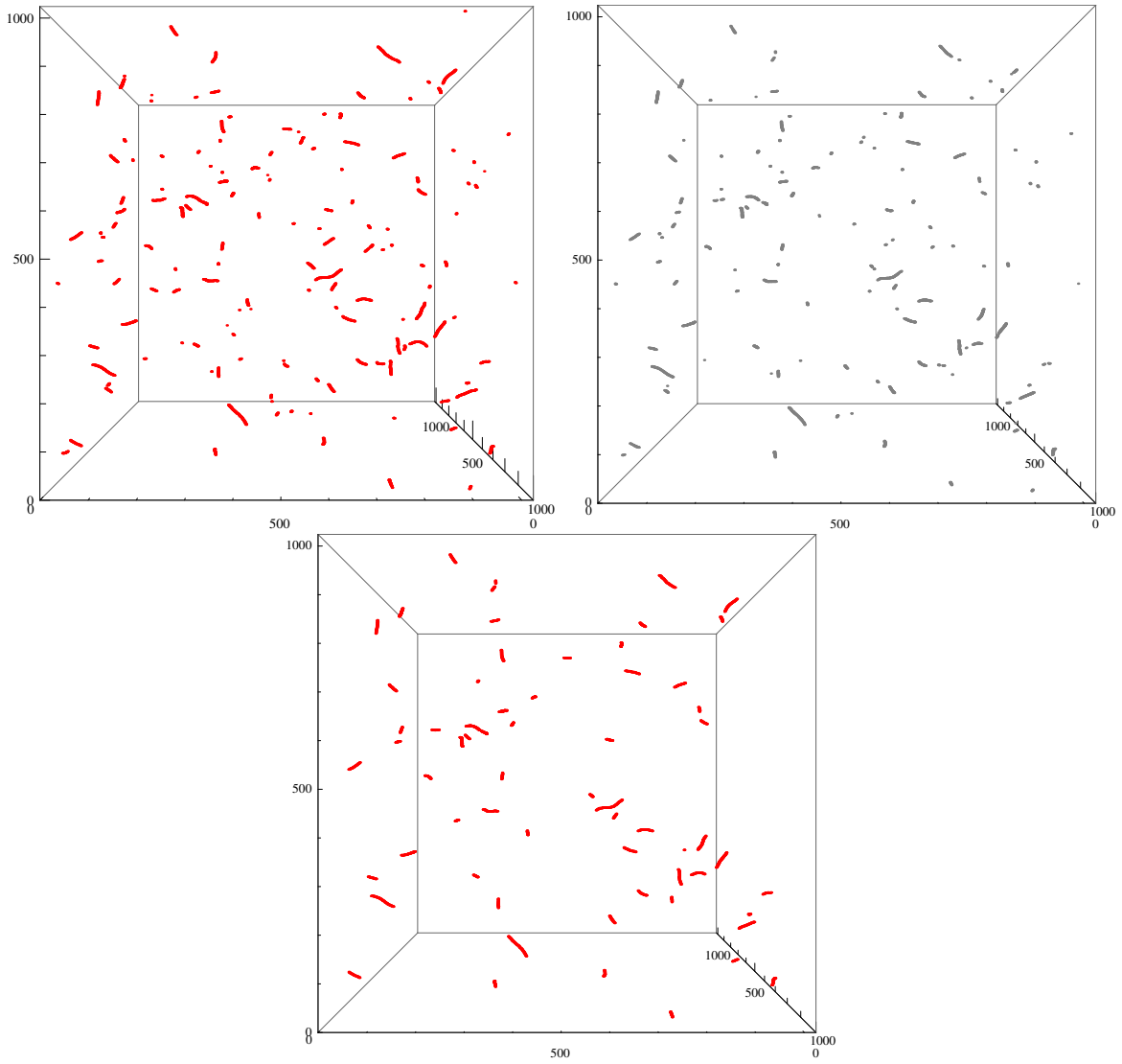

Figure 4.2: *Comparison of pq-segments calculated in 2 different manners for a 1024^3 lattice. In the left panel of the upper part the winding representation is shown where segments are identified following the recipe given in Sec. 4.1.3. In the right panel, in turn, segments are found by the interaction potential. Grey regions correspond to points where the interaction potential is bigger than the threshold value $V_{\rm int}^{\rm th} = 0.855$. In the lower panel every segment smaller than 20 lattice-points has been discarded following the winding-based method.*

4.2 Procedure to combine strings

Interconnected string networks contain three different types of strings: individual p- and q- strings and composed bound states. In order to ensure bound string formation in field theories, an interaction term is typically included (last part of Eq. (4.6)) which favors the individual string joining. Even though previous works have confirmed that bound strings can constantly form under the influence of this interaction term, it has been observed that their amount and length at the end of numerical simulations is below theoretical expectations. Moreover, it appear that their lifetime is also relatively short indicating that they tend to unzip as the different p- and q- strings

pull them in different directions.

One of the principal reasons for these discrepancies might be the limited dynamical range of numerical experiments, which is restricted by causality and computational resources. Initial conditions are typically set for the scalar and gauge fields of the system (or equivalently for their complex conjugates) and lead to the formation of the couple of ordinary Abelian gauge strings of the system. Therefore, in general, pq-strings are not present in numerical simulations from the beginning, instead one must wait until the formation of the bound states is energetically and dynamically favorable for the system. This is why it would be desirable to analyze whether discrepancies between numerical experiments and theoretical predictions are caused by the limited dynamical range or there is something more fundamental behind them.

In order to enlighten and analyze these issues we explore a different technique to simulate interconnected string networks: *string combination*. The idea is to have a whole pq-string network interacting with an ordinary solitonic cosmic string network (q-strings in this case). In order to accomplish this, we create a new *fake* pq-string network superposing conveniently p- and q-strings. Essentially the q-string network is doubled and an extra set of q-strings placed on top of the already existing p-strings. Hence the whole p-string network is converted into the desired bound and heavier pq-string network. An illustrative example can be seen in Fig 4.3, where we have included a snapshot of a string network before (left panel) and after (right panel) string combination. It can be seen that combination converts individual p-strings (in blue) of the left panel into pq-strings (in red) of the right one. String combination procedure introduces an innovative perspective into the analysis of the evolution of pq-bound states. Using an artificial initial configuration we will be able to determine if the system is comfortable with a high amount of heavy strings or on the contrary it prefers to break them into small pieces and decrease their relative relevance.

The procedure must be applied when the Abelian Higgs strings of the system are already formed. It would be meaningless to try to superpose fields before strings are formed, since it would not lead to a string combined scenario but to something different. This technique to combine different strings is somewhat different to that used in [166]. In that work the authors used a totally aligned phase distribution for the scalar fields to begin the simulation with a totally formed pq-string network. In our case, however, we apply the combination procedure to strings that are already formed. Indeed, given the symmetry of the equations of motion of our model, such initial conditions would lead to a totally indistinguishable pair of AH cosmic strings evolving in the same way, that would not reproduce the evolution of interconnected networks. Moreover, the initial pq-network of our combined simulations coexist with another *single* string network, as opposed to in [166] where the system was solely composed by pq-strings.

Step by step, the combination mechanism applied to fields can be summarized as follows: the system before combination of strings is composed by two (nearly) independent complex scalar fields, ϕ and ψ, set at their corresponding vacuum and with their corresponding strings (p and q respectively). String combination procedure leaves the first complex scalar field ϕ and its canonical conjugate unaltered:

$$\phi \to \phi = |\phi| e^{i\theta_{\rm A}} \,, \tag{4.20}$$

$$\Pi_{\rm A} \to \Pi_{\rm A} \,, \tag{4.21}$$

the gauge field associated to ϕ also remains unaltered.

The second field ψ, however, is substituted by a precise combination of both initial scalar fields:

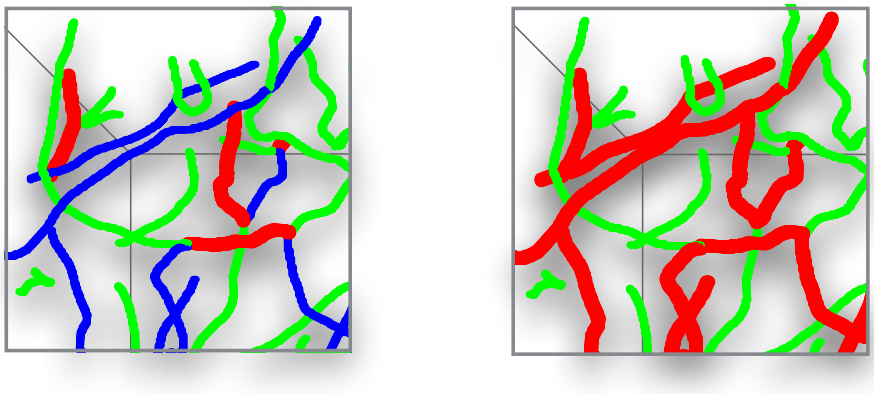

Figure 4.3: *Comparison of a patch of the simulation box before (left) and after (right) string combination. p-strings (in blue) of the left panel are completely converted in pq-strings (red strings) after combination.*

$$\psi \to \psi = |\phi||\psi| e^{i(\theta_{\rm A}+\theta_{\rm B})} \,. \tag{4.22}$$

This new scalar field vanishes when ϕ and/or ψ are zero, *i.e.* the strings associated to this new combined scalar field are located wherever original p- and q-strings are present. In some sense, we double the q-string network by adding a new set of q-strings at the position of the original p-strings.

The canonical conjugate of ψ must also be modified:

$$\Pi_{\rm B} \to \Pi_{\rm B} = \phi\Pi_{\rm B} + \psi\Pi_{\rm A} \,. \tag{4.23}$$

Finally, the new gauge field is the linear superposition of the original gauge fields:

$$\mathbf{B}_i \to \mathbf{B}_i = \mathbf{B}_i + \mathbf{A}_i \,, \tag{4.24}$$

$$\mathbf{E}_{{\rm B}i} \to \mathbf{E}_{{\rm B}i} = \mathbf{E}_{{\rm B}i} + \mathbf{E}_{{\rm A}i} \,. \tag{4.25}$$

We have observed that the evolution and the scaling dynamical range are optimized when the string combination is performed at the end of the dissipative phase, at $\tau_{\rm comb} = 105$, but before the beginning of the core growth phase. On the one hand, we let the system remove the energy excess caused by the random initial conditions, on the other we ensure that at the combination strings are already formed.

4.3 Results

In this section we present the most relevant results obtained in our simulations. We performed 5 matter plus 5 radiation realizations for both combined and normal simulations, using the parameters values as described in Sec. 4.1.2 and for $\kappa = 0.9$. The analysis will be mainly focused on combined simulations in the matter era (the results in radiation domination will be shown later), where one of the complex scalar fields of the model has been substituted by a combination of

both field in the initial stages of the simulation, in order to produce a whole network of bound pq-strings. We will explore the effects produced by these new initial conditions in the amount and evolution of different types of string and the new results will be combined with those obtained from *normal* simulations, where string combination has not been utilized. In addition, average velocity distributions of different networks will be analyzed. Velocities of interconnected networks, and specially velocities of pq strings, have been measured for the first time using field theory based velocity estimators. We will show as well as compare results of different type of simulations.

Any reasonable and useful description of string networks must be derived from simulations evolving in the scaling regime. Scaling ensures cosmological viability of such objects and enables extrapolation of the results to scales of cosmological interest. In the scaling regime characteristic lengths of the network evolve proportionally to the cosmic time, *i.e.* they grow linearly with the horizon. In the specific case of interconnected pq-networks, the scale invariant evolution was confirmed by different works [176, 200]. In order to confirm scaling of our different simulations, we calculate the typical length of the strings using two different methods.

The string separation or the characteristic length of the network is typically defined in terms of a reference volume V and the length of the strings within it L,

$$\xi = \sqrt{\frac{V}{L}}\,. \tag{4.26}$$

One way to derive L is to measure the length of each string summing the number of plaquettes pierced by them. This is the typical method and what we use to study the scaling of the different ingredients of our model and which we call $\xi_{\rm W}$. However, when the object to be explored is the whole system, one can estimate that value using field theoretical estimators such as the Lagrangian, with

$$L = -\bar{\mathcal{L}}V/\mu\,, \tag{4.27}$$

where μ is the string tension. The string separation determined by this method will be represented as $\xi_{\mathcal{L}}$.

Figure 4.4 shows characteristic lengths of the whole system measured using the two different methods mentioned in previous lines: Lagrangian method $\xi_{\mathcal{L}}$ (in black) and winding method $\xi_{\rm W}$ (in purple). The left panel shows the results for combined simulations, while the right panel shows the results for the normal case. The normal simulation achieves the scaling regime, as it was proven in previous works [176, 200], for $\tau \geq 150$. Remarkably, a similar result is obtained for the combined case, which reaches the scale invariant evolution more or less at the same simulation stage. A sudden step in $\xi_{\rm W}$ around $\tau \sim 100$, just before the start of the core growth phase, represents the string combination moment. Apparently it does not affect the latter evolution of the network towards scaling.

Interconnected string systems, however, are composed by three different type of strings. Hence a full confirmation of the scaling of the network requires further analysis and the study of the behavior of each individual set of strings. We start analyzing the behavior of individual p- and q-string systems, *i.e.* networks composed of loops or segments that are not forming pq-bound segments. We define the string separation for such cases as,

$$\xi_{\rm W}^{\rm p} = \sqrt{\frac{V}{L_{\rm p}}}\,, \qquad \xi_{\rm W}^{\rm q} = \sqrt{\frac{V}{L_{\rm q}}}\,, \tag{4.28}$$

where $L_{\rm p}$ and $L_{\rm q}$ are the total length of p- and q-strings where the length corresponding to

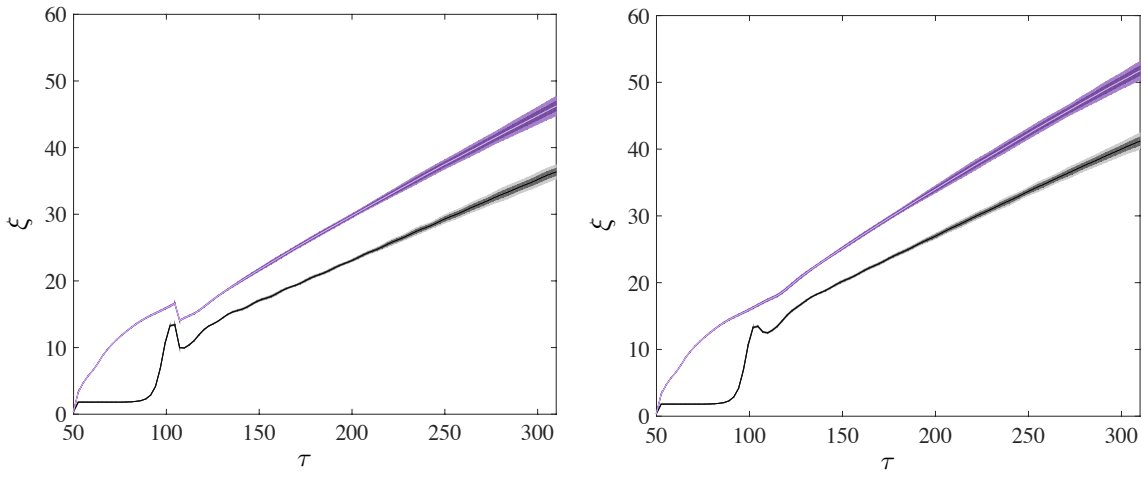

Figure 4.4: *Characteristic string length, ξ, measured using the Lagrangian (black line) and windings (purple line) for combined (left) and normal (right) simulations in the matter era. Shaded regions correspond to 1σ and 2σ confidence limits obtained averaging over 5 realizations.*

pq-segments has been subtracted.

Figure 4.5 includes the curves associated to those quantities: the blue colored region represents $\xi_{\rm W}^{\rm p}$ (p-strings), whereas the green is for $\xi_{\rm W}^{\rm q}$ (q-strings). It has to be noted that the starting point of the axis in this case is different, while global statistics of the system (total L, $\mathcal{L}$...) are collected for the whole simulated time, pq-segment identification procedure, and hence the calculation of $L_{\rm p}$ and $L_{\rm q}$, is only applied in the core growth phase, *i.e.* $\tau \geq 114$.

The blue line of the combined simulation reflects clearly that the p-string network is far from being scaling in the initial stages. The system approaches gradually the linear regime and it is achieved approximately at $\tau \sim 200$. On the contrary, individual string networks in the normal case appear to be scaling in the whole measured range. The difference between the blue and green curves in the left panel comes from the fact that the field ψ has been doubled and an extra set of q-strings created on top of the already existing p-strings. Hence, the initial length of p-strings is approximately zero $L_{\rm p} \sim 0$ (there is no free p-strings) and thus $\xi_{\rm W}^{\rm p}$ enormous. Nevertheless, the profile of the blue curve suggests that as time goes by the total length of p-strings increases considerably until the system starts following the linear dependence at $\tau \sim 200$.

It is evident that the p network needs a relaxation period after string combination, where part of the total length in bound states is transferred to p-strings. Such a period is clearer observed and understood analyzing the evolution of the pq-string fractions. We define two different fractions:

1. We measure the ratio of the total length of pq-strings to the length of the individual p-strings:

$$f_{\rm pq}^{\rm p} = \frac{L_{\rm pq}}{L_{\rm p}}\,, \tag{4.29}$$

   where $L_{\rm pq}$ is the sum of the length of all pq-segments.

2. Alternatively we want to measure what the fraction of the total length of pq-segments is with respect to the total length of the whole system:

$$f_{\rm pq}^{\rm Tot} = \frac{L_{\rm pq}}{L_{\rm p} + L_{\rm q} + L_{\rm pq}}\,. \tag{4.30}$$

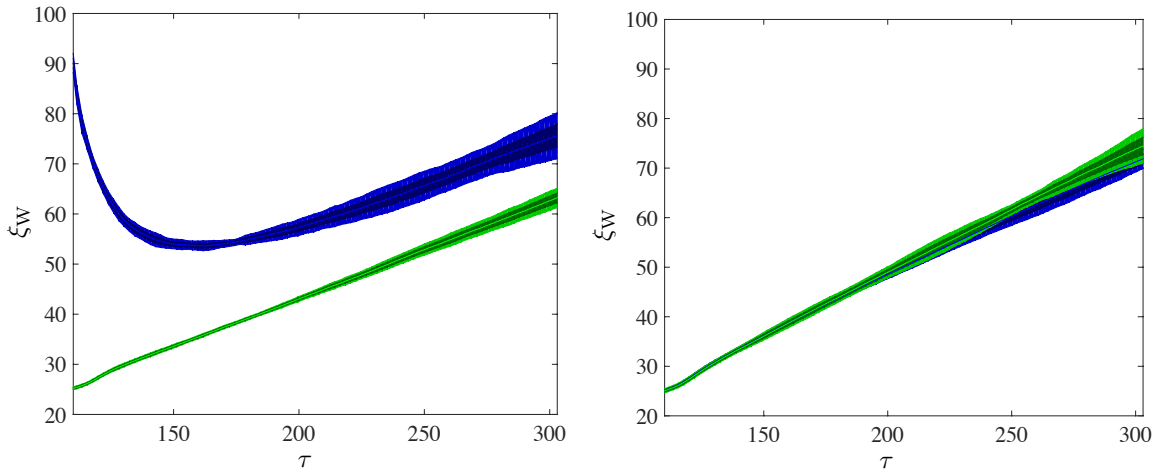

Figure 4.5: *Characteristic length of individual p- and q-strings measured using string windings for combined (left) and normal simulations (right). Shaded regions correspond to 1σ and 2σ confidence limits obtained averaging over 5 realizations.*

These two magnitudes are represented in Figure 4.6, $f_{\rm pq}^{\rm p}$ in blue and $f_{\rm pq}^{\rm Tot}$ in black. The figure corresponding to the normal simulation shows what previous works found: the total length of the pq-strings as compared to the total length of the whole system is really small, giving $f_{\rm pq}^{\rm Tot} \sim 0.02$ [200]. The blue line in this case is approximately twice the grey one because the lengths of p- and q-strings contribute at the same level to the total.

The trend exhibited by the string combined case is very different. Initially $f_{\rm pq}^{\rm p}$ is forced to be 1 by the combination process, that is, all p-strings are in pq states. However, the curve followed by this fraction shows that most of the length of pq-strings is converted into p-string's length. In other words, the system seems to not feel comfortable with such a high amount of bound states and wants to break them. For instance, by the time the network has finished the relaxation period $\tau \sim 200$, the fraction decreases to $f_{\rm pq}^{\rm p} \sim 0.4$. Apparently, the evolution of the individual strings provokes the unzipping of the bound states. The final evolution of the fraction after the relaxation period is smoother and approaches an asymptotic value of $f_{\rm pq}^{\rm Tot} \sim 0.05$, which is twice the quantity observed in normal simulations.

Scaling of the pq-segments has also been explored separately. We define the correlation length of pq-strings in the following way:

$$\xi_{\rm W}^{\rm pq} = \sqrt{\frac{V}{L_{\rm pq}}}\,. \tag{4.31}$$

Figure 4.7 shows that scaling is remarkably well achieved in simulations where strings have been combined. Furthermore, the linear proportionality is significantly better in this case than in normal simulations, where the characteristic length could barely be approximated to a straight line. The linear regime is reached at around $\tau \sim 200$, which is consistent with the relaxation behavior exhibited by the system in other observables. If we compare both simulations, one can see that the correlation length of bound states in the combined case is smaller than in normal simulations, which indicates that the pq-strings are in general more and longer in combined simulations. In both cases these correlation lengths are much bigger than the functions shown in Fig. 4.5.

Another interesting characteristic length of the pq-bound segments its their average physical

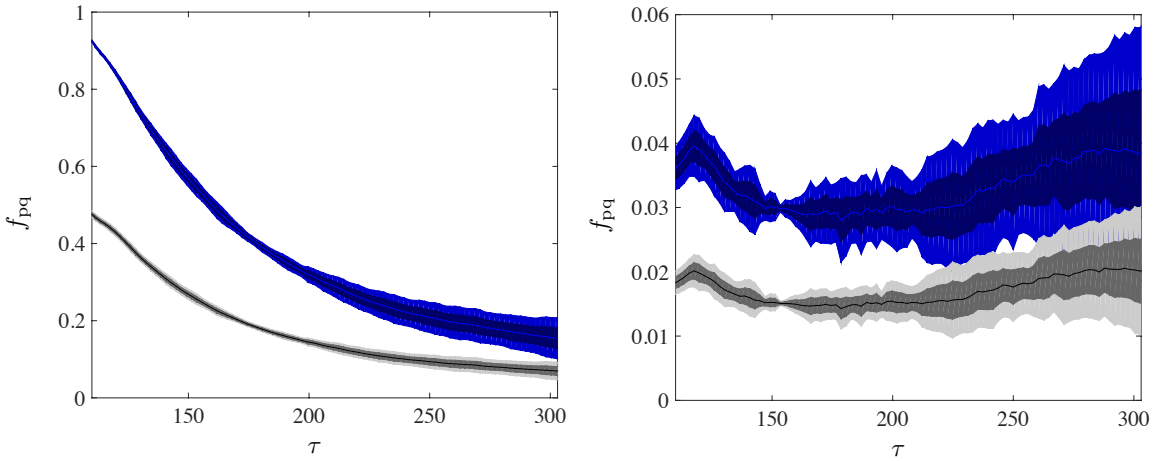

Figure 4.6: *pq-string fraction in combined (left) and normal simulations. The blue line corresponds to $f^{\rm p}_{\rm pq}$, while the black corresponds to $f^{\rm Tot}_{\rm pq}$. Shaded regions represent 1σ and 2σ errors obtained by averaging over 5 different realizations.*

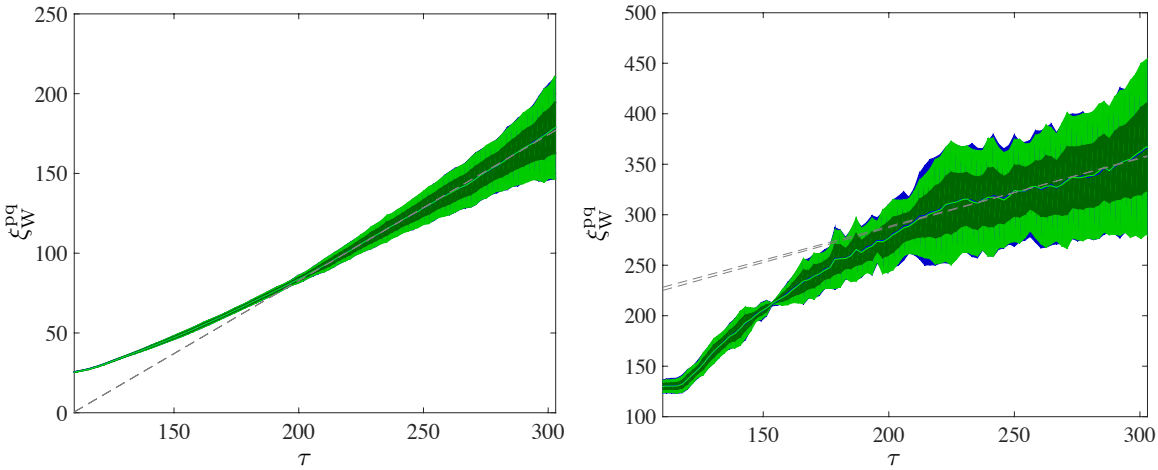

Figure 4.7: *Characteristic length of pq-segments measured using windings for string combined (left) and normal simulations.*

length. It is defined in the following manner:

$$\ell_{\rm pq} = \frac{L_{\rm pq}}{N_{\rm pq}}\,, \tag{4.32}$$

where $N_{\rm pq}$ is the total number of pq-segments. Figure 4.8 shows $\ell_{\rm pq}$ for both type of simulations. The profile of the curves is very different: whilst the average length in the normal case is approximately a linearly increasing function of time, the average physical length of the pq-strings in string combined simulations tends to an asymptotic constant value. The asymptote is located at $\ell_{\rm pq} \sim 55$ in the matter case and the curve is almost flat in the period of time after the system relaxation, *i.e.* $\tau \geq 200$. Interestingly, the average length in normal simulations remains below that value. The scale invariant evolution is generally better and faster acquired by combined simulations, where not only the whole system scales, but also p, q and pq-networks separately. One could expect that bigger simulations of the normal case with more dynamical range, would

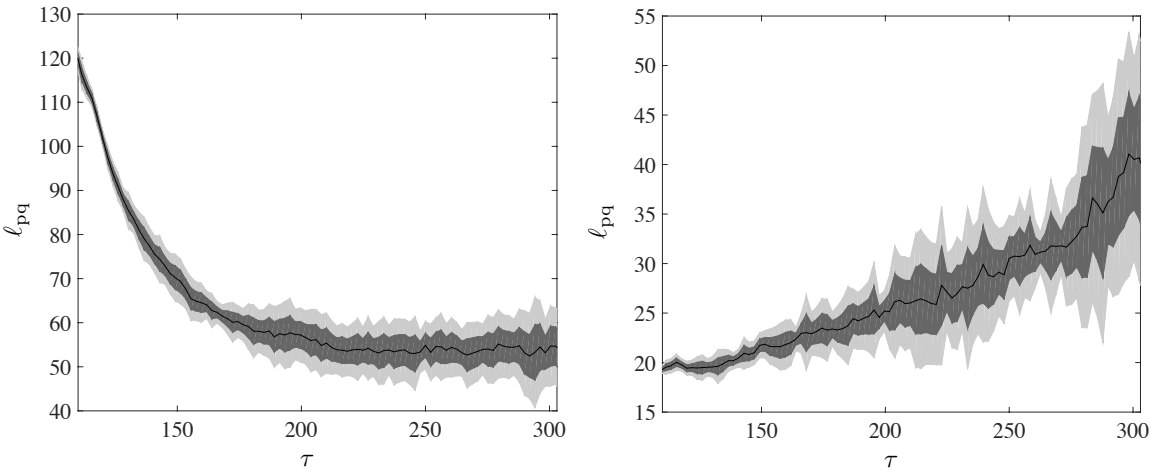

Figure 4.8: *pq-string average physical length in combined (left) and normal simulations. Shaded regions correspond to 1σ and 2σ errors obtained by averaging over 5 different realizations.*

tend towards the asymptotical evolution depicted by combined simulations.

We have also performed simulations in radiation dominated scenarios. We observe that in general the results extracted from matter dominated and radiation dominated cosmologies are very similar and no significant distinction can be made between both cases.

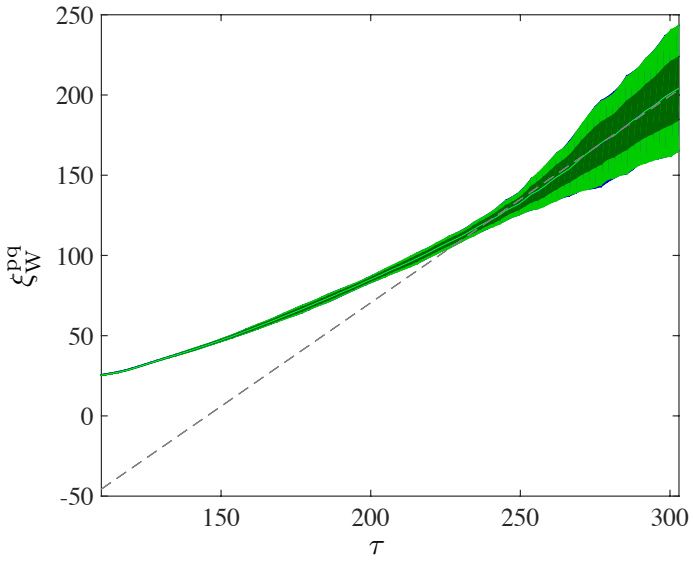

Figure 4.9: *Correlation length of pq-strings in combined simulations in the radiation domination era.*

The differences come mostly from the lower damping in the equations of motions produced by the different expansion rate of universes evolving in radiation domination. The lower damping term affects the relaxation period of string combined simulations. Figs. 4.9 and 4.10 show $\xi_{\rm W}^{\rm pq}$ and the average physical length of pq-strings in radiation domination eras. As it can be seen, both pictures reproduce essentially the evolution depicted in the matter case, but with the difference that the scale invariant evolution is acquired later. Scaling of the bound segments is also observed in radiation domination era and the scaling regime is achieved at $\tau \sim 225$. As it happened in

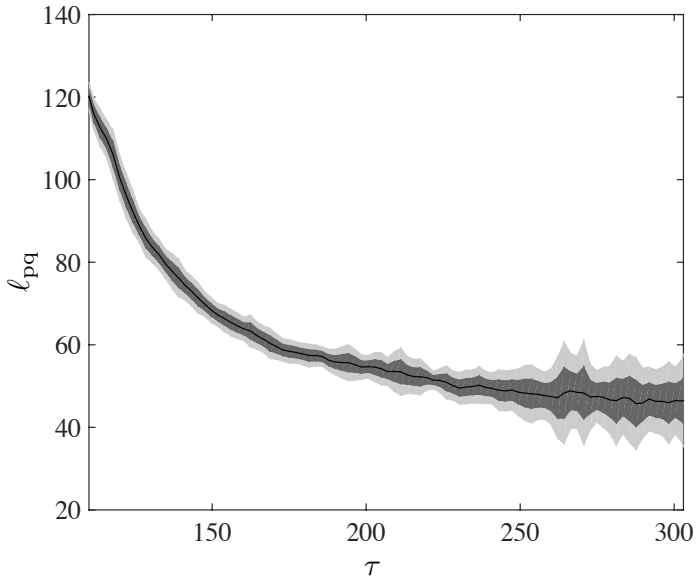

Figure 4.10: *Average physical length of pq-strings in combined simulations in radiation domination era.*

matter domination, the scaling exhibited by combined simulations is better than the behavior of the normal simulations.

The average physical length also tends towards an asymptotic value, as Fig. 4.10 shows. However, as with the scaling, the network in radiation domination needs more time to relax and the asymptote is reached later $\tau \sim 250$. The value for this case $\ell_{\rm pq} \sim 45$ is slightly below the asymptotic value obtained in matter domination.

Finally, we have also modified the coupling parameter of the interaction potential responsible for the pq-string formation, κ, so as to explore its relevance in the creation, evolution and amount of bound states. We increased its value to $\kappa = 0.95$ and performed simulations in both normal and combined scenarios. In fact, such value of κ is really close to the maximum value allowed for this model, as it is in indicated in Eq. (4.7).

On the one hand, our normal simulations confirm previous results of [200]: increasing the value of the coupling constant from $\kappa = 0.9$ to $\kappa = 0.95$ only produce a marginal increase of the fractions of the bound states and in general did not produce remarkable changes in the evolution of them. On the other hand, combined simulations with $\kappa = 0.95$ show that, despite the higher coupling constant of the attractive potential term, the overall dynamics of the system tends to split bound states and as in the case with $\kappa = 0.9$ their relative fraction decreases rapidly. In terms of numbers, we only observe minimal changes, which translate into slightly bigger values of the asymptotic length of the bound states, $\ell_{\rm pq} \sim 70$, and asymptotic total fraction $f_{\rm pq}^{\rm Tot} \sim 0.12$, in both matter and radiation eras.

4.3.1 Velocities

Average velocities of the network have been measured using the gauge invariant field theoretical velocity estimators proposed in [65, 108], which exploit the fact that the electric field and canonical momentum of the scalar field in moving strings can be obtained by boosting the static field distribution. The velocity estimators have the following form:

$$\langle \mathrm{v}^2 \rangle_{\mathrm{F}} = \frac{\mathbf{E}^2_{\mathcal{L}}}{\mathbf{B}^2_{\mathcal{L}}}\,, \tag{4.33}$$

$$\langle \mathrm{v}^2 \rangle_{\mathrm{G}} = \frac{2G_{\mathcal{L}}}{1+G_{\mathcal{L}}}\,, \tag{4.34}$$

where,

$$G_{\mathcal{L}} = \frac{\Pi^2_{\mathcal{L}}}{(\mathbf{D}\phi)^2_{\mathcal{L}}}\,. \tag{4.35}$$

The subscript $\mathcal{L}$ denotes a Lagrangian density weighting of each magnitude. This is used to ensure that only regions with non-vanishing Lagrangian density contribute to velocities, *i.e.* only strings, where the Lagrangian density is peaked, contribute to the calculation of the estimators. For a given quantity A the weighting is applied in the following way [108]:

$$A_{\mathcal{L}} = \frac{\int d^3x A\mathcal{L}}{\int d^3x \mathcal{L}}\,. \tag{4.36}$$

All values obtained are shown in Table 4.1. Fig. 4.11 also shows the evolution of the two velocity estimators in the matter domination era, field based in green and gradient based in red, for combined simulations (left panel) and normal simulations (right panel). The curves of the velocities are nearly flat for the whole core-growth phase, *i.e.* natural evolution of the equations of motion. Furthermore, for both estimators the curves are very similar, pointing to a mean value of $\langle \mathrm{v}^2 \rangle_{\mathrm{F}} \sim \langle \mathrm{v}^2 \rangle_{\mathrm{G}} \sim 0.26$ (see Table 4.1). There is no difference in the velocity distribution between combined cases and normal simulations.

	Matter				Radiation			
	Combined		Normal		Combined		Normal	
	$\kappa = 0.9$	$\kappa = 0.95$	$\kappa = 0.9$	$\kappa = 0.95$	$\kappa = 0.9$	$\kappa = 0.95$	$\kappa = 0.9$	$\kappa = 0.95$
$\langle \mathrm{v}^2 \rangle_{\mathrm{F}}$	0.259±0.005	0.261±0.006	0.261±0.007	0.264±0.006	0.306±0.004	0.307±0.006	0.303±0.004	0.305±0.006
$\langle \mathrm{v}^2 \rangle_{\mathrm{G}}$	0.259±0.005	0.260±0.006	0.264±0.007	0.266±0.006	0.307±0.004	0.307±0.005	0.306±0.004	0.310±0.006
$\langle \mathrm{v}^2 \rangle^{\mathrm{pq}}_{\mathrm{F}}$	0.28-0.37	0.29-0.35	0.28-0.35	0.28-0.34	0.36-0.44	0.36-0.41	0.35-0.41	0.35-0.40
$\langle \mathrm{v}^2 \rangle^{\mathrm{pq}}_{\mathrm{G}}$	0.27-0.34	0.27-0.32	0.28-0.33	0.27-0.31	0.33-0.39	0.33-0.38	0.33-0.37	0.33-0.37

Table 4.1: *Mean values of the velocity estimators of the whole network ($\langle \mathrm{v}^2 \rangle_{\mathrm{F}}$ and $\langle \mathrm{v}^2 \rangle_{\mathrm{G}}$) and of pq-strings ($\langle \mathrm{v}^2 \rangle^{\mathrm{pq}}_{\mathrm{F}}$ and $\langle \mathrm{v}^2 \rangle^{\mathrm{pq}}_{\mathrm{G}}$) for the different possibilities simulated averaged over 5 realizations. In the case of system velocity estimators we also include 1σ errors obtained by averaging the standard deviations in the range $\tau > 200$. The two values of the pq estimators correspond to the minimum and maximum mean values respectively.*

We also propose a similar estimator for the velocity of the pq-strings, $\langle \mathrm{v}^2 \rangle^{\mathrm{pq}}$. This estimator is based on the previous ones, but the Lagrangian weighting has been substituted by the interaction potential weighting. Hence Eq. (4.37) converts into:

$$A_{V_{\mathrm{int}}} = \frac{\int d^3x A V_{\mathrm{int}}}{\int d^3x V_{\mathrm{int}}}\,. \tag{4.37}$$

We have previously observed that pq-strings can be well located finding places where the value of the interaction potential is bigger than a threshold value $V_{\mathrm{int}} = 0.855$[1] obtained by

[1] It has to be noted that this is an approximated value motivated by trial and error inspections and thus results might suffer small changes if this number is different.

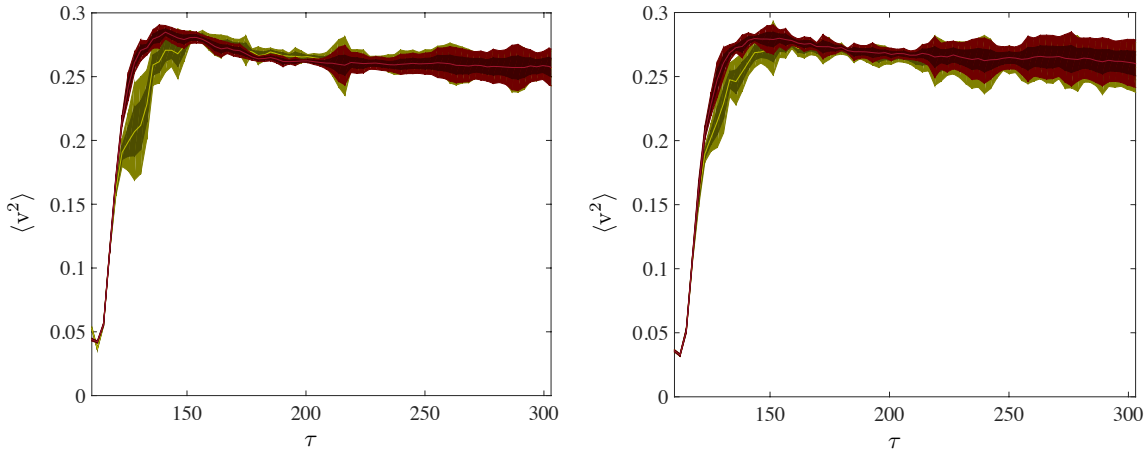

Figure 4.11: *Field (green) and gradient (red) Lagrangian weighted velocity estimators of the whole system in matter domination era. Left panel shows the result for combined simulations and right panel for normal simulations.*

inspection. Therefore we use this value to focus only on the velocity contribution made by bound states. Nevertheless, the pq-string velocity estimator is a mere tentative and as such the values associated to it should not be interpreted as exact estimations.

The results can be found in Table 4.1. In Fig. 4.12 we again compare combined simulations (left panel) with normal simulations (right panel), both in matter era.

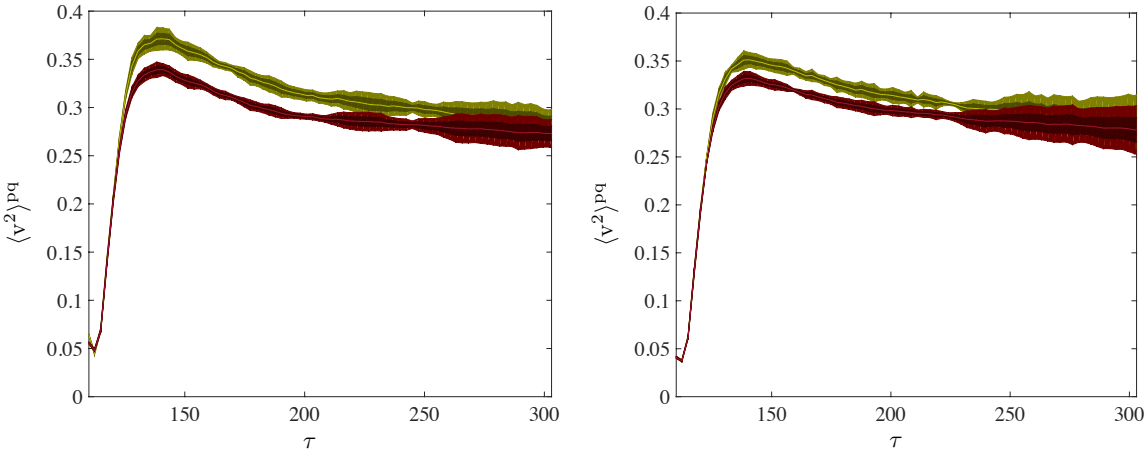

Figure 4.12: *Field (green) and gradient (red) velocity estimators weighted by the interaction potential for the pq-string network, in matter domination era. Left panel shows the result for combined simulations and right panel for normal simulations.*

In contrast to the estimators of the whole system, velocity estimators of the pq-strings show a decreasing tendency. Nevertheless their values lie always above those of their global counterparts, as Table. 4.1 shows. This decreasing trend can be understood taking into account that the interaction potential weighting also accounts for contributions of crossings of individual p- and q-strings, this is why their value is higher initially (more crossings, $\mathcal{O}(10^3)$) and lower in the final stages of the simulation ($\mathcal{O}(10^2)$), where the contribution is mainly due to the velocity of the segments. The difference between $\langle v^2 \rangle_{\rm F}^{\rm pq}$ and $\langle v^2 \rangle_{\rm G}^{\rm pq}$ might be caused by the uncertainty of the

interaction term weighting approximation.

Similarly to the global case, we observe little differences between combined simulations and normal simulations. The only difference is that the maximum peak in the velocity is slightly higher in the combined case, which might be a consequence of significantly higher density of pq-segments at the initial phases of the combined scenario.

As it can be seen in Table 4.1, simulations in radiation dominated cosmologies show $10\% - 15\%$ higher velocities, which have also the same evolution pattern of the matter dominated simulations. We also computed velocities for $\kappa = 0.95$, showing no differences with those obtained for $\kappa = 0.9$, all within 1σ.

4.4 Discussion

Interconnected FD-string networks are predicted in several brane inflation models. Such networks of fundamental strings can play a similar role of cosmic strings, but they differ in several aspects from ordinary solitonic strings. The main difference is the existence of heavy and stable bound states that form as a consequence of the joining of individual p F-strings and q D-strings and are called pq-strings. Theoretical models predict that the relative abundance of bound states can be comparable to that of their individual constituents and that the evolution of the whole system can be significantly affected by their presence.

Field theoretical simulations are one of the most interesting methods to explore some of the properties of superstrings networks. In this work we have simulated interconnected string networks using the effective model proposed in [174]. The model reproduces the evolution of interconnected superstring networks using a pair of ordinary Abelian Higgs strings coupled with an interaction term, which produces composed bound states. Bearing in mind the differences between solitonic string networks and superstring networks, *e.g.* different intercommutation probabilities or different tension scales, such effective proposals can be very useful to reproduce some of the dynamical features of superstrings.

Previous works on full field simulations of this model [200], confirmed the formation of pq-strings and observed that the evolution of the network is compatible with the scaling solution. Nevertheless, the authors also indicated the existence of some discrepancies between the results of the numerical experiments and theoretical predictions. On the one hand, the relative abundance and length of pq-strings were below theoretical expectations, which questioned the relative importance of the bound string in the evolution of the whole system. On the other hand, although bound strings form continuously due to the interaction potential their lifetime was small, indicating the existence of a efficient unzipping mechanism.

One of the main objectives of this work has been to determine whether the mentioned discrepancies appeared because the dynamical range of the numerical simulations, imposed by limited computational resources, was too short to properly mimic the evolution of realistic superstring networks, or on the contrary, there was a fundamental issue behind them. In order to enlighten this questions, we analyze the problem from an alternative (or even opposite) point of view. We explore a scenario where pq-strings are present nearly from the beginning of the simulations, instead of waiting for their formation from individual p- and q-strings. We call this procedure string combination, where one of the individual string networks is replaced by a whole network of bound states interacting with the remaining individual network. The objectives are twofold: first to see if the low relevance of the bound states is just a consequence of the initial conditions or on the contrary it is product of the natural evolution of this model. Second to determine the efficiency of the unzipping of the composed bound states into individual vortexes, comparing the initial and

final bound string abundances. We have performed combined simulations in matter and radiation domination eras and compared them with simulations where strings were not combined.

The main conclusion that can be extracted from combined simulations is that the system is not able to retain a high number of pq-strings in the system and tends to split the composed bound states into its constituents. Even though one of the two string networks of the system initially is completely at bound states $f_{\rm pq}^{\rm p} \sim 1$ (see left panel of Fig. 4.6), the pq-string fraction soon starts drastically to decrease. It is evident that the system does not feel *comfortable* with that configuration, and prefers to break the composed bound states into individual p- and q-strings. By the end of the simulation the relative length on bound states with respect to the total length of the system falls to $f_{\rm pq}^{\rm Tot} \sim 0.05$, *i.e.* only 5% of the total length is at pq-strings. The splitting of the pq-strings evidences the unzipping ability of the system. The dynamics of the Y-junctions at the boundaries of the pq-strings is more influenced by the tension applied by the individual free p- and q-strings than by the dynamics of the heavy string. Therefore we believe that an efficient unzipping mechanism should also be included in any reasonable effective model that aims to describe interconnected string networks.

Combined simulations, as simulations of [176, 200] did, also exhibit scale invariant evolution. The path towards the scaling regime, though, is somewhat different of that followed by normal simulations. Soon after strings have been combined, the system passes through a relaxation period where most of the pq-segments disappear and are converted into ordinary p- and q-strings. We observe several hints that point to this relaxation period such as the evolution of the fractional amount of pq-strings, the characteristic length of p-strings or the scaling of pq-segments. After the system relaxes the scaling regime is achieved. Remarkably, not only the whole system evolve in a scale invariant manner, but scaling is also achieved by every separate sub-network of the system, especially by the pq-string network. In this last case, the characteristic length of the pq network ($\xi_{\rm W}^{\rm pq}$) evolves in an almost perfectly linear way, whereas for the normal simulation it can be barely approximated to a straight line (see Fig. 4.7). We think that in general string combined simulations are able to improve the evolution of the network as well as of the sub-networks towards the scaling regime.

Another interesting outcome of combined simulations is that the average physical length of the pq-strings tends to an asymptotic value of $\ell_{\rm pq} \sim 55$ in matter domination and $\ell_{\rm pq} \sim 45$ in radiation domination. Its evolution is also clearly compatible with the relaxation period mentioned in previous lines. Conversely, the evolution of this quantity in normal simulations is clearly an increasing function of time, nearly linear. However, it can be observed that its value lies always below the asymptotic value obtained in the combined case. Considering scaling evolution has been improved by combined simulations, we expect that the outcome of a larger normal simulation would converge to the asymptotic evolution described by combined simulations. Furthermore, we think that the innovations introduced by this new method can be very useful to optimize the dynamical range/computational cost of such numerical experiments. In this direction, it would be really desirable to perform bigger normal simulations in order to determine whether both approaches converge.

Velocities of interconnected string networks and pq bound states have also been analyzed for the first time. We measure the root mean square velocities ~ 0.5 for the average velocity of the whole system and depending on the estimator between $\sim 0.5 - 0.6$ for the velocities of the bound states. Whilst the curves of the average velocities of the system are nearly flat, the velocities of the bound states exhibit a decreasing trend. Comparisons of the combined and normal simulations show no differences, which enforces our opinion of the validity of string combination method to describe interconnected networks.

In order to increase the binding energy of the bond states, we have also simulated cases for a larger value of the interaction potential coupling constant. We found that increasing the value from $\kappa = 0.9$ to $\kappa = 0.95$, which is close to the allowed maximum value, does not produce significant changes neither in the amount and lifetime nor in the relative relevance of the pq-strings in the global network evolution. Clearly the dynamics of the bound states is dictated by the evolution of the lighter individual strings, *i.e.* p- and q-strings. As it was pointed in [174], the formation of stable pq-strings is more favorable for strings with higher winding number than unity. However, no simulation performed during this work produced strings with winding number greater than one. These facts evidence that even though the model, through its interaction potential, is able to produce pq-strings, for the values of the model chosen in this work it is not able to produce bound states with binding energy as high as to make the existence of pq-strings in the network energetically favorable.

Nevertheless, it worthwhile to point that this model is not only limited to the parameter values employed during this work. On the contrary, it can be easily extended to different scenarios which could possibly increase the binding energy of bound states. For instance, simulations with different coupling constants would lead to the departure from the Bogomol'nyi limit. It would be interesting to investigate whether simulations out of the Bogomol'nyi bound are able to produce strings with higher winding numbers. An alternative set of models can be obtained by variation of the vacuum expectation values of the complex scalar fields. Systems composed by scalar fields with unequal vacuum expectation values would produce interconnected string networks composed of *individual* strings with different tensions, which would lead to the formation of heavier bound states. Moreover, networks of strings with different masses are expected to be closer to realistic superstring networks. It would be desirable that future field theoretical simulations exploit the limits of the parameter space of the model in order to produce more stable bound states that would play a relevant role in the dynamics of the system. Other effective field theory models can also be used in this regard.

5 General Conclusions

The central objective of this Thesis has been to investigate the properties and possible observational signatures of cosmic defects, mainly cosmic string, in cosmology. In order to accomplish this task, in the first half of the Thesis we have studied their observational effects through the small experimental windows that the extremely accurate data still allows. On the one hand, the relation between cosmic strings and the measured excess of relativistic species has been explored in Chapter 1. On the other, the role played by cosmic defects in the CMB B-mode polarization measurements has been determined in Chapter 2. In both works we have compared theoretical predictions with experimental observations. The second part of the Thesis has been more focused on extending the characterization of cosmic string networks via numerical simulations. We have updated energy-momentum correlations and CMB power spectra for Abelian Higgs strings in Chapter 3. Finally, in Chapter 4, we have employed field theory simulations to reproduce, using effective models, the cosmological evolution of interconnected cosmic superstrings.

As mentioned, the data when the work of Chapter 1 was performed suggested that the number of the relativistic species at the early universe was higher than predicted by the standard particle model. In this Chapter we have explored the origin of this apparent excess and link it to the existence of cosmic strings. The cosmological gravitational wave background induced by cosmic strings could be the responsible for the high number of relativistic species required to fit the data. We have found that cosmic strings can account for part of the excess, but that the correlations between them and the extra relativistic species depend on the dataset analyzed: if the dataset cover the low multipole region they are correlated, whereas if small scale data is included, correlation becomes anti correlation. The inclusion of non-CMB datasets, principally direct measurements of the Hubble parameter, induce a drastic reduction of the available parameter space and almost all correlations vanish. In most of the cases, the contribution of cosmic strings can be considered as the unique source of the excess, but the need of extra contributors is not rejected in either case. It has to be noted that all numerical results of this Chapter carry a considerable amount of uncertainty, mostly coming from the big differences in the prediction of the amount of gravitational waves of horizon sized and sub-horizon sized loops.

Motivated by the measurements of the CMB anisotropy B-modes at angular scales made by the BICEP2 collaboration, in Chapter 2 we have investigated the possibility that this signal could be created by cosmic defects. Even though the contribution of defects to CMB anisotropies is highly constrained by accurate temperature measurements, their contribution to polarization B-modes can still be dominant. We address the issue from two separate but complementary points of view: firstly we have tried to determine, qualitatively, whether cosmic defects could be the only responsible for the entire measured signal. In order to complement the qualitative statements, in the second part we performed a quantitative analysis of the parameter space fitting BICEP2,

alone and in combination with other CMB measurements, using models containing defects. The conclusion of the first part of the analysis has been clear: defects in general give a poor fit to the signal and thus the measured B-modes cannot be solely produced by cosmic defects. However, as we have determined, they can assist other primary sources such as primordial gravitational waves or astrophysical dust in fitting high-ℓ points. In general, as it was observed in previous works, astrophysical dust gives the best-fit to data, indicating that the ordinary astrophysics can account for the BICEP2 measurements. New and improved constraints are obtained for different defects considering a mixed dust plus defect model: $G\mu < 2.7 \times 10^{-7}$ at 95% C.L. for Abelian Higgs strings, $G\mu < 9.8 \times 10^{-7}$ at 95% C.L. for semilocal strings and $G\mu < 7.3 \times 10^{-7}$ at 95% C.L. for textures. These constraints are tighter than ones found by the *Planck* collaboration, which shows the importance that even the current B-mode polarization data has for constraining topological defects.

In Chapter 3 we have presented updated energy-momentum correlations and CMB power spectra for Abelian Higgs cosmic strings. Approximations and assumptions of previous works have been revisited and re-examinated in order to update predictions of field theory simulations of AH cosmic strings, mainly motivated by the increasingly accurate observational measurements of the CMB anisotropies in both temperature and polarization channels. We have performed the biggest field theory simulations of the AH model to date, which lead to a considerable increase in the simulated volume (x64) and dynamical range of the simulations. This has several effects, on the one hand we have been able to simulate four times longer in the core growth approximation, which enabled to directly simulate regions that could only be reached by extrapolation in previous works. Approximation of previous works has been successfully confirmed by the outcome of our longer simulations. On the other, the scaling regime has been achieved for the first time following the real equations of motion, both in radiation and in matter eras. We have observed that correlators of different simulations, with and without core growth approximation, compared at same simulation stages determined by the characteristic length of the system, are very similar. Taking advantage of this, the most reliable correlations from simulations of the real equations of motion and data from small-scales and high time ratios are incorporated in the new merged structure for the energy-momentum correlators. The treatment and computation of source functions, essential for CMB calculations, at cosmological transitions have also been improved. We have performed the first numerical simulations at cosmological transitions, *i.e.* radiation-matter and matter-Λ transitions, with which a new UETC interpolation method at transitions as well as new transition functions have been derived. The new method avoids inconsistencies of previous procedures, fits naturally into the structure of Einstein-Boltzmann integrators and is more accurate than previous methods in reproducing the real transition UETCs. Finally, armed with all innovations listed above we have update CMB power spectra predictions for AH cosmic strings. They differ considerably from previous results, mostly in the amplitude where new predictions are significantly higher, due to the new interpolation function that makes the radiation-matter transition significantly slower.

The final Chapter focuses on field theory simulations of interconnected superstring networks. In order to characterize some of the properties of such fundamental string networks, field theory simulations, based on effective models, can be used to reproduce the cosmological dynamics of interconnected string networks and bound states. Previous numerical simulations confirmed that bound states are constantly formed in field theoretical models and that such networks are compatible with the scale invariant evolution, which is an indispensable requirement for the cosmological survival of defect networks. Nevertheless discrepancies with theoretical predictions were indicated: the length and lifetime of pq bound states and their relevance in the overall dynamics were smaller than expected. We have tried to determine whether these discrepancies appear as a consequence

of limited dynamical range of previous works or something more fundamental was behind. Such a investigation has been performed using a new type of simulation, where strings have been combined so as to produce an entire network of bound states from the beginning of the simulations, coexisting with another cosmic string network. From combined simulations we have found that the overall evolution of the networks forces pq-strings to unzip into its constituents, but the left-over population of bound states is higher than the one in previous simulations, where strings were not combined. Combined simulations also scale better than normal simulations where strings are not combined. We also observe some hints indicating that the evolution of the combined simulations tend to an asymptotic evolution, where, for instance, the physical length of pq-strings remains constant. We expect that bigger normal simulations, *i.e.* without string combination, eventually would reach this asymptotic evolution. Moreover, we believe that the procedure of string combination could be very useful in saving computational time and cost, since the network archives scale invariant regime faster and better. Finally we also measure, for the first time, velocities of the network and pq-strings, using field theoretical estimators.

Bibliography

[1] `http://montepython.net`.

[2] Datasets and most relevant publications can be found in the following webpage: http://www.cosmos.esa.int/web/planck, .

[3] `rssd.esa.int/SA/PLANCK/docs/eslab47/Session09_Data_Processing/47ESLAB_April_04_10_30_Aumont.pdf`, .

[4] Datasets and most relevant publications can be found in the following webpage: http://map.gsfc.nasa.gov/.

[5] A. A. Abrikosov. On the Magnetic properties of superconductors of the second group. *Sov. Phys. JETP*, 5:1174–1182, 1957. [Zh. Eksp. Teor. Fiz.32,1442(1957)].

[6] F. S. Accetta and L. M. Krauss. The stochastic gravitational wave spectrum resulting from cosmic string evolution. *Nucl. Phys.*, B319:747, 1989.

[7] A. Achucarro and R. de Putter. Effective non-intercommutation of local cosmic strings at high collision speeds. *Phys. Rev.*, D74:121701, 2006.

[8] A. Achúcarro and T. Vachaspati. Semilocal and electroweak strings. *Phys.Rept.*, 327: 347–426, 2000.

[9] A. Achúcarro, A. Avgoustidis, A. Leite, A. Lopez-Eiguren, C. Martins, et al. Evolution of Semilocal String Networks: I. Large-scale Properties. *Phys.Rev.*, D89:063503, 2014.

[10] R. Adam et al. Planck intermediate results. XXX. The angular power spectrum of polarized dust emission at intermediate and high Galactic latitudes. 2014.

[11] R. Adam et al. Planck 2015 results. I. Overview of products and scientific results. 2015.

[12] P. Ade et al. Measurement of the Cosmic Microwave Background Polarization Lensing Power Spectrum with the POLARBEAR experiment. *Phys.Rev.Lett.*, 113:021301, 2014.

[13] P. Ade et al. Planck 2013 results. XV. CMB power spectra and likelihood. *Astron.Astrophys.*, 571:A15, 2014.

[14] P. Ade et al. Planck 2013 results. XXV. Searches for cosmic strings and other topological defects. *Astron.Astrophys.*, 571:A25, 2014.

[15] P. Ade et al. Planck 2013 results. XVI. Cosmological parameters. *Astron.Astrophys.*, 571: A16, 2014.

[16] P. Ade et al. BICEP2 I: Detection Of B-mode Polarization at Degree Angular Scales. *Phys. Rev. Lett.*, 112:241101, 2014.

[17] P. Ade et al. Planck 2015 results. XX. Constraints on inflation. 2015.

[18] P. Ade et al. Joint Analysis of BICEP2/$Keck$âĂŤ$Array$ and $Planck$ Data. *Phys.Rev.Lett.*, 114(10):101301, 2015.

[19] P. A. R. Ade et al. A Measurement of the Cosmic Microwave Background B-Mode Polarization Power Spectrum at Sub-Degree Scales with POLARBEAR. *Astrophys. J.*, 794(2): 171, 2014.

[20] P. A. R. Ade et al. Planck 2015 results. XIV. Dark energy and modified gravity. 2015.

[21] P. A. R. Ade et al. Planck 2015 results. XIII. Cosmological parameters. 2015.

[22] P. A. R. Ade et al. BICEP2 / Keck Array VI: Improved Constraints On Cosmology and Foregrounds When Adding 95 GHz Data From Keck Array. 2015.

[23] A. Albrecht, R. A. Battye, and J. Robinson. The Case against scaling defect models of cosmic structure formation. *Phys. Rev. Lett.*, 79:4736–4739, 1997.

[24] A. Albrecht, R. A. Battye, and J. Robinson. Detailed study of defect models for cosmic structure formation. *Phys.Rev.*, D59:023508, 1999.

[25] M. R. Anderson, F. Bonjour, R. Gregory, and J. Stewart. Effective action and motion of a cosmic string. *Phys.Rev.*, D56:8014–8028, 1997.

[26] H. Arodz. Expansion in the width: The case of vortices. *Nucl.Phys.*, B450:189–208, 1995.

[27] M. Aryal, A. Everett, A. Vilenkin, and T. Vachaspati. Cosmic string networks. *Phys.Rev.*, D34:434–439, 1986.

[28] B. Audren, J. Lesgourgues, K. Benabed, and S. Prunet. Conservative Constraints on Early Cosmology: an illustration of the Monte Python cosmological parameter inference code. *JCAP*, 1302:001, 2013.

[29] B. Audren, D. G. Figueroa, and T. Tram. A note of clarification: BICEP2 and Planck are not in tension. 2014.

[30] A. Avgoustidis and E. Shellard. Velocity-Dependent Models for Non-Abelian/Entangled String Networks. *Phys.Rev.*, D78:103510, 2008.

[31] A. Avgoustidis, E. Copeland, A. Moss, L. Pogosian, A. Pourtsidou, et al. Constraints on the fundamental string coupling from B-mode experiments. *Phys.Rev.Lett.*, 107:121301, 2011.

[32] A. Avgoustidis, E. J. Copeland, A. Moss, and D. Skliros. Fast Analytic Computation of Cosmic String Power Spectra. *Phys.Rev.*, D86:123513, 2012.

[33] A. Avgoustidis, A. Pourtsidou, and M. Sakellariadou. Zipping and Unzipping in String Networks: Dynamics of Y-junctions. *Phys. Rev.*, D91(2):025022, 2015.

[34] N. A. Bahcall and P. Bode. The Amplitude of mass fluctuations. *Astrophys. J.*, 588:L1–L4, 2003.

[35] N. A. Bahcall et al. The Cluster mass function from early SDSS data: Cosmological implications. *Astrophys. J.*, 585:182–190, 2003.

[36] R. Battye and A. Moss. Updated constraints on the cosmic string tension. *Phys.Rev.*, D82: 023521, 2010.

[37] R. Battye, B. Garbrecht, and A. Moss. Tight constraints on F- and D-term hybrid inflation scenarios. *Phys.Rev.*, D81:123512, 2010.

[38] R. A. Battye, J. Robinson, and A. Albrecht. Structure formation by cosmic strings with a cosmological constant. *Phys. Rev. Lett.*, 80:4847–4850, 1998.

[39] R. A. Battye, B. Garbrecht, and A. Moss. Constraints on Supersymmetric Models of Hybrid Inflation. *JCAP*, 0609:007, 2006.

[40] B. A. Berg. Introduction to Markov chain Monte Carlo simulations and their statistical analysis. 2004.

[41] L. M. A. Bettencourt, P. Laguna, and R. A. Matzner. Nonintercommuting cosmic strings. *Phys. Rev. Lett.*, 78:2066–2069, 1997.

[42] N. Bevis, M. Hindmarsh, M. Kunz, and J. Urrestilla. CMB power spectrum contribution from cosmic strings using field-evolution simulations of the Abelian Higgs model. *Phys.Rev.*, D75:065015, 2007.

[43] N. Bevis, M. Hindmarsh, M. Kunz, and J. Urrestilla. CMB polarization power spectra contributions from a network of cosmic strings. *Phys.Rev.*, D76:043005, 2007.

[44] N. Bevis, M. Hindmarsh, M. Kunz, and J. Urrestilla. Fitting CMB data with cosmic strings and inflation. *Phys.Rev.Lett.*, 100:021301, 2008.

[45] N. Bevis, M. Hindmarsh, M. Kunz, and J. Urrestilla. CMB power spectra from cosmic strings: predictions for the Planck satellite and beyond. *Phys.Rev.*, D82:065004, 2010.

[46] J. J. Blanco-Pillado, K. D. Olum, and B. Shlaer. Large parallel cosmic string simulations: New results on loop production. *Phys.Rev.*, D83:083514, 2011.

[47] J. J. Blanco-Pillado, K. D. Olum, and B. Shlaer. A new parallel simulation technique. *J.Comput.Phys.*, 231:98–108, 2012.

[48] J. J. Blanco-Pillado, K. D. Olum, and B. Shlaer. The number of cosmic string loops. *Phys. Rev.*, D89(2):023512, 2014.

[49] D. Blas, J. Lesgourgues, and T. Tram. The Cosmic Linear Anisotropy Solving System (CLASS) II: Approximation schemes. *JCAP*, 1107:034, 2011.

[50] S. I. Blinnikov and M. Yu. Khlopov. On possible effects of 'mirror' particles. *Sov. J. Nucl. Phys.*, 36:472, 1982. [Yad. Fiz.36,809(1982)].

[51] C. Bonvin, R. Durrer, and R. Maartens. Can primordial magnetic fields be the origin of the BICEP2 data? *Phys.Rev.Lett.*, 112:191303, 2014.

[52] M. Bridges, J. D. McEwen, M. Cruz, M. P. Hobson, A. N. Lasenby, P. Vielva, and E. Martinez-Gonzalez. Bianchi VII_h models and the cold spot texture. *Mon. Not. Roy. Astron. Soc.*, 390:1372, 2008.

[53] B. Carter and R. Gregory. Curvature corrections to dynamics of domain walls. *Phys.Rev.*, D51:5839–5846, 1995.

[54] C. Contaldi, M. Hindmarsh, and J. Magueijo. The Power spectra of CMB and density fluctuations seeded by local cosmic strings. *Phys.Rev.Lett.*, 82:679–682, 1999.

[55] E. J. Copeland and T. Kibble. Cosmic Strings and Superstrings. *Proc.Roy.Soc.Lond.*, A466: 623–657, 2010.

[56] E. J. Copeland, R. C. Myers, and J. Polchinski. Cosmic F and D strings. *JHEP*, 0406:013, 2004.

[57] E. J. Copeland, L. Pogosian, and T. Vachaspati. Seeking String Theory in the Cosmos. *Class.Quant.Grav.*, 28:204009, 2011.

[58] R. A. C. Croft, W. Hu, and R. Dave. Cosmological Limits on the Neutrino Mass from the Lya Forest. *Phys. Rev. Lett.*, 83:1092–1095, 1999.

[59] M. Cruz, N. Turok, P. Vielva, E. Martinez-Gonzalez, and M. Hobson. A Cosmic Microwave Background feature consistent with a cosmic texture. *Science*, 318:1612–1614, 2007.

[60] M. Cruz, E. Martinez-Gonzalez, P. Vielva, J. M. Diego, M. Hobson, and N. Turok. The CMB cold spot: texture, cluster or void? *Mon. Not. Roy. Astron. Soc.*, 390:913, 2008.

[61] T. Damour and A. Vilenkin. Gravitational wave bursts from cosmic strings. *Phys.Rev.Lett.*, 85:3761–3764, 2000.

[62] T. Damour and A. Vilenkin. Gravitational wave bursts from cusps and kinks on cosmic strings. *Phys.Rev.*, D64:064008, 2001.

[63] T. Damour and A. Vilenkin. Gravitational radiation from cosmic (super)strings: Bursts, stochastic background, and observational windows. *Phys.Rev.*, D71:063510, 2005.

[64] D. Daverio, M. Hindmarsh, M. Kunz, J. Lizarraga, and J. Urrestilla. Energy-momentum correlations for Abelian Higgs cosmic strings. 2015.

[65] D. Daverio, M. Hindmarsh, M. Kunz, J. Lizarraga, and J. Urrestilla. *In preparation*, 2016.

[66] D. Daverio, M. Hindmarsh, M. Kunz, J. Lizarraga, and J. Urrestilla. *In preparation*, 2016.

[67] D. David, M. Hindmarsh, and N. Bevis. Latfield2: A c++ library for classical lattice field theory. 2015.

[68] A. C. Davis and T. W. B. Kibble. Fundamental cosmic strings. *Contemp. Phys.*, 46:313–322, 2005.

[69] D. G. T. Denison, C. C. Holmes, B. K. Mallick, and A. F. M. Smith. *Bayesian Methods for Nonlinear Classification and Regression*. Wiley, 2002. URL `http://www.wiley.com/WileyCDA/WileyTitle/productCd-0471490369,descCd-tableOfContents.html`.

[70] M. R. DePies and C. J. Hogan. Stochastic Gravitational Wave Background from Light Cosmic Strings. *Phys. Rev.*, D75:125006, 2007.

[71] K. Dimopoulos. Primordial magnetic fields from superconducting cosmic strings. *Phys. Rev.*, D57:4629–4641, 1998.

[72] M. Doran. CMBEASY: an object oriented code for the cosmic microwave background. *JCAP*, 0510:011, 2005.

[73] F. Dubath, J. Polchinski, and J. V. Rocha. Cosmic String Loops, Large and Small. *Phys.Rev.*, D77:123528, 2008.

[74] J.-F. Dufaux, D. G. Figueroa, and J. Garcia-Bellido. Gravitational Waves from Abelian Gauge Fields and Cosmic Strings at Preheating. *Phys. Rev.*, D82:083518, 2010.

[75] J. Dunkley, R. Hlozek, J. Sievers, V. Acquaviva, P. Ade, et al. The Atacama Cosmology Telescope: Cosmological Parameters from the 2008 Power Spectra. *Astrophys.J.*, 739:52, 2011.

[76] R. Durrer. Gauge invariant cosmological perturbation theory: A General study and its application to the texture scenario of structure formation. *Fund. Cosmic Phys.*, 15:209–339, 1994.

[77] R. Durrer and M. Kunz. Cosmic microwave background anisotropies from scaling seeds: Generic properties of the correlation functions. *Phys.Rev.*, D57:R3199–R3203, 1998.

[78] R. Durrer, M. Kunz, and A. Melchiorri. Cosmic microwave background anisotropies from scaling seeds: Global defect models. *Phys.Rev.*, D59:123005, 1999.

[79] R. Durrer, M. Kunz, and A. Melchiorri. Cosmic structure formation with topological defects. *Phys.Rept.*, 364:1–81, 2002.

[80] R. Durrer, D. G. Figueroa, and M. Kunz. Can Self-Ordering Scalar Fields explain the BICEP2 B-mode signal? 2014.

[81] G. Dvali and A. Vilenkin. Formation and evolution of cosmic D strings. *JCAP*, 0403:010, 2004.

[82] C. Dvorkin, M. Wyman, and W. Hu. Cosmic String constraints from WMAP and the South Pole Telescope. *Phys.Rev.*, D84:123519, 2011.

[83] V. R. Eke, S. Cole, C. S. Frenk, and J. P. Henry. Measuring omega(0) using cluster evolution. *Mon. Not. Roy. Astron. Soc.*, 298:1145, 1998.

[84] S. M. Feeney, M. C. Johnson, D. J. Mortlock, and H. V. Peiris. A robust constraint on cosmic textures from the cosmic microwave background. *Phys. Rev. Lett.*, 108:241301, 2012.

[85] E. Fenu, D. G. Figueroa, R. Durrer, and J. Garcia-Bellido. Gravitational waves from self-ordering scalar fields. *JCAP*, 0910:005, 2009.

[86] E. Fenu, D. G. Figueroa, R. Durrer, J. García-Bellido, and M. Kunz. Cosmic Microwave Background temperature and polarization anisotropies from the large-N limit of global defects. *Phys. Rev.*, D89:083512, 2013.

[87] D. G. Figueroa, R. R. Caldwell, and M. Kamionkowski. Non-Gaussianity from Self-Ordering Scalar Fields. *Phys. Rev.*, D81:123504, 2010.

[88] D. G. Figueroa, M. Hindmarsh, and J. Urrestilla. Exact Scale-Invariant Background of Gravitational Waves from Cosmic Defects. *Phys.Rev.Lett.*, 110(10):101302, 2013.

[89] R. Flauger, J. C. Hill, and D. N. Spergel. Toward an Understanding of Foreground Emission in the BICEP2 Region. 2014.

[90] D. Forster. Dynamics of Relativistic Vortex Lines and their Relation to Dual Theory. *Nucl.Phys.*, B81:84, 1974.

[91] A. A. Fraisse, C. Ringeval, D. N. Spergel, and F. R. Bouchet. Small-Angle CMB Temperature Anisotropies Induced by Cosmic Strings. *Phys.Rev.*, D78:043535, 2008.

[92] J. Garcia-Bellido, R. Durrer, E. Fenu, D. G. Figueroa, and M. Kunz. The local B-polarization of the CMB: a very sensitive probe of cosmic defects. *Phys. Lett.*, B695:26–29, 2011.

[93] J. T. Giblin, Jr., L. R. Price, X. Siemens, and B. Vlcek. Gravitational Waves from Global Second Order Phase Transitions. *JCAP*, 1211:006, 2012.

[94] J. H. Goldstein et al. Estimates of cosmological parameters using the CMB angular power spectrum of ACBAR. *Astrophys. J.*, 599:773–785, 2003.

[95] A. H. Guth. The Inflationary Universe: A Possible Solution to the Horizon and Flatness Problems. *Phys. Rev.*, D23:347–356, 1981.

[96] D. Hanson et al. Detection of B-mode Polarization in the Cosmic Microwave Background with Data from the South Pole Telescope. *Phys. Rev. Lett.*, 111(14):141301, 2013.

[97] E. R. Harrison. Fluctuations at the threshold of classical cosmology. *Phys. Rev.*, D1: 2726–2730, 1970.

[98] B. Hartmann and J. Urrestilla. Gravitating (field theoretical) cosmic (p,q)-superstrings. *JHEP*, 07:006, 2008.

[99] W. K. Hastings. Monte Carlo sampling methods using Markov chains and their applications. *Biometrika*, 57(1):97–109, Apr. 1970. ISSN 1464-3510. URL `http://dx.doi.org/10.1093/biomet/57.1.97`.

[100] E. Hawkins et al. The 2dF Galaxy Redshift Survey: correlation functions, peculiar velocities and the matter density of the Universe. *Mon. Not. Roy. Astron. Soc.*, 346:78, 2003.

[101] M. Hindmarsh. Existence and stability of semilocal strings. *Phys.Rev.Lett.*, 68:1263–1266, 1992.

[102] M. Hindmarsh. Semilocal topological defects. *Nucl.Phys.*, B392:461–492, 1993.

[103] M. Hindmarsh. Signals of Inflationary Models with Cosmic Strings. *Prog.Theor.Phys.Suppl.*, 190:197–228, 2011.

[104] M. Hindmarsh and T. Kibble. Cosmic strings. *Rept.Prog.Phys.*, 58:477–562, 1995.

[105] M. Hindmarsh and A. Rajantie. Defect formation and local gauge invariance. *Phys.Rev.Lett.*, 85:4660–4663, 2000.

[106] M. Hindmarsh and P. Saffin. Scaling in a $SU(2)/Z_3$ model of cosmic superstring networks. *JHEP*, 0608:066, 2006.

[107] M. Hindmarsh, C. Ringeval, and T. Suyama. The CMB temperature bispectrum induced by cosmic strings. *Phys.Rev.*, D80:083501, 2009.

[108] M. Hindmarsh, S. Stuckey, and N. Bevis. Abelian Higgs Cosmic Strings: Small Scale Structure and Loops. *Phys.Rev.*, D79:123504, 2009.

[109] M. Hindmarsh, C. Ringeval, and T. Suyama. The CMB temperature trispectrum of cosmic strings. *Phys.Rev.*, D81:063505, 2010.

[110] G. Hinshaw et al. Nine-Year Wilkinson Microwave Anisotropy Probe (WMAP) Observations: Cosmological Parameter Results. *Astrophys.J.Suppl.*, 208:19, 2013.

[111] C. Hogan and M. Rees. Gravitational interactions of cosmic strings. *Nature*, 311:109–113, 1984.

[112] W. Hu. Lecture Notes on CMB Theory: From Nucleosynthesis to Recombination. *Lecture Notes*, 2008.

[113] E. Hubble. A relation between distance and radial velocity among extra-galactic nebulae. *Proc. Nat. Acad. Sci.*, 15:168–173, 1929.

[114] M. James, L. Perivolaropoulos, and T. Vachaspati. Detailed stability analysis of electroweak strings. *Nucl. Phys.*, B395:534–546, 1993.

[115] R. Jeannerot, J. Rocher, and M. Sakellariadou. How generic is cosmic string formation in SUSY GUTs. *Phys.Rev.*, D68:103514, 2003.

[116] N. T. Jones, H. Stoica, and S. H. Tye. The Production, spectrum and evolution of cosmic strings in brane inflation. *Phys.Lett.*, B563:6–14, 2003.

[117] K. Kajantie, M. Karjalainen, M. Laine, J. Peisa, and A. Rajantie. Thermodynamics of gauge invariant U(1) vortices from lattice Monte Carlo simulations. *Phys.Lett.*, B428:334–341, 1998.

[118] R. Keisler et al. A Measurement of the Damping Tail of the Cosmic Microwave Background Power Spectrum with the South Pole Telescope. *Astrophys. J.*, 743:28, 2011.

[119] T. Kibble. Topology of Cosmic Domains and Strings. *J.Phys.*, A9:1387–1398, 1976.

[120] J. B. Kogut and L. Susskind. Hamiltonian Formulation of Wilson's Lattice Gauge Theories. *Phys. Rev.*, D11:395–408, 1975.

[121] E. Komatsu et al. Seven-Year Wilkinson Microwave Anisotropy Probe (WMAP) Observations: Cosmological Interpretation. *Astrophys.J.Suppl.*, 192:18, 2011.

[122] M. Kunz and R. Durrer. Microwave background anisotropies induced by global scalar fields: The Large N limit. *Phys.Rev.*, D55:4516–4520, 1997.

[123] D. Larson et al. Seven-Year Wilkinson Microwave Anisotropy Probe (WMAP) Observations: Power Spectra and WMAP-Derived Parameters. *Astrophys. J. Suppl.*, 192:16, 2011.

[124] A. Lazanu and P. Shellard. Constraints on the Nambu-Goto cosmic string contribution to the CMB power spectrum in light of new temperature and polarisation data. *JCAP*, 1502 (02):024, 2015.

[125] A. Lazanu, E. Shellard, and M. Landriau. CMB power spectrum of Nambu-Goto cosmic strings. *Phys.Rev.*, D91(8):083519, 2015.

[126] J. Lesgourgues. The Cosmic Linear Anisotropy Solving System (CLASS) I: Overview. 2011.

[127] A. Lewis and S. Bridle. Cosmological parameters from CMB and other data: A Monte Carlo approach. *Phys. Rev.*, D66:103511, 2002.

[128] A. R. Liddle and D. H. Lyth. COBE, gravitational waves, inflation and extended inflation. *Phys. Lett.*, B291:391–398, 1992.

[129] A. D. Linde. A New Inflationary Universe Scenario: A Possible Solution of the Horizon, Flatness, Homogeneity, Isotropy and Primordial Monopole Problems. *Phys.Lett.*, B108: 389–393, 1982.

[130] J. Lizarraga, I. Sendra, and J. Urrestilla. Correlations between cosmic strings and extra relativistic species. *Phys. Rev.*, D86:123014, 2012.

[131] J. Lizarraga, J. Urrestilla, D. Daverio, M. Hindmarsh, M. Kunz, and A. R. Liddle. Can topological defects mimic the BICEP2 B-mode signal? *Phys.Rev.Lett.*, 112:171301, 2014.

[132] J. Lizarraga, J. Urrestilla, D. Daverio, M. Hindmarsh, M. Kunz, et al. Constraining topological defects with temperature and polarization anisotropies. *Phys.Rev.*, D90(10):103504, 2014.

[133] L. Lorenz, C. Ringeval, and M. Sakellariadou. Cosmic string loop distribution on all length scales and at any redshift. *JCAP*, 1010:003, 2010.

[134] C.-P. Ma and E. Bertschinger. Cosmological perturbation theory in the synchronous and conformal Newtonian gauges. *Astrophys. J.*, 455:7–25, 1995.

[135] M. Maggiore. Gravitational wave experiments and early universe cosmology. *Phys. Rept.*, 331:283–367, 2000.

[136] M. Majumdar and A. Christine-Davis. Cosmological creation of D-branes and anti-D-branes. *JHEP*, 0203:056, 2002.

[137] G. Mangano, G. Miele, S. Pastor, T. Pinto, O. Pisanti, and P. D. Serpico. Relic neutrino decoupling including flavor oscillations. *Nucl. Phys.*, B729:221–234, 2005.

[138] J. Martin, C. Ringeval, R. Trotta, and V. Vennin. Compatibility of Planck and BICEP2 in the Light of Inflation. 2014.

[139] C. Martins and E. Shellard. Extending the velocity dependent one scale string evolution model. *Phys.Rev.*, D65:043514, 2002.

[140] C. J. A. P. Martins and E. P. S. Shellard. Quantitative string evolution. *Phys. Rev.*, D54: 2535–2556, 1996.

[141] P. McDonald et al. The Linear theory power spectrum from the Lyman-alpha forest in the Sloan Digital Sky Survey. *Astrophys. J.*, 635:761–783, 2005.

[142] N. Metropolis, A. W. Rosenbluth, M. N. Rosenbluth, A. H. Teller, and E. Teller. Equation of State Calculations by Fast Computing Machines. *The Journal of Chemical Physics*, 21(6): 1087–1092, June 1953. ISSN 0021-9606. URL `http://dx.doi.org/10.1063/1.1699114`.

[143] C. W. Misner, K. S. Thorne, and J. A. Wheeler. *Gravitation*. W. H. Freeman, San Francisco, 1973.

[144] J. Moore, E. Shellard, and C. Martins. On the evolution of Abelian-Higgs string networks. *Phys.Rev.*, D65:023503, 2002.

[145] K. J. M. Moriarty, E. Myers, and C. Rebbi. Dynamical Interactions of Flux Vortices in Superconductors. *Phys. Lett.*, B207:411, 1988.

[146] M. J. Mortonson and U. Seljak. A joint analysis of Planck and BICEP2 B modes including dust polarization uncertainty. 2014.

[147] A. Moss and L. Pogosian. Did BICEP2 see vector modes? First B-mode constraints on cosmic defects. *Phys.Rev.Lett.*, 112:171302, 2014.

[148] P. Mukherjee, J. Urrestilla, M. Kunz, A. R. Liddle, N. Bevis, et al. Detecting and distinguishing topological defects in future data from the CMBPol satellite. *Phys.Rev.*, D83: 043003, 2011.

[149] S. Naess et al. The Atacama Cosmology Telescope: CMB Polarization at $200 < \ell < 9000$. *JCAP*, 1410(10):007, 2014.

[150] H. B. Nielsen and P. Olesen. Vortex Line Models for Dual Strings. *Nucl.Phys.*, B61:45–61, 1973.

[151] M. Obradovic, M. Kunz, M. Hindmarsh, and I. T. Iliev. Particle motion in weak relativistic gravitational fields. *Phys.Rev.*, D86:064018, 2012.

[152] S. Olmez, V. Mandic, and X. Siemens. Gravitational-Wave Stochastic Background from Kinks and Cusps on Cosmic Strings. *Phys.Rev.*, D81:104028, 2010.

[153] K. D. Olum and V. Vanchurin. Cosmic string loops in the expanding Universe. *Phys.Rev.*, D75:063521, 2007.

[154] U.-L. Pen, D. N. Spergel, and N. Turok. Cosmic structure formation and microwave anisotropies from global field ordering. *Phys. Rev.*, D49:692–729, 1994.

[155] U.-L. Pen, U. Seljak, and N. Turok. Power spectra in global defect theories of cosmic structure formation. *Phys.Rev.Lett.*, 79:1611–1614, 1997.

[156] A. A. Penzias and R. W. Wilson. A Measurement of excess antenna temperature at 4080-Mc/s. *Astrophys. J.*, 142:419–421, 1965.

[157] W. J. Percival et al. Baryon Acoustic Oscillations in the Sloan Digital Sky Survey Data Release 7 Galaxy Sample. *Mon.Not.Roy.Astron.Soc.*, 401:2148–2168, 2010.

[158] L. Pogosian and T. Vachaspati. Cosmic microwave background anisotropy from wiggly strings. *Phys.Rev.*, D60:083504, 1999.

[159] J. Polchinski. Introduction to cosmic F- and D-strings. pages 229–253, 2004.

[160] J. Polchinski and J. V. Rocha. Analytic study of small scale structure on cosmic strings. *Phys.Rev.*, D74:083504, 2006.

[161] J. Polchinski and J. V. Rocha. Cosmic string structure at the gravitational radiation scale. *Phys.Rev.*, D75:123503, 2007.

[162] W. H. Press, B. S. Ryden, and D. N. Spergel. Dynamical Evolution of Domain Walls in an Expanding Universe. *Astrophys. J.*, 347:590–604, 1989.

[163] A. Rajantie. Formation of topological defects in gauge field theories. *Int.J.Mod.Phys.*, A17: 1–44, 2002.

[164] A. Rajantie. Defect formation in the early universe. *Contemp. Phys.*, 44:485–502, 2003.

[165] A. Rajantie. 'Phase transitions in the early universe' and 'Defect formation'. In *COSLAB Workshop on Cosmological Phase Transitions and Topological Defects Porto, Portugal, May 22-24, 2003*, 2003.

[166] A. Rajantie, M. Sakellariadou, and H. Stoica. Numerical experiments with p F- and q D-strings: The Formation of (p,q) bound states. *JCAP*, 0711:021, 2007.

[167] A. C. S. Readhead et al. Extended Mosaic Observations with the Cosmic Background Imager. *Astrophys. J.*, 609:498–512, 2004.

[168] A. Refregier, A. Amara, T. D. Kitching, A. Rassat, R. Scaramella, and J. Weller. Euclid Imaging Consortium Science Book. 2010.

[169] D. Regan and E. Shellard. Cosmic String Power Spectrum, Bispectrum and Trispectrum. *Phys.Rev.*, D82:063527, 2010.

[170] C. Reichardt, L. Shaw, O. Zahn, K. Aird, B. Benson, et al. A measurement of secondary cosmic microwave background anisotropies with two years of South Pole Telescope observations. *Astrophys.J.*, 755:70, 2012.

[171] A. G. Riess, L. Macri, S. Casertano, M. Sosey, H. Lampeitl, et al. A Redetermination of the Hubble Constant with the Hubble Space Telescope from a Differential Distance Ladder. *Astrophys.J.*, 699:539–563, 2009.

[172] C. Ringeval, M. Sakellariadou, and F. Bouchet. Cosmological evolution of cosmic string loops. *JCAP*, 0702:023, 2007.

[173] J. V. Rocha. Scaling solution for small cosmic string loops. *Phys.Rev.Lett.*, 100:071601, 2008.

[174] P. Saffin. A Practical model for cosmic (p,q) superstrings. *JHEP*, 0509:011, 2005.

[175] M. Sakellariadou. A Note on the evolution of cosmic string/superstring networks. *JCAP*, 0504:003, 2005.

[176] M. Sakellariadou and H. Stoica. Dynamics of F/D networks: The Role of bound states. *JCAP*, 0808:038, 2008.

[177] S. Sarangi and S. H. Tye. Cosmic string production towards the end of brane inflation. *Phys.Lett.*, B536:185–192, 2002.

[178] M. Sazhin and M. Khlopov. Cosmic strings and gravitational lens effects. *SOVIET ASTRONOMY*, 33(1):98, 1989.

[179] R. J. Scherrer and A. Vilenkin. 'Lattice-free' simulations of topological defect formation. *Phys.Rev.*, D58:103501, 1998.

[180] I. Sendra and T. L. Smith. Improved limits on short-wavelength gravitational waves from the cosmic microwave background. *Phys. Rev.*, D85:123002, 2012.

[181] Q. Shafi and A. Vilenkin. Spontaneously broken global symmetries and cosmology. *Phys.Rev.*, D29:1870, 1984.

[182] E. Shellard. Cosmic String Interactions. *Nucl.Phys.*, B283:624–656, 1987.

[183] B. Shlaer, A. Vilenkin, and A. Loeb. Early structure formation from cosmic string loops. *JCAP*, 1205:026, 2012.

[184] X. Siemens and K. D. Olum. Gravitational radiation and the small scale structure of cosmic strings. *Nucl. Phys.*, B611:125–145, 2001. [Erratum: Nucl. Phys.B645,367(2002)].

[185] X. Siemens and K. D. Olum. Cosmic string cusps with small scale structure: Their forms and gravitational wave forms. *Phys. Rev.*, D68:085017, 2003.

[186] X. Siemens, J. Creighton, I. Maor, S. Ray Majumder, K. Cannon, et al. Gravitational wave bursts from cosmic (super)strings: Quantitative analysis and constraints. *Phys.Rev.*, D73: 105001, 2006.

[187] X. Siemens, V. Mandic, and J. Creighton. Gravitational wave stochastic background from cosmic (super)strings. *Phys.Rev.Lett.*, 98:111101, 2007.

[188] J. L. Sievers et al. The Atacama Cosmology Telescope: Cosmological parameters from three seasons of data. *JCAP*, 1310:060, 2013.

[189] K. M. Smith, C. Dvorkin, L. Boyle, N. Turok, M. Halpern, et al. On quantifying and resolving the BICEP2/Planck tension over gravitational waves. 2014.

[190] T. L. Smith, E. Pierpaoli, and M. Kamionkowski. A new cosmic microwave background constraint to primordial gravitational waves. *Phys. Rev. Lett.*, 97:021301, 2006.

[191] G. F. Smoot et al. Structure in the COBE differential microwave radiometer first year maps. *Astrophys. J.*, 396:L1–L5, 1992.

[192] K. Sousa and J. Urrestilla. CMB Anisotropies by Collapsing Textures. *Springer Proc. Math. Stat.*, 60:409–413, 2014.

[193] D. Spergel and U.-L. Pen. Cosmology in a string dominated universe. *Astrophys.J.*, 491: L67–L71, 1997.

[194] K. Story, C. Reichardt, Z. Hou, R. Keisler, K. Aird, et al. A Measurement of the Cosmic Microwave Background Damping Tail from the 2500-square-degree SPT-SZ survey. *Astrophys.J.*, 779:86, 2013.

[195] M. Tegmark et al. Cosmological parameters from SDSS and WMAP. *Phys. Rev.*, D69: 103501, 2004.

[196] N. Turok. Causality and the Doppler peaks. *Phys.Rev.*, D54:3686–3689, 1996.

[197] N. Turok. A Causal source which mimics inflation. *Phys. Rev. Lett.*, 77:4138–4141, 1996.

[198] N. Turok and D. Spergel. Global Texture and the Microwave Background. *Phys.Rev.Lett.*, 64:2736, 1990.

[199] S.-H. H. Tye, I. Wasserman, and M. Wyman. Scaling of multi-tension cosmic superstring networks. *Phys.Rev.*, D71:103508, 2005.

[200] J. Urrestilla and A. Vilenkin. Evolution of cosmic superstring networks: A Numerical simulation. *JHEP*, 0802:037, 2008.

[201] J. Urrestilla, N. Bevis, M. Hindmarsh, M. Kunz, and A. R. Liddle. Cosmic microwave anisotropies from BPS semilocal strings. *JCAP*, 0807:010, 2008.

[202] J. Urrestilla, P. Mukherjee, A. R. Liddle, N. Bevis, M. Hindmarsh, et al. Degeneracy between primordial tensor modes and cosmic strings in future CMB data from the Planck satellite. *Phys.Rev.*, D77:123005, 2008.

[203] J. Urrestilla, N. Bevis, M. Hindmarsh, and M. Kunz. Cosmic string parameter constraints and model analysis using small scale Cosmic Microwave Background data. *JCAP*, 1112: 021, 2011.

[204] T. Vachaspati. Electroweak strings. *Nucl. Phys.*, B397:648–671, 1993.

[205] T. Vachaspati and A. Achúcarro. Semilocal cosmic strings. *Phys.Rev.*, D44:3067–3071, 1991.

[206] T. Vachaspati and A. Vilenkin. Gravitational Radiation from Cosmic Strings. *Phys.Rev.*, D31:3052, 1985.

[207] T. Vachaspati and A. Vilenkin. Evolution of cosmic networks. *Phys.Rev.*, D35:1131, 1987.

[208] L. Van Waerbeke et al. Cosmic shear statistics and cosmology. *Astron. Astrophys.*, 374: 757–769, 2001.

[209] V. Vanchurin, K. D. Olum, and A. Vilenkin. Scaling of cosmic string loops. *Phys.Rev.*, D74:063527, 2006.

[210] G. J. Verbiest and A. Achucarro. High speed collision and reconnection of Abelian Higgs strings in the deep type-II regime. *Phys. Rev.*, D84:105036, 2011.

[211] P. T. P. Viana, R. C. Nichol, and A. R. Liddle. Constraining the matter power spectrum normalization using the SDSS/RASS and reflex cluster surveys. *Astrophys. J.*, 569:L75, 2002.

[212] P. Vielva, E. Martinez-Gonzalez, M. Cruz, R. B. Barreiro, and M. Tucci. CMB polarization as a probe of the anomalous nature of the Cold Spot. *Mon. Not. Roy. Astron. Soc.*, 410: 33, 2011.

[213] A. Vilenkin. Gravitational radiation from cosmic strings. *Phys. Lett.*, B107:47–50, 1981.

[214] A. Vilenkin and E. Shellard. *Cosmic strings and other topological defects*. Cambridge University Press, 1994.

[215] G. R. Vincent, M. Hindmarsh, and M. Sakellariadou. Scaling and small scale structure in cosmic string networks. *Phys.Rev.*, D56:637–646, 1997.

[216] E. T. Vishniac, K. A. Olive, and D. Seckel. Cosmic Strings and Inflation. *Nucl.Phys.*, B289: 717, 1987.

[217] S. Weinberg. *Gravitation and Cosmology*. John Wiley and Sons, New York, 1972. ISBN 0471925675, 9780471925675. URL `http://www-spires.fnal.gov/spires/find/books/www?cl=QC6.W431`.

[218] M. Wyman, L. Pogosian, and I. Wasserman. Bounds on cosmic strings from WMAP and SDSS. *Phys.Rev.*, D72:023513, 2005.

[219] J. Yokoyama. Natural way out of the conflict between cosmic strings and inflation. *Phys.Lett.*, B212:273, 1988.

[220] J. Yokoyama. Inflation can save cosmic strings. *Phys.Rev.Lett.*, 63:712, 1989.

[221] Ya. B. Zeldovich. A Hypothesis, unifying the structure and the entropy of the universe. *Mon. Not. Roy. Astron. Soc.*, 160:1P–3P, 1972.

[222] W. Zurek. Cosmological Experiments in Superfluid Helium? *Nature*, 317:505–508, 1985.

[223] W. Zurek. Cosmological experiments in condensed matter systems. *Phys.Rept.*, 276:177–221, 1996.